

NASA Technical Memorandum 4091

Superconducting Gravity Gradiometer Mission

Volume II: Study Team Technical Report

Edited by

Samuel H. Morgan

George C. Marshall Space Flight Center

Marshall Space Flight Center, Alabama

Ho Jung Paik

University of Maryland

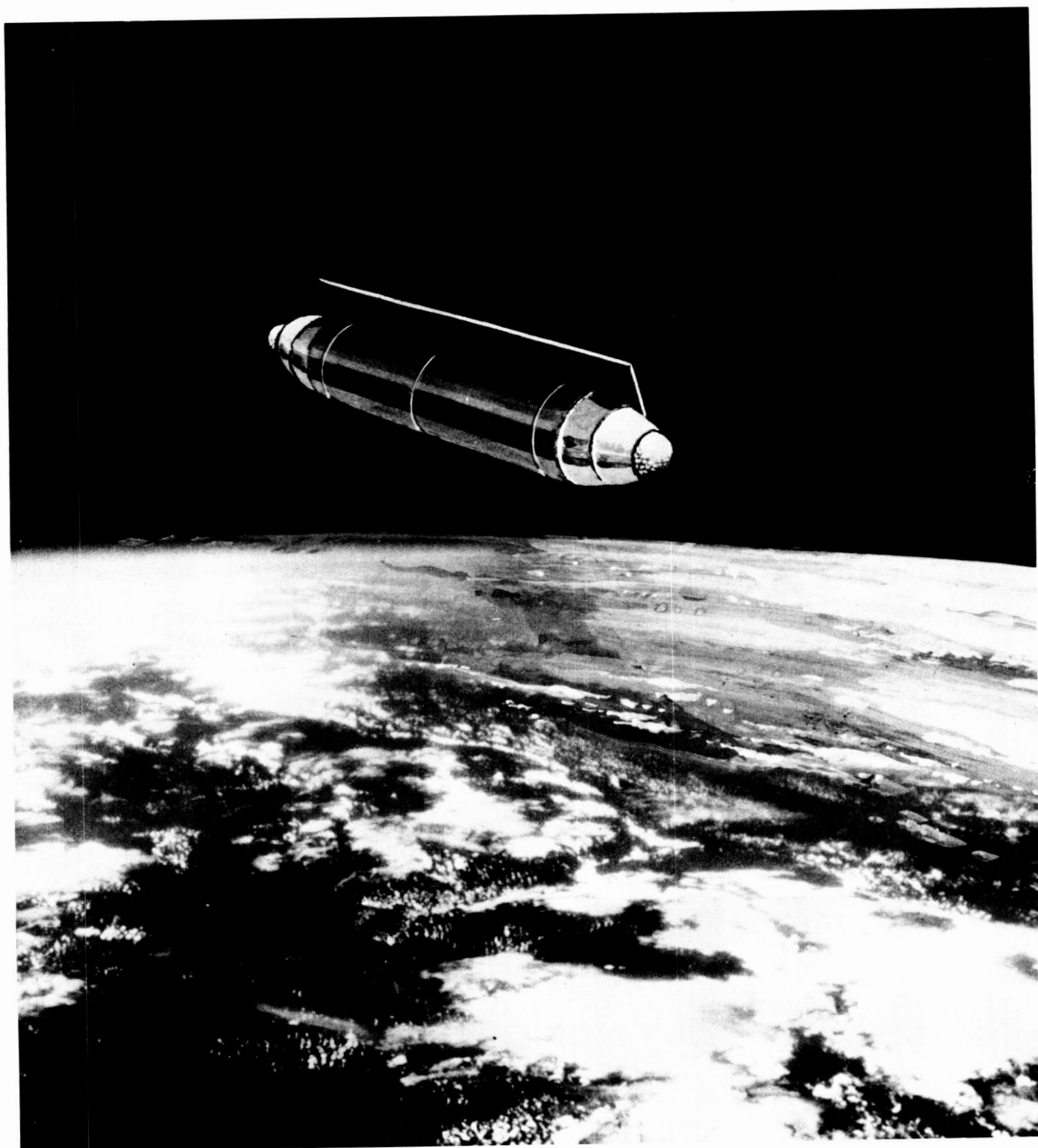
College Park, Maryland



National Aeronautics
and Space Administration

Scientific and Technical
Information Division

1988



ORIGINAL PAGE IS
OF POOR QUALITY

ORIGINAL PAGE IS
OF POOR QUALITY

FOREWORD

Accurate knowledge of the Earth's gravity field is fundamental to geophysics, oceanography, and geodesy. Since 1958, NASA has used artificial satellites and space platforms to measure and map the Earth's gravity. Currently, the gravity field is derived indirectly through global measurement of satellite perturbations or over the oceans by means of satellite altimetry. Each of these techniques has severe limitations in obtaining the required resolution and accuracy needed to address the important scientific problems.

During the past two decades, serious efforts have been made to develop moving-base gradiometers. Spaceborne gradiometers will permit dense, precise, and direct global measurements of gravity. An advanced gradiometer, utilizing superconducting technology, has been under development for the past several years through NASA, Air Force, and Army sponsorship. The Superconducting Gravity Gradiometer (SGG) promises to meet the science and applications requirements for the 1990's in both measurement accuracy (a few mgal) and spatial resolution (50 km). In addition, the SGG can be applied to tests of fundamental laws of physics and navigation. Recent advances at the very frontier of physics, the unification of the fundamental forces of Nature into one grand law, predict a departure from Newton's inverse square law of gravitation. A test of the gravitational inverse square law of unprecedented precision could be made utilizing a spaceborne SGG.

In 1985, the various federal and university activities involved with the development of the SGG were brought together under a study team to develop a total system concept for a space-qualified three-axis SGG integrated with a six-axis accelerometer. This report discusses the science and applications objectives of the SGG mission (SGGM), the instrument requirements and design, preliminary mission concepts, an analysis of a flight test program, and the study team's recommendations and proposed plan for achieving a SGG satellite mission. A companion volume, "Volume I: Study Team Executive Summary Report," presents a synopsis of this study.

TABLE OF CONTENTS

	Page
SGG STUDY TEAM MEMBERSHIP	x
1.0 INTRODUCTION	1
2.0 SCIENCE AND APPLICATIONS OBJECTIVES.....	6
2.1 Primary Mission Objectives: Geophysics	6
2.1.1 Introduction.....	7
2.1.2 The Lithosphere.....	8
2.1.3 The Mantle	12
2.1.4 Oceanography	18
2.1.5 Temporal Variations in Gravity	21
2.1.6 Summary	25
2.2 Secondary Mission Objectives: Fundamental Laws of Physics.....	27
2.2.1 Null Test of Gravitational Inverse Square Law	27
2.2.2 New Tests of General Relativity	30
2.3 Additional Objectives and Potential Spinoffs.....	33
2.3.1 Inertial Navigation.....	33
2.3.2 Orbit Calculations	34
2.3.3 Planetary Science.....	35
2.3.4 Other Applications.....	35
3.0 SUPERCONDUCTING GRAVITY GRADIOMETER	38
3.1 Instrument and Platform Requirements	38
3.1.1 Geophysics	39
3.1.2 Inverse Square Law Experiment.....	45
3.1.3 Gravitomagnetic Field Experiment	48
3.2 Instrument Design.....	51
3.2.1 Three-Axis Superconducting Gravity Gradiometer	51
3.2.2 Six-Axis Superconducting Accelerometer	55
3.2.3 Six-Axis Shaker.....	58
3.3 Status of Instrument Development.....	58
3.4 Ground Test Requirements.....	62
4.0 MISSION AND SPACECRAFT CONCEPTS	65
4.1 Orbit Selection	66
4.1.1 Spacecraft Orientation Considerations	69

TABLE OF CONTENTS (Continued)

	Page
4.2 Spacecraft Alternative Concepts.....	71
4.2.1 Experiment Module.....	71
4.2.2 Attitude Control Considerations.....	82
4.2.3 Summary of Alternative Concepts	89
4.2.4 Other Potential Carriers	91
4.2.5 Launch and Descent Phase.....	92
4.3 Option I: Earth-Fixed or Inertial Mode.....	93
4.3.1 Option I-A: Ion Propulsion	93
4.3.2 Option I-B: Hydrazine Propulsion.....	107
4.3.3 Summary	111
4.4 Option II: Earth-Fixed Mode.....	111
4.4.1 Option II-A: Cylindrical Spacecraft	112
4.4.2 Option II-B: Modified GRM Spacecraft	116
4.4.3 Summary	119
5.0 FLIGHT TEST PROGRAM	123
5.1 Flight Test Objectives	124
5.2 Instrument Calibration.....	125
5.3 Shuttle Attached Options	126
5.3.1 Low Cost Approach.....	126
5.3.2 Soft-Mounted Mode	129
5.3.3 Free-Floating Mode	131
5.4 Shuttle Detached Option	131
6.0 STATUS AND POTENTIAL OF TECHNOLOGY ADVANCES	136
6.1 Guidance, Navigation, and Control.....	136
6.2 Instrument Cooling	136
6.3 High-Temperature Superconductivity.....	138
6.4 Propulsion.....	139
7.0 CONCLUSIONS AND RECOMMENDATIONS	140
7.1 Conclusions	140
7.1.1 Program.....	140
7.1.2 Instrument	140
7.1.3 Mission.....	140

TABLE OF CONTENTS (Concluded)

	Page
7.2 Recommendations	142
7.2.1 Program	142
7.2.2 Instrument	142
7.2.3 Mission	142
REFERENCES	144
APPENDICES	
A. BACKGROUND ON GRAVITY	153
B. GRADIOMETRY FUNDAMENTALS	157
C. ERROR ANALYSIS FOR A GRADIOMETER MISSION	167
D. NULL TEST OF INVERSE SQUARE LAW	173
E. SUPERCONDUCTING GRAVITY GRADIOMETER	179
F. PREDICTED DISTURBANCES	187
G. CONTROL SYSTEM SIMULATION	207

LIST OF ILLUSTRATIONS

Figure	Title	Page
1-1.	Elements of SGGM program	4
2-1.	Schematic model of crustal structure and the predicted (Bouger or free air) gravity anomaly over a completely eroded orogen	11
2-2.	(a) The observed geoid at spherical harmonic degrees 2 to 9; (b) the predicted geoid from mantle tomography for a rigid Earth	15
2-3.	Schematic diagram showing constant density surfaces (dashed lines) and pressure gradient forces (arrows) through a western boundary current such as the Gulf Stream in geostrophic balance.....	20
2-4.	Present-day rate of change in the radial position of the surface of the solid Earth calculated from simplified model of postglacial rebound.....	23
2-5.	Summary of requirements for gravity measurement accuracy as a function of spatial resolution for the problems discussed in Section 2	26
2-6.	Forces in Nature	28
2-7.	Expected resolution of α as a function of λ for $\nabla^2 \phi$ experiments in Earth orbit (dotted lines).....	30
3-1.	Superconducting Gravity Gradiometer	37
3-2.	RMS signal amplitudes for vertical-vertical component of gravity gradient tensor as function of harmonic degree for two altitudes	40
3-3.	Angular pattern of gravity gradiometer response to a spherical mass.....	46
3-4.	Single-axis portion of the three-axis SGG.....	52
3-5.	Cross sectional view of one of the six accelerometers of the three-axis SGG.....	53
3-6.	Expected sensitivity of the SGG as a function of signal frequency	54
3-7.	Six-axis superconducting accelerometer	55
3-8.	Expected (a) linear acceleration and (b) angular acceleration sensitivities of SSA as functions of signal frequency.....	56
3-9.	Three-axis SGG and the SSA mounted on the six-axis shaker	57

LIST OF ILLUSTRATIONS (Continued)

Figure	Title	Page
3-10.	Three-axis SGG and SSA control block diagram	59
3-11.	SGG development schedule	61
4-1.	SGGM alternative spacecraft concepts	64
4-2.	Gravity gradiometer orbital lighting geometry	67
4-3.	Time in 100 percent Sun and time in Earth's shadow per orbit	68
4-4.	Ground track for SGGM	69
4-5.	Spacecraft orbital orientation options	70
4-6.	Characteristics of candidate dewars	73
4-7.	Comparison of SGGM dewar concept and COBE dewar	75
4-8.	SGG Experiment Module concept	77
4-9.	SGG Experiment Module concept — modified GRM	79
4-10.	Gravity Probe-B proportional thruster system	81
4-11.	Experiment Module isolation utilizing cryogen vent gas for control	83
4-12.	SGGM spacecraft pointing	84
4-13.	Attitude control module block diagram	86
4-14.	SGG control block diagram	87
4-15.	Linear acceleration controller	88
4-16.	Comparison of SGGM spacecraft concepts	90
4-17.	SGGM descent to operational orbit — propellant requirements	92
4-18.	Free flyer spherical configuration — ion propulsion	94
4-19.	Multimission Modular Spacecraft module location	96
4-20.	Propellant requirements as function of drag versus specific impulse	97
4-21.	Required xenon propellant for six-month mission and volumetric penalty versus specific impulse	98

LIST OF ILLUSTRATIONS (Continued)

Figure	Title	Page
4-22.	Power transmission block diagram and requirements for free floating Experiment Module option.....	100
4-23.	Xenon ion thruster performance	101
4-24.	Option I-A power flow diagram and requirements.....	102
4-25.	Thermal control model and requirements	104
4-26.	Heat flux through front face of MLI versus insulation thickness.....	105
4-27.	Required radiator area for removal of heat generated by Experiment Module electronics.....	106
4-28.	Communications and data management system using MMS.....	109
4-29.	Option I-B (hydrazine propulsion) spacecraft configuration	110
4-30.	Option II-A (Earth-fixed only) spacecraft configuration	113
4-31.	Thruster sizing impact on translational and attitude stability.....	115
4-32.	GRM propulsion system schematic diagram.....	117
4-33.	Option II-A, solar array characteristics.....	118
4-34.	Option II-A, power flow diagram.....	119
4-35.	Option II-B, modified GRM concept	120
5-1.	SGG Flight Test modes	122
5-2.	Orbiter pointing capability.....	127
5-3.	SGG Flight Test configuration - modified IRT hardware.....	128
5-4.	Suspended experiment mount concepts for soft mounting	130
5-5.	SGGM Flight Test - free-floating mode concept	132
5-6.	Comparison of spartan capabilities and SGG flight experiment requirements	133
5-7.	SGG Flight Test - detached mode concept	134

LIST OF TABLES

Table	Title	Page
3-1.	Required Control/Knowledge of Instrument and Platform Parameters for Geodesy	42
3-2.	Additional Required Control/Knowledge of Instrument and Platform Parameters for Inverse Square Law Experiment	45
3-3.	Required Control/Knowledge of Instrument and Platform Parameters for Gravitomagnetic Field Experiment in Earth-Fixed Orientation.....	50
3-4.	Power Requirements Estimate	60
3-5.	Major Research Tasks Achieved.....	62
4-1.	Baseline Orbit Characteristics for SGGM	67
4-2.	Ground Rules and Assumptions for SGG Dewar Design	72
4-3.	Experiment Module Weight/Size Summary	78
4-4.	Option I-A and I-B Weight Summaries.....	95
4-5.	Weight and Power Requirements for Thermal Control	106
4-6.	C&DH Requirements and Characteristics.....	108
4-7.	Comparison of Ion and Hydrazine Propulsion Systems for SGGM	112
4-8.	Option II-A Weight Summary	114
5-1.	Summary of Flight Test Options	123
5-2.	Weight Summary for SGG Flight Utilizing IRT Hardware	129
6-1.	Cryogenic Cooling Techniques	137
7-1.	Typical SGGM Error Sources.....	143

SUPERCONDUCTING GRAVITY GRADIOMETER
STUDY TEAM

Dr. Samuel H. Morgan	Marshall Space Flight Center	Study Manager
Dr. Ho Jung Paik	University of Maryland	Instrument PI
Dr. Rudolf Decher	Marshall Space Flight Center	
Mr. Tom Fischetti	Technology Management Consultants, Inc.	
Mr. Seymor Kant	Goddard Space Flight Center	
Dr. Andrew Lazarewicz	Air Force Geophysics Laboratory	
Dr. Marcia McNutt	Massachusetts Institute of Technology	
Dr. M. Vol Moody	University of Maryland	
Dr. David Sonnabend	Jet Propulsion Laboratory	
Dr. Eugene Urban	Marshall Space Flight Center	

Former Study Team Members

Dr. H. Baussus von Luetzow	U. S. Army Engineer Topographic Laboratories
Dr. H. Anthony Chan	University of Maryland
Mr. Charles J. Finley	NASA Headquarters
Capt. Terry J. Fundak	Air Force Geophysics Laboratory
Mr. Werner D. Kahn	Goddard Space Flight Center
Dr. Jurn-Sun Leung	University of Maryland
Mr. Joe Parker	Marshall Space Flight Center

GEOFYSICS SCIENCE RATIONALE

The Geophysics Science Rationale in this report was obtained from a Science Workshop held at the Air Force Academy, Colorado Springs, Colorado, during February 8-9, 1987. The complete workshop report is published separately [1]. The workshop participants were:

Dr. Marcia McNutt, Chairperson	Massachusetts Institute of Technology
Dr. John Apel	APL, Johns Hopkins University
Dr. Lindrith Cordell	U.S. Geological Survey
Mr. Charles J. Finley	NASA Headquarters
Mr. Thomas Fischetti	Technology Management Consultants, Inc.
Dr. Edward A. Flinn	NASA Headquarters
Dr. Bradford Hager	California Institute of Technology
Dr. Albert Hsui	Air Force Geophysics Laboratory
Dr. Andrew Lazarewicz	Air Force Geophysics Laboratory
Dr. Ho Jung Paik	University of Maryland
Dr. David Sandwell	University of Texas
Dr. David Smith	Goddard Space Flight Center
Dr. David Sonnadend	Jet Propulsion Laboratory
Dr. Louis Walter	Goddard Space Flight Center

ACKNOWLEDGMENTS

The Study Team wishes to thank the following individuals for their contributions to the work summarized in this report:

NASA Headquarters

Dr. Edward A. Flinn, Chief of NASA's Geodynamics Branch, provided overall review and guidance.

Marshall Space Flight Center

The Engineering Study Team in the Preliminary Design Office of the Program Development Directorate. Mr. Joe Parker was the lead engineer for this study team.

Mr. M. E. Nein, Advanced Systems Office, assisted in the Conceptual Design of Option I-B.

Dr. G. S. Nurre and Dr. Michael E. Polites, System Dynamics Laboratory, provided contributions on the analysis of the Attitude Control System.

Ms. Gail Ralls and Ms. Carol Key of the Advanced Systems Office typed the report.

Jet Propulsion Laboratory

Dr. Emanuel Tward provided portions of the information on instrument cooling discussed in Section 4.2.1.

Goddard Space Flight Center

Mr. Tom Keating of the GSFC Advanced Mission Analysis Office, the GRM Manager, provided contributions related to the GRM spacecraft and systems.

Other University and Industrial Contributors

Dr. Huseyin Iz (ST Systems Corporation) and Dr. Richard H. Rapp (Ohio State University) made major contributions on error analysis for satellite gradiometry that are presented in this report as Appendix C.

Dr. John R. Glaese, Ms. Karen A. Bishop, and Mr. Thomas G. Howsman (Control Dynamics Company) performed the control system simulation presented in Appendix G.

ABBREVIATIONS AND ACRONYMS

ACS	Attitude Control System
AFGL	Air Force Geophysics Laboratory
AFOSR	Air Force Office of Scientific Research
BOL	Beginning of Life
C&DH	Communications and Data Handling
COBE	Cosmic Background Explorer
DISCOS	Disturbance Compensation System
DOD	Department of Defense
EOL	End of Life
EOS	Earth Observing System
EPS	Electric Power System
ESA	European Space Agency
ESSA	Electrically Steerable Spherical Array
ETL	Army Engineers Topographic Laboratories
GNC	Guidance, Navigation and Control
GP-B	Gravity Probe-B
GPS	Global Positioning System
GRADIO	Satellite Gradiometer Mission
GRM	Geopotential Research Mission
GSFC	Goddard Space Flight Center
GUT	Grand Unification Theory
HST	Hubble Space Telescope
IMU	Inertial Measuring Unit
INS	Inertial Navigation System
IRAS	Infrared Astronomy Satellite
IRT	Infrared Telescope
IRU	Inertial Reference Unit
JPL	Jet Propulsion Laboratory
LAGEOS	Laser Geodynamics Satellite
MLI	Multilayer Insulation
MMS	Multimission Modular Spacecraft
MPES	Multi-Purpose Experiment Supporting Structure
MSFC	Marshall Space Flight Center
NAS	National Academy of Sciences
NASA	National Aeronautics and Space Administration
QCD	Quantum Chromodynamics

ABBREVIATIONS AND ACRONYMS (Concluded)

QED	Quantum Electrodynamics
RCS	Reaction Control System
RIU	Remote Interface Unit
RTG	Radioisotope Thermoelectric Generator
SAFE	Solar Array Flight Experiment
SEM	Suspended Experiment Mount
SEPS	Solar Electric Propulsion System
SGG	Superconducting Gravity Gradiometer
SGGM	Superconducting Gravity Gradiometer Mission
SQUID	Superconducting Quantum Interference Device
SSA	Six-Axis Superconducting Accelerometer
STS	Space Transportation System
TDRSS	Tracking Data Relay Satellite System
TOPEX	Ocean Topography Experiment
TRASYS	Thermal Radiation Analysis System
TSS	Tethered Satellite System

DEFINITION OF SYMBOLS

<u>Symbol</u>	<u>Definition</u>
a	Equatorial radius of Earth
α	Coupling constant of non-Newtonian potential
α	Thermal absorption factor
b/sec	Bits/second
β	Coupling constant of transducer
c	Velocity of light
C'_{ij}	Centrifugal acceleration tensor in the instrument coordinate
$ \delta \hat{n} $	Magnitude of misalignment vector
$\delta \hat{n}_{+\ell}$	Misalignment vector of gradiometer sensitive axes with respect to the baseline
$\delta \hat{n}_-$	Misalignment vector of gradiometer sensitive axes with respect to each other
$\partial v / \partial i$	SQUID transfer function
$\delta \sigma_{23}$	Scale factor mismatch
E	Unit of acceleration gradient (10^{-9} sec^{-2})
$E_A(f)$	Input energy resolution of SQUID
ϵ	Dimensionless parameter characterizing the relativistic "electric" correction to gravity gradient
ϵ	Thermal emittance factor
η	Coupling coefficient of SQUID
f	Frequency (Hz)
f	Gradiometer signal frequency
f_o	Resonance frequency of proof mass
$(\Delta f)_{\ell}$	Effective bandwidth of measurement for ℓ -th harmonic component
F_D	External disturbance forces on spacecraft
F_E	Internal disturbance forces on spacecraft
G	Universal gravitation constant

<u>Symbol</u>	<u>Definition</u>
g	Earth's gravitational acceleration
gal	Acceleration of $10^{-2} \text{ m sec}^{-2}$
Γ_{ij}	Gravity gradient tensor
$\vec{\Gamma}_E$	Earth's gravity gradient tensor
I_1, I_2	Persistent current in a superconducting loop
I_{SP}	Specific impulse of propulsion system (seconds)
J_2	Harmonic coefficient corresponding to the oblateness of the Earth
\vec{J}_E	Angular momentum vector of Earth
k_B	Boltzmann's constant
ℓ	Gradiometer baseline
ℓ	Degree of spherical harmonic
λ	Range of non-Newtonian gravitational potential
λ	Geocentric latitude angle
λ	Wavelength of Earth's gravity field
m	Mass of proof mass
M_E	Mass of Earth
μ	Dimensionless parameter characterizing the relativistic "magnetic" correction to gravity gradient
\hat{n}	$\hat{n} = (\eta_\eta, \eta_\xi, \eta_\zeta)$ unit vector pointing in direction of measurement
Ω	Satellite attitude rate
Ω_E	Angular rate of the Earth
Ω_O	Orbital angular velocity of satellite
$\vec{\Omega}$	$\vec{\Omega} = (\Omega_r, \Omega_\theta, \Omega_\phi)$ angular velocity of SGG with respect to inertial frame
P	Pressure
$P_\ell(\cos \theta)$	Normalized Legendre polynomial of degree ℓ
Pa	Unit of pressure ($N \text{ m}^{-2}$)

<u>Symbol</u>	<u>Definition</u>
ψ	Angle of instrument orientation with respect to North
Φ	Gravitational potential
Φ	Geopotential
Φ_g	Gravity potential of Earth
Φ_r	Rotational potential of Earth
Φ_t	Tidal potential of Earth
ϕ	Geocentric longitude
$Q(f)$	Effective quality factor of proof mass
r	Radial distance of mass to center of source
r	Orbital radius from center of Earth
R_E	Radius of Earth
R_{ojo}^i	Riemann tensor
$R_{\mu\nu}$	Ricci tensor
ρ	Density
ρ_w	Density of sea water
S	Block size for gravity map (degrees)
$S_{\Gamma, \ell}(f)$	Required gravity gradient instrument noise power spectral density for harmonic degree ℓ
$S_{\Gamma}(f)$	Gravity gradient instrument noise power spectral density
T	Temperature (K)
T	Mission duration
T_c	Transition temperature for superconductivity
$T_{\mu\nu}$	Energy-momentum tensor
τ	Proper time
θ	Geocentric colatitude (referred to North Pole)
\vec{u}	Geostrophic velocity
η	Surface elevation

TECHNICAL MEMORANDUM

SUPERCONDUCTING GRAVITY GRADIOMETER MISSION

Volume II: Study Team Technical Report

1.0 INTRODUCTION

During the past three decades measurements and observations from space have stimulated a major revolution in Earth Science. Fundamental new knowledge of the Earth, its continents, oceans, atmosphere, biosphere, and ice covers has revealed a complex and dynamic Earth system that could only have been imagined before the era of space observations. This scientific revolution has in turn increased the need for new and more accurate observations and data in order to understand this complex system. Fundamental to Earth Science is knowledge of the Earth's gravitational and magnetic fields.

Within NASA, both the Geodynamics Program and the Solar System Exploration Program require accurate gravity field measurements. In addition, NASA's Astrophysics Program has an interest in gravity measurements that relate to tests of General Relativity and other fundamental laws of physics. The U.S. Department of Defense (DOD) also has vital interests in gravity field measurements and associated technology development for application to positioning and guidance.

Among the goals of the Geodynamics Program is to further understand the solid Earth and ocean dynamics. The Geodynamics Program includes analysis of existing data to produce models of gravity and magnetic fields, scientific interpretations of the models, and the development of instruments and missions that collect better data, improve the models, and advance geophysics. Because of the vital importance of this area, the National Academy of Sciences (NAS) has recommended that "...the determination of an improved gravitational field through space measurements should be an objective of the highest priority ..." [2].

Since 1958, data from over 20 artificial satellites have been utilized to map the gravity field of the Earth [3]. Among the Earth satellite missions being considered by NASA in the near future is a joint gradiometer mission with the European Space Agency (ESA). This mission is designed to measure spatial variations in the Earth's gravity over the entire globe to a resolution of 100 km. This mission concept utilizes the French Gradio gradiometer and U.S. technology for dual-spacecraft suspension and GPS tracking. If approved, this joint mission will occur in late 1993.

During the late 1990's and into the next century, investigations in geodynamics will require even greater sensitivity and resolution than the Gradio could provide. Advanced instrument development has been underway during the past several years to exploit the full advantage the space environment offers for making extremely sensitive gravity measurements. Among the instruments proposed, gravity gradiometers show great promise. The success of the Bell Aerospace/Textron gravity gradiometer, as a navigation aid and as a moving base gravity mapping system, has shown that the measurement of gravity gradients¹ is possible even in the very "noisy" environment

1. Gravity gradient has units of sec^{-2} . However, this unit is too large for real gradients. A more useful unit, the Eötvös (1 Eötvös = $1 \text{ E} = 10^{-9} \text{ sec}^{-2}$) has been defined (see Appendix A).

of ships, aircraft, and land vehicles [4]. Therefore, a gradiometer-based mapping mission, which goes beyond the resolution of the Gradio, is the next logical step in providing the scientific community with more accurate, high resolution geophysics data. A survey of gravity gradiometers for space applications is given in the report of a Spaceborne Gravity Gradiometer Workshop held in 1982 [5]. The gradiometer under development that holds the greatest predicted performance, both for geophysics and other areas of science and applications, is the Superconducting Gravity Gradiometer (SGG).

An SGG with a sensitivity of $10^{-4} \text{ E Hz}^{-1/2}$ is under development to meet the gravity field measurement objectives discussed in the next section. The Superconducting Gravity Gradiometer Mission (SGGM) will include a three-axis SGG integrated with a Six-Axis Superconducting Accelerometer (SSA) and carried on a single satellite to map the Earth's gravitational field. Another promising orbital application of the SGG is to test fundamental laws of physics. For example, the SGGM would provide an excellent opportunity to carry out a much desired test of the Newtonian gravitational inverse square law with high precision on the distance scale of 10 to 10^4 km (see Appendix D). Tests of the General Theory of Relativity, Einstein's theory of gravity, could also be made with an SGG instrument of sufficient sensitivity. In particular, it appears possible to detect the Lense-Thirring term in gravity gradient that is produced by the angular momentum of the Earth. In addition to these orbital applications, there are also a number of other applications for both the accelerometer alone and the integrated gradiometer/accelerometer system.

Cryogenic technology is essential for obtaining very sensitive gravity measurements because of the very weak nature of the gravitational interaction. Superconducting technologies at liquid helium temperatures ($T \leq 4.2 \text{ K}$, the normal boiling point of liquid helium) are very important in realizing highly sensitive and stable gravity sensors in addition to the obvious reduction of thermal noise in the system. Moreover, the properties of superfluid helium and superconductors can be utilized to obtain the very quiet thermal, mechanical, and electromagnetic environments required for the operation of such sensitive instruments.

The superconducting gravity gradiometer and ancillary technologies now under development (see Appendix E) will permit a space mission with a gravity measurement accuracy of a few mgal ($1 \text{ gal} = 1 \text{ cm sec}^{-2}$) and a spatial resolution goal of 50 km for the global gravity map of the Earth, and of achieving a resolution of 10^{-10} for the inverse square law test. An orbital lifetime of six months to a year, at a nominal altitude of 160 to 200 km in polar orbit, is desirable. The cryostat will be kept at a fixed temperature around 1.5 K to take advantage of the properties of superfluid helium. Near infinite heat conductivity of the superfluid eliminates temperature gradients inside the cryostat and prevents helium boiling.

The measurement precision required to address the scientific questions posed for the SGGM dictates platform requirements for very low disturbance levels, precise pointing and control, and isolation from internal and external disturbances that are more severe than most other satellite missions. The required instrument sensitivity makes it impossible to verify the instrument performance unambiguously in Earth-based laboratories. Therefore, critical technologies must be integrated in a precursor Shuttle flight test to verify that the key elements of the science payload will meet the mission requirements, and further to insure an acceptable risk level for the full-duration science mission.

The development of a spaceborne SGG and a related six-axis cryogenic accelerometer at the University of Maryland under joint funding by the National Aeronautics and Space Administration (NASA), the Air Force Geophysics Laboratory (AFGL), and

the U.S. Army Engineer Topographic Laboratories (ETL) has been underway since 1980. Related work (funded by NASA) dealing with gravity field science requirements and with methods for acquisition and analysis of gradiometer data is being conducted by the Goddard Space Flight Center (GSFC). The Jet Propulsion Laboratory (JPL) is studying SGG isolation and in-flight measurements of the SGG parameters. Prior to these activities, the gradiometer development was sponsored at Stanford University by the Air Force Office of Scientific Research (AFOSR) [6].

During the fall of 1985, at the direction of NASA Headquarters and through the cooperation of other agencies, the various federal and university activities were brought together under a Gradiometer Study Team directed by the Marshall Space Flight Center (MSFC). The Study Team membership is listed in the front of this report. The objectives of the Study Team are:

1. To develop a total system concept for a space qualified three-axis superconducting gravity gradiometer integrated with a six-axis superconducting accelerometer.
2. To examine and recommend methods for flight test of the gravity gradiometer package in space.
3. To examine methods for the acquisition, processing, and analysis of space derived gravity gradiometer data.
4. To develop a detailed plan for an initial spaceborne cryogenic gravity gradiometer flight test in the early 1990's.

This report is a summary of the plans and progress made thus far by the Study Team in accomplishing these objectives.

Recommendations for future Earth Science missions have recently been published in a Space Science Board Report [7]. The scientific objectives of the SGG flight mission are twofold: (1) the primary mission objective is to make dense and very accurate measurements of the Earth's gravity field for geophysical studies, and (2) the secondary mission objectives are to carry out tests of fundamental laws of physics. The latter objectives, although considered as secondary for this mission, relate to our fundamental understanding of Nature, and are no less scientifically important than the primary mission goals. Obviously, if both primary and secondary objectives could be accomplished on a single cost-effective mission, one that would address important scientific issues of the geophysics and physics communities, the attractiveness of the SGGM would be greatly enhanced.

Combining both objectives on a single mission will be largely influenced by whether the instrument, spacecraft, and operational requirements for the secondary objectives can be met without severely impacting the primary mission. The decision will ultimately depend on many factors including projected program cost, the success of the instrument development, and support from other discipline areas within NASA and the physics community.

The program requirements necessary to accomplish the SGGM are given in broad outline form in Figure 1-1. Sections in this report where the particular program elements are discussed are indicated within parentheses in the figure. The laboratory development and tests required to produce a space quality SGG instrument and associated systems will proceed in parallel with the development of the flight test

1-800-7

(SECTION 2)

SUPERCONDUCTING GRAVITY GRADIOMETER PROGRAM

PRIMARY OBJECTIVE: GLOBAL GRAVITY MEASUREMENT ACCURATE TO WITHIN A FEW mgal AND RESOLUTION TO 50km

SECONDARY OBJECTIVES: (A) PERFORM NULL TEST OF INVERSE SQUARE LAW OF GRAVITATION TO RESOLUTION OF 10^{-10}
(B) TESTS OF EINSTEIN'S THEORY OF GENERAL RELATIVITY

(SECTION 4)

SGG SCIENCE MISSION

ORBIT SGG MISSION ABOARD FREE FLYING SATELLITE FOR SIX MONTHS TO MEET MISSION OBJECTIVES

(SECTION 5)

SGG SHUTTLE FLIGHT TEST

CONDUCT A FLIGHT TEST OF THE EXPERIMENT MODULE (SGG INSTRUMENT/DEWAR/ ASSOCIATED, SELECTED SYSTEMS) ABOARD SHUTTLE TO VERIFY INSTRUMENT SPACE PERFORMANCE; INSTRUMENT CALIBRATION, NOISE LEVELS;...; VALIDATE ANALYTICAL MODELS.

(SECTION 3)

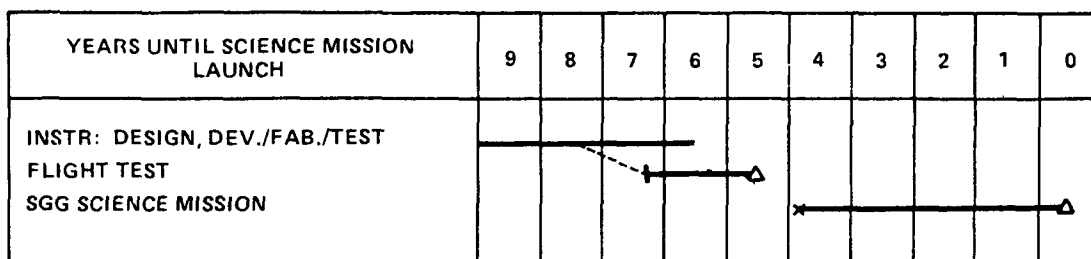
SGG INSTRUMENT DEVELOPMENT/TESTS

EVOLUTIONARY DEVELOPMENT OF 3-AXIS GRADIOMETER INTEGRATED WITH SIX-AXIS ACCELEROMETER AND ASSOCIATED SYSTEMS. ANALYTICALLY VERIFY PERFORMANCE. INSTRUMENT, SELECTED SYSTEMS REUSED FOR FLIGHT TEST.

(SECTION 3,5)

DEVELOPMENT/GROUND TEST OF EXP. MODULE

DEVELOPMENT, FABRICATION AND TEST OF COMPLETE EXPERIMENT MODULE. EARTH TEST OF INTEGRATED FLIGHT TEST EXPERIMENT MODULE.



X - NEW START
△ - FLIGHT MISSION

Figure 1-1. Elements of SGM program.

Experiment Module. (It is anticipated that an upgraded version of the laboratory SGG will be flown in the Shuttle test.) After the space performance of the instrument has been verified through the flight test, a total system including Experiment Module and spacecraft will proceed toward development.

The next two sections of this report discuss the Science and Applications Rationale and Gradiometer Instrument Requirements, respectively. This is followed by a discussion of the instrument design, status, and an outline of the ground test requirements. The preliminary mission analysis and alternative spacecraft concepts are included in Section 4. Section 5 includes options for a proposed flight test program. Section 6 outlines future technology advances that might benefit the SGGM. The final section includes the Recommendations and Conclusions of the Study Team. Appendices are included to elaborate on several areas that are briefly discussed in the text. Included are a general discussion on gradiometer fundamentals, the analysis associated with mapping the gravity field fine structure, technical papers on the null test of the inverse square law and the principle of the superconducting gravity gradiometer, details on some of the disturbances such as atmospheric drag and carrier acceleration levels, and the results of a preliminary computer simulation of the SGGM control system.

The primary purpose of the preliminary engineering study described in this study was to establish feasibility of the SGGM. The products of this analysis include conceptual designs, requirements for tests and developments, engineering analyses, and an identification of items requiring further in-depth study. Additional trade studies, alternative designs and approaches, and certainly more penetrating engineering analyses will emerge in subsequent studies as the program evolves.

2.0 SCIENCE AND APPLICATIONS OBJECTIVES

The primary purpose of this section is to discuss the scientific rationale for the geophysics mission. However, it would be an understatement of the importance of the technology, and the value of the investigations of fundamental laws of physics, if one were to focus on the gravity mapping mission exclusively. Therefore, the physics experiments and several potential applications and spinoffs from the SGG are also discussed in this section.

2.1 Primary Mission Objectives: Geophysics

In rationalizing the need for geophysics data of any type, one tends to, and in fact needs to, presume that more accuracy and higher resolution will provide the needed clues in understanding geophysical phenomena. In the Earth sciences, the quest for information on a larger scale has generally taken a subordinate role to more narrowly defined objectives. Generally, the Earth scientist has made a case for more data only when he needs to prove or disprove a specific theory. Many times, however, new data serves a different master and initiates additional questions and provides new insights into understanding our geophysical environment. Therefore, in addition to the pursuit of measurements for narrowly defined goals aimed at a specific problem, NASA should go beyond the currently projected measurement accuracy and expand the frame of reference for scientific investigations.

The requirements for global gravity data for geophysics investigations to complement other data sources are well documented [4]. Generally, the requirements fall into two general scientific categories, (1) geodynamics and (2) oceanography. The importance of gravity data to both of these areas was highlighted by the following. In 1982, the NAS published a report in which "...the accuracy and scope of the measurements [that would lead to] the greatest scientific advances..." in the Earth sciences were identified [2]. In solid Earth dynamics, the NAS concluded that the measurement of the gravitational field is, by itself, the third primary science objective for the 1980's. Since the measurement of the gravitational field of the Earth is a primary objective for both solid Earth and ocean dynamics, and an important secondary objective for continental geology, the NAS determined that a major improvement in both the accuracy and resolution of the global gravity field is "...an objective of highest priority for the 1980's."

The geophysics rationale in this section is excerpted, verbatim in most cases, from a NASA workshop report [1]. As the design of the SGG evolved, the need for a detailed geophysics rationale grew for this experiment. In the spring of 1987, a diverse team of geoscientists assembled to write this section, reviewing and updating similar previous works. It soon became evident that the team's efforts would be much more productive if its goals were to define the state-of-the-art, and current needs in gravimetry applications not directly related to any particular measurement technique. As a result, the NASA report was written, addressing broadly the various types of gravity data required for the advancement of geophysical understanding of the Earth. This chapter excerpts the relevant sections which pertain specifically to the SGGM. We express grateful appreciation to the authors of the NASA report for their contributions, and by no means intend to take credit for their work. This section is the product of their work and talents.

Before introducing the geophysics rationale, one must understand the quantities one intends to measure, and their relevance to physical quantities (see Appendix A). The fundamental quantity is the gravitational potential (a scalar value), which has little direct and measurable connection with the real world. Gravitational acceleration (a three-component vector) is the first spatial derivative of the potential, and is a directly measurable quantity whose relation to geophysical parameters is well understood. Gravity gradients (a nine-component tensor, five of which are independent) are the first spatial derivatives of gravitational acceleration, or the second spatial derivatives of the gravitational potential. Although gravity gradients are often considered in three components (diagonal elements), the cross components among the derivatives (off-diagonal components) are needed to complete the full tensor form, containing all the information existing in the geopotential and gravity fields. The higher the derivative form, the more detailed information is apparent about the more local structure of the field.

While the potential falls off as r^{-1} , the acceleration fields fall off as r^{-2} , and the gradient fields fall off as r^{-3} . So the higher derivatives "see" a shorter distance, and more detailed structural information is apparent over a more localized area. This means the gravity gradient signals are much weaker than acceleration signals when measured in Earth orbit, and require much more sensitive instrumentation than gravimeters in space. The problem, however, is that gravimeters are in true free fall while in orbit, and the measured acceleration values are close to zero because the Earth's field is exactly opposed by centrifugal force. This is not true for the gravity gradient, which is a function of r^{-3} and has non-vanishing components in all three directions, while the centrifugal acceleration gradient is half the vertical gravity gradient and is in the orbital plane. So, while the gravity gradient is small by nature, it is directly measurable in Earth orbit.

Current gravity models determined from satellite orbits are indirectly derived from satellite tracking. Since the total energy of an orbiting satellite is conserved, the kinetic energy of the orbit is balanced by the gravitational energy, so the gravitational potential can be derived from tracking data. The SGGM uses the superconducting gravity gradiometer which is capable of directly measuring the gradients at orbital altitudes.

With this background, the geophysics rationale for this mission will now be discussed.

2.1.1 Introduction

Increasingly, the concepts of our planet's composition, structure and history are undergoing unification as scientists explore and study the Earth on scales ranging from the global to the sub-microscopic. The description of the gravity field is one of the most important data sets required to gain a comprehensive understanding of the Earth because it reflects a broad spectrum of phenomena over a wide range of spatial scales. For example, on the global scale, the gravity field is affected by the structure and dynamics of the core-mantle boundary and long-range variations in the mantle and the lithosphere. On the continental scale, gravity data provide information on mantle convection and large vertical isostatic adjustments, while on the regional scale, gravity data are necessary for understanding the process of mountain building.

It is clear that the models which must be created cannot be developed using only one type of observation, even if they have been carried out at different spatial scales.

The need to consider a phenomenon from several observational aspects is an integral part of the scientific method: without it, we cannot hope to gain the insights we seek. However, this consideration leads to another important aspect of the gravity field; it reflects, and can be related to, parameters which are derived by other disciplines. For example, the gravity field integrates the effects of variable bulk modulus observed in seismology, the variations in rock density and inferred compositions observed in geochemistry, and lithospheric stresses observed in tectonics. Gravity field data thus serve an important function through integration of other data in model development. Furthermore, such data have been extremely useful in the development of our concepts of the structure, composition and evolution of other planets and the Moon; concepts which are additionally important because, by comparison, they help us learn more about the Earth.

Detailed gravity data have been acquired in some geophysically important areas of the Earth. Additionally, with the advent of the space age, global data sets with broad spatial resolution have become available. Now, the improved technical capabilities of superconducting gravity gradiometers present the possibility of providing precise global gravity data with high spatial resolution which could provide much of the information essential to gaining fundamental understanding of the solid Earth.

This section discusses the role of such gravity measurements in studying and understanding several of the unifying questions in solid Earth science. The discussions include recommendations for the accuracy required to meet the scientific needs. Their achievement can be envisioned through the cryogenic technology currently under development.

2.1.2 The Lithosphere

That satellite gravity field observations can yield major advances in our understanding of the lithosphere has been amply demonstrated. Specifically, altimeter data from SEASAT and GEOS-3 have led to a significant increase in our understanding of the thermo-mechanical structure and evolution of oceanic lithosphere. The potential for accurate global gravity data to improve our understanding of lithospheric properties and processes is even more apparent for the continents, which are considerably more complex and less readily explained by plate tectonic concepts than the ocean basins. For example, evidence is mounting that the differences in the mechanical properties of continental and oceanic lithosphere are not simply explained by the presence of the thick, granitic continental crust, but rather requires thermal and/or compositional differences extending to depths of 200 km or more. At present, gravity data accurate to ± 4 mgal at 100-km resolution are publicly available for only 22 percent of the Earth's land area, with political and geographical barriers preventing further acquisition by means of standard ground surveys. In order to comprehend the origin, evolution, and resource potential of that part of the planet which we inhabit, global gravity missions are a primary scientific priority. Even in the ocean basins, there remain a number of outstanding problems which cannot be addressed by another altimeter mission due to the requirement that the gravity field be continuous at the shoreline. Here, those problems concerning the oceanic and continental lithosphere that could best be addressed by a satellite gradiometer mission are summarized.

2.1.2.a Trenches

The largest gravity anomalies on Earth occur at trenches where oceanic lithosphere is subducted into the mantle. These zones are responsible for creating the

greatest thermal, seismic, and geochemical anomalies found within the Earth. The underthrust plate is flexed and deformed by a number of loads, including stresses from motion relative to the convecting mantle, the weight of the overlying plate, the negative buoyancy of its own cold mass, thermal stress, and the density changes associated with phase changes in the mantle. With sea surface gravity observations [8] and altimeter observations [9], it has been possible to calibrate rheology of the deformed lithosphere. Earthquake hypocenters [10] and travel time anomalies [11] provide maps of the geometry of the downgoing plate. Thermal plate models allow us to calculate the load associated with the cold slab [12]. If one had a gravity of geoid map continuous from the undeformed sea floor, across the outer rise, trench, forearc, and island to the overriding plate, it would be possible to calculate the stresses acting on the underthrust plate, and thereby learn much about lithosphere/asthenosphere interaction and mantle rheology.

2.1.2.b Rifts

Delineation and analysis of active and ancient continental rifts are important for understanding this fundamental element of continental lithosphere tectonics and favored habitat for mineral and petroleum resources. Gravity studies in particular have long been important in the discovery and study of rifts. For example, before the 1300-km long Central North American Rift System [13] was identified as such, it was known as the "mid-continent gravity high" [14]. Gravity studies played a crucial role in the studies of the Rio Grande rift in demonstrating the continuity of geologic structure along what was previously considered to be a string of disjointed and unrelated small basins [15,16]. Gravity also provided the first clue [17] to a buried Pre-Cambrian rift in the Mississippi embayment [18]. Worldwide, any long river or sedimentary basin may indicate a rift, but additional gravity data are generally needed to test the possibility. Scanty gravity data in the Amazon basin, for example, hint at a very large positive gravity anomaly [19]. In combination with extensive intrusive diabase sills, the anomaly suggests a very large rift system. Airborne or orbiting sensors would be especially useful in this area because of its remoteness and the difficulty of surface travel. In North America, hundreds of kilometers of unsuspected, buried fossil rifts have been mapped during the last 20 years, primarily using gravity anomalies or gravity plus aeromagnetic information. The emerging pattern in the American mid-continent is a complicated network of rifts. Doubtless similar networks will be found on other continents, including Antarctica. These are the Earth's stretch marks, their pattern not yet completely mapped nor understood.

Gravity data contribute to the analysis of rifts as well as to their delineation. Mass-budget considerations, as used by Cordell [20], for example, constrain estimates of crustal extension. Gravity, heat flow, and seismic data are, together, the basic tools for estimating thinning of the crust and lithosphere in active rifts [21].

2.1.2.c Batholiths

Batholiths are, in a sense, small rifts, and are another example of a buried geologic feature which can be effectively studied by the gravity method. Batholiths are sought for their associated mineral deposits, but these intrusive bodies have additional, purely scientific interest as well. Batholiths tend to be tabular in shape and their orientation provides a measure of tectonic strain axes at time of emplacement — Nature's hydrofrac experiment. In several cases, such as the mid-Tertiary batholiths in the San Juan Mountains of Colorado [22] and the Southern Rocky Mountains in New Mexico [23], the trends observed are contrary to expectation. In favorable situations, gravity and magnetic anomalies over batholiths can be combined to determine the age

of the intrusive body, by in-situ paleomagnetic methods. Dating by this method is crude, but can be important where large areas are covered by a sedimentary-rock veneer. Most batholiths in true cratonic crust occur in Andean-type convergent margins and the best place to study them is the Cordillera of the Americas. Here, however, gravity coverage is only adequate in the western United States, where relationships are complicated by post-subduction stretching by perhaps 100 percent.

2.1.2.d Sedimentary Basins and Passive Margins

The study of sediment deposits in continental basins and on passive margins has historically been the mainstay of Earth sciences. The accumulation and preservation of fossiliferous strata in sedimentary basins provided the first systematic basis for a geologic time scale. An inventory of the Earth's petroleum reserves begins with an inventory of sedimentary basin-fill volumes, and most geologists and geophysicists make their living thereby.

The principal research topics include: why do basins and margins subside? Why are the same basins periodically reactivated? Do sediment onlap/offlap patterns at passive margins reflect changes in eustatic sea level or temporal variations in lithospheric rheology? Gravity anomalies bear on these problems in several ways. For example, gravity maps of the Michigan Basin reveal a high-density body at the base of the sedimentary strata thought to correspond to a magnetic intrusion [24]. Cooling of this magma body may have supplied the driving force for basic subsidence. Additionally, gravity observations plus data on depths to distinct stratigraphic horizons yield estimates of the elastic thickness of the basin lithosphere as a function of time. The elastic thickness in turn constrains models of the long-term thermal evolution of the basin. Thus, gravity observations supply key information on both the driving forces for basin subsidence and the history of how those forces affect the mechanical behavior of the lithosphere.

Sedimentary basins and their associated oil deposits hidden under ice sheets, allochthonous crystalline rock, and at offshore continental margins probably still remain to be discovered. Global gravity data with ~ 50 km spatial resolution, combined with bathymetry and radar ice-thickness data, would be required here.

2.1.2.e Mountain Belts

Gravity observations have already played a major role recently in completely overturning the accepted notion that mountain belts on the Earth's surface are compensated by simple crustal thickening through a form of Airy isostasy. Karner and Watts [25] noted a consistent asymmetry in the Bouguer gravity field across the Alps and Appalachians. The Bouguer gravity low, which results from the low-density material at depth compensating the excess mass of the mountains, is consistently offset towards the foreland basin to the west of the Appalachians and to the north of the Alps, while a prominent gravity high, unassociated with any topographic feature and not predicted by Airy isostasy, appears in the hinterland on the opposite side of the orogens (Fig. 2-1). Karner and Watts [25] demonstrated that this gravity pattern is consistent with a model in which the mountains are buttressed by a stiff elastic plate which has underthrust the mountains from the direction of the foreland in the process of continent-continent collision. The amplitude of the deflection of the elastic plate, as revealed by the magnitude of the Bouguer gravity low, requires loading by both the mountainous topography and by a buried high-density body in the hinterland, the mass presumably responsible for the Bouguer gravity high. This new model for the structure of mountain belts has thus established the importance of

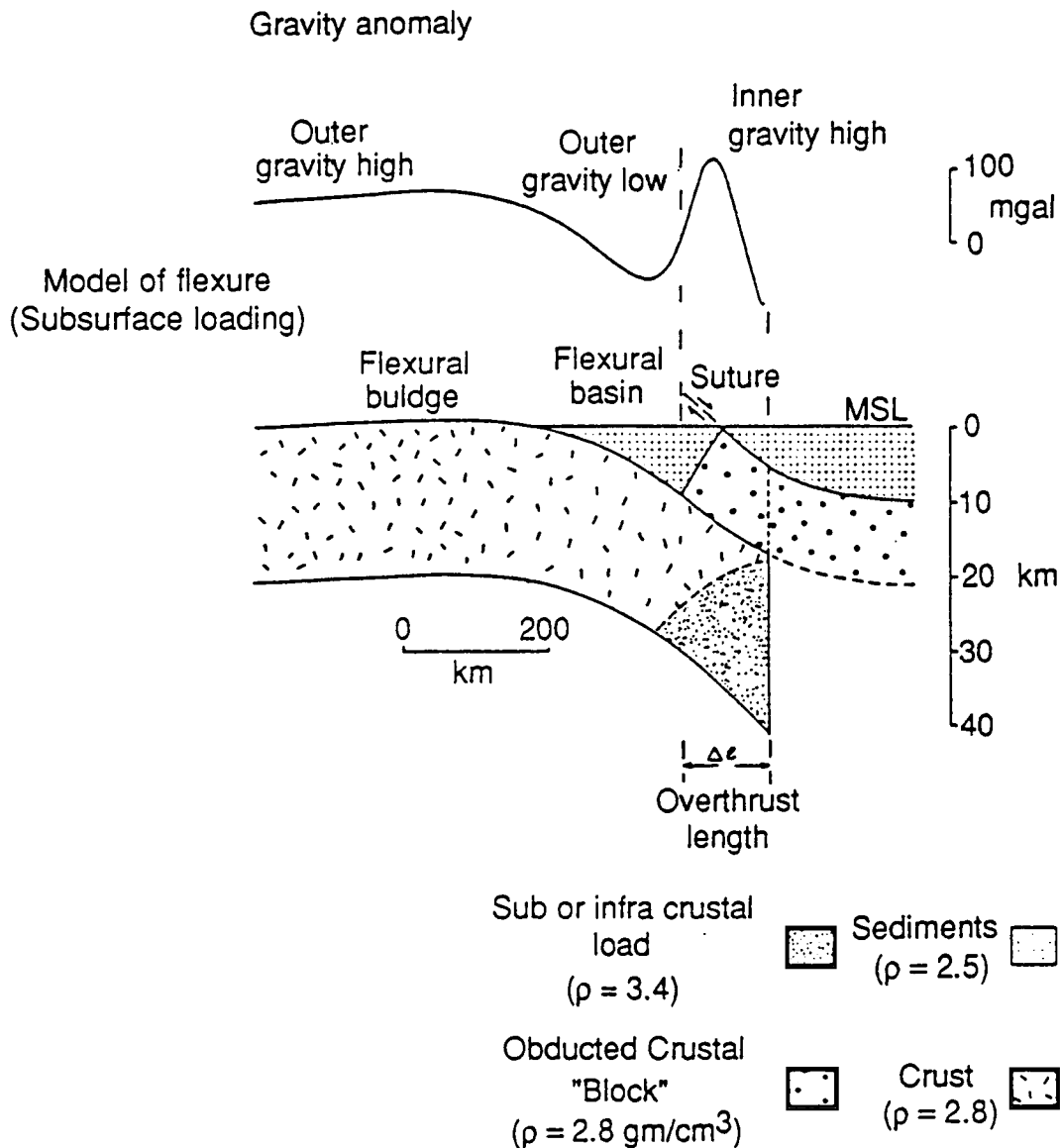


Figure 2-1. Schematic model of the crustal structure and the predicted (Bouguer or free air) gravity anomaly over a completely eroded orogen. The flexure of the elastic plate on the left side is maintained by the weight of either an obducted block from the overriding plate or some intracrustal load. The gravity anomaly is characterized by a positive-negative couple in which the low in the foreland is due to flexural depression of the basement and the high in the hinterland is caused by the excess mass of the buried load (Karner and Watts [25]).

both elastic flexure in describing the rheology of continental lithosphere and of subsurface loads in maintaining the deflection of foreland basins despite erosion of topographic loads.

Despite the importance now placed on buried loads in describing the conditions of mechanical equilibrium at mountain belts, the nature of these buried loads remains obscure. Subsurface loads from cold slabs [26], dense obducted blocks [25], and

normal stress applied from flow in the mantle [27] have all been used to supply forces and bending moments to the lithosphere beneath mountain belts. Do all these factors contribute to the compensation of orogenic belts at different times in their geologic evolution, or do the peculiarities of plate collision lead to fundamentally different loading conditions at different locations? We require additional studies of thrust belts at all stages of evolution with a variety of pre-collision tectonic settings (e.g., presence or absence of back-arc basins, different ages of colliding plates, etc.). A wide range exists on Earth; unfortunately, we lack observations of the gravity field over many, particularly the very youngest collision zones, due to difficult terrain and/or political problems with access.

Gravity coverage over continental orogens at wavelengths of 50 to 100 km (i.e., less than the flexural wavelength of the lithosphere) with an accuracy of 1 to 3 mgal would allow testing of models of lithospheric rheology, mechanisms of plate loading, causes of vertical tectonics in orogens and the details of continental suturing. For example, McNutt and Kogan [28] used statistics of gravity anomalies in Eastern Europe and Central Asia to argue that steeply plunging continental plates beneath thrust belts are characterized by a low value of elastic plate thickness even for very old lithosphere. They explain their result as the effect of massive brittle and ductile failure of the plates at high strains. The unavailability of unclassified gravity profile across the orogens used in their study prevents them from testing their hypothesis with forward modeling.

2.1.2.f Deep Structure of the Continental Lithosphere

The thickness of oceanic plates has been determined based on the cooling half space model. Generally speaking, it varies from almost zero thickness at the mid-ocean ridges to about 100-km thick beneath old oceanic basins. However, the thickness of continental lithosphere has not yet been agreed upon. The results of seismic studies on the thickness of continental lithosphere are controversial, with maximum thicknesses ranging from no more than 200 km [29] to over 400 km [30]. The flexural observations from foreland basins adjacent to mountain ranges point to an asymptotic thermal plate thickness for continental lithosphere of the order of 250 km or greater, at least twice that for oceanic lithosphere. The question remains as to how much a cold continental keel can be maintained against convective destabilization. One viable hypothesis for the deep structure of continents proposes a chemically-induced density reduction in the lower continental lithosphere that offsets the density increase from cooling [31]. Regardless of whether the bottom of the lithosphere is defined as a thermal boundary or a chemical boundary, density anomalies will exist at a depth between 100 to 400 km across the boundary of a "continental root." This horizontal density variation will give a surface gravity anomaly of about 1 to 5 mgal. The anticipated wavelength of the gravity anomaly will coincide with the length scale of the continent. Thus, an improved constraint on the thickness of the continental lithosphere can be derived based on improved surface gravity data and proper modeling of mantle thermal structure adjacent to the roots of continental lithospheres. Earth scientists do not have, at present, a precise global gravity field to search for the gravity signal from deep continental thermal structure.

2.1.3 The Mantle

The problem of mantle convection is fundamental to understanding the evolution of the Earth. The outgassing of the oceans and atmosphere, the differentiation of the crust, volcanism, and all tectonics — continental as well as oceanic — are ultimately dependent on energy sources within the mantle and core, and upon the

transport of this energy and material by flow driven by thermal or compositional buoyancy. The oceanic crust and lithosphere are part of this convecting system: they make up its uppermost, cold thermal boundary layer. This motion is associated with a flow pattern coming to the surface at the mid-ocean ridges or other rifting areas and returning to the interior at subduction zones. Most oceanic crust, as well as its associated lithosphere, is recycled to the interior. The continental lithosphere, which consists of the continental crust and sizable pieces of sub-continental mantle, rides on top of the convective system. The velocities of the system are of the order of centimeters per year, the heat transport is an average of 0.08 W m^{-2} . These values, together with the thermal and rheological properties of rocks, indicate that the system must be more complicated than the smoothest flow necessary for the observed plate motions. Phenomena such as changes in the plate tectonic pattern on time scales of tens of millions of years, long-term episodicity of volcanism in tectonically complex areas such as western North America, exceptionally high heat flow on the continental side of subduction zones, and higher than predicted heat flow and topography in some parts of ocean basins, all suggest that there are secondary scales of mantle flow not directly connected to the precisely measured plate tectonic pattern. Observations which see through the lithosphere and into the mantle are needed. The gravitational field provides one such observable.

2.1.3.a Gravity Anomalies in a Dynamic Earth

Convective patterns within the mantle are manifested as surface gravity anomalies through the internal density variations which drive the mantle flow and through deformations of its boundaries (both surface and internal). However, determining the gravity anomalies caused by a given distribution of density anomalies in a dynamic planet includes more physics than just calculating the gravitational effects of these density anomalies alone. This is because the stresses and mantle flow associated with those density contrasts result in dynamically maintained topography at the Earth's surface and at the core-mantle boundary, and any other possible internal structure. As a first approximation, the total mass displaced in any column by this boundary deformation is about equal to the mass anomaly due to density contrasts in that column – a sort of dynamic isostasy. The mass anomalies caused by this dynamic compensation have an effect opposite in sign to the mass anomalies due to interior density contrasts. The net gravitational effect, including the effects of dynamic topography, depends upon how this dynamic compensation is distributed among the boundaries of the convecting system [32]. Due to the fall-off of gravitational interaction with distance, the gravitational attraction of the deformed bottom boundary is attenuated more at the surface of the Earth than the gravitational attraction of the interior density contrasts, which are in turn attenuated more than the effects of the deformed upper surface.

It is instructive to construct dynamic gravity "kernels" which show the total gravitational response, including the effects of dynamic topography, due to a mass anomaly of a given wavelength placed at some depth in the mantle. These kernels [33] depend strongly on the internal mechanical structure of the mantle. For a uniformly viscous Earth, the fall-off of gravitational effect with depth results in the gravity signal from the deformation of the upper surface being larger than that of the density contrast itself, resulting in a negative gravity anomaly for a positive density contrast for all wavelengths and depths. Viscosity increasing with depth leads to less surface deformation and more deformation of the core-mantle boundary, making the kernels more sensitive to the interior density contrasts themselves. A substantial viscosity increase with depth can lead to a net positive gravity anomaly for a positive density contrast.

If the mantle is chemically stratified, boundaries between chemically distinct layers will also support dynamic topography, with a resultant contribution to the net gravity field. Density contrasts near the 670-km seismic discontinuity would be almost completely compensated for if it were a chemical discontinuity, and would result in negligible gravity anomalies. As discussed below, the gravitational signatures of deep subducted slabs provide powerful tests of the presence of chemical stratification in the mantle [34].

In summary, the net gravity anomaly in a dynamic planet is the result of near cancellation of large effects. The magnitude and sign of the result is a sensitive function of the spatial variation in rheology and the presence or absence of chemical stratification. Matching gravity observations provides a very sensitive test of a dynamic model.

In order to examine gravity signatures produced within the mantle, it is necessary to first understand how much of the observed gravity signature arises from topography on the Earth's free surface. While dynamic topography can be predicted by a flow model, high quality observational constraints on bathymetry and topography are lacking. Without these data, some mantle dynamic processes cannot be discriminated with high confidence. Additionally, variations of the geomagnetic field are the result of convective motions within the outer liquid core. Dynamic motions within the outer core couple with the dynamic mantle through their common interface at the core-mantle boundary, leading to torques that speed up or slow down the Earth's rotation, leading to changes in the length of day. Motions in the core are as yet poorly constrained. Therefore, in order to eventually integrate dynamic models for the Earth's mantle and core, it is also necessary to have a global data set of the Earth's magnetic field with comparable resolution.

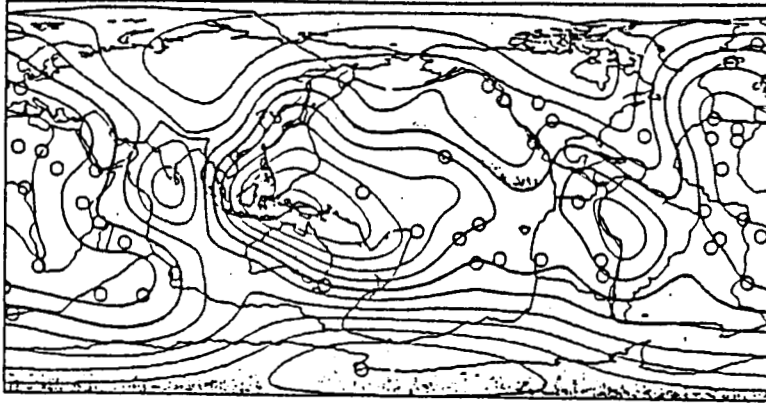
2.1.3.b Seismic Tomography and Gravity Anomalies

Imaging of Earth structure using seismic tomography is a discipline of geophysics currently undergoing explosive development. Spatial variations in seismic velocities have been obtained on a wide range of scales, from local [35] to regional [36,37] to continental [38] to plate [39] to global [40 through 45]. One ultimate aim of geodynamics is to understand the physical processes causing these variations in seismic velocities. Are they the result of thermal differences associated with mantle convection, chemical differences caused by differentiation of the mantle and lithosphere, or some other process, such as anisotropy resulting from preferred alignment of crystals? Seismology by itself cannot discriminate among these hypotheses, whereas gravity can, since the magnitude and sign of the relationship between seismic velocity and density associated with each of the explanations are different.

For any assumed relationship between density and seismic velocity, the gravity field associated with tomographically-deduced velocity variations can be calculated. The gravity signal also depends on the mantle viscosity due to the dynamic boundary deformations produced by the density anomalies. Model solutions for a mantle with viscosity increasing significantly with depth can account for 90 percent of the gravity variations in wavelengths longer than 4000 km (Fig. 2-2) [45].

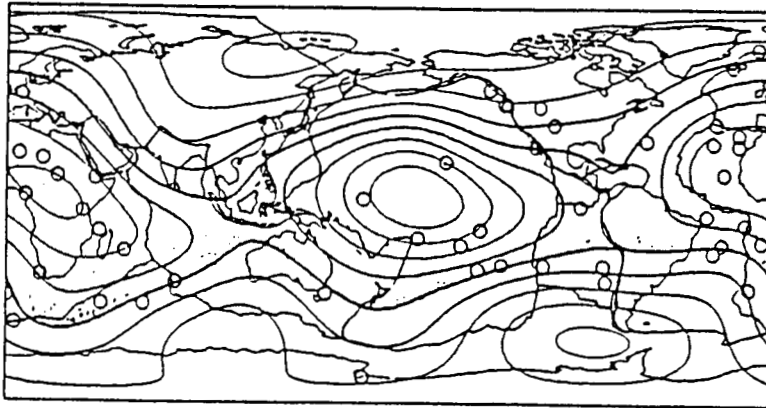
As seismic tomography, now in its infancy, attains much greater detail in mapping the velocity anomalies of the mantle, there will develop a stronger need for an improved gravity field at shorter wavelengths to match the predictions. The appropriate accuracy needed for these comparisons depends upon the scale of the seismic model. Accuracies from 1 mgal at 100-km wavelengths to 0.01 mgal at 500-km

OBSERVED GEOID: DEGREE 2-9



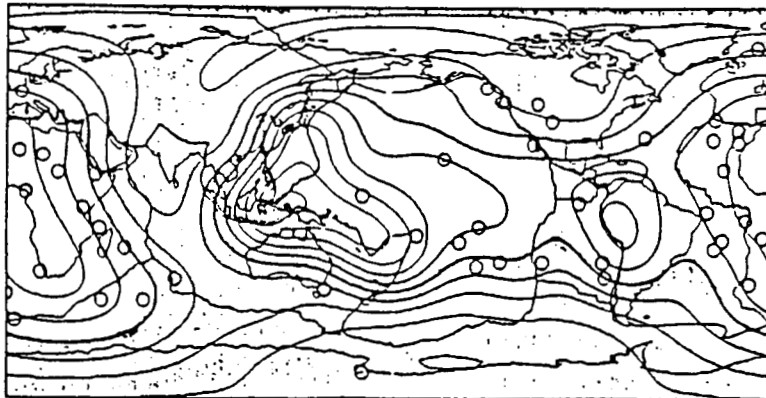
contour interval: 20 m

STATIC GEOID: DEGREE 2-6



contour interval: 100 m

CC-LM, SLAB, T-UM PREDICTED GEOID: DEGREE 2-9



contour interval: 20 m

Figure 2-2. (a) The observed geoid at spherical harmonic degrees 2 to 9. (b) The predicted geoid from mantle tomography for a rigid Earth. This has the right pattern but the wrong sign. (c) The prediction of the dynamic model - a remarkably good fit. Open circles show locations of hot spots (from Hager and Clayton [45]).

wavelengths are required in order to discriminate among models at a level of about 10 percent of the expected gravitational signal.

2.1.3.c Viscosity of the Mantle

The thermal state and mechanical behavior of the mantle are strongly dependent on its viscosity structure. There are two major issues to be resolved. From laboratory creep studies of minerals under mantle conditions (i.e., high temperature and high pressure), it is inferred that mantle rock should deform according to a power law non-Newtonian rheology [46]. However, a Newtonian model for the mantle has been utilized to delineate mantle viscosity structure; such a model can approximately fit both the isostatic glacial rebound data and the gravity data around Hudson Bay in Canada [47]. A possible implication is that due to the possible existence of volatiles and inhomogeneities within the mantle, its deformation mechanism may be modeled as a Newtonian fluid. The second issue concerns the magnitude of mantle viscosity. Some studies find that the viscosity of both the upper and lower mantle is about 10^{21} Pa sec [48], while other studies indicate that the viscosity of the lower mantle is approximately one order of magnitude higher, accompanied by an asthenosphere viscosity of 10^{19} Pa sec [45]. Studies utilizing non-Newtonian rheology indicate that the viscosity of the lower mantle is probably not constant but changes with a two- to three-order-of-magnitude variation across the lower mantle [49]. Geoid highs over subducted slabs can also be explained using a non-Newtonian model [50]. As discussed earlier, both issues can be addressed and plausible mantle deformation mechanisms can be discriminated using a set of gravity measurements that are dense and high resolution, e.g., 1 mgal accuracy over 500-km wavelengths, together with seismic tomographic studies and convection model computations [45].

2.1.3.d Vertical Scale of Mantle Convection

The vertical scale of the mechanical structure of mantle flow is a subject of current debate. Geochemical isotopic studies have been interpreted as suggesting the existence of a multi-layer structure [51]. However, geophysical arguments indicate that a single layer convective regime is more likely [52]. If multi-layer convection exists, it is hypothesized that the 670-km seismic discontinuity will be the boundary between separate flow systems in the upper and lower mantle. Due to the upwelling and down-going currents associated with mantle flows, undulations or vertical displacements at this boundary will occur with a wide range of wavelengths [53]. Due to the attenuating effects of distance, the ones with most signal will be in the range of several thousand km [54]. The gravitational characteristics of a chemically stratified mantle are quite different from those of a mantle with uniform composition. Consequently, high resolution gravity data can be used to better delineate the competing hypotheses.

The depth of slab penetration can be studied particularly effectively with better gravity data. Based on seismic investigations of travel time [55], subducting slabs are thought to be able to penetrate into the lower mantle. Since seismic anomalies are directly related to density variations, the existence of deep penetrating slabs can be examined with the gravity data derived from the proposed global measurements. The gravitational signature of a deep subducted slab is particularly sensitive to the presence or absence of a chemical discontinuity at 670-km depth. If a discontinuity is present, dynamic compensation of the slab will occur at that depth, resulting in smaller gravity anomalies for a given density contrast. The current long wavelength gravity field (>4000 km) can be satisfied by either a model with normal slab density and mantle-wide flow or a model with high slab densities (caused by phase changes)

and a chemical barrier to flow. The models can be discriminated using shorter wavelengths. Since subducting slabs lie beneath island arcs and typically span the ocean-continent transition, altimetric geoids are not sufficient to study this problem and gravity fields such as those obtained by a gravity-measuring satellite are required. The expected signal strength will be above 0.1 mgal with a length scale dictated by the angle of a subducting slab and the speed of slab subduction; a typical wavelength will be about 100 km.

2.1.3.e Small-Scale Convection

A variety of scales and styles of convection may occur in the mantle. When a Rayleigh-Benard convective layer of constant viscosity is under horizontal shear in the laboratory, longitudinal rolls occur [56]. Such transverse rolls may exist beneath moving oceanic plates. Because of the uncertainties in the vertical scale, the horizontal scale expected is not known. It has been argued, based on stability analyses, that longitudinal rolls can exist only if the upper mantle viscosity is extremely low [57]. More recent calculations [58] indicate that, if such longitudinal rolls exist, they may have a typical horizontal wavelength of about 150 km with an amplitude of 5 mgal. One of the major discoveries of the Seasat altimeter mission is gravity undulations with the predicted wavelength, amplitude, and orientation in the Central Pacific [59]. However, in the Indian Ocean, crossgrain features with the same wavelength but even larger amplitude (20 to 60 mgal) are thought to be due to buckling of the lithosphere in response to N-S compression of the Indian plate as it collides with Asia [60,61]. Even lithospheric boudinage, a pinch and swell instability resulting from plate-wide tensile stresses [62], might be capable of producing some of the crossgrain lineations. Therefore, before crossgrain lineations are used to constrain models of small-scale convection, we must map them with greater accuracy and in more detail to determine their origin. Do these features contain information concerning asthenospheric viscosity, or are they indicative of lithospheric stress and rheology? An improved gravity data set not only will be able to verify the existence or absence of such structures, it will also be able to delineate where such rolls begin and where they terminate as a function of plate age and spreading velocity. An accuracy of 1 mgal at 100-km resolution would allow these features to be traced to 20 percent of their amplitude.

Beneath the continents there is direct observational evidence from seismic tomography that small scale convection also occurs. For example, below the Transverse Ranges in Southern California a curtain of high-velocity material extending down to a depth of 250 km is evidence of convective downwelling of the cold thermal boundary layer at the base of the lithosphere [37]. This feature may explain the dynamics of the Big Bend of the San Andreas Fault. The gravity signature of this feature is calculated to be up to 15 mgal in amplitude with a wavelength of about 150 km. A model of the local gravity field [26] indicates that this feature is, to a large extent, compensated from above by flexure of the overlying plates. In this particular instance, both gravity observations and velocity anomaly maps from seismic tomography were necessary in order to understand the interaction of the lithosphere with the asthenosphere. Once this system response is well calibrated, it may be possible to identify regions of downwelling beneath continents from gravity and the surface geology alone.

2.1.3.f Mantle Plumes

While the volcanoes associated with hotspots are lithospheric features, the source and ultimate cause of hotspot activity lies in the mantle below. Candidates for the formation and feeding of hotspots include chimney-like thermal plumes [63], isolated

hot blobs [64], and stripping away of the base of the lithosphere by convective instability [65]. For each of these models, it is possible to predict a dynamic gravity model which could then be tested by observation. The depths of origin of hotspots can be addressed by looking at the long-wavelength gravity variations. In order to separate the dynamic topography due to deep circulation from crustal and lithosphere effects, understanding the shorter wavelength variations is essential.

2.1.4 Oceanography

The ocean plays an exceedingly important role in establishing the overall heat, energy, and moisture balance of the Earth's surface. Together with the atmosphere, it is responsible for the redistribution and transformation of incoming solar radiation deposited at tropical latitudes, mainly into the ocean. In order to understand how the oceans and atmosphere regulate the Earth's heat and moisture, maps of global oceanic surface currents (both steady and time-varying), tides, and other temporal variations are required. These fluid motions produce dynamic area surface topography which is the departure of actual sea surface from the marine geoid. The measurement of the equipotential via gravity observations, when used in conjunction with satellite altimetry to measure the total sea surface, can yield this dynamic topography. Thus, physical oceanography finds itself intimately bound up with global gravity.

2.1.4.a Gravity and Ocean Circulation

In the absence of other forcing, a uniform, motionless ocean on the rotating Earth would take up surface displacements that would conform to the surface marine geoid, which is the equipotential surface for the total gravity and rotational fields. At depth, constant density surfaces would also conform to other equipotential surfaces, so that no density-driven flows would occur. When seawater of density ρ_w moves on the Earth rotating at an angular velocity $\vec{\Omega}_E$, the sea surface no longer conforms to the equipotential surface, nor do constant density surfaces at depth conform to other equipotentials. Even in the steady state, constant currents are profoundly affected by gravity. To see this, consider the Navier-Stokes equation for a frictionless fluid moving in a rotating coordinate system, simplified for the case of time- and space-independent horizontal currents with velocity \vec{u} . In vector form, that equation is

$$\begin{aligned} \frac{\partial \vec{u}}{\partial t} + (\vec{u} \cdot \vec{\nabla}) \vec{u} &= 0 \\ &= -2\vec{\Omega}_E \times \vec{u} - \frac{1}{\rho_w} \vec{\nabla} p - \vec{\nabla} \phi, \end{aligned} \quad (2.1)$$

where p is pressure. The geopotential $\phi = \phi(x, y, z)$ is the potential energy per unit mass of water due to the sum of the Earth's gravity field $\phi_g(x, y, z)$ and the Earth's rotational potential $\phi_r(x, y, z)$. For the case of steady flow, the astronomically determined tidal potential $\phi_t(x, y, z, t)$ is neglected.

In a coordinate system that is logically tangent to the surface geoid at the point in question, equation (2.1) decomposes into vertical and horizontal components:

$$\begin{aligned}
0 &= - \frac{1}{\rho_w(z)} \frac{\partial p}{\partial z} - \frac{\partial \Phi}{\partial z} \\
&= - \frac{1}{\rho_w(z)} \frac{\partial p}{\partial z} - g \quad ,
\end{aligned}
\tag{2.2}$$

and

$$0 = - 2 (\vec{\Omega} \times \vec{u})_h - \frac{1}{\rho_w} \vec{\nabla}_h p \quad ,
\tag{2.3}$$

where z is vertical and positive upward and g is the local gravitational acceleration.

Equation (2.2) is the hydrostatic equation in a fluid whose density $\rho_w(z)$ varies in the vertical. Equation (2.3) is the well-known geostrophic equation, which states that in the steady state, the horizontal component of Coriolis force, $-2(\vec{\Omega}_E \times \vec{u})_h$, is balanced by the development of a horizontal pressure gradient, $\vec{\nabla}_h p = \partial p / \partial x \hat{i} + \partial p / \partial y \hat{j}$, where \hat{i} and \hat{j} are unit vectors in the x - and y -directions, respectively. This horizontal gradient is created by the ocean tilting its constant pressure surface during its approach to equilibrium so that a hydraulic head arises in opposition to the horizontal Coriolis force. The resultant near-surface configuration is shown in Figure 2-3, which illustrates schematically a vertical section across the Gulf Stream. The surface elevation η , or setup, across the current is of order 1 m above the geoid on the Sargasso Sea side of the gyre, while the slope on the inshore side is generally a few tens of centimeters below the equipotential.

The slope of the sea surface elevation $\vec{\nabla}_h \eta$ with respect to the geoid is proportional to the surface current velocity. To see this, decompose equation (2.3) into x - and y -components of horizontal geostrophic surface current:

$$u_x = (g/f) \partial \eta / \partial y \quad ,
\tag{2.4}$$

and

$$u_y = -(g/y) \partial \eta / \partial x \quad ,
\tag{2.5}$$

in which $f = 2\Omega_E \cos \theta$, and the fact that the horizontal hydrostatic pressure gradient at the surface is related to the hydraulic setup via $\vec{\nabla}_h p = \rho g \vec{\nabla}_h \eta$ has been used. Thus, if one can measure the slope of the sea surface $\vec{\nabla}_h \eta$ relative to the geoid, one may obtain estimates of the horizontal component of geostrophic velocity \vec{u} at right angles to the slope components. The slopes also allow estimates of the kinetic energy per unit volume of the flow (proportional to $1/2 \rho \vec{u}^2$) and the potential energy stored in surface elevations and depressions ($1/2 \rho g \eta$).

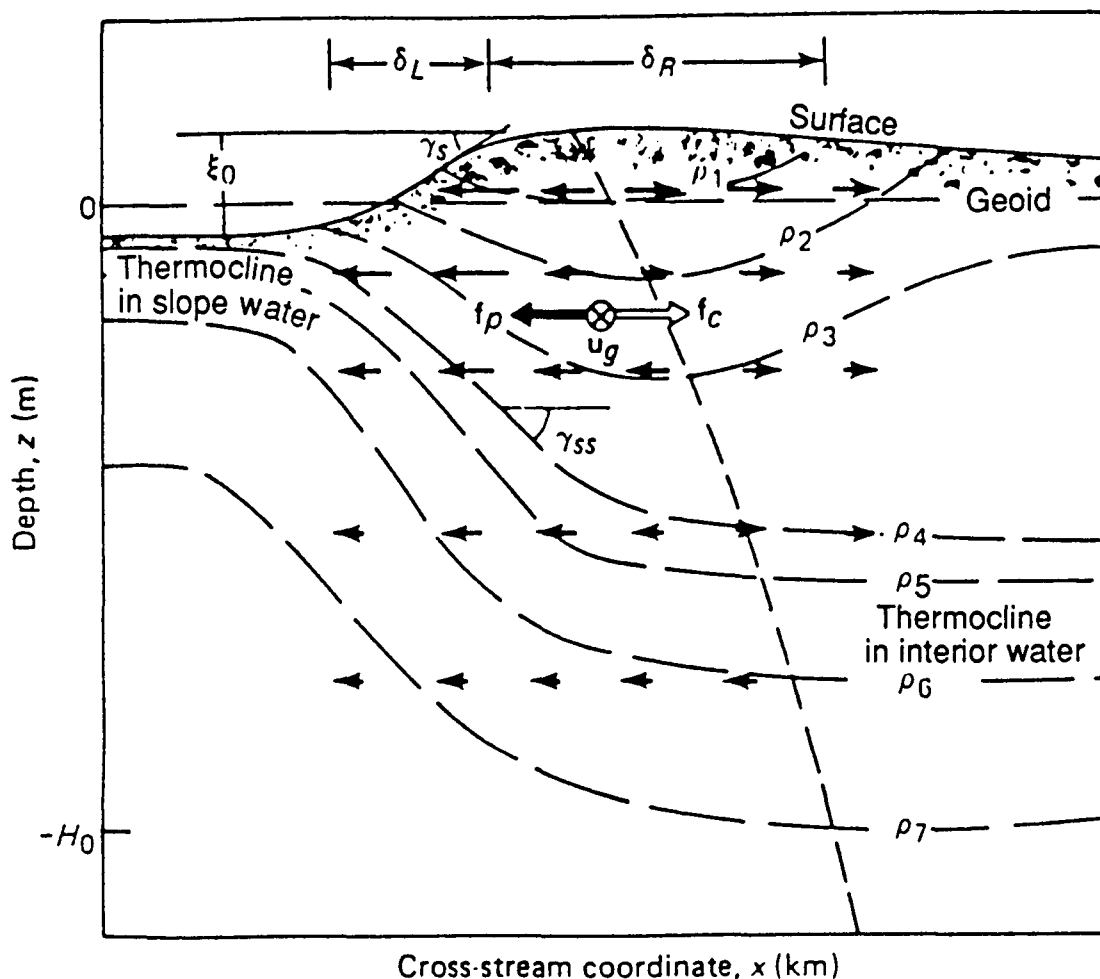


Figure 2-3. Schematic diagram showing constant density surfaces (dashed lines) and pressure gradient forces (arrows) through a western boundary current such as the Gulf Stream in geostrophic balance. The resulting flow is into the paper.

2.1.4.b Experimental Determination of Dynamic Topography

The altitude of a satellite above the sea surface can now be determined using precision radar altimeters. An accurate determination of the satellite orbit yields the height of the sea surface from the reference ellipsoid, which, combined with knowledge of the geoid, can yield the dynamic sea surface topography. From the slope of the surface elevation, one obtains the surface current velocity field using equations (2.4) and (2.5). Current accuracies in the measurement of satellite orbits are of order 50 cm, whereas total area surface height can be much better determined via altimetry to within a very few centimeters. Averaging over limited space and time intervals reduces the overall error in surface heights, exclusive of geoid errors, to the order of ± 10 cm. This leaves the determination of geoid heights above the reference ellipsoid as the largest remaining error source in the measurement of sea surface currents. In the main, it is in the precision determination of marine geoidal undulations that oceanography finds itself a companion discipline to solid Earth geophysics and gravity.

Although the geostrophic equations were derived above for the steady state, they are valid for motions whose characteristic times for change are of order of a few

days at mid-latitudes. A satellite altimeter in an exactly repeating orbit can use the temporal variations in η along repeated segments of subsatellite tracks to determine the time-varying component of surface velocity. This quantity gives the fluctuating component of the oceanic surface circulation but leaves the mean value completely undetermined in the absence of the geoid. Since the mean circulation generally enters into important oceanic process to the same order as the fluctuations, the lack of knowledge of the mean current is tantamount to understanding only half of the extant ocean dynamics.

From this discussion, it may be concluded that knowledge of the geoid (or gravity field) in conjunction with satellite altimetry can yield the surface current velocity and the surface values of kinetic and potential energy of the flow on a near-global spatial scale and on time scales in excess of several days. Combined with some reasonable qualitative knowledge of the subsurface characteristics of the flow, the general three-dimensional, time-varying circulation of the oceans may be determined for the first time. This is a major objective of the World Ocean Circulation Experiment (WOCE), which is scheduled to begin in the late 1980's and to run for five or more years. Once the marine geoid is determined with sufficient accuracy, altimetry data gathered in conjunction with WOCE as well as all previous altimetric measurements of the topography of the sea then become useful in determining the mean and time-varying circulation at the time of the observation. Since oceanography has always been a data-starved science, the vitalization of such historical data enlarges the useful data base significantly.

2.1.5 Temporal Variations in Gravity

A less obvious but equally important application for high-precision satellite gradiometry is the detection of time variations in the field. In most geophysical and geodetic studies, gravity is assumed to be static. Such an assumption is usually justifiable because expected changes in the field over typical observing lifetimes ($\sim 10^2$ years) are relatively small. However, the precision of the proposed SGG is such that heretofore undetected changes in gravity over 6 months will be sensed. Furthermore, subsequent missions of similar design could provide additional time samplings of the field, thereby better resolving ongoing variations. Effects causing changes in gravity include ocean and solid Earth tides, postglacial rebound, secular melting of the ice caps, seasonal variations in ground water (e.g., snowpack), and great earthquakes. The magnitudes of these effects have been estimated in a recent study by Wagner and McAdoo [66].

The characteristic periods for these effects range from minutes to thousands of years but to a large extent are global in nature, with the exception, perhaps, of the effects of great earthquakes. The cause of these changes in gravity are the orbital motion of the Sun and Moon, and changes in the physical state of the solid Earth, oceans, and atmosphere. Some effects that should give rise to temporal variations in gravity detectable with an extremely sensitive gravity gradiometer are discussed below. It is difficult to anticipate all such effects, and thus it is particularly in the frontier area of temporal variations in gravity that completely unexpected discoveries could result.

2.1.5.a Tides

The tides span a wide range of frequencies between about 12 hours and 19 years, and are related to the periods associated with the orbital motions of the Earth

about the Sun, the Moon about the Earth, and the rotational period of the Earth on its axis. A spacecraft in orbit about the Earth will sense all these changes in gravity (at least in principle) and also those induced by its own motion over the tidally distorted Earth, primarily a once per orbital revolution effect. Because the frequencies of the tides are well known, they are separable from the signals of other sources of gravity anomalies, and provide new information of significant value to solid Earth and ocean dynamics.

To an observer on the surface of the Earth, the largest times are those at, or near, the diurnal frequency of the Earth's rotation. To an observer on a spacecraft in orbit, the primary frequency is that associated with movement of the spacecraft orbit with respect to the Moon (and Sun). Thus, the lunar diurnal tide at the spacecraft has a period of about 14 days. Unless the Earth's tidal response varies with longitude, the 12-hour diurnal tide will not be sensed by the spacecraft. For the solid Earth, which is free to respond, this is generally true. The ocean's tidal response is not independent of longitude, due to boundary conditions imposed by the continents, etc.

The tidal distortions of the Earth that are sensed at the spacecraft cannot be ascribed to either the Earth or ocean but only as a combined tidal effect. Some of these tidal variations in gravity can cause very large perturbations of a spacecraft orbit and the measurement of gravity gradient at altitude will provide considerable information about the tides. This technique has already been used to estimate the long wavelength components of at least 12 tides. Generally, these tidal solutions provide new information on the ocean tides on the assumption that good models already exist for the solid Earth. In turn, these ocean tidal solutions then can be used to improve our knowledge of Earth-Moon interactions, including the change in the Moon's orbit and the deceleration of the Earth on its axis due to the transfer of angular momentum from the Earth to the Moon.

In oceanography, the gravity tides detected at spacecraft altitude can be combined with the altimetric solutions for the tides, which provide the tidal geometry, and used as constraints in global ocean tide models that take into account additional effects, such as tidal loading of the continents and energy dissipation at the sea floor. In some cases, the components observed gravitationally at spacecraft altitude are undetectable on the Earth's surface (or inseparable from other tides) because of their small amplitude. The gravity tide becomes the only source of information about these tides.

2.1.5.b Postglacial Rebound

The most recent episode of Pleistocene deglaciation began roughly 18,000 years ago. The massive continental sheets of ice were largely melted 5000 years ago [48]. Although the melting has nearly ceased, the solid Earth continues to rebound in response to this deglaciation. This rebound continues today because of the high average viscosity (order 10^{22} Pa sec) of the Earth's mantle. Concomitant changes in the gravity field also continue today.

Figure 2-4 shows the present day rebound rate. The largest rebound rates (~ 0.01 m yr⁻¹) occur in areas where ice caps were thickest. When the rebound is decomposed in spherical harmonics, the largest components occur at very low degree and order (≤ 6). Using the expression given before relating displacement of the solid Earth to gravity anomaly, the maximum gravity change per year is 10^{-3} mgal. Such small variations in gravity associated with the second spherical harmonic have been

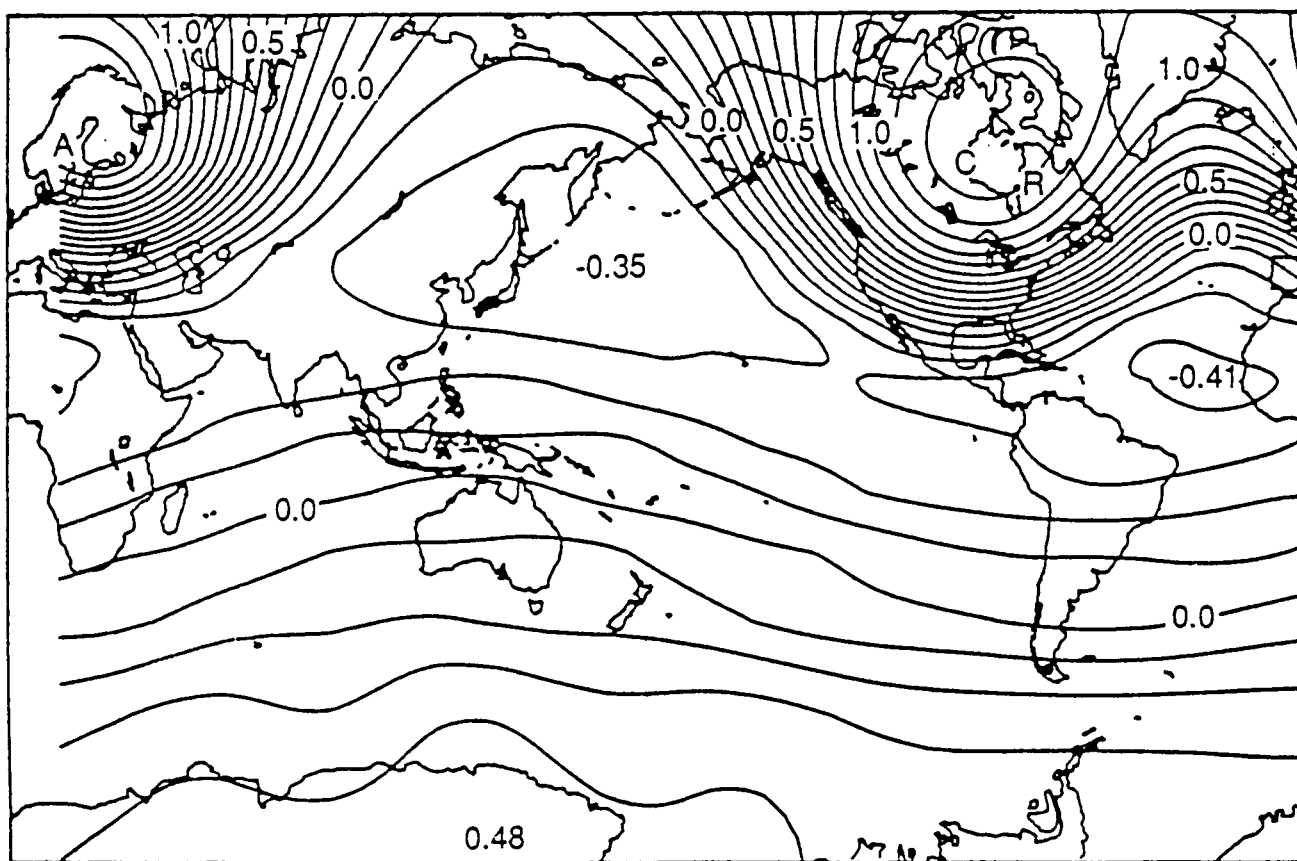


Figure 2-4. Present-day rate of change in the radial position of the surface of the solid Earth calculated from simplified model of postglacial rebound.
Units are cm yr^{-1} (from Wagner and McAdoo [66]).

measured as perturbations in the orbit of LAGEOS [67] and been used to estimate the viscosity of the lower mantle. Higher harmonics of glacial rebound have not been observed from satellites although in several areas they are well constrained by shore-line emergence data [48]. Rebound of these higher harmonics contains information on radial variations in the viscosity of the upper mantle and asthenosphere, important for dynamic models of the Earth.

To understand the full extent and mechanism of the rebound, we require global models of the gravity field at wavelengths of 3000 km or longer and an accuracy of 10^{-3} mgal repeatedly measured at various epochs over a period of about a decade. Although changes in all the medium-to-long wavelength harmonics occur, those most easily detectable are restricted to the very low degree terms. There is reasonable expectation that variations up to degree and order four will be observable from low Earth orbit. Detailed knowledge of rebound will help solve the problem of the lateral and vertical variation of mantle viscosity.

2.1.5.c Glacial Melting and Atmospheric Warming

One of the most important variations in gravity is due to the slow secular melting of glaciers [68]. Climate studies show an accelerated warming of the atmosphere over the last century that is believed to be caused by increases in atmospheric carbon dioxide associated with burning of fossil fuels and deforestation. Global warming may induce glacial melting resulting in sea level increases and coastal flooding.

Accurate satellite gradiometer missions could monitor the small changes in the global gravity field caused by the redistribution of mass from the glaciers to the oceans. The current estimate of yearly sea level rise, caused by melting of small glaciers, is 5×10^{-4} m. However, this number is very uncertain because only a few glaciers have been monitored over the last century [68]. The yearly change in gravity over the oceans due to glacial melting is only 2×10^{-5} mgal. In glaciated areas, the yearly gravity change may be somewhat higher because the area is smaller.

Although these predicted temporal variations in gravity are extremely small, they are global and could perhaps be measured by a satellite gravity gradiometer which can render the highest resolution at long wavelengths by virtue of its long integration time. One method of increasing the signal associated with secular glacial melting is to measure over a longer period of time. This could be done with two or more missions spaced at five-year intervals.

2.1.5.d Seasonal Variations in Groundwater and Excitation of the Chandler Wobble

The Chandler wobble is an apparent 427-day precession of the Earth's instantaneous pole of rotation about its axis of greatest moment of inertia. The Earth's anelasticity damps the Chandler wobble such that, in the absence of some excitation, the rotation pole and axis of figure would eventually coincide. The rate at which the wobble is damped depends upon the largely unknown viscosity structure of the mantle and core. Its Q (i.e., π times damping time divided by wobble period) would lie anywhere between 70 and 600. If the wobble is not being re-excited very often, such as, for example, by mass movements associated with occasional great earthquakes then its Q must be very large. If the forcing is more frequent, then Q must be small. A knowledge of the mechanism which excites the Chandler wobble would constrain its Q , which in turn would reveal the viscoelastic structure of the lower mantle and core.

Winter in the Northern Hemisphere is accompanied by a dramatic increase in continental water storage associated with the development of ice deposits and snow-packs [69]. Previous studies have suggested that this seasonal fluctuation in groundwater storage excites the Chandler wobble [69,70], implying a small Q . To test whether groundwater fluctuations excite the Chandler wobble and to determine its Q , better observations are needed. Due to a lack of hydrologic and meteorologic data, especially in Asia, the spatial and temporal variations in groundwater are not accurately determined. Typical annual variations in surface groundwater height over the continents are 0.1 m. During the seasons, this water is transferred from the oceans to the continents and back to the oceans. Gravity variations associated with this mass transfer will be about 4×10^{-3} mgal. To determine the transfer function between the excitation and the observed wobble, the mission should last several years. A shorter mission (about 6 months) could be used to confirm that groundwater plays a major role in exciting the Chandler wobble.

2.1.5.e Volcanoes and Earthquakes

Gravity data have a key role in monitoring precursors to volcanic eruptions and in determining the response of the Earth to faulting. For example, Rundle [71] has calculated the gravity changes associated with magma loading. Observatories at Hawai [72] and Mt. Saint Helens [73] have detected these gravitational changes caused by magma inflation events, which signal impending eruptions. Walsh and Rice [74], and Savage [75] have modeled the change in surface gravity associated with dip-slip faulting. For an infinitely long thrust fault, they find that the slip-induced changes in

vertical gravity are proportional to changes in elevation. Upward continuation of the gravity signal from an earthquake to spacecraft altitude has been carried out by Wagner and McAdoo [66]. For the 1964 Alaska earthquake they show that a spacecraft passing over the region at 160-km altitude would have its velocity changed by approximately $15 \times 10^{-6} \text{ m sec}^{-2}$ in a period of about 50 sec as a result of the co-seismic vertical motion, indicating a change of about 0.1 to 1 mgal over an area of about 400 km². Changes of this magnitude, if detectable from near Earth orbit, might lead to the study of pre- and post-seismic behavior on a global scale.

2.1.6 Summary

Accurate knowledge of the global gravity field is fundamental to understanding the structure and dynamics of the Earth. Although the relationships between gravity data and known geophysical and geological features are generally understood, gravity models alone cannot be inverted into unique geophysical models. Historically, gravity models have served as strong constraints for geophysical models, and have depended heavily on complementary data from other fields (e.g., seismology, petrology).

SGGM will measure the three diagonal components of the gravity gradient tensor at orbital altitudes. To support analysis of these data, the SGGM must be very accurately tracked in orbit. The tracking alone yields the approximate shape of the geoid at satellite altitude. Another related NASA project, TOPEX, will attempt to quantify the effect of gravity differently. TOPEX will measure the satellite distance above the sea surface with a radar altimeter comparable to the one used in the SEASAT mission. Although it can be used to determine the oceanic geoid to a much higher spatial resolution than is now available, TOPEX will probably be used to increase the knowledge of the time dependence of the sea surface by the use of repeat tracks. SGGM will measure the geoid and could make a direct gravity measurement at higher altitudes (160 to 200 km). Combining these two sets of data will result in Earth gravity models of unprecedented quality in both accuracy and resolution.

Currently, NASA's and DOD's gravity modeling programs are based on analysis of satellite tracking, satellite altimetry, and surface gravity measurements. As the quality of these data improve, so do the models of the Earth's gravity field. These models of the geopotential still lack the coverage, accuracy, and resolution to address some fundamental problems on the origin and structure of geological features on the Earth's surface, the mechanical properties of the Earth's lithospheric plates, and large-scale circulation of the oceans and major current systems. Of particular interest are the inadequately mapped geographical areas which include large parts of the Asian continent, the polar regions, and tectonic areas such as the collision zones of the Andes and Himalayas. These areas have not been mapped largely due to political problems and the hostile environments for mapping crews.

Contemporary gravity field models do provide information of sufficient accuracy and detail in some tectonic regimes of the Earth so that significant correlations with geological features have been made. However, it is highly desirable to extend the global geopotential models to much shorter wavelengths (e.g., 50 km worldwide) so that the structure, composition, and physical state of the Earth can be studied in more detail. This spatial resolution could also be of great use for oceanographers, as it is also close to the Rossby cutoff for oceanography.

Figure 2-5 summarizes the gravity anomaly accuracy requirements for various geophysics disciplines as a function of horizontal spatial resolution. Also shown in the figure is a horizontally ruled region representing the range of resolution expected

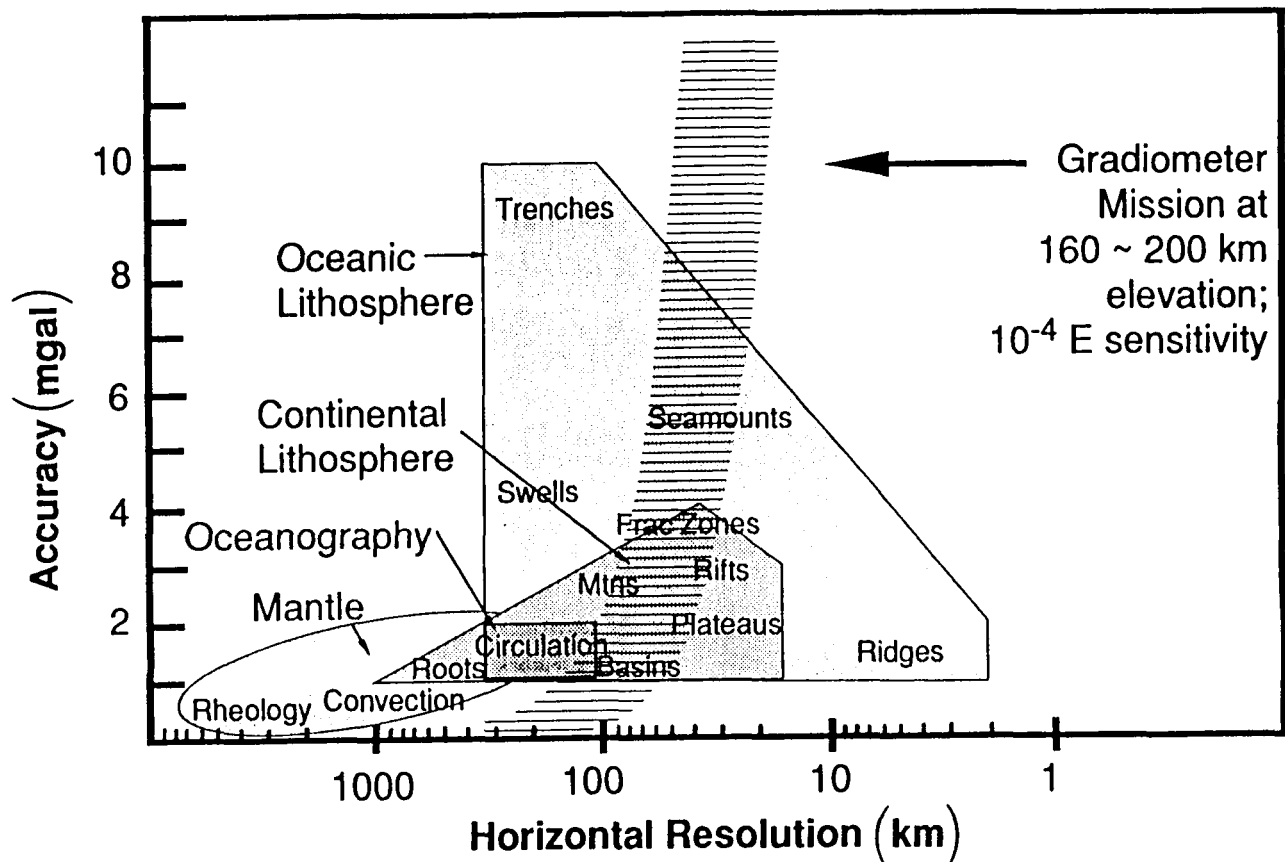


Figure 2-5. Summary of requirements for gravity measurement accuracy as a function of spatial resolution for the problems discussed in Section 2.

from the SGGM. An altitude range of 160 to 200 km and an instrument sensitivity of 10^{-4} E are assumed. The spread in the expected gravity anomaly accuracy is partially due to the effect of the satellite altitude h , and partially due to different assumptions and methods that have been used for various error analyses and simulation studies of the gradiometer mission (Appendix C). Although more refined simulation studies are needed to obtain a more reliable gravity anomaly accuracy for each set of altitude and instrument sensitivity, some general statements can be made regarding the gradiometer mission. Due to the exponential attenuation of the short-wavelength signal as a function of altitude (see Appendix A), a high-sensitivity instrument in a low-altitude orbit is essential to recover short-wavelength components. Studies indicate that a 10^{-4} E gradiometer at an altitude of 160 and 200 km can resolve spherical harmonic components up to degree 500 and 400, respectively. On the other hand, the total uncertainty in the recovered gravity anomaly is a relatively weak function of altitude since errors come from all frequencies (see Appendix C).

The SGGM will provide the baseline for the NASA gravity program for the 1990's and beyond. Satellite altimetry has brought revolutionary advances in understanding the suboceanic solid Earth. SGGM will extend this revolution to the study of the structure and evolution of the continents through precise gravity measurements. SGGM will also contribute to an understanding of the suboceanic solid Earth through greatly improved coverage of the gravity field at the continental edges, which are important to ocean crust and lithosphere evolution. The SGGM will sense the gravity field fine structure, and therefore contribute to the structure of geological features

on the Earth's surface, the mechanical properties of the Earth's lithospheric plates, and the forces that may drive their motion and oceanographic phenomena by improving the geoid models for the oceans. A high resolution, worldwide gravity model will address the continual problem of connecting the continental and oceanic gravity data bases at the continental coastlines. SGGM will contribute significant insight into the deep interior of the Earth. The gravity field will elucidate the pattern and energetics of the thermal convection in the mantle which drives the plate motions. The mission will give the first comprehensive, high resolution coverage of the areas of great tectonic interest: the collision belts of the Himalayas and the Andes, and rift zones such as those in East Africa. These areas can be measured using airborne systems with high accuracy and spatial resolution, but large scale geographic coverage is extremely difficult, if not impossible. Understanding these major tectonic processes is essential to comprehending the state and evolution of the continents.

2.2 Secondary Mission Objectives: Fundamental Laws of Physics

In addition to benefiting the geophysics community, a further benefit from the SGGM, and one that has motivated the high SGG instrument accuracies being sought, is a test of the inverse square law of gravitation. If sufficient instrument and platform accuracy can be achieved, the SGGM can be used as a very strong test of the inverse square law of gravitation, and also for new tests of General Relativity.

2.2.1 Null Test of the Gravitational Inverse Square Law

There are four known fundamental forces in Nature: two long-range forces, gravitational and electromagnetic, and two short-range forces, strong and weak. Speculation on the possible existence of an intermediate-range force, a "Fifth Force," has also recently received prominent coverage in the literature [76]. Beginning with Einstein, who tried in vain to unify the gravitational and electromagnetic forces by combining his General Relativity theory (gravitation) and Maxwell's theory (electromagnetism), there has been a steady effort by physicists to formulate a single ultimate theory which encompasses all of the forces in Nature. Important progress has been made during the past decade, but from a different direction. By using a quantum-field-theoretic approach, called "Unified Field Theory," electromagnetism and weak interactions have been brought together as manifestations of the same phenomenon. Advancement of another successful quantum field theory for the strong interaction, called "Quantum Chromodynamics (QCD)," reinforces the belief that all the forces in Nature can be ultimately unified. There is now a major effort among the particle physicists to complete the "Grand Unified Theory (GUT)", which combines the strong interaction with the already unified electro-weak interaction.

One of the interesting predictions resulting from grand unification efforts is the existence of a new particle (or particles) which may be manifested as an intermediate-range force between electrically neutral bodies. Similar predictions have been made by workers in the "Supersymmetry-Supergravity" theory, a parallel effort to unify all the known forces. In addition to the massless graviton, which is presumably responsible for Newtonian-Einsteinian long-range gravity, additional massive particles have been proposed to complete the symmetry in the supergravity theory. Since all the above proposed particles are supposed to mediate forces between neutral bodies and have finite masses, they should cause apparent violation of the gravitational inverse square law in the ranges determined by their masses. Figure 2-6 summarizes the fundamental forces in Nature and their relationship with the unified theories. The theories which contain the prediction of a possible "Fifth Force" are indicated.

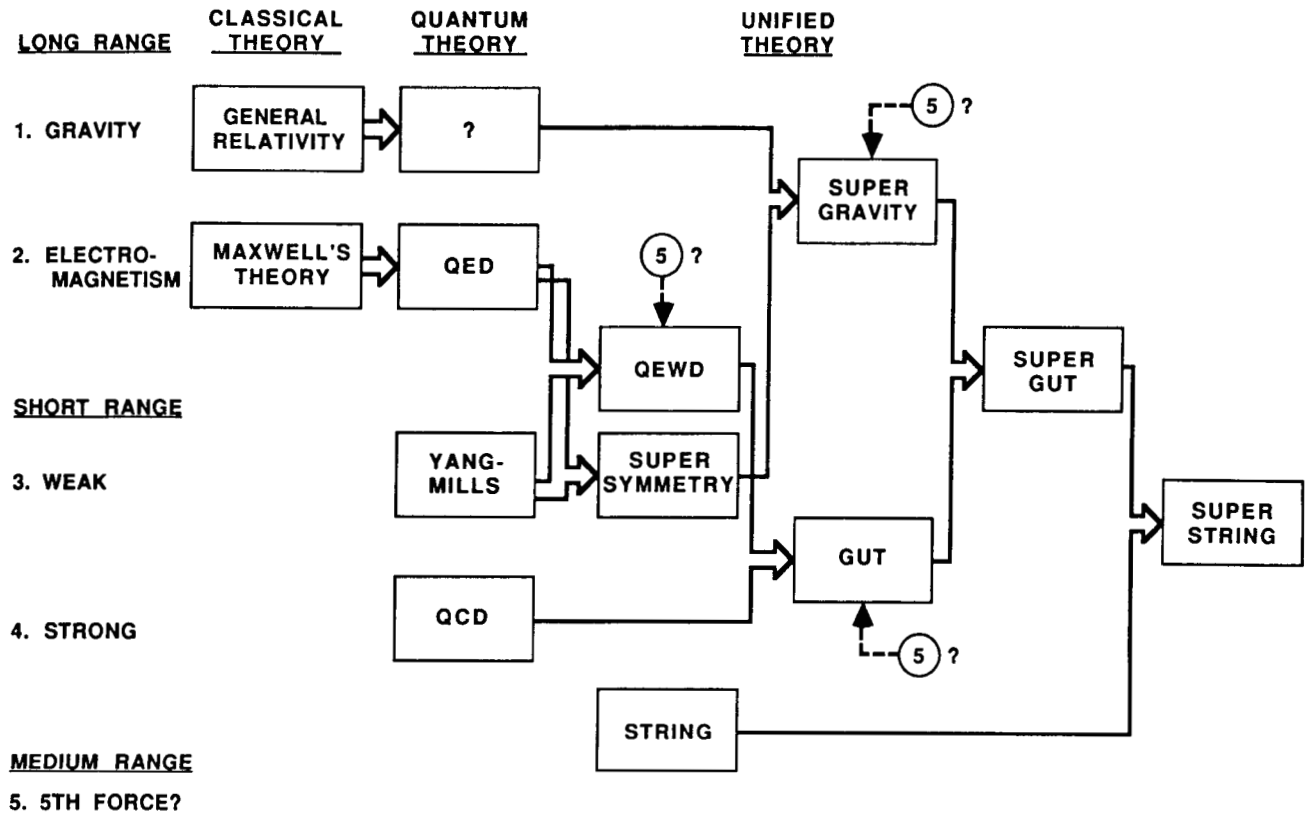


Figure 2-6. Forces in Nature.

Because of the limited range and accuracy with which the laws of gravitation have been tested to date, the experimental limits for the coupling strengths of the new particles are very poor in the range below the Earth's radius. Moreover, it has been reported that the geophysically determined gravitational constant G is consistently higher than the laboratory value G_0 [77]. This result can be interpreted as a manifestation of a non-Newtonian potential of the form:

$$\Phi(r) = - G_{\infty} \frac{m}{r} (1 + \alpha e^{-r/\lambda}) \quad , \quad (2.6)$$

where $\alpha = - (7.2 \pm 3.6) \times 10^{-3}$ and λ could be anywhere between 10 m to 10 km. More recently, Fischbach et al. [78] have claimed that the re-analysis of the original Eötvös experiment reveals an apparent violation of the Equivalence Principle. This could be interpreted as a manifestation of a short-range force with a composition-dependent coupling constant. In order to validate these claims, and provide guidance to ongoing theoretical attempts in understanding the laws of Nature, it is important to improve the limits of the inverse square law in all ranges.

Although many Earth-based experiments are being conducted, a satellite experiment can obtain high resolution data for the inverse square law in the range between 10 to 10^4 km, which is inaccessible by laboratory experiments. Recently, a new experimental approach to test the inverse square law has been proposed and demonstrated by scientists at the University of Maryland (see Appendix D). Unlike the classical Cavendish experiments in which the force equation, equation (2.6), is checked by

measuring forces and distances between two test masses, the new experiment [79] tests its differential form, the Poisson equation for the potential:

$$\nabla^2 \phi(r) = - \frac{G_{\infty} m}{r} \left(0 + \frac{\alpha}{\lambda^2} e^{-r/\lambda} \right), \text{ at } r \neq 0, \quad (2.7)$$

where $\nabla^2 (1/r) = -4\pi \delta(r)$ has been used to eliminate the Newtonian contribution. Therefore, one could perform a null experiment for Newtonian gravity if one could construct a detector which measures $\nabla^2 \phi(r)$. This new experiment has the important advantage of being independent of source geometry and density irregularities, which set practical limits to the accuracy and range of Cavendish-type experiments. Further, if $\alpha \neq 0$, a non-zero result of $\nabla^2 \phi(r)$ would be a direct measure of α and λ , as can be seen from equation (2.7). A null result would be equally important in discriminating against competing theories of gravity and particle physics.

Since $\nabla^2 \phi$ is the trace of Γ_{ij} , the gravity gradient tensor, one could detect $\nabla^2 \phi$ by simply summing the outputs of three diagonal component (Γ_{ii}) gradiometers. For the SGGM, the satellite is proposed to be in a low altitude (160 to 200 km) circular polar orbit. In this configuration, ϕ will be modulated at twice the orbital frequency of the satellite due to the oblateness of the Earth (~ 20 km between the equator and the poles). Therefore, one could analyze the $\nabla^2 \phi$ frequency spectrum to look for a violation of the inverse square law.

The resolution of the coupling constant of the non-Newtonian potential, $|\alpha_{\min}|$, expected for Earth-orbit experiments, is plotted in Figure 2-7 (dotted lines). The upper curve is the resolution expected from a Shuttle mission at 300 km altitude with a duration of 7 days. The lower curve corresponds to the resolution expected for the SGGM at 200 km altitude with an orbital lifetime of 6 months. Instrument sensitivities of $10^{-2} \text{ E Hz}^{-1/2}$ and $10^{-4} \text{ E Hz}^{-1/2}$, at the signal frequency of $4 \times 10^{-4} \text{ Hz}$, have been used for these plots. Also plotted in the figure are the claimed violations of the inverse square law [77] (shaded area) and limits obtained indirectly from the Earth surface gravity data [80], from the lunar surface gravity data, and from the GM_E values determined by the LAGEOS mission [81] and lunar ranging data [82], where M_E is the mass of the Earth.

Figure 2-7 shows that the limit of validity of the inverse square law can be improved by several orders of magnitude on the geological scale of distance by means of the proposed experiment. This would be a highly desirable result which can contribute greatly to the development of modern theories of gravity and particle physics.

As will be discussed in Section 3.1, however, this physics experiment imposes stringent requirements for attitude control of the spacecraft and the stability of the gradiometer scale factors that are many orders of magnitude beyond those required for the geodesy mission, if one wishes to obtain the highest resolution allowed by the sensitivity of the instrument.

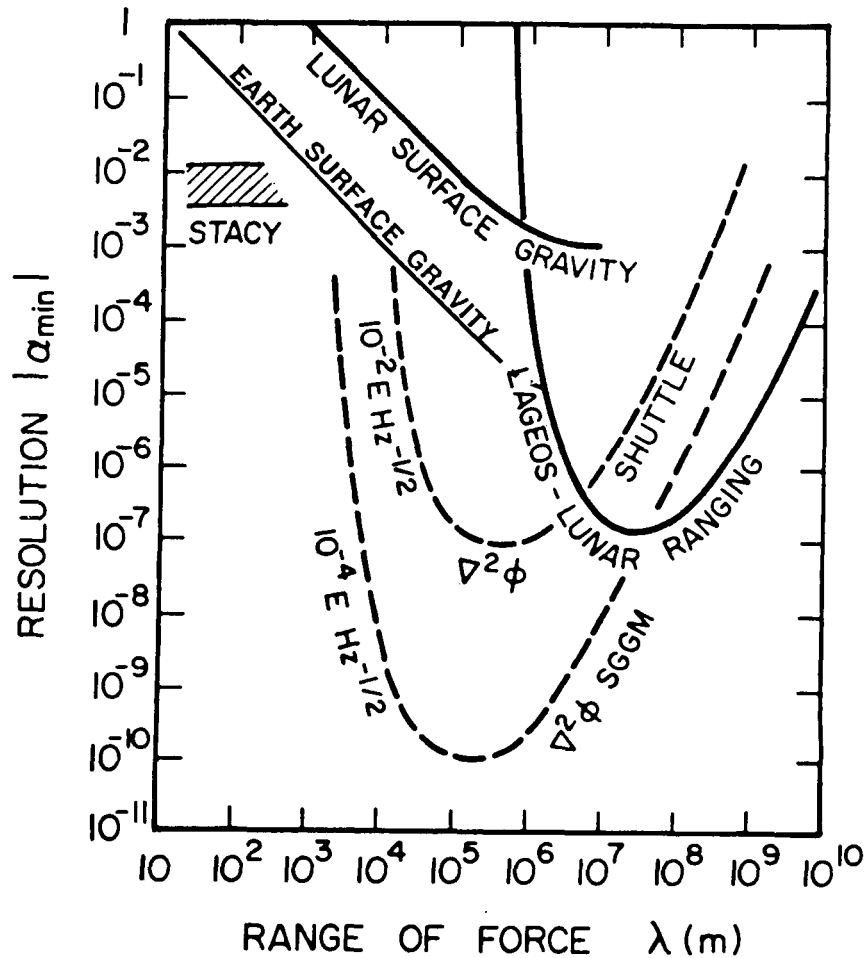


Figure 2-7. Expected resolution of α as a function of λ for $\nabla^2 \phi$ experiments in Earth orbit (dotted lines).

2.2.2 New Tests of General Relativity

Einstein's General Theory of Relativity is widely accepted as the correct theory of gravity. Unlike Newton's theory, Einstein's theory contains a velocity-dependent term in gravitational interaction, analogous to the magnetic field in electrodynamics. This results in dragging of local inertial frames, the so-called Lense-Thirring effect, as well as gravitational radiation [83]. This dynamical aspect of General Relativity has never been tested although the static feature of the theory has been checked repeatedly by such classical tests as the perihelion shift of Mercury and light bending experiments. An international effort to detect gravitational radiation is underway. The Gravity Probe-B (GP-B) mission is an attempt to detect the Lense-Thirring effect by measuring the precession of superconducting gyros in Earth orbit [84]. A highly sensitive superconducting gravity gradiometer in Earth orbit may provide another way to check the dynamical prediction of General Relativity. If this experiment could be performed with a resolution comparable to that expected of GP-B, it would provide a highly desirable independent check of the GP-B results.

The experiment in which the gravitomagnetic field due to the angular momentum of the Earth is directly observed with an orbiting gravity gradiometer was originally

suggested by Braginsky and Polnarev [85]. More detailed analyses of the tidal matrix that a gravity gradiometer is expected to see in Earth orbit has been obtained by Mashhoon and Theiss [86]. The Riemann (gravity gradient) tensor for a spherical Earth for an observer in a polar orbit can be written in isotropic polar coordinates (r, θ, ϕ) as

$$\Gamma_{ij} = -c^2 R_{0j0}^i = \frac{G M_E}{r^3} \begin{bmatrix} 2-3\epsilon & 0 & 9\mu \sin \omega_O \tau \\ 0 & -1+3\epsilon & 3\mu \cos \omega_O \tau \\ 9\mu \sin \omega_O \tau & 3\mu \cos \omega_O \tau & -1 \end{bmatrix}, \quad (2.8)$$

where

$$\epsilon = \frac{G M_E}{rc^2} \quad (2.9)$$

and

$$\mu = \frac{G J_E}{r^3 c^2 \Omega_O} \quad (2.10)$$

are dimensionless parameters characterizing the "electric" and "magnetic" correction to the gravity gradient due to General Relativity. Here M_E and J_E are the mass and angular momentum of the Earth; r , Ω_O , and τ are the radius of the orbit, the angular velocity of the satellite, and the proper time, respectively. For a near-Earth orbit, $\epsilon = 7 \times 10^{-10}$ and $\mu = 1.5 \times 10^{-11}$, respectively. On the other hand, the SGG with $10^{-4} \text{ E Hz}^{-1/2}$ sensitivity can resolve the Newtonian gravity gradient ($3 \times 10^3 \text{ E}$) of the Earth to 8×10^{-12} in 6 months. Both the above relativistic effects would therefore be detectable if the Newtonian background could be removed to the required level.

Notice in equation (2.8) that the relativistic "electric" terms appear in diagonal components of the gravity gradient tensor and are constant in time as the Newtonian components. It is therefore very difficult to separate them from the large Newtonian background. Rather than attempting to detect individual correction terms, it would be easier to perform a null test for the sum of the diagonal terms. The tracelessness of the Riemann tensor is a general property of Einstein's field equations:

$$R_{\mu\nu} = \frac{4\pi G}{c^2} T_{\mu\nu}, \quad (2.11)$$

which is also borne out in equation (2.8). The inverse square law experiment discussed in Section 2.2.1 becomes a null test for Einstein's field equations when the

resolution of the experiment exceeds the level of the relativistic correction ϵ . If the satellite is in an elliptical orbit, the Newtonian background is fully modulated so that ϵ can be resolved with a signal-to-noise ratio of 100 with a gradiometer of $10^{-4} \text{ E Hz}^{-1/2}$ sensitivity. If, however, the satellite is in a circular orbit and the oblateness of the Earth is used as the signal, the gradiometer sensitivity must be improved to $10^{-5} \text{ E Hz}^{-1/2}$ for this experiment.

The relativistic magnetic terms should be easier to detect than the electric correction terms because they appear as off-diagonal components of the tidal matrix, and are also modulated once per orbit. There are many ways to separate the magnetic terms from the Newtonian terms. In order to detect off-diagonal components of the tensor using inline component gravity gradiometers, it is necessary to orient the sensitive axes of the gradiometer away from the coordinate axes, thus performing a rotational transformation of the tensor. For example, the instrument axes could be rotated through an angle ψ around the vertical (\hat{r}). New tidal matrix components are then obtained by

$$\Gamma'_{11} = \Gamma_{rr} \quad , \quad (2.12a)$$

$$\Gamma'_{22} = \Gamma_{\theta\theta} \cos^2 \psi + \Gamma_{\theta\phi} \sin 2\psi + \Gamma_{\phi\phi} \sin^2 \psi \quad , \quad (2.12b)$$

$$\Gamma'_{33} = \Gamma_{\theta\theta} \cos^2 \psi - \Gamma_{\theta\phi} \sin 2\psi + \Gamma_{\phi\phi} \sin^2 \psi \quad . \quad (2.12c)$$

Since $\Gamma_{\theta\phi}$ contains the magnetic component, the signal can be separated by setting $\psi = 45 \text{ deg}$ and differencing Γ'_{22} and Γ'_{33} :

$$\Gamma'_{22} - \Gamma'_{33} = 6\mu \frac{G M_E}{r^3} \cos \omega_o \tau \quad . \quad (2.13)$$

The coefficient 6μ can be determined by Fourier analysis of difference signal $\Gamma'_{22} - \Gamma'_{33}$.

One of the most important error sources for this experiment is the once-per-orbit modulation of the Newtonian terms by the eccentricity of the orbit. It is interesting to note that this error is reduced to a second order error by the above signal differencing process (see Section 3.1.3). Residual Newtonian terms are coupled through pointing errors for the sensitive axes and a scale factor mismatch between the two horizontal axes. As a result, the scale factor stability requirement is reduced considerably from that required for the inverse square law experiment.

A preliminary error analysis [87] shows, however, that the pointing errors and the centrifugal acceleration errors do not cancel out completely. The attitude requirement for this experiment is therefore similar to that for the inverse square law experiment. Another serious technical question may be whether the gravity gradiometer

will have drift low enough to render a noise spectral density of $10^{-4} \text{ E Hz}^{-1/2}$ or better at frequencies as low as the Schuler frequency ($1.9 \times 10^{-4} \text{ Hz}$), where the signal is expected to appear.

Both the null test of Newton's inverse square law and the detection of Einstein's gravitomagnetic field are important scientific investigations. The possibility of conducting these exciting experiments in fundamental physics enhances the attractiveness of the SGGM.

2.3 Additional Objectives and Potential Spinoffs

While the primary goal of the SGGM is a gravity survey mission, there are other fundamental reasons for further development of the gravity gradiometer. Included among the applications of the instrument are INS/gradiometer orbit station keeping and pointing, and stable platforms. Other possible applications include power relay to Earth, land-based communications, Earth observations, autonomous navigation, spaceplane navigation, micro-g work stations, "drift-free" gravimeters for in situ gravity measurements, conventional INS calibration, Earth-based stable platform control sensors, and many others that will only become apparent with developmental research.

In order to produce an instrument capable of making the above measurements, it will be necessary to create the world's most accurate acceleration sensor. If the measurement of gravity gradients and linear and angular accelerations can be made at the levels proposed, then a new class of inertial instruments will be possible. The ramifications of such a fundamental leap in inertial instrument accuracy could well change a large number of fields that depend upon motion detection and the measurement of gravity.

2.3.1 Inertial Navigation

The classical building block of a navigation system is dead reckoning which presupposes that one knows exactly where one is and the direction and distance to where one wants to be. Given perfect instrumentation, and no external forces, one can follow one's position along the desired track. Of course, noise levels in instrumentation and path descriptions contaminate these estimates of position. By adding inertial instrumentation, i.e., accelerometers and gyros, one can passively estimate external forces, including gravitational, allowing real-time corrections and improving position and navigation estimates. For example, in space or under the sea, a perfect instrument and knowledge of the gravitational field along the path would allow one to reproduce a path without the aid of external navigation aids. The present error budget for a high accuracy Inertial Navigation System (INS) is divided among the INS system errors, gravity and geodesy errors, and control issues. Accurate testing and calibration of INS's address the former two (see Section 2.3.4).

Separating kinetic from gravitational acceleration can be made in two ways. First, external positioning and navigation aids could determine kinetic accelerations. Given access, even occasionally, to an external navigation aid (e.g., Global Positioning System), corrections or calibrations may be obtained, yielding information about one's unmodeled navigation environment. Thus, reproducibility of a given path, and corrections for external effects can be strongly enhanced. Secondly, accurate gravity models can estimate the gravitational acceleration.

The development of the cryogenic gravity gradiometer and six-axis accelerometer would open an entirely new chapter in the field of inertial sensors. The uses for such instrumentation span the entire acceleration spectrum: from DC devices such as gravimeters through tilt meters, seismometers, and navigation devices for aircraft and spacecraft, and platform stabilization systems for pointing. It will also be possible to separate inertial and gravitational accelerations in real time.

Gravity measurements and navigation (including station-keeping and measurements at fixed points) are intimately related. Focusing on one area traditionally has required estimates of the other. As both improve, it becomes feasible to measure gravitational acceleration and navigate simultaneously, i.e., processing signals for gravity estimates and navigation solutions simultaneously. As the speed and accuracy with which gravity measurements can be made increases, and are linked with highly accurate and precise tracking, the difference between the measurements made by a navigation system and that of a classical gravimeter are beginning to blur. As these measurements start to blend, it becomes necessary to measure not only the total acceleration but also the relative acceleration between the various reference frames for most applications. Using external aids and signal processing techniques, with the aid of a gravity gradiometer which only senses differences of acceleration and rotation, it has become possible to separate the various quantities to near real time. Thus, such an INS/gradiometer system would yield simultaneous kinetic and gravimetric measurements.

2.3.2 Orbit Calculations - Geodesy

The positioning, navigation, and orientation of satellites is of crucial importance to many missions using these satellites. Radio-navigation satellites (e.g., GPS, TRANSIT) generally cannot provide more accurate positioning to the user than the accuracy with which we know the satellite's own position. Satellite altimetric missions (e.g., GEOSAT, SEASAT, GEOS) provide their scientific data in the form of ranges from satellite to the ocean surface. Since the quantity desired is the distance from the center of the Earth to the sea surface, the satellite position relative to the Earth must be known. Satellite-to-satellite communications, especially those depending on lasers, depend on accurately positioned satellites. Recently, accurately positioned satellites (i.e., GPS) have been used to perform accurate geodetic measurements on the Earth's surface, including direct measurements of plate tectonics.

Typical best accuracies available today are 0.1 to 10 meters for satellite positions: geodetic measurements using GPS have accuracies approaching 1 part in 10^7 , with improvement to 1 part in 10^8 expected in the near future. The latter accuracies are possible from extensive post-mission processing and long real-time averaging. Orbit accuracies of 0.1 m will bring tracking errors in line with the other components of the error budget in satellite geodesy problems.

Satellite orbits closely follow geodesic paths, partially defined by the Earth's gravity field. Tracking systems use all available information including radar ranges (time delay and Doppler shifts) and gravity models to create a best-fit solution to all variables. Obviously, better determination of gravity fields at orbital altitudes improves orbit solutions, which in turn yield superior satellite-derived geodetic positions.

2.3.3 Planetary Science

Gravity field observations of planetary bodies, in conjunction with other observations, such as imagery and altimetry, provide estimates of interior structure models, which in turn place constraints on thermal history and planetary evolution. Primarily, the gravity data reveal the internal lateral density distribution, and the loading pressures that must be sustained over geologic time (millions to billions of years) by isostatic adjustment, or support by either elastic plates or dynamical convective forces. For example, the mascons on the Moon and Mars require dense material in their lowland basins, and uplift of dense mantle, to explain the large position gravity anomalies associated with them. The offset of the lunar center of gravity from the geographical center may be explainable by variations in global crustal thickness. Results from models that use isostatic adjustment at depth produce values that, in some cases, are so unrealistic that one is led to dynamic support models. An example is Beta Regio on Venus.

Presently, most gravity observations are acquired from Doppler radio tracking of orbiting spacecraft, at accuracies of about 1 mm sec^{-1} . Unfortunately, from the standpoint of gravity studies, this data is both undesirably noisy and has awkward gaps due to occultations. These data are primarily line-of-sight data profiles, making global coverage difficult; such coverage is possible if the spacecraft is orbiting the planet. Such data is capable of resolving about 5 mgal crustal anomalies of dimensions comparable to, or larger than the orbital altitude. Of course, lower altitudes have greater data losses due to occultations.

Although a planetary science mission (other than to the Moon) utilizing an SGG cooled by liquid helium may not be practical at this time, the closed cycle refrigerators under development may render SGG planetary missions feasible in the near future (see Section 6.2). Furthermore, a granular compound which exhibits superconductivity at temperature above 90 K has recently been discovered. Since this field is expanding rapidly, it is expected that materials with even higher transition temperatures will be found, and that new superconducting materials will soon be produced in useful forms for device applications. If a sensitive SGG could operate at liquid nitrogen temperatures (66 to 80 K), a planetary mission carrying an SGG would certainly be feasible, because a reasonably compact liquid nitrogen dewar with a lifetime of many years in space could be constructed with available technology (Section 6.3).

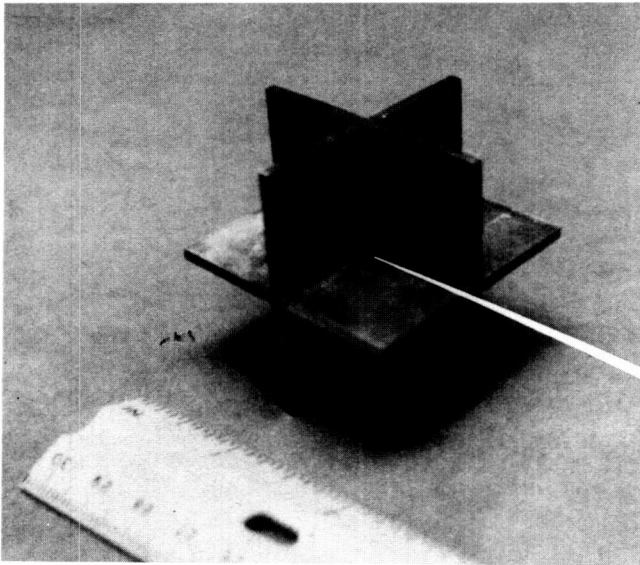
2.3.4 Other Applications

Earth Rotation: The rotating Earth is in an accelerated frame. Changes in the length of a day and polar wobble alter this accelerated frame. Currently, determination of these effects is made using astronomic observations (e.g., LAGEOS, Very Long Baseline Interferometry). A "perfect" accelerometer and gradiometer system, however, should also show these Earth rotation anomalies. Very accurate determinations of the Earth's rotational acceleration can also be used as a clock or a longitude sensor.

Seismology: A seismometer is simply an accelerometer tuned to earthquake frequencies. A great deal of information has been obtained about the Earth using seismic data. Microseismicity, or background seismic activity of the Earth, is generally characterized as noise. However, some general properties of the Earth can be deduced from these data. It is possible that the elusive clues to earthquake prediction may be buried in these background signals. Again, improved seismic instrumentation, based on the technology developed for the SGGM may prove very useful in determining geophysical parameters which may contribute to saving lives and property.

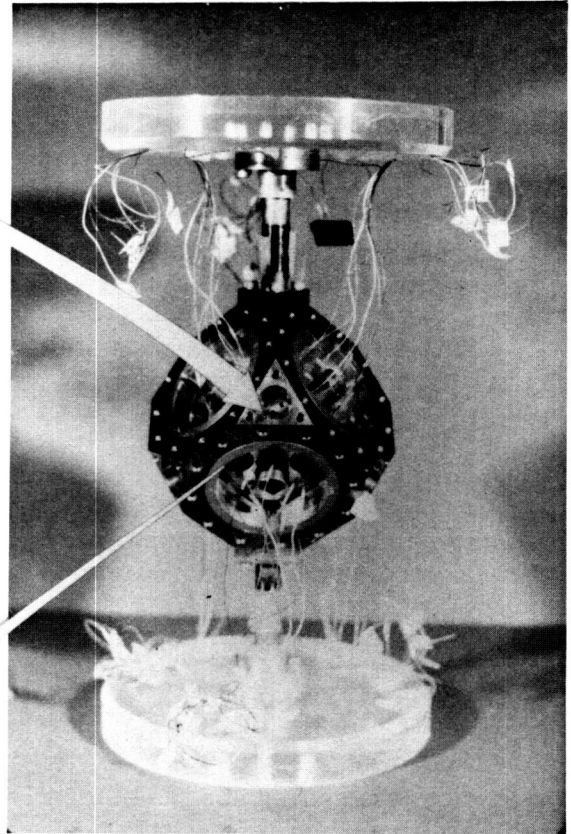
Mineral Exploration: Techniques for mineral exploration may also be advanced with SGGM technology. Mineral deposits have very small effects on local gravity, but with a very sensitive multi-axis gravimeter and gradiometer, such deposits might have significant signatures.

Calibration and Testing of INS's: Not all platforms requiring highly accurate measurements of the acceleration environment can carry cryogenic support, as is required here. However, simpler instrumentation can be developed with very high precision, or resolution, that is not dependent on cryogenic support. Advanced instrumentation can be calibrated or initialized using more accurate cryogenic systems. The testing and calibration of all types of inertial test facilities is limited by the ability to monitor and control the testing environment. For example, in highly accurate inertial navigation systems, environmental inputs now mask the true inertial instrument performance. Seismic noise, polar wobble, crustal instability, change in the water table, tidal action, and cultural noise are all geophysical signals that limit testing. It is now no longer possible to test high accuracy inertial systems adequately. In the future, it will not be possible to improve INS without improving the testing platforms, and without a better understanding of the test environment. This can only be done with better sensors, better signal processing, and a better understanding of the underlying geophysics. The superconducting INS/gradiometer system can be used to monitor and control the testing platforms with great precision.

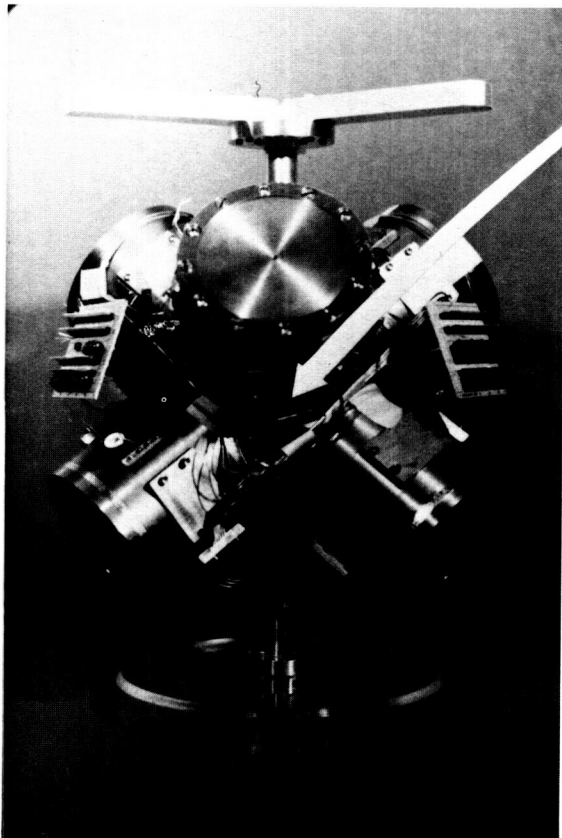


ORIGINAL PAGE IS
OF POOR QUALITY

**ACCELEROMETER NIOBIUM
PROOF MASS**



**SUPERCONDUCTING 6-AXIS
ACCELEROMETER**



PROTOTYPE 3-AXIS SGG

Figure 3-1. Superconducting Gravity Gradiometer.

3.0 SUPERCONDUCTING GRAVITY GRADIOMETER (Fig. 3-1)

The Equivalence Principle of Einstein holds that it is impossible, even in principle, to separate gravity and acceleration by a local measurement. However, by making a differential measurement over a baseline, one can cancel out acceleration and detect gravity without being confused by platform motions. This is because platform accelerations have no spatial gradients. Although torsion balances have been used to measure gravitational force gradients for over two centuries, only in the past two decades have serious efforts been made to develop moving base gravity gradiometer. In the fall of 1986, drawing on successful shipboard testing since 1983, the first moving base tests of a gravity gradiometer in an aircraft were made by Bell Aerospace. Today, primarily due to superconducting transducer work for low temperature gravitational wave detectors [88], extremely sensitive gradiometer instruments based on superconducting technology have been developed.

In a superconducting instrument, the inconvenience of cryogenic operation is offset by the opportunity to utilize many properties of superconductors to obtain improvement in the sensitivity and stability of gravity sensors. In addition to the obvious reduction of thermal noise and high mechanical stability of the instrument, the quantization of magnetic flux can be used to obtain "perfectly" stable means of signal transduction, scale factor matching, and proof mass levitation. The availability of Superconducting Quantum Interference Devices (SQUIDs) at liquid helium temperatures is another important factor that makes the superconducting device attractive. SQUIDs are highly sensitive flux measuring devices which are based on the Josephson tunneling and fluxoid quantization in superconducting loops. Commercial SQUIDs employed in the SGG research have input coils that convert small currents into magnetic fluxes. The sensitivity of these instruments is 1.5×10^{-12} A Hz^{-1/2} and the dynamic range is 10^8 Hz^{1/2}. A SQUID device, when used as a detector in a superconducting transducers, is theoretically capable of measuring the relative position of a proof mass with an accuracy better than 10^{-16} m! This is truly remarkable when one recalls that the radius of an atomic nucleus is of the order of 10^{-15} m.

Since a gradiometer must detect a very weak differential gravity signal in the midst of large platform accelerations and other environmental disturbances, the scale factor and common mode rejection stability of the instrument is extremely important in addition to its immunity to temperature and electromagnetic fluctuations. Flux quantization, the Meissner effect, and properties of liquid helium can be utilized to meet these challenges.

3.1 Instrument and Platform Requirements

For the measurement of the Earth's gravity field, an instrument design goal of 3×10^{-4} E Hz^{-1/2} has been established [5]. Studies have shown (see Appendix C) that a three-axis gradiometer flown in a 200-km polar orbit and having a precision of 10^{-4} E can be used to determine gravity anomalies to a total uncertainty of about 1 mgal for a 1 deg x 1 deg block. The signal frequency band is from 10^{-3} Hz to about 0.1 Hz, corresponding to spatial resolutions of 4,000 to 40 km. For the fundamental tests of the laws of gravity, a sensitivity level of 10^{-4} E Hz^{-1/2} or higher

is desired. However, the frequency band over which this sensitivity is needed is restricted to the vicinity of the signal frequencies, 2×10^{-4} Hz for the inverse square law test, and 4×10^{-4} Hz for the gravitomagnetic field experiment.

The three-axis configuration is essential for the basic science experiments, and is also desirable for geodesy because of the desired redundancy in instrumentation and the capability of performing cross checks between the three sets of data. Further, the $\nabla^2\phi$ output could be used to monitor the attitude rate Ω of the satellite, which in turn reflects the orbit dynamics in the geocentric orientation of the spacecraft. It appears, therefore, that a three-axis diagonal component gradiometer is a reasonable compromise between a single-axis and a full tensor instrument.

While it is an extremely demanding task to realize the 10^{-4} E Hz $^{-1/2}$ instrument sensitivity, an even bigger challenge is how such a sensitive instrument can be isolated from the not-so-benign mechanical, electromagnetic, and thermal environments in the spacecraft. A porous plug has been successfully used for the Infrared Astronomy Satellite (IRAS) to confine superfluid helium in low gravity, and liquid helium sloshing motion has been found to be manageable [89]. For the SGGM, however, any residual helium motion, and structural vibrations caused by thruster firings, may be severe sources of noise.

3.1.1 Geophysics

In this section, a heuristic derivation is given of the gravity gradient signal spectrum that the gradiometer is expected to encounter at the orbital altitude and the instrument noise spectral density required to detect it. The instrument requirement is then translated into platform control/knowledge requirements in terms of spectral densities, using an analytic error model of the SGG. The numerical values derived in this section should be considered preliminary, since a sophisticated simulation of the control loops and signal processing algorithms must be carried out to obtain full effects of various error sources. On the other hand, full simulation studies cannot be performed until the control system is designed (see Appendix G). Nevertheless, the required instrument sensitivity derived from the simple analysis given in this section, 3×10^{-4} E Hz $^{-1/2}$ for a 200-km orbit, agrees with the values obtained by other, more sophisticated, error analyses of a gradiometer mission (see Appendix C).

The spectral density of the Earth's gravity gradient at satellite altitudes has been computed by various authors [90-93]. Figure 3-2 represents the rms signal amplitudes for the vertical-vertical component (Γ_{rr}) of the gravity gradient tensor as a function of harmonic degree ℓ expected at two different satellite altitudes: 160 and 200 km. The gradiometer signal frequency f corresponding to ℓ is computed by

$$f = (\Omega_0/2\pi) \ell = (1.9 \times 10^{-4} \text{ Hz}) \ell, \quad (3.1)$$

where $\Omega_0 = (GM_E/R_E^3)^{1/2} = 1.2 \times 10^{-3}$ rad sec $^{-1}$ is the orbital angular velocity of the satellite. This frequency scale is denoted at the top of Figure 3-2. A spatial resolution of 50 km, which corresponds to $\ell = 400$, therefore requires a bandwidth from zero to approximately 0.1 Hz. In order to eliminate aliasing errors, a sampling frequency of 1 Hz could be used.

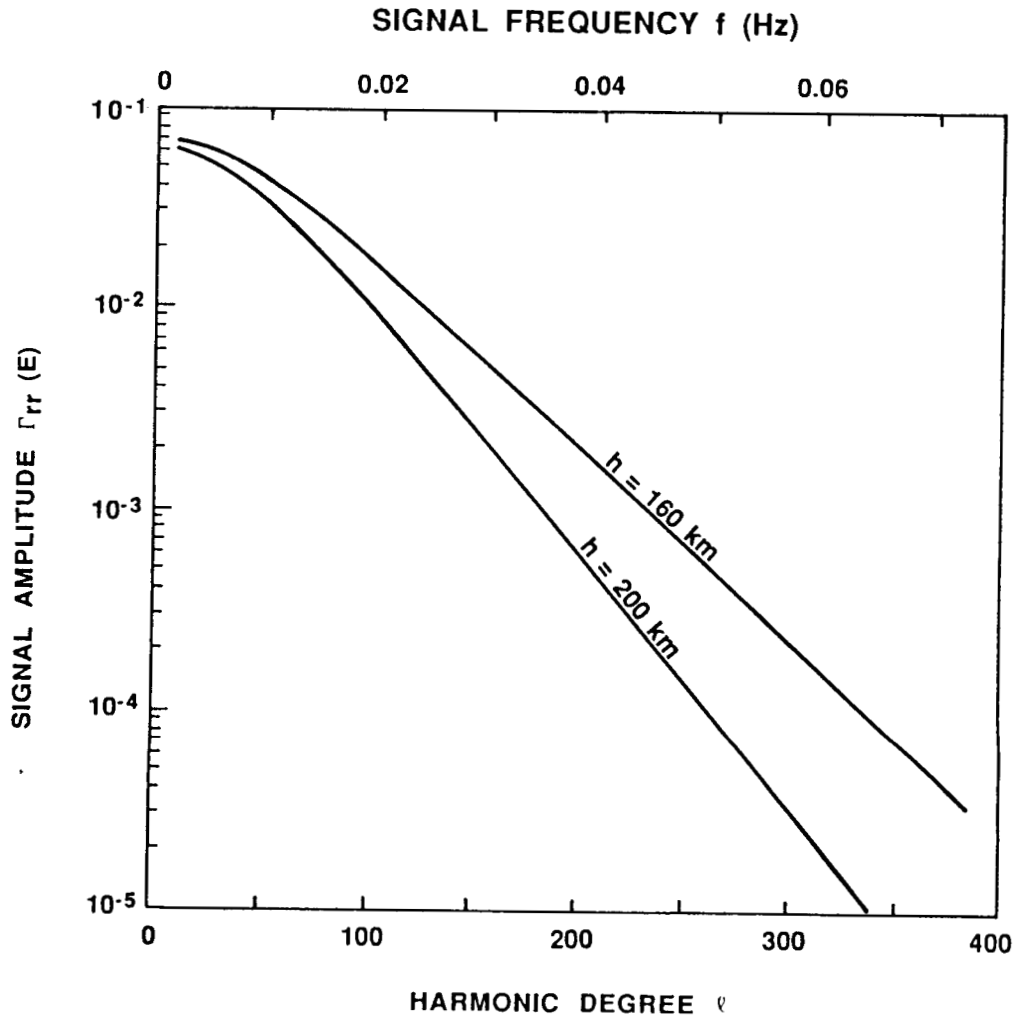


Figure 3-2. RMS signal amplitudes for vertical-vertical component of gravity gradient tensor as a function of harmonic degree for two altitudes.

It is desirable to translate the expected signal spectrum (in E) of Figure 3-2 into an instrument spectral density requirement (in $E \text{ Hz}^{-1/2}$) versus frequency. In order to do this, one has to determine the effective measurement bandwidth, $(\Delta f)_\ell$ for each harmonic ℓ . In an ideal case when the measurement is limited by random noise of the instrument, one can show that

$$(\Delta f)_\ell \approx (2\ell+1)/T, \quad (3.2)$$

where T is the mission duration. For $\ell = 400$ and $T = 6$ months, $(\Delta f)_\ell = 5 \times 10^{-5}$ Hz is obtained so that the required instrument spectral density

$$S_{\Gamma, \ell}^{1/2}(f) = \Gamma_{rr, \ell} (\Delta f)_\ell^{-1/2}, \quad (3.3)$$

becomes 4×10^{-3} and $3 \times 10^{-4} \text{ E Hz}^{-1/2}$ for $h = 160$ and 200 km , respectively. In practice, the situation is more complicated since additional errors arise from the finite sampling interval and finite track spacing as well as from other systematic error sources. Equations (3.2) and (3.3), however, indicate an important fact: since both $\Gamma_{rr,\ell}$ and $(\Delta f)_\ell^{-1/2}$ are larger at lower values of ℓ , much higher instrument noise could be tolerated at lower signal frequencies for the same signal-to-noise ratio.

Many geophysics objectives enumerated in Section 2.1 call for a resolution of 2 to 3 mgal at a wavelength of 100 km, or a spatial resolution of 50 km (Fig. 2-5). The wavelength λ and block size S (in degrees) are related to the harmonic degree ℓ by

$$\ell = (40,000 \text{ km})/\lambda = 180 \text{ deg sec}^{-1} . \quad (3.4)$$

Therefore, the above objective corresponds to a gravity anomaly uncertainty of 2 to 3 mgal for a $1/2 \text{ deg} \times 1/2 \text{ deg}$ block. Figure C-2 of Appendix C indicates that a gradiometer sensitivity of 10^{-4} E is required for this, assuming a six-month mission at 160 km altitude. For a signal bandwidth of 0.1 Hz, one finds the spectral density requirement of the instrument: $3 \times 10^{-4} \text{ E Hz}^{-1/2}$. It is desirable to extend this sensitivity down to 10^{-3} Hz in order to satisfy the objectives for seismic tomography and temporal variation of the Earth's gravity field.

In Table 3-1, the instrument performance requirements for geodesy are summarized together with the platform control/knowledge requirements corresponding to two levels of gravity gradient noise: 10^{-2} and $10^{-4} \text{ E Hz}^{-1/2}$. Control to the required level is preferred. However, if certain requirements cannot be satisfied by control, measurement and compensation must be performed. The error model for the SGG has been derived [94,95]. \vec{T}_E represents the gravity gradient tensor of the reference ellipsoid. The requirement on the scale factor drift is based on the desirability of maintaining the scale factor calibration to within 1 percent over the entire orbital lifetime. This requirement could be eliminated if a provision is made to continually upgrade the instrument calibration. For example, when the gradiometer is in the inertial orientation, the Earth's gravity gradient is modulated once per orbit and could, therefore, be used as a calibration signal. For the Earth-fixed orientation, the gravity data at the poles, which is obtained every orbit, could be used to obtain a relative calibration of scale factors from orbit to orbit. The dynamic range required for the worst case is $3 \times 10^7 \text{ Hz}^{1/2}$, or 10^8 for 0.1 Hz bandwidth. This is within the dynamic range of a superconducting gradiometer in feedback operation.

In order to compute the linear acceleration requirement, a residual misalignment between the sensitive axes of the two component accelerometers of $|\delta \hat{n}_-| = 10^{-7}$ is assumed which is equivalent to a passive common mode rejection to 1 part in 10^7 . Even with such a common mode rejection factor, the $10^{-4} \text{ E Hz}^{-1/2}$ gradiometer requires a linear vibration level either not to exceed $2 \times 10^{-8} g_E \text{ Hz}^{-1/2}$, or to be compensated to the same accuracy. The large gravity gradient bias of the Earth

TABLE 3-1. REQUIRED CONTROL/KNOWLEDGE OF INSTRUMENT AND PLATFORM PARAMETERS FOR GEODESY

1-3072-7-4D		GEOPHYSICS GOAL: $3 \times 10^{-4} \text{ E Hz}^{1/2}$ AT $f = 0.1 \text{ Hz}$				
PARAMETER	ERROR MECHANISM	ORIENTATION	REQUIRED CONTROL/KNOWLEDGE			
INSTRUMENT NOISE	$S_{\Gamma}^{1/2}(f)$		$10^{-2} \text{ E Hz}^{-1/2}$	$10^{-4} \text{ E Hz}^{-1/2}$		
SCALE FACTOR DRIFT	$\Gamma \, d\sigma/dt$		$2 \times 10^{-6} \text{ hr}^{-1}$	$2 \times 10^{-6} \text{ hr}^{-1}$		
DYNAMIC RANGE	$\Gamma_{E, \text{MAX}}/S_{\Gamma}^{1/2}(f)$	INERTIAL EARTH-FIXED	$3 \times 10^5 \text{ Hz}^{1/2}$ $10^3 \text{ Hz}^{1/2}$	$3 \times 10^7 \text{ Hz}^{1/2}$ $10^5 \text{ Hz}^{1/2}$		
LINEAR ACCELERATION	$-\frac{1}{\rho} \delta \dot{\mathbf{n}} \cdot \vec{a}(f)$		$2 \times 10^{-6} \text{ g Hz}^{-1/2}$	$2 \times 10^{-8} \text{ g Hz}^{1/2}$		
ALTITUDE STABILITY	$(\dot{\mathbf{n}} \cdot \vec{\nabla}) \dot{\mathbf{n}} \cdot \vec{\Gamma}_E \delta h(f)$		$7 \text{ m Hz}^{-1/2}$	$7 \times 10^{-2} \text{ m Hz}^{-1/2}$		
POINTING STABILITY	$2 \vec{\theta}(f) \dot{\mathbf{n}} \cdot \vec{\Gamma}_E \cdot \dot{\mathbf{n}}$	INERTIAL EARTH-FIXED	$2 \times 10^{-6} \text{ rad Hz}^{-1/2}$ $3 \times 10^{-4} \text{ rad Hz}^{-1/2}$	$2 \times 10^{-8} \text{ rad Hz}^{-1/2}$ $3 \times 10^{-6} \text{ rad Hz}^{-1/2}$		
ATTITUDE RATE	$\vec{\Omega}(f) \cdot \vec{\Omega}(f) - [\dot{\mathbf{n}} \cdot \vec{\Omega}(f)]^2$		$3 \times 10^{-6} \text{ rad s}^{-1} \text{ Hz}^{-1/4}$	$3 \times 10^{-7} \text{ rad s}^{-1} \text{ Hz}^{-1/4}$		
ATTITUDE ACCELERATION	$\delta \dot{\mathbf{n}}_x \times \dot{\mathbf{n}} \cdot \vec{\alpha}(f)$		$10^{-6} \text{ rad s}^{-2} \text{ Hz}^{-1/2}$	$10^{-8} \text{ rad s}^{-2} \text{ Hz}^{-1/2}$		
INSTRUMENT TEMPERATURE	$(\partial \Gamma / \partial T) S_{\Gamma}^{1/2}(f)$		$10^{-2} \text{ K Hz}^{-1/2}$	$10^{-4} \text{ K Hz}^{-1/2}$		
ELECTRONICS TEMPERATURE	$(\partial \Gamma / \partial T_e) S_{\Gamma_e}^{1/2}(f)$		$1 \text{ K Hz}^{-1/2}$	$10^{-2} \text{ K Hz}^{-1/2}$		

(3×10^3 E in vertical direction) requires an altitude stability of the spacecraft. In Table 3.1, \hat{n} represents a unit vector pointing in the direction of measurement.

A most difficult source of error for a sensitive gravity gradiometer is angular vibrations (see Appendix B). The pointing stability error modulates the Earth's bias gradient. The attitude rate produces a centrifugal acceleration which also competes directly with the gravity gradient signal. In addition, the attitude acceleration causes a gradiometer output through another misalignment angle of the gradiometer, $\delta \hat{n}_{+\ell}$ (misalignment of the average sensitive axis of one gradiometer with respect to its baseline vector). $|\delta \hat{n}_{+\ell}| = 10^{-5}$ is assumed.

Notice that the attitude error modulates the cross component of the bias gradient $\Gamma_{E,ij}$. Clearly, this error is minimized by using an Earth-fixed orientation of the spacecraft for which $T_{E,ij}$ is small due to the near spherical symmetry of the Earth. Its maximum value of 18 E, found from the last term of equation (3.10) has been used to compute the attitude requirement for the Earth-fixed orientation. The Earth-fixed orientation, however, entails an increased centrifugal acceleration error due to the bias attitude rate of the instrument, which equals the orbital angular velocity of the spacecraft Ω_o .

Fortunately, this centrifugal acceleration error can be removed to the first order by using geometric properties of the three-axis gradiometer. The gravity gradient tensor in a frame rotating with an angular velocity $\vec{\Omega} = (\Omega_r, \Omega_\theta, \Omega_\phi)$ with respect to an inertial frame can be written as

$$\Gamma'_{ij} = \begin{pmatrix} \Gamma_{rr} + (\Omega_\theta^2 + \Omega_\phi^2) & \Gamma_{r\theta} - \Omega_r \Omega_\theta & \Gamma_{r\phi} - \Omega_r \Omega_\phi \\ \Gamma_{r\theta} - \Omega_r \Omega_\theta & \Gamma_{\theta\theta} + (\Omega_\phi^2 + \Omega_r^2) & \Gamma_{\theta\phi} - \Omega_\theta \Omega_\phi \\ \Gamma_{r\phi} - \Omega_r \Omega_\phi & \Gamma_{\theta\phi} - \Omega_\theta \Omega_\phi & \Gamma_{\phi\phi} + (\Omega_r^2 + \Omega_\theta^2) \end{pmatrix}. \quad (3.5)$$

In the Earth-fixed orientation of the spacecraft, which is in a polar orbit, $\vec{\Omega} = \Omega_o \hat{\phi} + \delta \vec{\Omega}$ so that

$$\Gamma'_{ij} = \begin{pmatrix} \Gamma_{rr} + (\Omega_o^2 + 2 \Omega_o \delta \Omega_\phi) & \Gamma_{r\theta} & \Gamma_{r\phi} - \Omega_o \delta \Omega_r \\ \Gamma_{r\theta} & \Gamma_{\theta\theta} + (\Omega_o^2 + 2 \Omega_o \delta \Omega_\phi) & \Gamma_{\theta\phi} - \Omega_o \delta \Omega_\theta \\ \Gamma_{r\phi} - \Omega_o \delta \Omega_r & \Gamma_{\theta\phi} - \Omega_o \delta \Omega_\theta & \Gamma_{\phi\phi} \end{pmatrix}, \quad (3.6)$$

to the first order in $\delta \vec{\Omega}$. Since $\sum_i \Gamma_{ii} = 0$ by the Laplace equation, the sum of the diagonal components uniquely determines the centrifugal acceleration error:

$$\sum_i \Gamma'_{ii} = 2 (\Omega_o^2 + 2 \Omega_o \delta \Omega_\phi) \quad . \quad (3.7)$$

Therefore, the true gravity gradient signals are recovered by

$$\begin{aligned} \Gamma_{rr} &= \Gamma'_{rr} - \frac{1}{2} \sum_i \Gamma'_{ii} = \frac{1}{2} (\Gamma'_{rr} - \Gamma'_{\theta\theta} - \Gamma'_{\phi\phi}) \quad , \\ \Gamma_{\theta\theta} &= \Gamma'_{\theta\theta} - \frac{1}{2} \sum_i \Gamma'_{ii} = \frac{1}{2} (\Gamma'_{\theta\theta} - \Gamma'_{\phi\phi} - \Gamma'_{rr}) \quad , \\ \Gamma_{\phi\phi} &= \Gamma'_{\phi\phi} \quad . \end{aligned} \quad (3.8)$$

The attitude rate error has, therefore, been reduced to a second order effect, as shown in Table 3.1. Orientation errors and scale factor mismatch among the three axes will in general prevent perfect cancellation of the first order centrifugal acceleration errors. It is clear, however, that these errors will be multiplied by the centrifugal acceleration terms to make the overall errors second-order effects. Notice that the unique determination of the centrifugal acceleration by the gradiometer itself is possible only with an instrument that measures the diagonal components of the tensor directly because the trace must be computed.

For the SGGM with $10^{-4} \text{ E Hz}^{-1/2}$ sensitivity, the state-of-the-art accelerometers and gyros may be sensitive enough to resolve the linear and angular motions of the platform to the required levels. However, it is important to measure the motion of the platform directly at the cryogenic end in order to avoid errors associated with relative motions between the inertial sensors and the gradiometer. It appears necessary that the gravity gradiometer instrument be designed with an internal capability of measuring linear and angular accelerations with sufficient accuracy. A combination of a star tracker, Sun sensor, and/or horizon sensor must be provided to zero-update the inertial instruments.

With the centrifugal acceleration reduced to a second-order error, the Earth-fixed orientation appears to be a better option, considering the dynamic range and pointing stability requirements. We will see in Section 5 that consideration of aerodynamic drag also makes the geocentric orientation a natural choice.

Electromagnetic interference does not appear to be a problem because superconductors permit nearly perfect electromagnetic shielding; however, care should be taken to eliminate magnetic contamination inside the shields. Also, the instrument should be cooled in a low magnetic field. An SGG can be rather sensitive to fluctuations in the ambient temperature. The three-axis SGG has been designed with the capability of balancing out the effects of a temperature drift in the superconducting circuit [96] (see Appendix E). The residual temperature sensitivity is expected to be less than 1 E K^{-1} . The resulting temperature control requirement of $10^{-4} \text{ K Hz}^{-1/2}$ for the helium bath is not difficult to satisfy.

3.1.2 Inverse Square Law Experiment

More stringent requirements for the instrument and the spacecraft arise for the inverse square law experiment. Additional requirements (over those required for geodesy) for the instrument are listed in Table 3-2 for a Shuttle experiment and for the free flyer. The Earth-fixed orientation has been assumed. The nature of the null experiment imposes requirements on the scale factors: the orthogonality and match among the three gradiometer axes.

TABLE 3-2. ADDITIONAL REQUIRED CONTROL/KNOWLEDGE OF INSTRUMENT AND PLATFORM PARAMETERS FOR INVERSE SQUARE LAW EXPERIMENT

PARAMETER	ERROR MECHANISM	REQUIRED CONTROL/KNOWLEDGE	
MISSION		7 DAYS AT 300 km ALTITUDE	180 DAYS AT 200 km ALTITUDE
RESOLUTION	$ \alpha_{\min} $	10^{-7}	10^{-10}
INSTRUMENT NOISE	$S_{\Gamma}^{1/2} (f)$	$10^{-2} E \text{ Hz}^{-1/2}$	$10^{-4} E \text{ Hz}^{-1/2}$
SCALE FACTOR DRIFT	$d\sigma / dt$	$2 \times 10^{-11} \text{ hr}^{-1}$	$2 \times 10^{-14} \text{ hr}^{-1}$
ORTHOGONALITY	$\vec{\phi} \times \hat{n} \cdot \vec{\Gamma}_E \cdot \vec{\phi} \times \hat{n}$	$3 \times 10^{-4} \text{ rad}$	10^{-5} rad
POINTING	$\vec{\theta} \times \hat{n} \cdot \vec{\Gamma}_E \cdot \vec{\theta} \times \hat{n}$	$3 \times 10^{-4} \text{ rad}$	10^{-5} rad
ATTITUDE RATE	$4 \Omega_o \delta \Omega_{\phi} (f)$	$2 \times 10^{-9} \text{ rad s}^{-1} \text{ Hz}^{-1/2}$	$2 \times 10^{-11} \text{ rad s}^{-1} \text{ Hz}^{-1/2}$

First, the orthogonality requirement for the sensitive axes is considered. Since it is impossible to align the sensitive axes of the gradiometer to 1 part in 10^{10} , it is important to find a way to make the gradient error second order in the error angle. For a spherical Earth, the gravity gradient is a maximum along the vertical direction and a minimum along any direction lying on the horizontal plane, as shown in Figure 3-3. The gradient errors arising from the non-orthogonality of the sensitive axes and the pointing error of the spacecraft will, therefore, be of the second order in those error angles if an Earth-fixed orientation is chosen for the gradiometer. However, because the time-varying signal for the inverse square law arises from the oblateness of the Earth, more careful analysis is required, and is given below. The relevant expansion of the potential for the inverse square law experiment is

$$\phi(r, \theta, \phi) = \frac{-GM_E}{r} \left[1 - \left(\frac{a}{r} \right)^2 J_2 P_2(\cos \theta) \right], \quad (3.9)$$

where a and J_2 are the equatorial radius and the harmonic coefficient corresponding to the oblateness of the Earth, respectively. The inline component gravity gradient along a direction \hat{n} can be computed from equation (3.9):

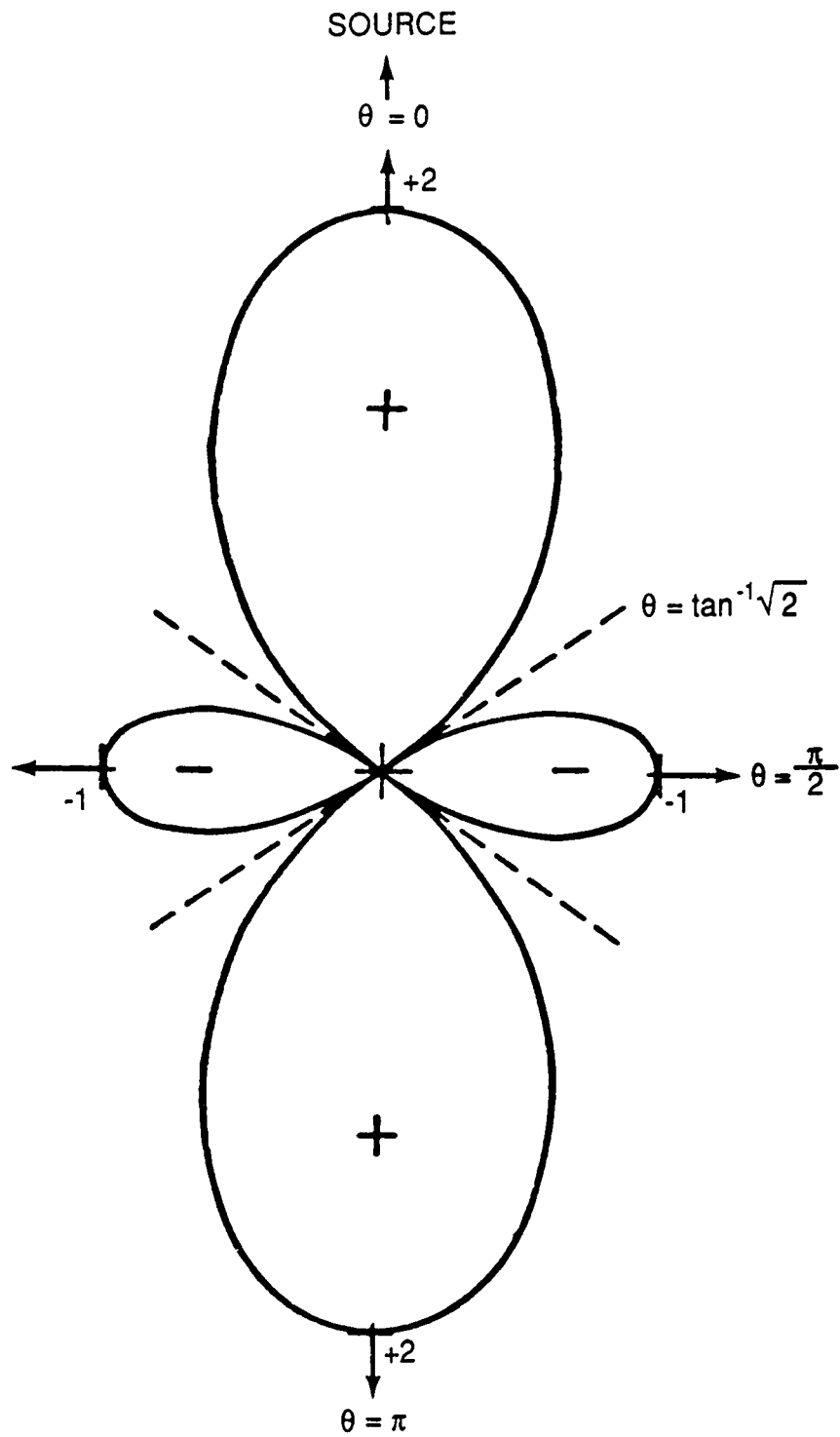


Figure 3-3. Angular pattern of the gravity gradiometer response to a spherical mass.

$$\begin{aligned}
\Gamma_{nn}(r, \theta, \phi) = & \frac{GM_E}{r^3} (-n_\eta^2 - n_\xi^2 + 2 n_\zeta^2) \\
& + \frac{3 GM_E}{r^5} a^2 J_2 \frac{1}{4} [(3 n_\eta^2 + n_\xi^2 - 4 n_\zeta^2) - (5 n_\eta^2 + 7 n_\xi^2 - 12 n_\zeta^2) \cos 2\theta] \\
& + \frac{3 GM_E}{r^5} a^2 J_2 4 n_\zeta n_\xi \sin 2\theta, \quad (3.10)
\end{aligned}$$

where (n_η, n_ξ, n_ζ) represent components of \hat{n} along the east (η), north (ξ), and up (ζ) directions of the local geographic frame of the satellite, respectively. Equation (3.10) shows that, even in the Earth-fixed orientation, the J_2 term contributes a first-order angular error, as given by the last term of equation (3.10). This term is, however, phase-shifted 45 deg from the signal term, which is proportional to $\cos 2\theta$ and, therefore, can be filtered out in the data analysis. The orthogonality error thus contributes a second-order error as long as the pointing error can also be kept within the orthogonality error. The required orthogonality and pointing errors are then 3×10^{-4} and 10^{-5} rad for the inverse square law resolution of 10^{-7} and 10^{-10} , respectively, as can be seen in Table 3-2. Alignment and attitude control to these levels are feasible.

While it alleviates the orthogonality requirements, the Earth-fixed orientation results in a tighter attitude rate requirement, compared to the inertial orientation, for the inverse square law experiment. The method of canceling the centrifugal acceleration errors, discussed in the previous section, cannot be applied here since the Laplace equation for the gravitational potential cannot be assumed a priori. Equation (36) shows that the twice-per-orbit component of $\delta \Omega_\phi$ is the only angular velocity component that contributes to the first order centrifugal acceleration error. This component must be measured with a sensitivity of 2×10^{-9} and 2×10^{-11} rad s $^{-1}$ Hz $^{-1/2}$, respectively, for the Shuttle flight test and for the free flyer science mission. Detection and control of the attitude rate to those levels provide the greatest challenge in the inverse square law experiment.

Next, the scale factor match and stability are discussed. Matching the three scale factors to 1 part in 10^{10} , or even to 1 part in 10^7 , in a time short compared to the lifetime of the mission is impossible because of instrument noise. If the scale factors are stable to this level for the entire duration of the mission, their relative magnitudes can be matched to the same level in principle in the post-mission data analysis. This procedure is not practical, however, when one looks for an unknown parameter, because the condition $\nabla^2 \phi = 0$ may have to be imposed for such an analysis, which then eliminates the signal. It will be simpler to rotate the gradiometer about one of its diagonal axes, with a certain time interval, to interchange the sensitive axes permutatively and average the data obtained in the three orientations. The terms

due to a scale factor mismatch will then cancel, while the contribution from a non-Newtonian force will survive [97]. This cancellation will not be exact due to a change of gravity signal from orientation to orientation which results from a drift in orbital altitude and a track advancement with respect to the Earth. The orbital altitude will be stable or known to 1 m, which is 5 parts in 10^5 over 200 km. The scale factors can then be matched to this level and, upon averaging over three orientations, the errors due to scale factor mismatch then become less than 1 part in 10^{10} . The same method could be used with less rigor to satisfy the requirement for the Shuttle experiment.

It will be difficult to achieve a scale factor stability of 10^{-10} yr^{-1} . Although the persistent currents are known to be stable to this level and the mechanical stability at such a level may be realized in a zero-g, cryogenic environment, drifts in the room temperature electronics will not permit such a stability level. However, one could take advantage of the stability of quantized flux by summing the current signals at the input of an additional SQUID before amplification. An alternative would be a continuous calibration of the SQUID transfer function $\partial v / \partial i$. For this purpose, a common sinusoidal current-to-voltage calibration current can be fed to the three detection SQUIDS in the gradiometer. The detected voltage for this calibration signal in the three circuits then provide the relative calibration of $\partial v / \partial i$ between the three axes. This, combined with the stability of the gravity gradiometer current scale factor, then establishes the stability of the overall scale factor.

3.1.3 Gravitomagnetic Field Experiment

As was pointed out earlier, the null test of Einstein's field equations requires a gradiometer sensitivity of $10^{-4} \text{ E Hz}^{-1/2}$ in an elliptical orbit, or $10^{-5} \text{ E Hz}^{-1/2}$ in a circular orbit. In this section, we consider only the detection of the Lense-Thirring effect.

In Section 2.2.2, a method has been proposed by which the large Newtonian terms arising from the eccentricity of the orbit are removed. This method relies on geometric properties of a particular Earth-fixed orientation with the gradiometer axes pointing up, south-west, and south-east. When the signals along the two horizontal directions are differenced, the Newtonian signal modulated by the ellipticity of the orbit couples through the scale factor mismatch ($\delta \sigma_{23}$) and through the pointing errors of the sensitive axes as

$$\frac{3\delta r}{r} (\Gamma_E \delta \sigma_{23} + \vec{\theta} \times \hat{n} \cdot \vec{\Gamma}_E \cdot \vec{\theta} \times \hat{n}) , \quad (3.11)$$

where $\Gamma_E = GM_E/r^3 = 1400 \text{ E}$. Thus, Newtonian gravity errors have become second and third order, respectively.

We now examine the effect of the proposed signal differencing scheme on the centrifugal acceleration. The centrifugal acceleration components in the instrument coordinates can be shown [87] to be

$$C'_{11} = \Omega_o^2 + 2 \Omega_o \delta \Omega_\phi ,$$

$$C'_{22} = \frac{1}{2} \Omega_o^2 + \Omega_o \delta \Omega_\phi + \Omega_o \delta \Omega_\theta + \Omega_o^2 \delta \theta_r , \quad (3.12)$$

$$C'_{33} = \frac{1}{2} \Omega_o^2 + \Omega_o \delta \Omega_\phi - \Omega_o \delta \Omega_\theta - \Omega_o^2 \delta \theta_r .$$

Upon differencing between the two horizontal axes, one finds

$$C'_{22} - C'_{33} = 2 \Omega_o \delta \Omega_\theta + 2 \Omega_o^2 \delta \theta_r . \quad (3.13)$$

These are the first order errors that survive the signal differencing. The only attitude rate that contributes to the first order error is the once-per-orbit component of $\delta \Omega_\theta$. The required knowledge/control level of this quantity is similar to that for $\delta \Omega_\phi$ in the inverse square law experiment.

Notice, however, that the centrifugal acceleration produces another first order error term through the once-per-orbit modulation of the satellite yaw angle, $\delta \theta_r$.

This first-order pointing error nullifies the advantage of the Earth-fixed orientation for the gravitomagnetic field experiment. Therefore, if this experiment were to be performed by a dedicated mission, it would be logical to use inertial orientation which is a better frame for very stringent attitude control. In this report, the analysis is confined to an Earth-fixed frame so that the requirements for the physics experiments can be more easily compared to those for geophysics. The analysis of the experiment in a local inertial frame has been presented elsewhere [87].

Table 3-3 summarizes the control/knowledge requirements for the instrument and platform parameters that correspond to the gradiometer noise level of $10^{-5} \text{ E Hz}^{-1/2}$ and the mission duration of six months. The resulting resolution of $\delta \mu / \mu = 0.02$ is equivalent to that of GP-B. An orbit ellipticity error of 10^{-6} is assumed which corresponds to $\delta r = 6 \text{ m}$. Notice that the scale factor match and pointing requirements are trivial to satisfy for this experiment. The gravitomagnetic field experiment, therefore, looks easier to design than the inverse square law test. It appears that a GP-B quality telescope would satisfy the attitude requirement of the SGG gravitomagnetic field experiment [86].

Another challenge facing the two physics experiments is the need for low instrument noise at signal frequencies as low as 2×10^{-4} and $4 \times 10^{-4} \text{ Hz}$. The gravity signal may be up-converted by spinning the spacecraft. This is not an easy task, however, because the spin stabilization would break the symmetry chosen to reduce certain types of errors, and would also stiffen the already stringent attitude rate requirement further. Therefore, low noise performance of the SGG at frequencies down to the 10^{-4} Hz region appears to be essential for the success of these experiments.

TABLE 3-3. REQUIRED CONTROL/KNOWLEDGE OF INSTRUMENT AND PLATFORM
PARAMETERS FOR GRAVITOMAGNETIC FIELD EXPERIMENT
IN EARTH-FIXED ORIENTATION

PARAMETERS	ERROR MECHANISM	REQUIRED CONTROL/KNOWLEDGE
RESOLUTION	$\delta \mu/\mu$	0.02
INSTRUMENT NOISE	$s^{1/2} (f)$	$10^{-5} \text{ E Hz}^{1/2}$
DYNAMIC RANGE	$\Delta \Gamma_E, \text{MAX} (s^{1/2} (f))$	$10^6 \text{ Hz}^{1/2}$
ORBIT ELLIPTICITY	$\delta r/r$	10^{-6} (6m)
SCALE FACTOR MATCH	$3 (\delta r/r) \Gamma_E \delta \sigma_{23}$	6×10^{-7}
POINTING	$3 (\delta r/r) \vec{\theta} \times \hat{n} \cdot \vec{\Gamma}_E \cdot \vec{\Gamma}_E \cdot \vec{\theta} \times \hat{n}$	$8 \times 10^{-4} \text{ rad}$
ATTITUDE	$2 \Omega_0^2 \delta \theta_r (f)$	$3 \times 10^{-9} \text{ rad Hz}^{-1/2}$
ATTITUDE RATE	$2 \Omega_0 \delta \Omega_\theta (f)$	$4 \times 10^{-12} \text{ rad s}^{-1} \text{ Hz}^{1/2}$
ATTITUDE ACCELERATION	$\delta \hat{n}_g \times \hat{n} \cdot \vec{\alpha} (f)$	$10^{-9} \text{ rad s}^{-2} \text{ Hz}^{1/2}$
LINEAR ACCELERATION	$-\frac{1}{2} \delta \hat{n}_- \cdot \vec{a} (f)$	$2 \times 10^{-9} g_E \text{ Hz}^{1/2}$
INSTRUMENT TEMPERATURE	$(\partial \Gamma / \partial T) s_T^{1/2} (f)$	$10^{-5} \text{ K Hz}^{1/2}$

3.2 Instrument Design

A prototype single-axis SGG (Model I) has been developed through NASA support by the University of Maryland. The instrument has been carefully evaluated and has been shown to agree very closely with an analytic model [94,98]. Development of a detailed error model of the instrument, and experimental demonstration of the theory, has led to a design of a sophisticated three-axis SGG [96]. An intermediate sensitivity model of a three-axis SGG (Model II) has been assembled and is currently undergoing tests. At the same time, an engineering model for a flight test (Model III), with a design sensitivity of $10^{-4} \text{ E Hz}^{-1/2}$, is being assembled. In order to detect the linear and angular acceleration components of the gradiometer platform with sufficient sensitivity, an SSA is also under development, with support from AFGL [99]. A prototype SSA has been assembled and is undergoing tests. In this section, designs and operating principles of these instruments are described, along with those of a six-axis shaker, which is used to control the platform. A more detailed discussion of Model III is given in Appendix E.

3.2.1 Three-Axis Superconducting Gravity Gradiometer

Figure 3-4 schematically shows a single-axis portion of the Model III three-axis SGG. Two superconducting niobium proof masses, confined by mechanical springs to move along the line-of-sight between them, are levitated against gravity, for ground development and test, by dc magnetic fields produced by the persistent current I_{c2} in a superconducting loop (dotted line). In space, the proof masses are "levitated" in both directions by symmetric persistent currents $I_{c1} \approx I_{c2}$. Persistent currents I_{d1} and I_{d2} are stored in two sensing loops (solid line) constructed with superconducting sensing coils and an input coil to a SQUID. A common acceleration is balanced by adjusting the ratio I_{d1}/I_{d2} so that the SQUID is sensitive only to a differential acceleration. An identical superconducting circuit with the sense of one persistent current reversed can be coupled to the proof masses to read the common acceleration (not shown in the figure).

A three-axis gravity gradiometer is an assembly of three sets of single-axis units in three orthogonal directions. Orthogonality and scale factor matching between the three components are assured by careful alignment and calibration. In order to obtain the required sensitivity with a modest-size flight instrument, a superconducting "negative spring," which can compensate the rigidity of mechanical springs by passive means and effectively create a "free-mass" instrument, has been incorporated into the design (see Appendix E). Sensitivity to common mode accelerations, due to misalignment of sensitive axes of the accelerometers, is reduced by means of a three-dimensional residual balance, which is achieved by introducing an appropriate amount of cross coupling at the input of the three-axis gradiometer, using additional persistent currents. The linearity and dynamic range of the instrument are improved by means of a "force rebalance" feedback. Figure 3-5 shows the cross sectional view of one of the six accelerometers forming the three-axis SGG.

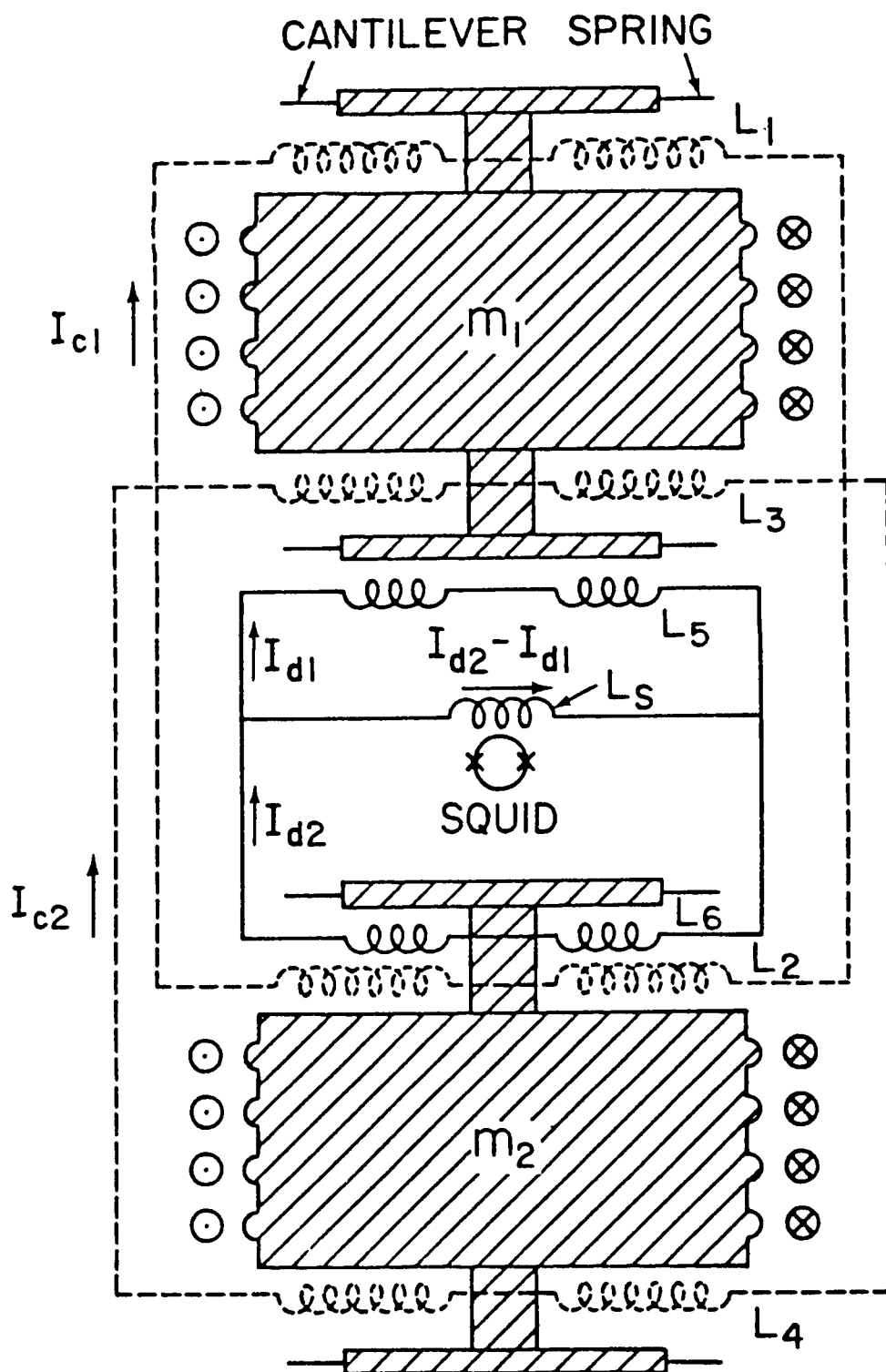


Figure 3-4. Single-axis portion of the three-axis SGG.

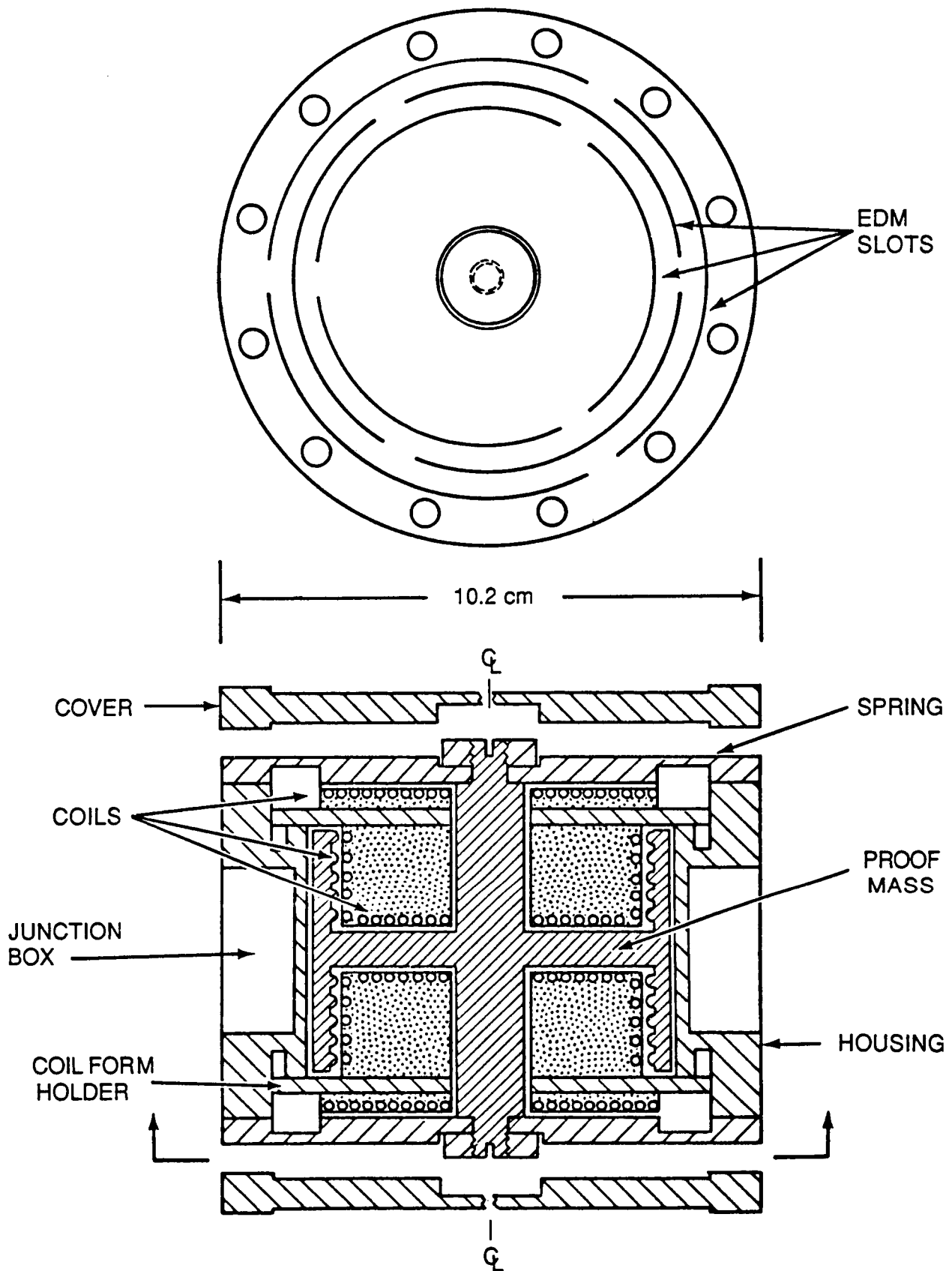


Figure 3-5. Cross sectional view of one of the six accelerometers of the three-axis SGG.

The instrument noise power spectral density is given [95] by

$$S_T(f) = \frac{8}{m \ell^2} \left[k_B T \frac{2\pi f}{Q(f)} + \frac{(2\pi f_0)^2}{2\beta\eta} E_A(f) \right], \quad (3.14)$$

where m , f_0 , $Q(f)$, and T are the mass, resonance frequency, quality factor, and temperature of the proof masses, respectively; ℓ is the baseline of the gradiometer; β and η are the coupling coefficients of the transducer and the SQUID, respectively; and $E_A(f)$ is the input energy resolution of the SQUID. Limits from the two noise terms in equation (3.14) are plotted in Figure 3-6 as functions of $Q(f)$ and f_0 . For the other parameters, design values: $m = 0.8$ kg, $T = 1.5$ K, $\ell = 0.19$ m, $\beta\eta = 0.25$, and $E_A(f) = 3 \times 10^{-30}$ J Hz $^{-1/2}$ (commercial DC SQUID) have been used. The SGG sensitivity goal of 3×10^{-4} E Hz $^{-1/2}$ can be met in the frequency range from 5×10^{-4} to 0.5 Hz, if the effective quality factor $Q(f)$ is 10^5 , and the proof mass resonance frequency, f_0 , is lowered (by the superconducting negative spring) to 1 Hz. For the inverse square law and relativity experiment, in which the signal is 2×10^{-4} and 4×10^{-4} Hz, respectively, one could tune f_0 down to 0.1 Hz and realize a sensitivity of 10^{-5} E Hz $^{-1/2}$.

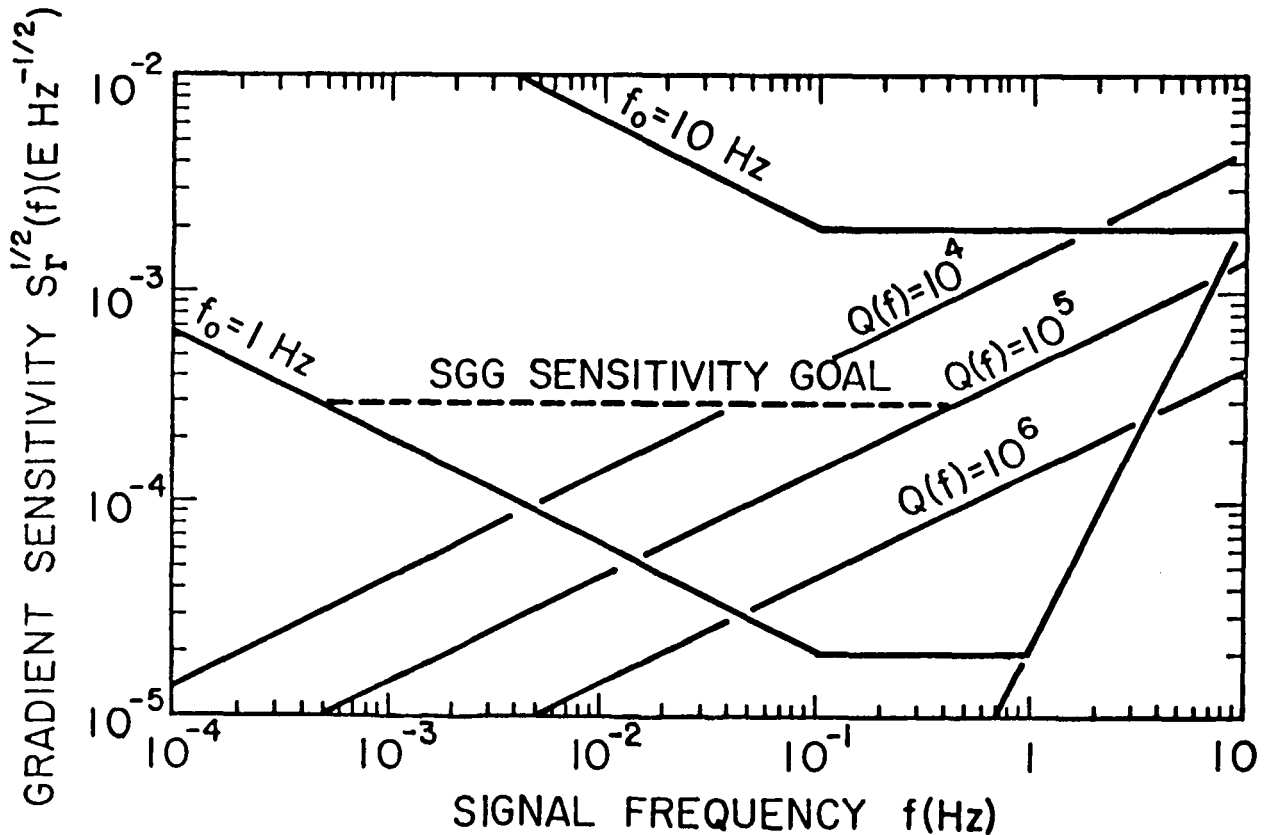


Figure 3-6. Expected sensitivity of the SGG as a function of signal frequency.

Use of persistent currents for levitation, common mode balance, and sensing assures extreme stability for the transducer. Further, the voltage-to-current conversion factor of the SQUID can be calibrated against the flux quantum, which is a fundamental constant. With these advantages, combined with enhanced mechanical stability of materials at liquid helium temperatures, and the thermal stability of superfluid helium, the goal of instrument drift less than $2 \times 10^{-6} \text{ E hr}^{-1}$ should be achievable.

3.2.2 Six-Axis Superconducting Accelerometer

In order to measure the linear and angular accelerations of the platform to the required precision, an SSA (Fig. 3-7) is being developed in parallel with the gradiometer [99]. The SSA senses the rigid body motion in all six degrees-of-freedom of a single levitated niobium proof mass. The accelerometer sensing is accomplished by using 24 superconducting "pancake" coils organized as six inductance bridges, coupled

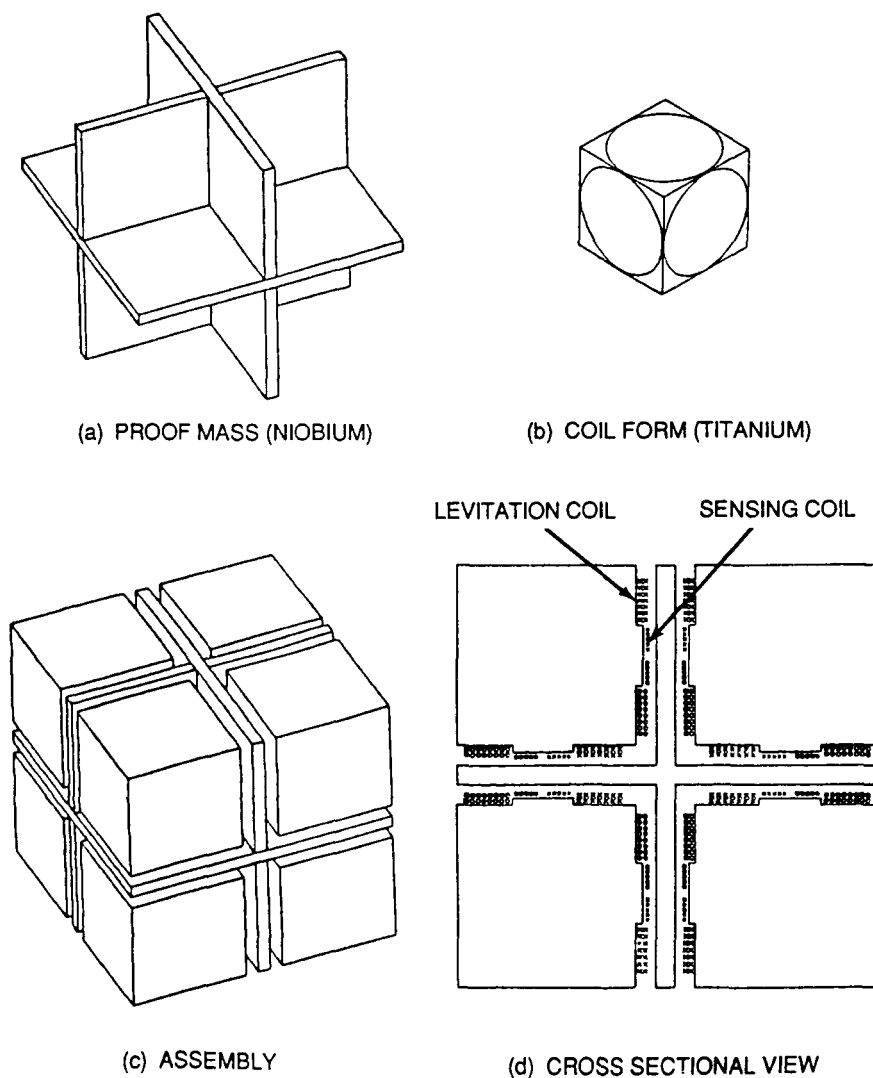


Figure 3-7. Six-axis superconducting accelerometer.

to a single SQUID. The position of the proof mass in six degrees-of-freedom is proportional to the unbalance of each of the six inductance bridges. Each degree of freedom occupies a separate bandwidth in the SQUID output. Levitation and feedback are accomplished by using a second set of 24 superconducting pancake coils organized as six sets of four inductors. The accelerometer is operated in a force rebalance mode. Figure 3-8 shows the expected sensitivities of the six-axis accelerometer as functions of signal frequency. With the proof mass resonance frequency of 1 Hz and $Q = 10^4$, a linear sensitivity of $10^{-13} \text{ g}_E \text{ Hz}^{-1/2}$ and an angular sensitivity of $10^{-11} \text{ rad sec}^{-2} \text{ Hz}^{-1/2}$ are expected. The device occupies a 10.2 cm cube.

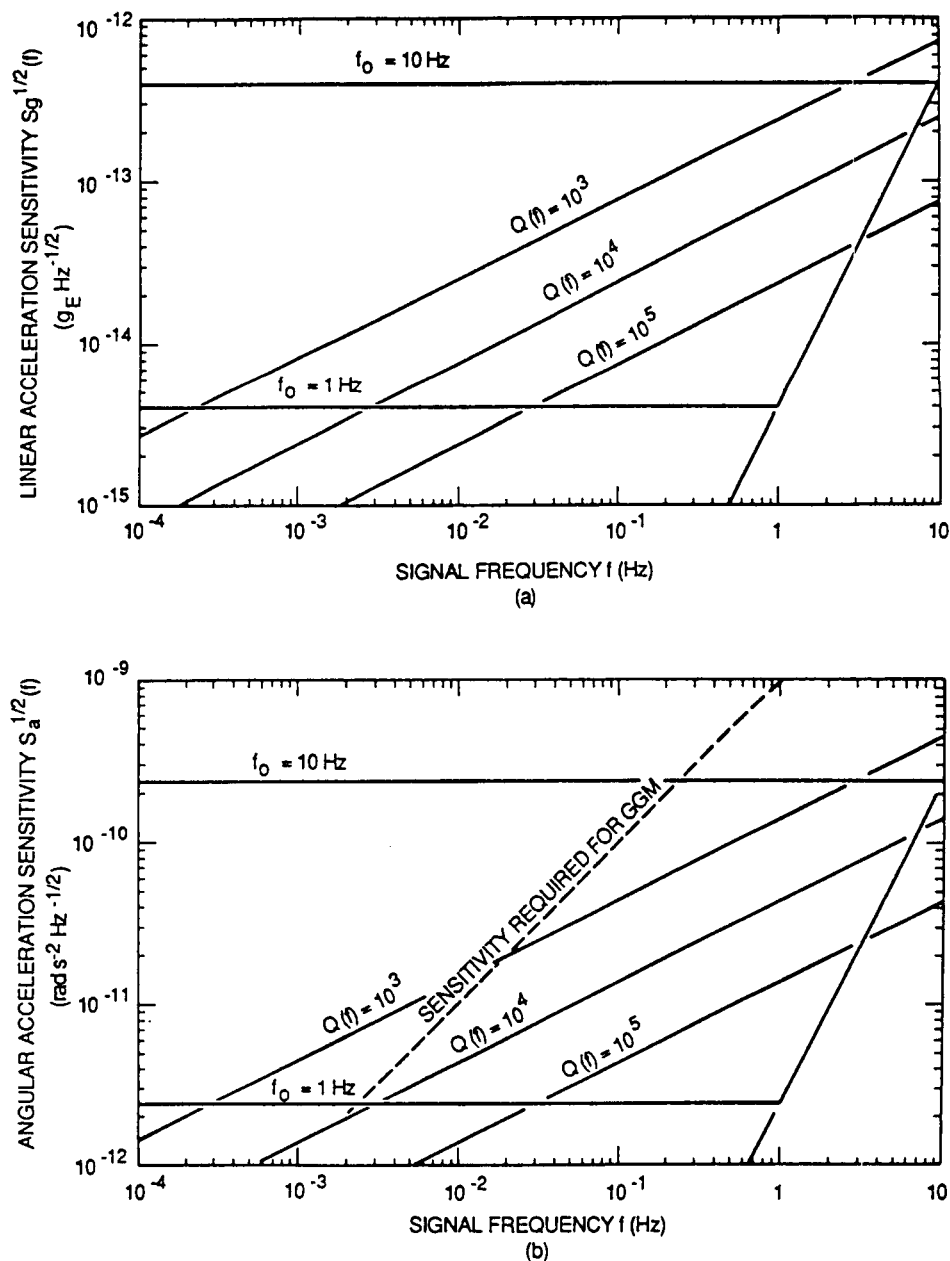


Figure 3-8. Expected (a) linear acceleration and (b) angular acceleration sensitivities of the SSA as functions of signal frequency.

Figure 3-9 shows a top view of the three-axis SGG integrated with the SSA and mounted on a six-axis shaker. Six component accelerometers constituting the three-axis gradiometer (the two accelerometers for the z-direction are not shown) are mounted on a titanium cube which houses the six-axis accelerometer. The entire assembly fits within a 30-cm diameter sphere and weighs about 40 kg. If a six-axis shaker is installed inside the dewar, the diameter and weight will increase to 50 cm and 60 kg, respectively. If the entire dewar can be shaken, the six-axis shaker can be omitted and a smaller dewar used. The linear acceleration vector is measured with redundancy by both the gradiometer and the six-axis accelerometer. This redundancy will allow alignment of the sensitive axes between the gradiometer and the accelerometer.

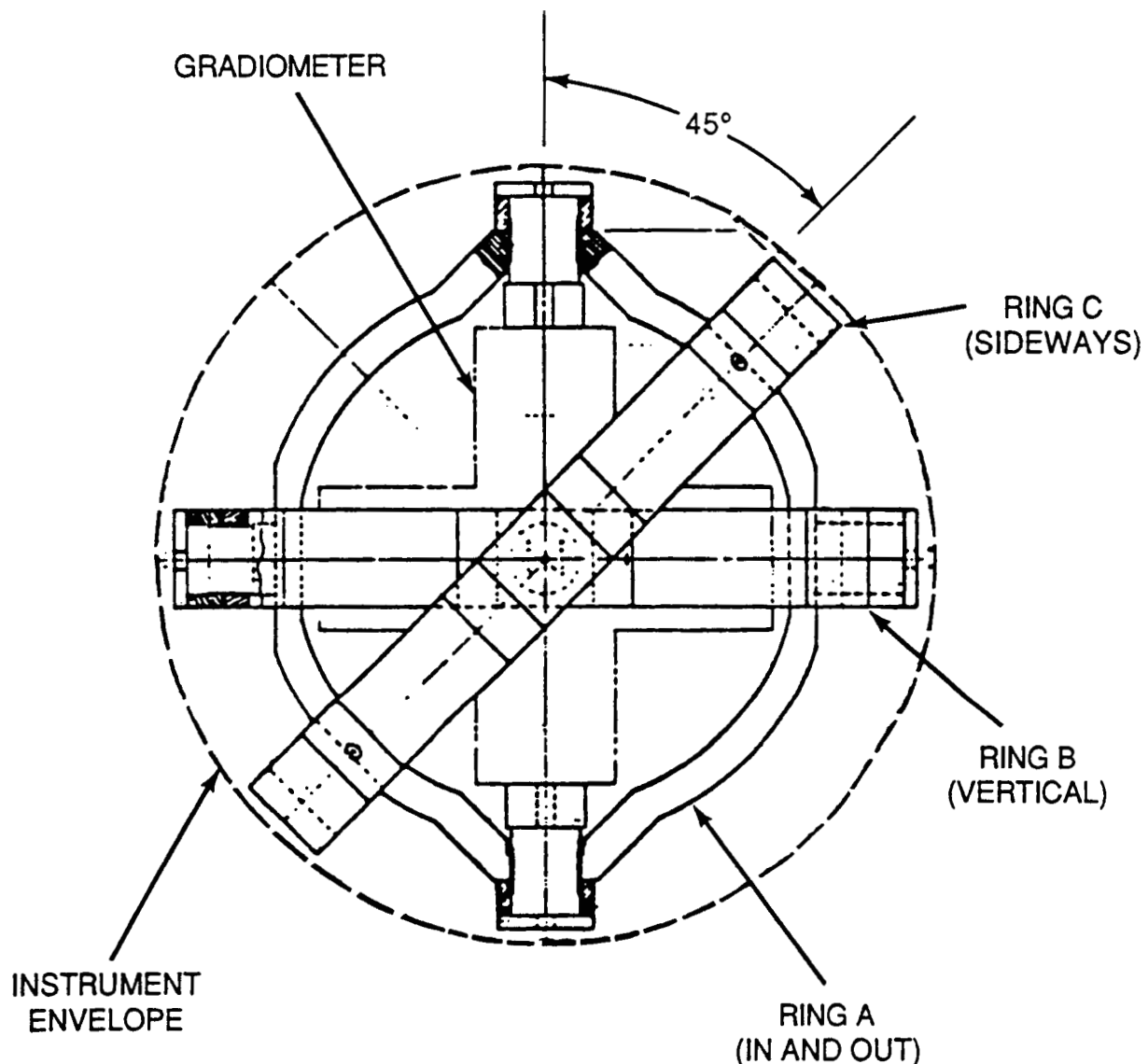


Figure 3-9. Three-axis SGG and SSA mounted on the six-axis shaker (top view).

3.2.3 Six-Axis Shaker

The six-axis shaker contains six piezoelectric crystal stacks which are driven in proper combination to produce motions in six degrees-of-freedom. The purpose of the shaker is two-fold. First, it permits calibration of the accelerometers and common mode balance of the gradiometer. Gradiometer calibration can be obtained by providing a known centrifugal acceleration by means of the angular shaker or from its response to a known linear acceleration in the "accelerometer mode," in which the two component accelerometer signals are added [98]. Second, the accelerometer outputs can be fed back to the shaker to realize a stabilized platform.

The block diagram for the detection and control electronics of the integrated system of three-axis gradiometer, six-axis accelerometer, and six-axis shaker is shown in Figure 3-10. The total power consumption (shown in Table 3-4) is estimated to be 450 W during the peak period of initialization and 150 W during normal operation. The power generated in the cryogenic space will be about 1 W during initialization, and less than 1 mW during normal operation. Data rates of $640 \text{ bits sec}^{-1}$ in each of the six gradiometer channels and $6400 \text{ bits sec}^{-1}$ for each channel of the six-axis accelerometer are required.

3.3 Status of Instrument Development

An SGG capable of satisfying the instrument requirements for the SGGM has been under development since 1980. The development of an SSA began in 1985. The instrument research and development has demonstrated that superconducting technology not only can be utilized to lower the intrinsic noise of the instrument, but also can meet many of the practical challenges of operating a sensitive gravity measuring instrument in a noise environment.

A relatively simple prototype, single-axis SGG Model I, was first constructed in order to investigate the basic physics of such an instrument. A detailed analysis of the instrument dynamics was also carried out, including extensive error modeling. Thorough experimental tests of the instrument have shown that the superconducting device closely follows the analytical model. The performance level of $0.3 \text{ to } 0.7 \text{ E Hz}^{-1/2}$ achieved with this instrument in the laboratory, without any active control or compensation, represents the best reported sensitivity of any gradiometer to date. The instrument has already been used successfully to perform a laboratory version of a null test of the gravitational inverse square law [100].

Based on the experience obtained with this first instrument and additional superconducting technologies developed to improve the performance of the superconducting gradiometer, advanced designs of three-axis SGG (Models II and III) were produced. Incorporated into the new design are such notable concepts as "push-pull magnetic levitation" and "three-dimensional residual common mode balance" (see Appendix E). Various feedbacks are applied to control the instrument and the platform. The Model III SGG represents a further improvement over Model II, in that it contains another innovation, a "superconducting negative spring" (see Appendix E). This third generation SGG should be able to meet the instrument noise goal for the SGGM, $3 \times 10^{-4} \text{ E Hz}^{-1/2}$.

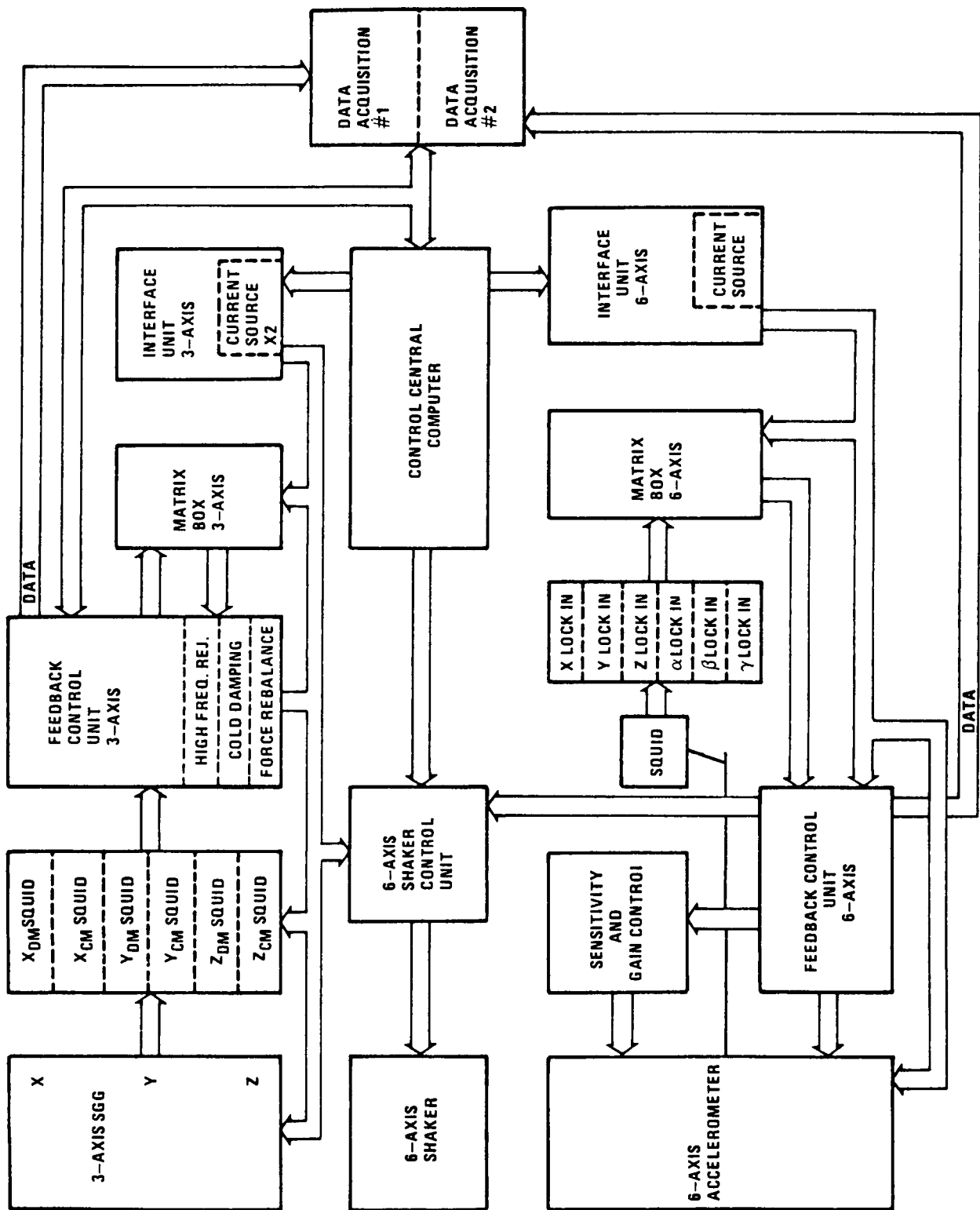


Figure 3-10. Three-axis SGG and SSA control block diagram.

TABLE 3-4. POWER REQUIREMENTS ESTIMATE

FUNCTION	POWER (WATTS)
SHAKER CONTROL UNIT	10X3
SQUIDS	2X7
FEEDBACK UNIT FOR SGG	4X6
MATRIX BOX FOR SGG	1/2X6
INTERFACE UNIT	1
CURRENT SOURCE	1-PEAK X 3
DATA ACQUISITION	30X2
SENSITIVITY AND GAIN CONTROL	20
FEEDBACK UNIT FOR SSA	20
LOCK-IN FOR SSA	12
MATRIX BOX FOR SSA	1/2X6
INTERFACE UNIT FOR SSA	1
TOTAL	146W
TOTAL PEAK	446W

Error analysis of the instrument has indicated the need to monitor the attitude of the gradiometer platform, in general, to an accuracy which is orders of magnitude lower than can be determined using conventional gyroscopes. Therefore, the University of Maryland group has under development a new instrument, an SSA, which is capable of measuring the linear and angular acceleration vectors of the platform simultaneously. A prototype SSA (Model I) is being tested, and an improved version of the SSA (Model II) is under construction.

The three-axis Model II SGG has been assembled and is being tested. The noise performance has been improved to $0.1 \text{ E Hz}^{-1/2}$ without active platform stabilization. Further improvement in performance will require platform stabilization by using the SSA. The first single-axis portion of the Model III SGG is being assembled. The superconducting negative spring has been tested.

The assembly of the three-axis Model III SGG and the Model II SSA will be completed in 1989. Following tests of the separate instruments, the two devices will be integrated by mid-1990. The instrument development schedule is shown in Figure 3-11, where the major milestones are normalized to the new start date. It is expected that the basic laboratory tests and automation of the new instrument will be completed by the end of 1991.

Table 3-5 summarizes the past accomplishments and remaining major tasks for the development of the instrument. No technical difficulty is expected in demonstrating

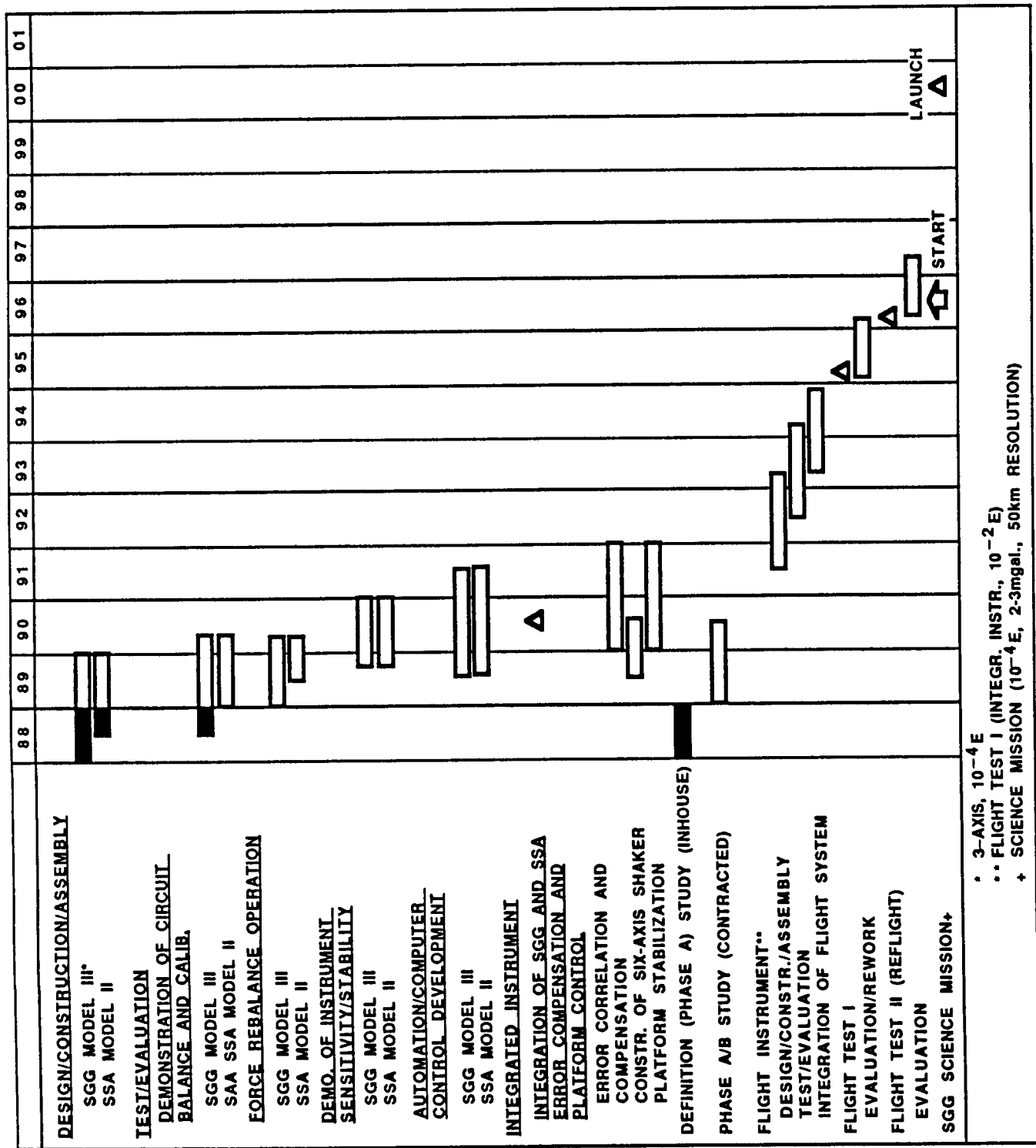


Figure 3-11. Superconducting gravity gradiometer development schedule.

TABLE 3-5. MAJOR INSTRUMENT RESEARCH TASKS ACHIEVED

● PROTOTYPE SINGLE-AXIS SGG (MODEL I)

- COMMON MODE REJECTION, CALIBRATION DEMONSTRATED
- NOISE SPECTRUM MEASURED
- MAJOR ERROR SOURCES IDENTIFIED
- INVERSE SQUARE LAW EXPERIMENT CARRIED OUT

● IMPROVED THREE-AXIS SGG (MODEL II)

- TEMPERATURE COMPENSATION INCORPORATED
- THREE-AXIS RESIDUAL BALANCE INCORPORATED
- HARDWARE CONSTRUCTION COMPLETED
- PARTIAL TESTS OBTAINED

● FURTHER IMPROVED THREE-AXIS SGG (MODEL III)

- SUPERCONDUCTING NEGATIVE SPRING DEMONSTRATED
- SINGLE-AXIS PORTION CONSTRUCTED

● INSTRUMENT ERROR MODELING

- DYNAMIC ERROR ANALYSIS OBTAINED
- PLATFORM REQUIREMENTS GENERATED
- CONSTRUCTED AND TESTED SSA (MODEL I)

the instrument and associated hardware. However, it appears that a major new effort must be devoted to the automation and error compensation of the instrument in the next few years. With adequate support of all these efforts, the flight test program could be initiated in FY91 with an orbital flight test in 1995.

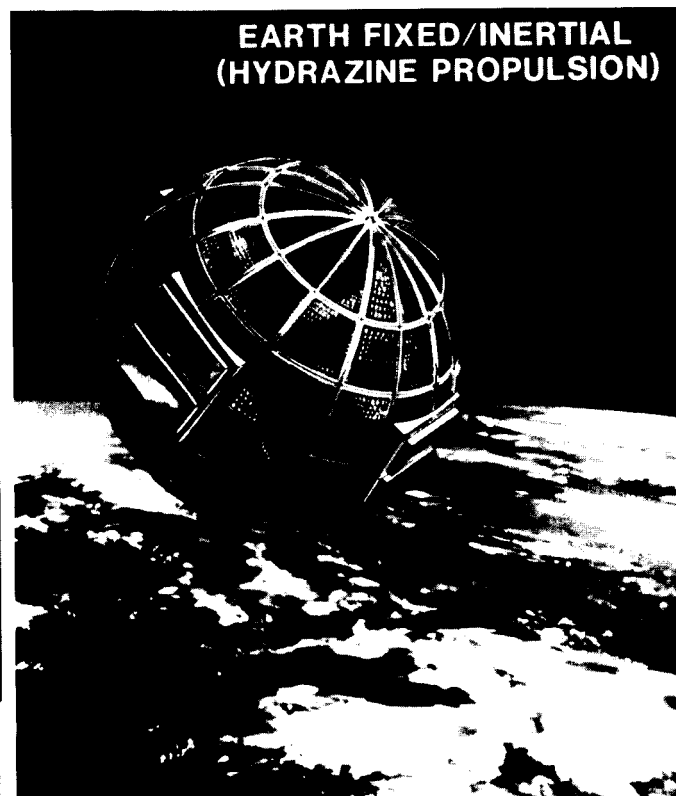
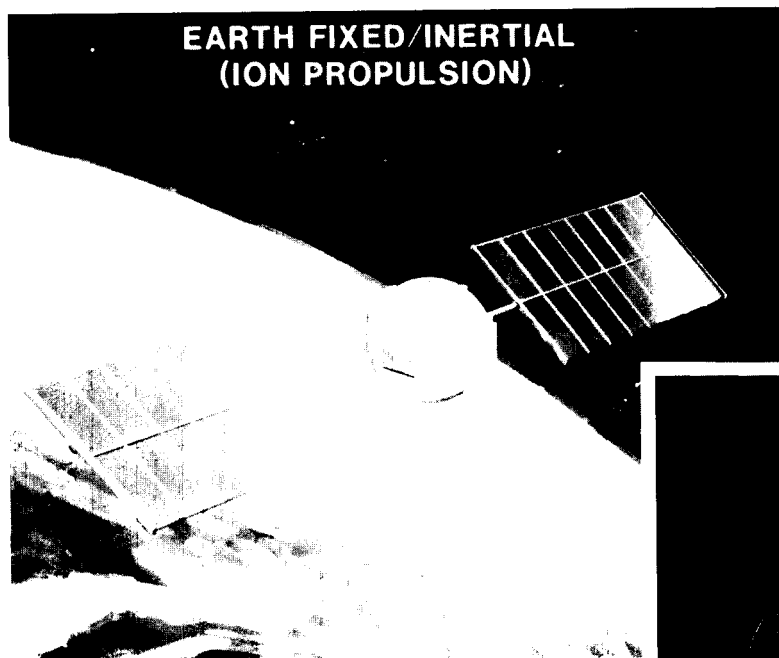
3.4 Ground Test Requirements

The SGGM flight hardware is expected to be a modification of the laboratory prototype three-axis gravity gradiometer (Model III SGG) integrated with six-axis accelerometer (Model II SAA). Since extensive experience will be obtained with the prototype instrument prior to the construction of the flight instrument, the ground test of the flight instrument should be relatively straightforward.

First, the dynamics of the instrument, such as transfer functions, common mode rejection characteristics, force rebalance, and cold damping feedbacks will be examined and compared with the predictions of a theoretical model, and with the performance of the prototype instrument. The instrument noise, errors associated with platform motions and temperature drift, and the scale factor stability will then be evaluated carefully. The scale factor match and orthogonality can be studied by using the gradiometer as the null detector in the inverse square law experiment.

A complete computer control for charging persistent currents, common mode balance, and calibration will have to be demonstrated. The performance of this automatic initialization will determine the strategy for the flight test. Therefore, this computer control must be optimized to permit startup in the shortest feasible time. A compensation algorithm for major error sources, such as centrifugal acceleration, will have to be developed and demonstrated. The integrity of the instrument against both mechanical and electrical shock excitation must also be assured.

Both the gravity gradiometer and the accelerometer will be magnetically levitated against gravity during the ground tests, by applying asymmetric currents into the levitation circuits. In space, the levitation coils will be charged symmetrically with equal currents. In order to simulate the zero-g environment, each component of the gradiometer may be tested with its sensitive axis oriented horizontally. Additionally, one could envision a drop-tower test, or airplane flight of the instrument, prior to an orbital test flight. However, the low-g time of ~ 4 sec for a drop-tower, or 20 sec for a KC-135 flight obtainable in such experiments, is deemed to be too short to permit proper initialization and stabilization of the gradiometer and accelerometer instrument. Therefore, the orbital test will be the first opportunity to operate the instrument in a zero-g environment.



ORIGINAL PAGE IS
OF POOR QUALITY

Figure 4-1. SGGM alternative spacecraft concepts.

4.0 MISSION AND SPACECRAFT CONCEPTS

In order to establish references against which primary and secondary mission requirements and various trades could be examined, the engineering studies discussed in this report considered four alternative spacecraft concepts. These concepts included two major configurations, a spherical spacecraft design and a long cylindrical concept. The spherical configuration was further divided into an ion propulsion option and an option that would utilize a hydrazine propulsion system. The cylindrical configuration was also divided into two separate options, a new spacecraft design and a modification of the design for the previously planned Geopotential Research Mission (GRM) spacecraft. Other potential carriers such as the Space Station, the Earth Observing System (EOS) platform, and the Tethered Satellite System (TSS) were also briefly examined.

The GRM would have measured variations in the gravity and magnetic field over the entire globe to a resolution of 100 km by utilizing two drag-free satellites at 160 km altitude in polar orbits, linked by precise Doppler. The GRM is no longer being considered as part of NASA's future program in Earth Science. However, significant efforts have been made in the preliminary design of the GRM spacecraft and systems over the past five years [101]. Since many of the GRM requirements (e.g., low altitude orbit, minimum disturbances, and precise control requirements) are similar in nature to those of SGGM, utilization of subsystem designs for GRM was considered where appropriate. Likewise, the GP-B mission [102], like SGGM, must meet very stringent spacecraft requirements, and the GP-B systems were examined for possible applicability to SGGM.

NASA's future launch vehicle fleet is now undergoing study and some future unmanned science missions will most likely be launched by Expendable Launch Vehicles (ELV). However, this study assumed that the STS would launch the SGGM. Therefore, the additional Shuttle safety and operational constraints have been included. As the program evolves, it will become necessary to select the launch vehicle and design the mission and spacecraft accordingly. Recovery or servicing (e.g., cryogen resupply) of the spacecraft was not considered.

As discussed in Section 3, requirements such as spacecraft control and gradiometer scale factors are more severe for the inverse square law test than for geophysics applications. The gravitomagnetic field experiment would also require attitude control similar to the inverse square law. Thus, the physics experiments could require a separate mission if the implementation of the more stringent spacecraft requirements prove too costly or too advanced for the late 1990's time period. In addition, since the null test of General Relativity requires an order of magnitude improvement in gradiometer sensitivity, this experiment may have to be relegated to a later flight of an improved (i.e., $\sim 10^{-5}$ E Hz^{-1/2} sensitivity) instrument. In a separate mission, the spacecraft and orbit would be optimized to suit the low frequency nature of the physics experiments. For example, a higher altitude and longer duration mission may be chosen, perhaps with spin stabilization of the spacecraft. Spacecraft concepts were included in this study that would accommodate both the geophysics or physics experiments.

The major tasks of this study were to establish mission feasibility and to identify critical systems. The most critical element identified was control of the spacecraft. While the Attitude Control System (ACS) was analyzed in this study, more in-depth

study is needed. Many other subsystems are state-of-the-art. Particular areas that were identified as critical, and require future in-depth study, are discussed further in Section 7.

4.1 Orbit Selection

Even though the SGG will be an extremely sensitive instrument, a low altitude orbit must be selected to provide the desired measurement accuracy. For example, by increasing the orbital altitude from 160 to 200 km, the desired high-frequency gravity signal will be attenuated by an order of magnitude (Appendix C). The highest degree of the spherical harmonics that can be resolved by a 10^{-4} E gradiometer then decreases approximately from 500 to 400 (see Appendix C). However, the lower orbit will result in higher atmospheric drag, producing disturbances that must be compensated for at the expense of additional propellant. For example, the drag forces on a 3-m sphere would increase by a factor of about 5 if the altitude is decreased from 200 to 160 km (see Figure F-10 of Appendix F). This would require larger propellant tanks, resulting in more spacecraft weight and volume. The larger spacecraft cross section would then create more drag, forcing one to repeat this, perhaps diverging, cycle.

In selecting the best altitude compromise, the results from Appendix C were utilized. Orbit altitude implications are summarized in Figures C-1 and C-2 of Appendix C. For a gradiometer precision of 10^{-4} E, a 160-km orbit appears to provide a gravity anomaly uncertainty of 1 to 4 mgal for $1/2$ deg x $1/2$ deg blocks. For the same instrument precision, a 200-km orbit is estimated to provide a total anomaly uncertainty of about 4 to 7 mgal for $1/2$ deg x $1/2$ deg blocks and about 0.8 to 2 mgal for 1 deg x 1 deg blocks. Although this does not yield the desired 2 to 3 mgal uncertainty for the $1/2$ deg x $1/2$ deg block, the maximum resolvable harmonic degree does approach 400, which corresponds to the desired 50-km horizontal resolution, albeit with a signal-to-noise ratio of unity. Therefore, an orbital altitude of 200 km was selected for this study.

The requirement for orbit altitude control or knowledge ($7 \text{ cm Hz}^{-1/2}$) was discussed in Section 3. The gravity anomaly uncertainty depends fairly strongly on orbit position error. It was postulated in this study that the Global Positioning System (GPS) will be able to adequately provide the required orbit position knowledge during the time frame in which the SGGM is expected to be operational (late 1990's).

The characteristics of the orbit that was selected are summarized in Table 4-1. A Sun synchronous orbit (inclination 96.3 deg) will provide the desired Earth coverage and maximize the time the spacecraft is in full sunlight. This would provide efficient power production and aid in minimizing thermal cycling (and thus induced thermal-mechanical vibrations) of the spacecraft. However, it remains to be determined whether the loss of coverage within a few degrees of the poles would be acceptable for the geophysics investigations. This should be investigated in future trade studies.

Figure 4-2 shows the orientation of the orbit with respect to the Sun. The orbit was selected with a six o'clock node in order to maximize the time in sunlight. Even though the orbit is Sun synchronous, the spacecraft will enter the Sun's shadow for short periods of time near the summer and winter solstices. Figure 4-3 shows the amount of time spent in the Earth's shadow per orbit during one year. Between the shadow periods the spacecraft is in constant sunlight. The time in 100 percent Sun, for various Sun synchronous altitude and inclination combinations, is listed in the figure.

TABLE 4-1. BASELINE ORBIT CHARACTERISTICS FOR SGGM

TYPE	SUN SYNCHRONOUS
ALTITUDE	200.8 km
INCLINATION	96.3 DEG
GROUND TRACK	
- DENSITY	53.5 km
- REPEAT FREQUENCY	46 DAYS
MISSION LIFETIME	6 MONTHS

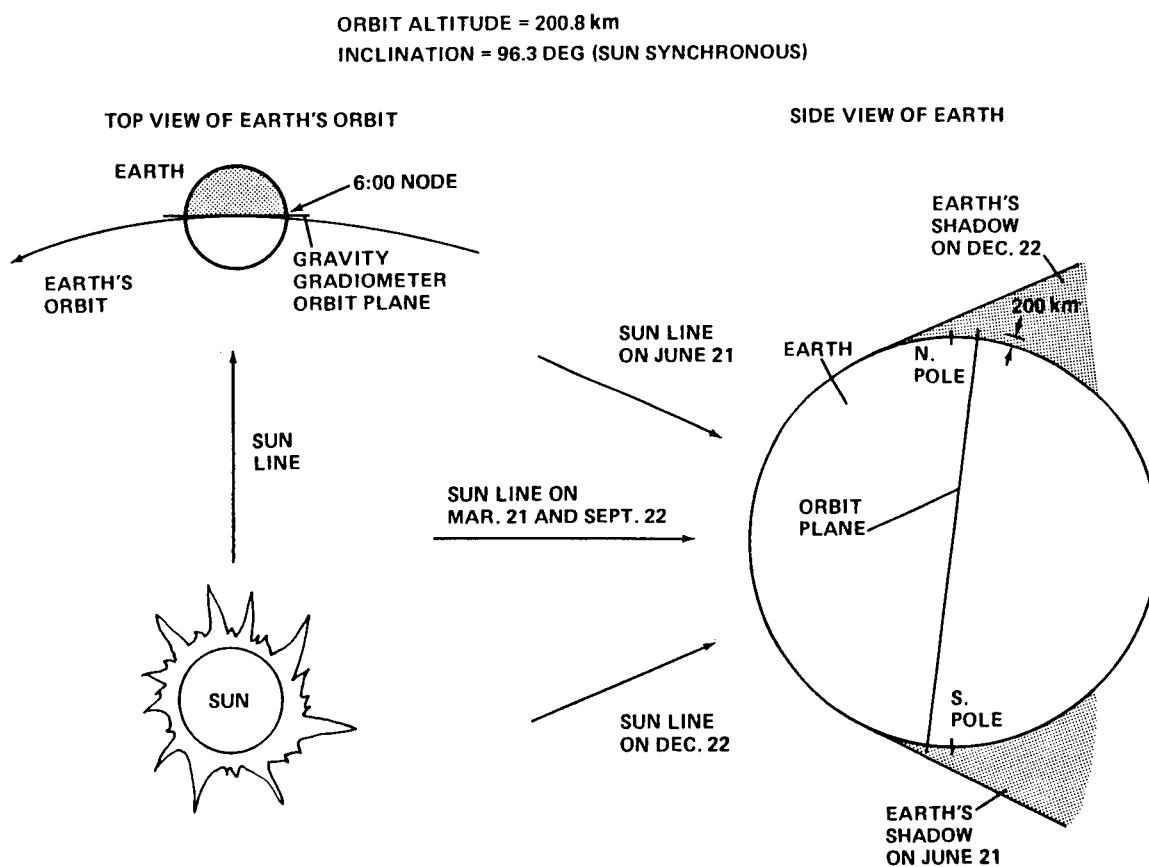
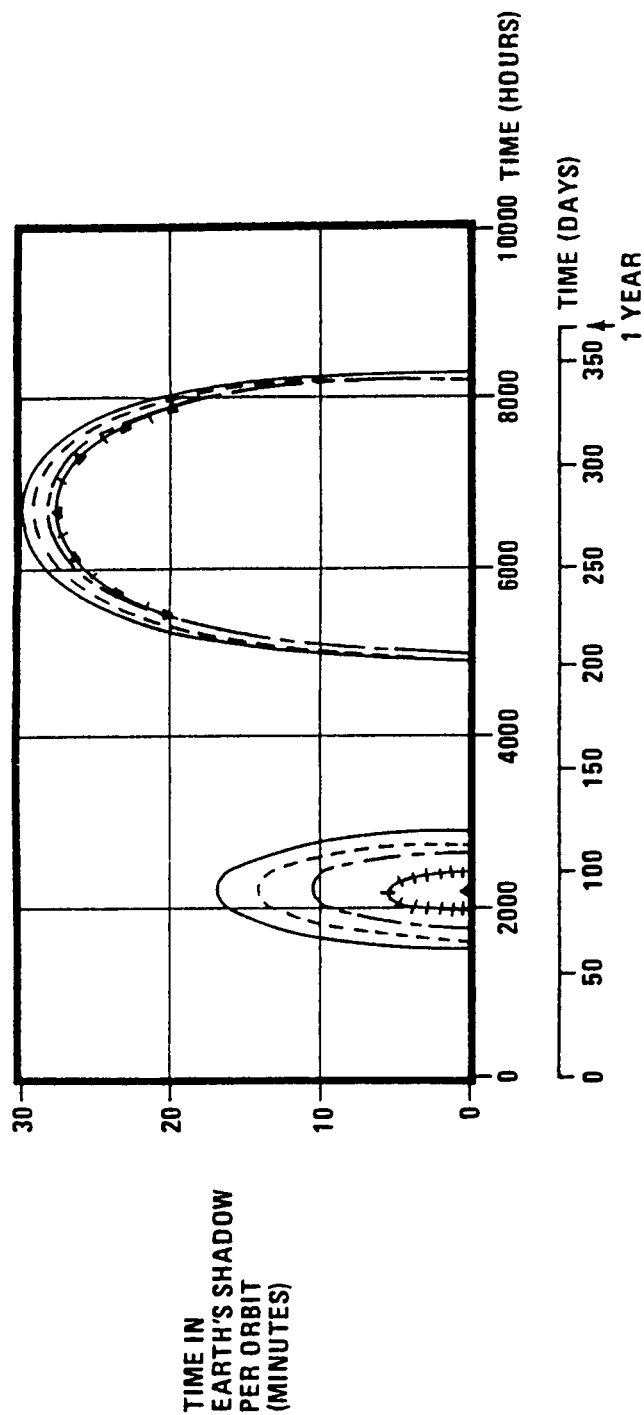


Figure 4-2. Gravity gradiometer orbital lighting geometry.



($T_0 = 6:00$ AM, MARCH 21)

ORBIT ALT. (km)	INCLINATION (DEG.)	TIME IN 100% SUN (DAYS)
200	96.3	81.5
225	96.4	88.6
250	96.5	95.7
275	96.6	106.3
285	96.6	234.0

Figure 4-3. Time in 100 percent Sun and time in Earth shadow per orbit.

Figure 4-4 illustrates the density of spacecraft ground tracks over a portion of the United States. A series of ground tracks spaced 53.5 km apart would form a crisscross pattern and repeat every 23 days or about 8 times during the 6-month mission. This would approximately meet the 50-km spacing goal of the mission.

ORBIT ALT. (MEAN) = 200.8 km

ORBIT INCLINATION = 96.3 DEG

46 DAY REPEATING ORBIT (NO ATMOSPHERIC DRAG)

53.5 km GROUND TRACK SPACING

OES PLOT GENERATED
11-JUN-86 15:20:13

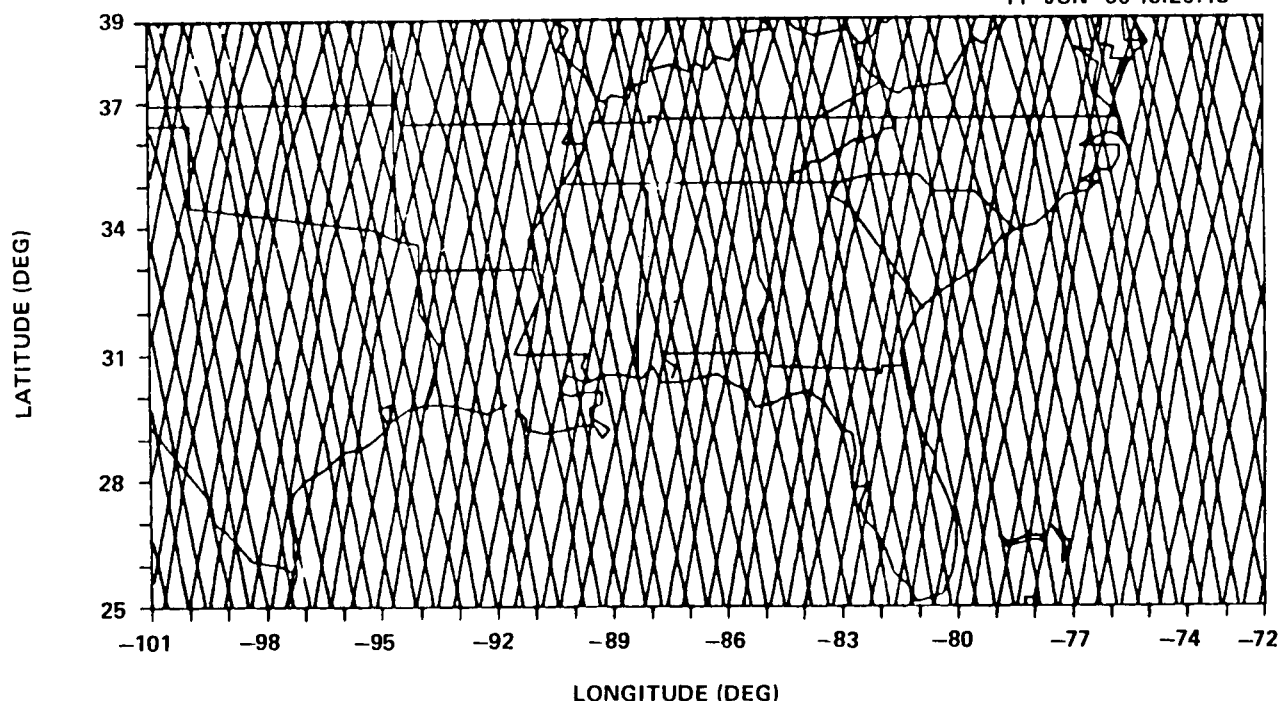


Figure 4-4. Ground track for SGGM.

4.1.1 Spacecraft Orientation Considerations

Because the primary and secondary mission objectives may prefer different spacecraft orientations, the studies included an examination of spacecraft concepts that can be: (1) either inertial or Earth-fixed (a spherical configuration), utilizing a single spacecraft design or (2) Earth-fixed only (long, cylindrical configurations, similar to GRM, with the axis of the cylinder parallel to the direction of flight). For the Earth-fixed mode (Fig. 4-5), a spacecraft orbiting at 200 km will rotate at a rate of $1.2 \times 10^{-3} \text{ rad sec}^{-1}$ about the normal to the orbit plane, while for the inertial mode, the spacecraft remains fixed to an inertial reference throughout the orbit.

In order to assess mission objectives as they pertain to spacecraft orientation, one notes that the gravity gradient is maximum along the vertical direction and a minimum in the horizontal plane (see Fig. 3-3). To reduce the gradient errors,

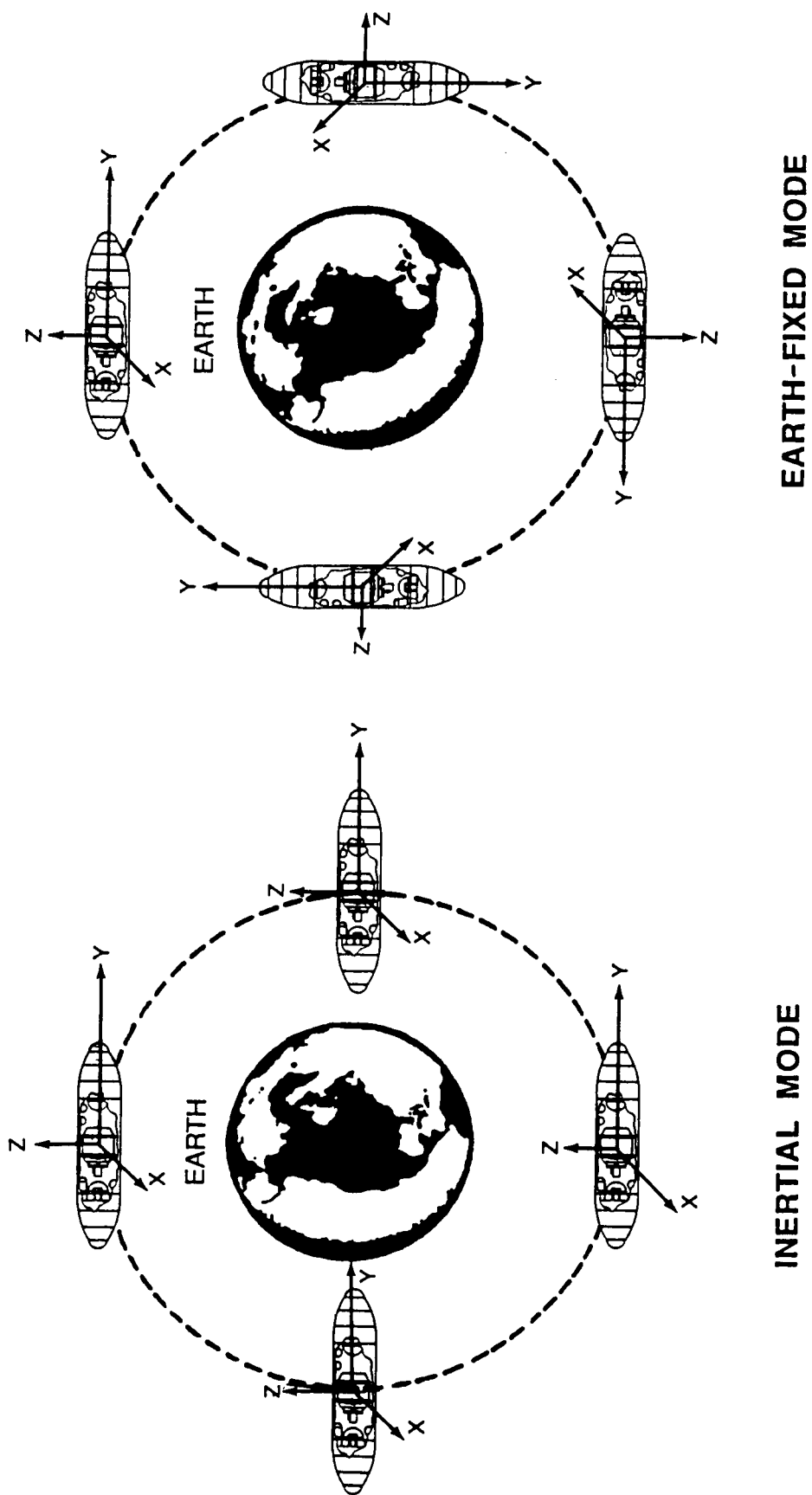


Figure 4-5. Spacecraft orbital orientation options.

arising from the non-orthogonality of the sensitive axes and the pointing error of the spacecraft, to second order in these error angles, an Earth-fixed mode is preferred for the null test of the inverse square law as well as for the tests of General Relativity. On the other hand, the requirements for control of knowledge of attitude rate are in general several orders of magnitude more severe for the Earth-fixed mode. Fortunately, the centrifugal acceleration errors can be removed to the first order by using the gradiometer itself for the primary (geophysics) mission objective (see Section 3.1.1). Therefore, for geophysics applications, either orientation would be acceptable.

4.2 Spacecraft Alternative Concepts

The inherent sensitivity of gravity gradiometers to disturbances translates into very demanding spacecraft requirements. For example, external disturbances, such as aerodynamic drag, must be compensated for through the spacecraft propulsion/control systems. Likewise, internal disturbance sources such as self-gravity, thermal-mechanical noise, reaction wheel disturbances, bearing noise, thruster noise, gimbal motion, solar array motion, liquid helium boiloff and slosh, and propellant motion or unbalance must be eliminated, greatly reduced, or in some cases, accurately known. Vibration is also an important concern since it is a coupling mechanism between instrument errors and instrument performance. Vibration can also cause attitude errors. These problems combine to make the design of the spacecraft a particularly demanding task.

The design of the Experiment Module, which contains the SGG instrument, dewar, electronics, interface modules, and other systems, is discussed first in this section. The ACS has been identified as the most critical subsystem and is discussed next. Details of the four alternative concepts that were considered are then presented. The final portion of this section contains a brief discussion of the Space Station, EOS Platform, and TSS, as potential carriers of the SGG.

4.2.1 Experiment Module

Providing a cryogenic environment ($T \leq 1.5$ K) for the SGG during the six-month mission is a key and common element to all spacecraft concepts studied. The core technology exists through actual space flight experience for superfluid helium instrument cooling. The most notable mission of this type was IRAS, in which a 0.6 m diameter infrared telescope performed an all-sky survey over the mission's 10-month lifetime. The mission terminated with the exhaustion of the 550 liters of superfluid helium, which maintained the focal plane at approximately 1.7 K throughout the mission [89].

In addition to stored cryogen systems, radiators and active coolers could be considered. However, temperatures required for superconducting instruments cannot be provided by simple passive radiator systems since the T^4 dependence of their cooling practically limits their use to temperatures greater than about 50 K. Also, no space qualified active cooler currently exists which is capable of achieving the temperatures required by the SGG. Existing mechanical refrigerators which are being developed, chiefly for DOD space applications, have concentrated on achieving temperatures as low as 8 K. These refrigerators typically are designed for much larger cooling powers than is required by the SGG. The use of such refrigerators may be possible if either a lower temperature stage is developed to achieve the lower required

operating temperature, or, alternatively, higher temperature superconducting materials under development can be used in the SGG, thus allowing higher temperature operation (see Section 6.3). Even under these circumstances, the mechanical vibrations produced by mechanical refrigerators may make them unsuitable for use with so sensitive an instrument. Active coolers, incorporating non-mechanical adsorption and absorption compressors, are being developed now, and would not be a source of vibration, thus making them candidates for a long-life mission. Such refrigerators may be available in the mid-1990's.

Based on the above considerations, the cryogenic system chosen for this study was a superfluid helium dewar. The SGG integrated with the dewar, attached electronics, and systems, constitute an Experiment Module that is common to all spacecraft concepts studied (except the modified GRM concept) as well as most of the flight test concepts discussed in Section 5.

One of the major dewar design constraints is to keep the dewar as small as practical, so that the overall spacecraft cross section remains as small as possible, in order to minimize aerodynamic drag. The ground rules and assumptions used in the conceptual design of the cryogenic system are listed in Table 4-2.

TABLE 4-2. GROUND RULES AND ASSUMPTIONS FOR SGG DEWAR DESIGN

6 MONTHS MINIMUM MISSION LIFETIME

MAINTAIN SGG INSTRUMENT NEAR 1.5 K FOR LIFE OF MISSION

ACCOMMODATE 55 CM DIAMETER SPHERICAL ENVELOPE OF INSTRUMENT

HELIUM BOILOFF BASED ON PREVIOUS DEWARS (IRAS, IRT)

**INTERIOR VEHICLE WALL TEMPERATURE BASED ON STEADY STATE
BACKWALL (NON-SOLAR SIDE)**

DEWAR COMPONENTS RADIATE TO BACKWALL TEMPERATURE

**TRANSIENT RESPONSE FOR BOILOFF DURING ASCENT AND PRELAUNCH
NEGLECTED**

The approach used was to consider first those dewars that had been flown in space, are under development, or are now being designed for future space missions. Among the missions considered were: IRAS [89], the Cosmic Background Explorer (COBE) [103], GP-B [102], and the Infrared Telescope (IRT) [104] flown on Space-lab. Characteristics of candidate dewars are shown in Figure 4-6. The COBE dewar is a larger and improved version of the IRAS dewar. Some of the COBE changes from the ELV launched IRAS were required to make the COBE dewar compatible with the manned STS. However, COBE is now planned for an ELV launch.

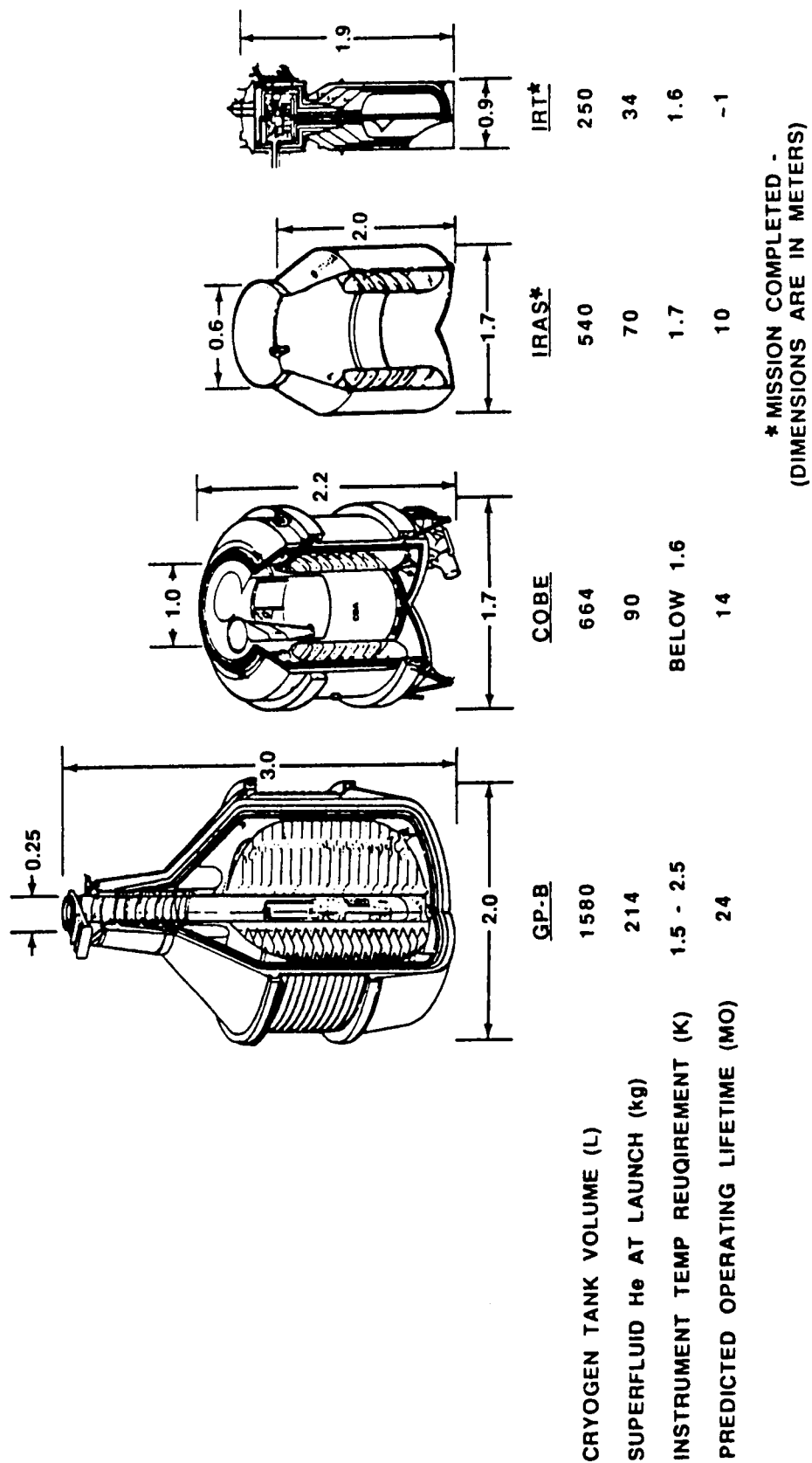


Figure 4-6. Characteristics of candidate dewars.

After carefully examining the candidates, the COBE dewar was found to be capable of meeting the SGGM requirements. However, the COBE dewar is actually larger than necessary to meet the SGGM requirements. To use a dewar larger than required would result in a larger spacecraft and thus introduce, among other problems, additional drag. The development of a suitable dewar does not appear to be a major cost or technology driver; and costs would certainly result from modifying an existing dewar that was designed for other purposes. Therefore, a new dewar based on the COBE design is recommended (Fig. 4-7). One should note, however, that some of the dewar requirements would be different if the SGGM is to be launched by an ELV [103].

The analysis of the SGGM dewar relied on design and empirical data from the COBE and IRAS dewar systems. The liquid helium boiloff from the SGGM dewar is a function of the heat input to the dewar, and is based on the IRAS design and analysis. Empirical data based on the detailed thermal analysis and testing of the COBE dewar were also utilized [103]. The COBE dewar should maintain near-superfluid helium temperatures with a 9.6-mW internal heat load. The SGGM internal heat load is estimated to be 10 to 12 mW, similar to that of IRAS. The systems mounted on the dewar would radiate to the interior surface of the spacecraft. It is also assumed that the interior wall temperature of the spacecraft can be maintained at the temperature of the back wall. Any transient boiloff losses of helium from the dewar during pre-launch and ascent to orbit were neglected since this is estimated to represent only about 8 to 10 percent of the liquid helium in the dewar.

The dewar size was determined by considering the amount of helium required for a six-month mission as a function of the total heat flux absorbed by the dewar (see plot in Fig. 4-7). This heat flux consists of an IR flux from the spacecraft, conduction soak-back from the external electronics mounted on the dewar shell, and the internal heat generated by the SGGM instrument located in the dewar. Since only IR fluxes from the spacecraft contribute as external environmental factors, a low emissivity coating of the dewar surface will minimize these effects. Nominal total heat fluxes are based on the IRAS mission, and range from 44 to 56 mW [89]. A total heat flux of 49.5 mW would require approximately 260 liters (37 kg) of helium.

The IRAS included almost 600 electrical conductors that had to be routed out of the dewar. These included 390 coaxial conductors from the focal plane instruments, and 180 wires from the dewar. The coaxial conductors were routed out of the dewar along the lower support straps to the electrical connectors located in the lower girth ring. Wires for temperature sensors, liquid level sensors, and motor operated valves were exited from the dewar through the main dewar fill line and vent lines. This is an important consideration in order to prevent the possibility of gas leakage, if one were to use insulated electrical feedthroughs from the helium space into the guard vacuum [103].

The COBE dewar will have 842 electric conductors exiting from it. To minimize conduction losses, stainless steel coaxial and manganin conductors with the smallest practical cross section were utilized. The total heat load from electrical conductors is about 7 percent of the total 48-mW heat load of the COBE dewar.

The SGGM will require about as many electrical conductors routed from the dewar as COBE. However, based on the IRAS and COBE experience discussed above, this should not present a serious problem.

SGG DEWAR
SIZE AS
FUNCTION OF
HEAT FLUX
ABSORBED
(6 MONTHS)

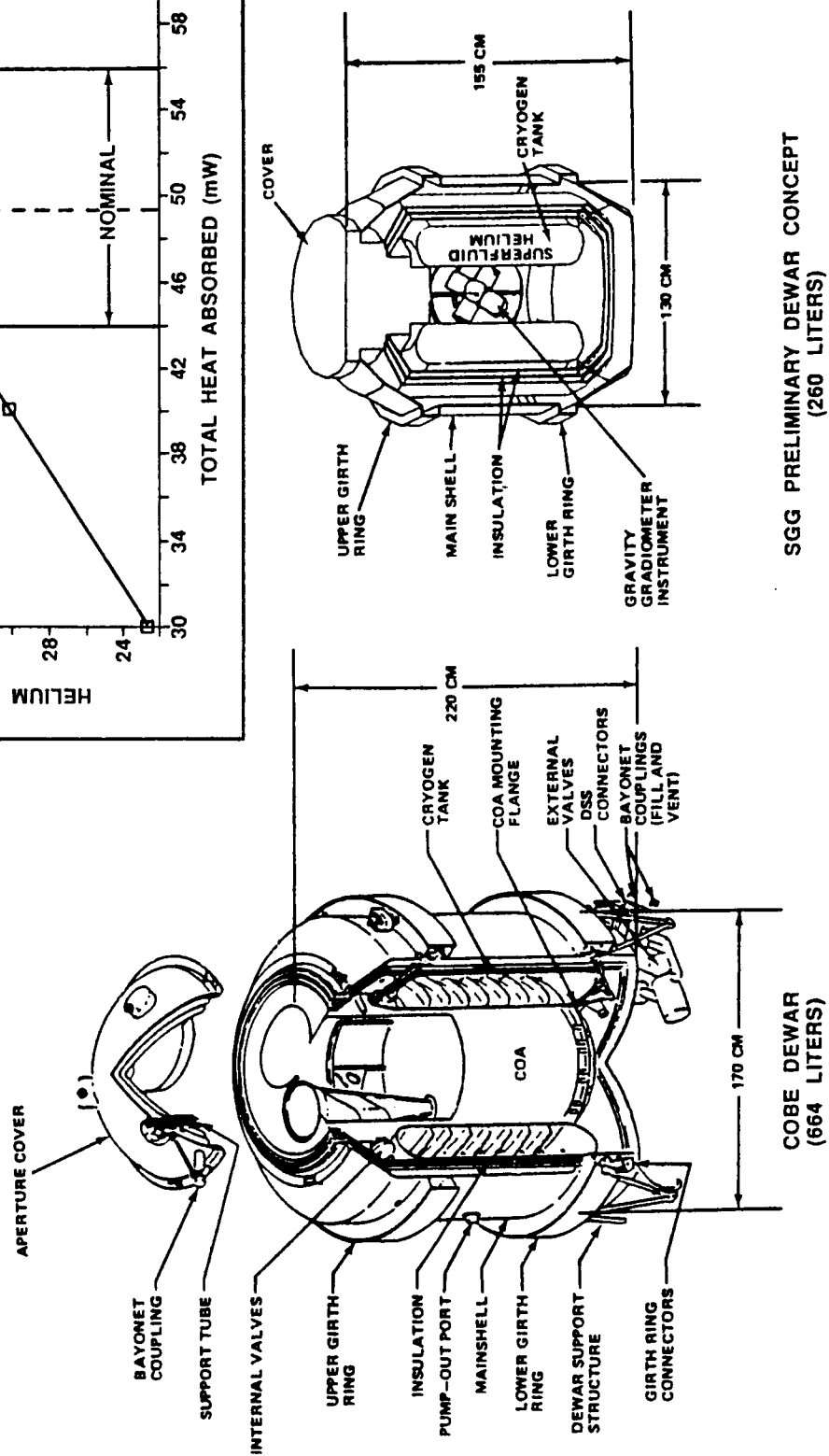
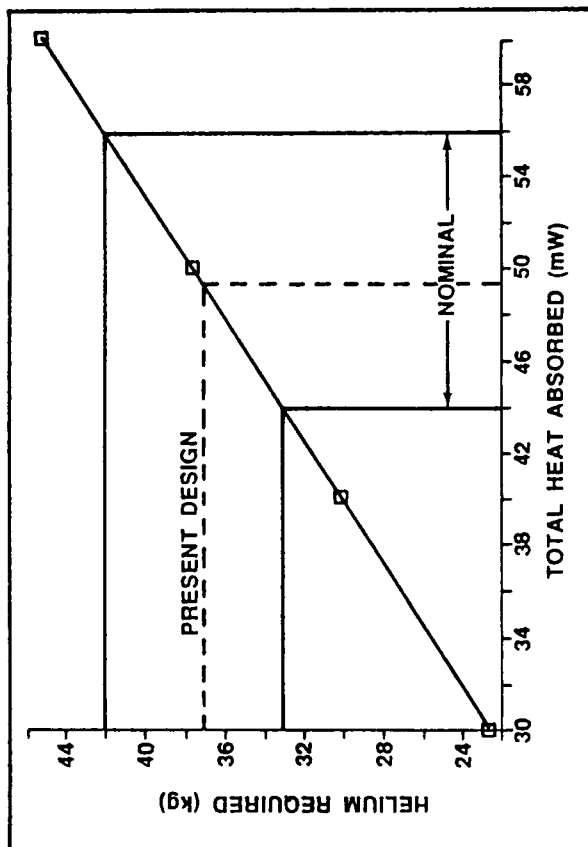


Figure 4-7. Comparison of SGM dewar concept and COBE dewar.

A conceptual design of the SGGM Experiment Module is shown in Figure 4-8. Electronics packages, a sensor to align the SGG and external navigation base, star trackers, remote interface units, and rate gyros are elements that could be mounted to the external shell of the dewar. The Experiment Module is estimated to weigh approximately 467 kg. Details are shown in Table 4-3.

In Section 4.4.2, a spacecraft concept based on a modification of the GRM design is discussed. This concept would attempt to accommodate an Experiment Module within the 1-m diameter constraint of the GRM spacecraft. Although this would provide a lower drag spacecraft, it would require a very long, thin, and inefficient dewar with a high surface-to-volume ratio. One could make risky assumptions about the radial thickness of the insulation jacket, but a dewar of this design would increase the heat load to the helium and consequently degrade the mission lifetime. In fact, it has been estimated that the hold-time of similar, "ideal" dewars scales as the square of their diameters [105]. To contain the same helium volume (260 L) as the 1.3 x 1.5-m dewar would require a dewar at least 2.75 m in length (Fig. 4-9). This design is not recommended. The above discussion illustrates the challenge that one must address in designing a dewar that will maximize cryogen lifetime within the constraints imposed by a spacecraft with a minimum (low drag) diameter cross section.

Both the external spacecraft and cryogenic system thermal designs are critical to mission life. Detailed thermal analysis depends on the specific spacecraft design and is discussed in Section 4.3.1.

Experiment Module Isolation: Non-gravitational disturbances that exceed the limitations discussed in Section 3.1 must be either compensated for or removed. A drag free spacecraft, like GRM or GP-B, has a proof mass shielded from external forces so that it follows a true gravitational orbit, with the spacecraft forced to follow the proof mass. The SGGM does not require a drag free orbit because the gravity gradient is measured in situ by a single instrument without referring to the orbital characteristics. However, the severe restrictions on acceptable acceleration levels make the isolation of the SGG an area of concern, and a system similar to a drag free system may offer a solution.

Alternative approaches being investigated for SGG isolation include free floating the SGG, and "soft" mounting it in the spacecraft. The free-floating approach requires precise control of the Experiment Module's position relative to the spacecraft, and techniques to transmit power and data to the SGG. For example, the Experiment Module could float within a cavity at the center of the spacecraft. The outer spacecraft would be controlled by the primary propulsion system which counteracts external disturbances, such as drag, and essentially flies the spacecraft around the Experiment Module. An auxiliary control system, or vernier system, is also needed for fine control of the Experiment Module. The alternative approaches under investigation to provide the vernier control are magnetic eddy current forcing and a control system similar to GP-B that utilizes the helium boiloff gas.

A magnetic suspension system could be used either as an active isolator or as an intermittent drag-free device, with drag-free times depending on the magnitude of the drag forces and the dimensions of the cavity [106]. The SGG could be housed in a conducting shell, and released within a cage of magnetic repulsion coils. When collision with the cage is imminent, the coils would be activated. Other configurations, such as placing the magnetic active elements near the Experiment Module support points, might also be used. The position of the instrument package relative to the containment structure could be sensed by radio frequency or optical techniques.

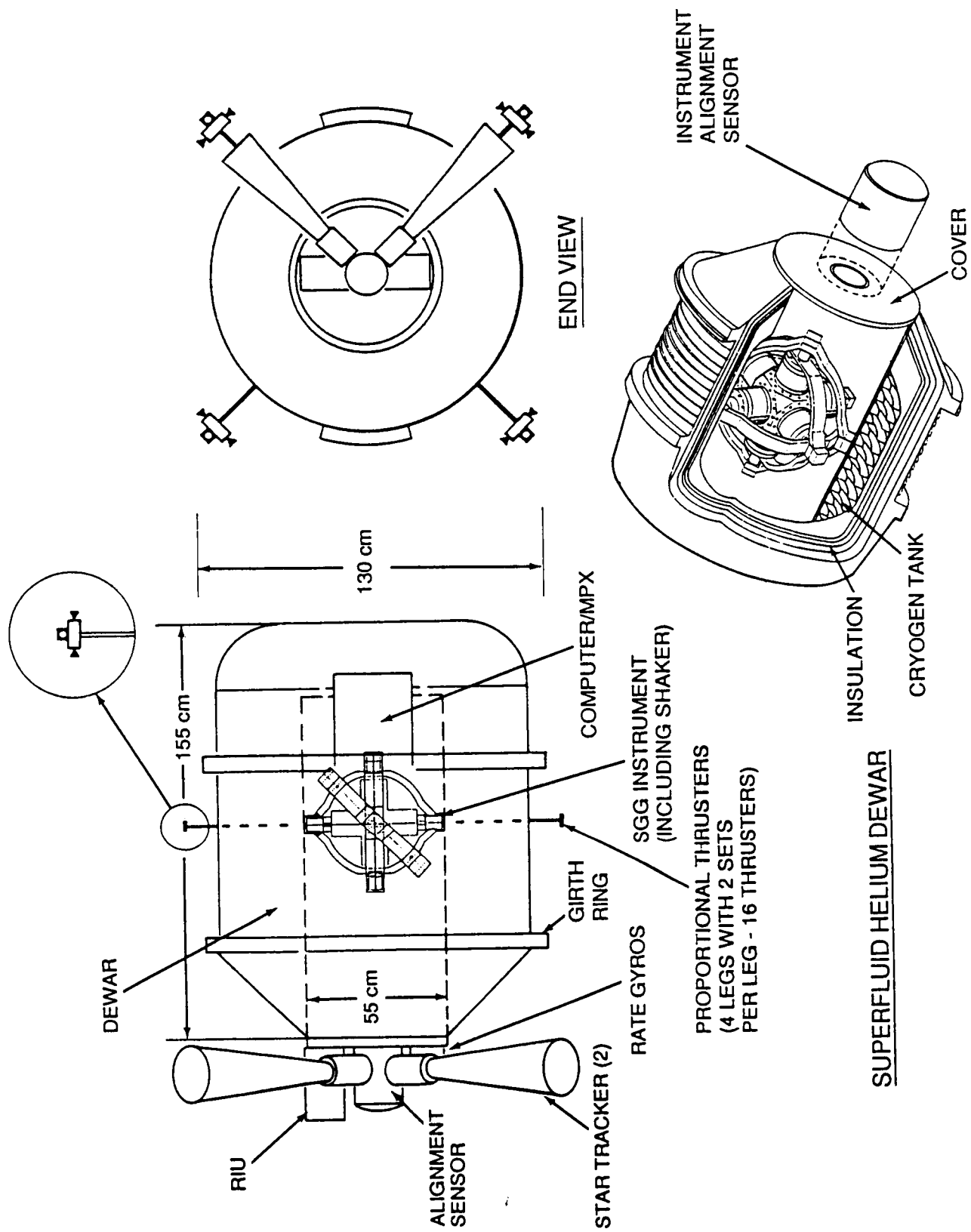


Figure 4-8. SGG Experiment Module concept.

TABLE 4-3. EXPERIMENT MODULE WEIGHT/SIZE SUMMARY

<u>COMPONENT</u>	<u>QUANTITY</u>	<u>UNIT WEIGHT</u> <u>(kg)</u>	<u>UNIT SIZE</u> <u>(cm)</u>
SGG INSTRUMENT	1	100	55 (DIA.)
DEWAR	1	176	155 X 130 (DIA.)
INSULATION/THERMAL CONTROL	1	49	-
OTHER SYSTEMS			
RIU	1	1.7	8 X 20 X 18
C&DH	1	6	-
COMPUTER MPX	1	4.5	15 X 10 X 5
STAR TRACKER	2	9	15 X 15 X 30
SUN SHADES	2	1	-
ALIGNMENT SENSOR	1	6.8	23 X 30 (DIA.)
RATE GYROS	2	4.3	16 X 19.3 X 21
PROPORTIONAL THRUSTERS	8	1.7	10 X 10 X 7
ELECTRONICS	1	8	15 X 15 X 20
TUBING	-	36	-
CONTINGENCY	-	36	-
TOTAL		<hr/> 467.2	

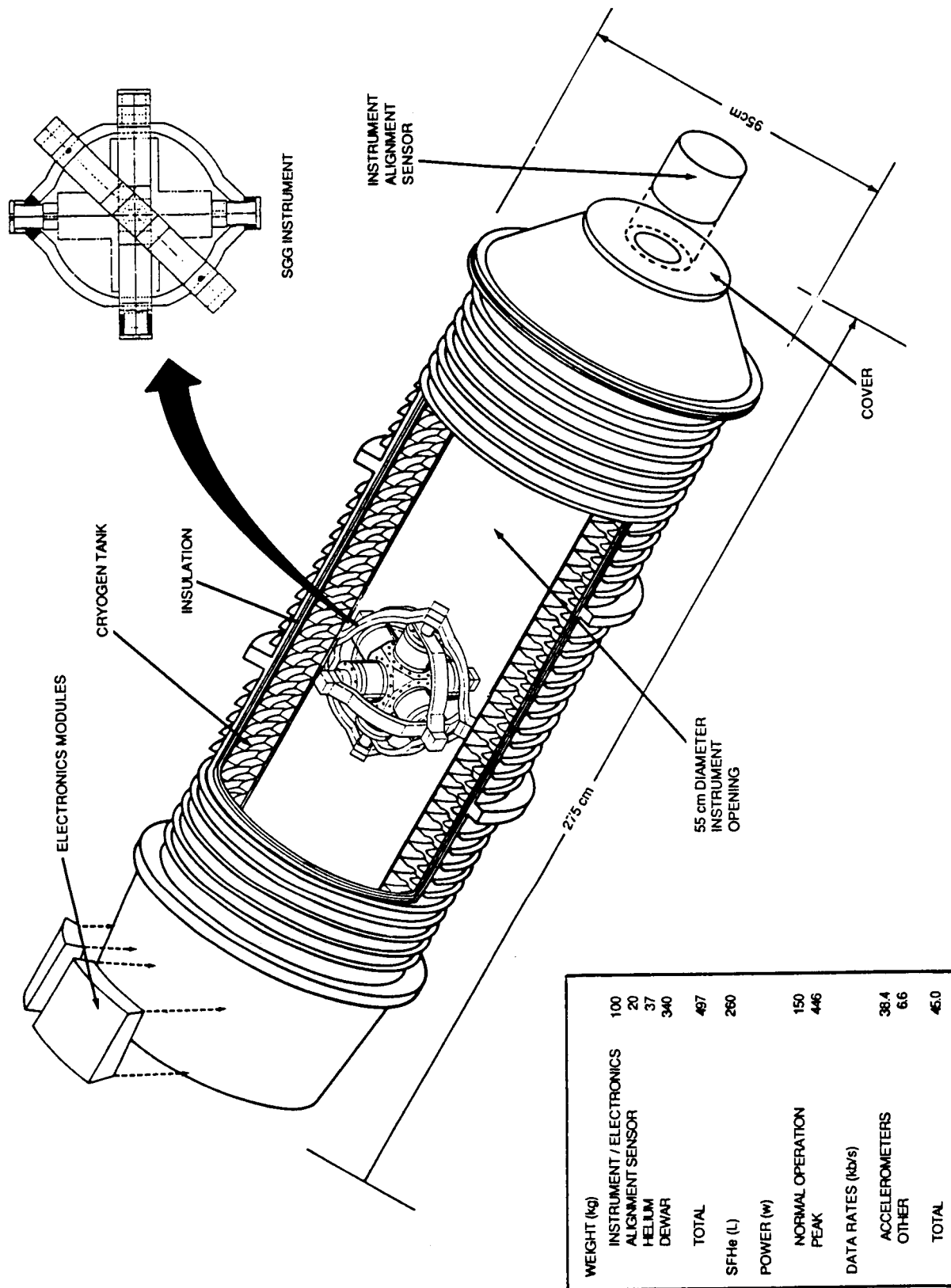


Figure 4-9. SGG Experiment Module concept - modified GRM.

Several methods exist, and no problems in determining the Experiment Module position are expected [106]. The Experiment Module power requirements could be met by microwave transmission across the cavity gap, as discussed in Section 4.3. An RF link to transmit the data across the gap is also discussed in Section 4.3, and should pose no problems.

Magnetic suspension isolation has been under investigation by JPL for some time. Areas of concern include the required "softness" of the restoring forces and vibrations (and their damping times) that could be produced by the eddy current link. Another problem arises because of the sensitivity of the SGG to external magnetic fields. Means would have to be developed to shield the SGG from the magnetic fields produced by the suspension system.

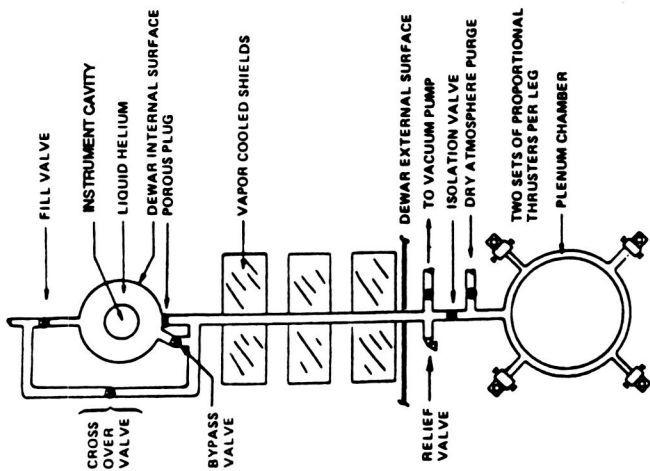
The GP-B spacecraft utilizes helium boiloff gas from the cryogenic system to provide propulsion for drag compensation and attitude control. This is not possible for SGGM because the much higher drag forces experienced at the lower SGGM altitude cannot be counteracted using helium boiloff alone. However, drag compensation of just the free-floating Experiment Module may be possible. Figure 4-10 illustrates the basic concept of the GP-B propulsion systems.

In conventional spacecraft auxiliary propulsion systems, thrusters are operated on-off where the closure occurs abruptly, and the valve is left with a positive closing force when off. By contrast, in the GP-B proportional thruster system (Fig. 4-10), the helium gas must flow unrestricted, continually, and the valve is open at all times. By combining two partially open valves which nominally would carry one-half of the flow each, a proportional flow valve can be made by operating them differentially. A valve plunger moves to cover one thruster throat while opening the other further. Thus, if the gas is expelled in opposite directions, the increase in force on one side and reduction on the other produces a net force. By placing this device at a moment arm, a torque can be generated. Thus, the need for both attitude control and translational thrusting can be met.

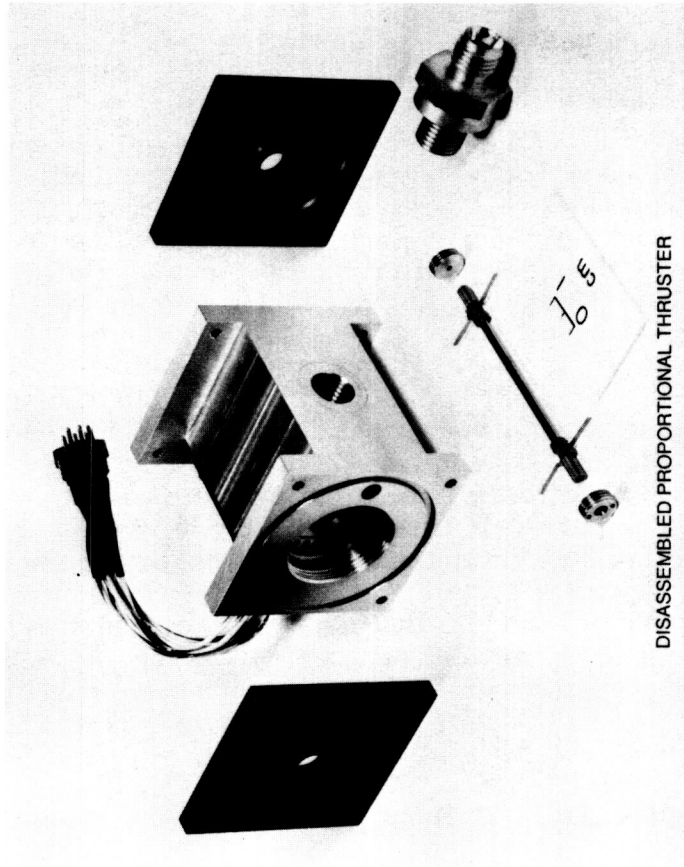
The proportional thrusters would function as a vernier control system to maintain precise control of the Experiment Module within the spacecraft cavity. After the helium leaves the porous plug, it is used to cool the dewar heat shields and exit via a line, as shown schematically in Figure 4-10. The helium gas would then pass through a plenum chamber surrounding the dewar and be routed through the external spacecraft structure by four small tubes. Attached to each tube are two orthogonal pairs of opposed proportional thrusters. Any one of the thruster pairs is capable of generating thrust or providing non-propulsive venting. Because the forces can be controlled at very low and precise levels, Experiment Module control should be very fine.

The helium boiloff rate, and thus the amount of propellant available as a function of time, depends on the heat input to the dewar. During the mission, there will also be differences between helium supply and control system demand, which must be accommodated. In the GP-B design, the system vents any excess boiloff non-propulsively and uses a porous plug (or dewar) heater for augmentation during a deficiency. The amount of excess cryogen that must be included will depend on thruster specific impulse, actual boiloff flow rate range, and the number of times the higher thrust requirements and low boiloff conditions coincide.

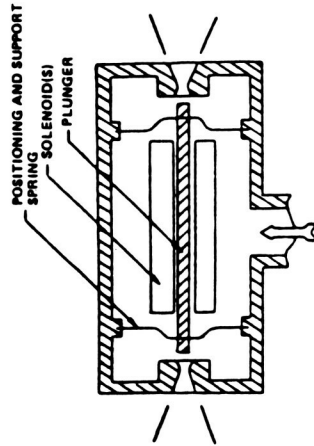
The thrust level available for the thrusters is directly dependent on the pressure of the vented gaseous helium. During the GP-B Phase B study, detailed analyses



ACQUISITION AND DISTRIBUTION SYSTEM



DISASSEMBLED PROPORTIONAL THRUSTER



PROPORTIONAL THRUSTER ASSEMBLY

- THRUST LINEAR WITH PLUNGER POSITION
- FLOW AREA CONSTANT
- CHAMBER PRESSURE DEPENDENT UPON HEAT LEAK INTO DEWAR
- PLUNGER GAP AT NEUTRAL POSITION IS: G-D7/8

ORIGINAL PAGE IS
OF POOR QUALITY

Figure 4-10. Gravity Probe-B proportional thruster system.

and laboratory experimentation of the propulsion system were conducted [102]. The GP-B spacecraft control system required response to thrust commands as low as 0.001 mN and a maximum thrust of 13 mN (twice the maximum thrust of 6.5 mN per thruster). The studies concluded that the system appears feasible and capable of handling the GP-B requirements.

The amount of clearance between spacecraft and Experiment Module, and several other issues relating to this approach, cannot be adequately examined until detailed simulations (see Appendix G) of the spacecraft control system have been completed. However, the proportional thruster system would present a particularly attractive solution since it would convert the problem of managing the cryogen vent gas into a solution for isolating and controlling the SGG. Moreover, the technology would be largely proven since it is now being developed for GP-B.

In both of the above approaches, the Experiment Module would be isolated from the relatively high drag forces by the surrounding spacecraft surfaces. The SSA would serve as the proof mass and provide signals for control. Two star trackers would be mounted on the Experiment Module for attitude determination, and an alignment system would be required to determine alignment between the external base (star trackers/external Experiment Module structure) and the SGG located within the dewar. This configuration is illustrated in Figure 4-11. The mechanism (not shown in the figure) to latch and support the Experiment Module during prelaunch, launch and ascent, and to release it once orbit has been achieved, will be necessary.

4.2.2 Attitude Control Considerations

A gravity gradiometer is inherently sensitive to angular rates. For example, a rate of $3 \times 10^{-7} \text{ rad sec}^{-1}$ produces the same signal as a gradient of 10^{-4} E (see Appendix B for a derivation). Therefore, attitude rates must be controlled or known with high precision, in order to recover the real gradients. This places strong demands on the ACS. The following discussion outlines the results of an assessment of this area and describes a preliminary ACS concept. It is strongly recommended that in-depth analysis be devoted to the ACS in subsequent studies. Some of the concern indicated here can only be adequately addressed through more penetrating analysis, such as high fidelity guidance and control simulations. The preliminary results of a computer simulation of the control system are given in Appendix G.

Attitude Control System Concept: The design of the ACS obviously depends on the particular spacecraft configuration under consideration. The following description of an ACS is based on the cylindrical spacecraft configuration (Option II) discussed in Section 4.4.

In order to understand the implications of the attitude control requirements, it was assumed that the spectral content of the relevant parameters could be determined over a small, low frequency range. The required attitude control or knowledge for geophysics applications (Table 3.1) and an instrument in the Earth-fixed mode is $3 \times 10^{-6} \text{ rad Hz}^{-1/2}$. For 1 Hz bandwidth, this translates to 0.6 arcsec. The SGG pointing requirements are illustrated in Figure 4-12. In addition, when one considers that the 0.6-arcsec SGG pointing requirement is with respect to an Earth-fixed coordinate system, the requirement becomes even more demanding. With the Earth-fixed SGG, all measurements made by the star trackers are in a moving field, because of the spacecraft motion. The tracking is not continuous and accuracy may be compromised by such an implementation.

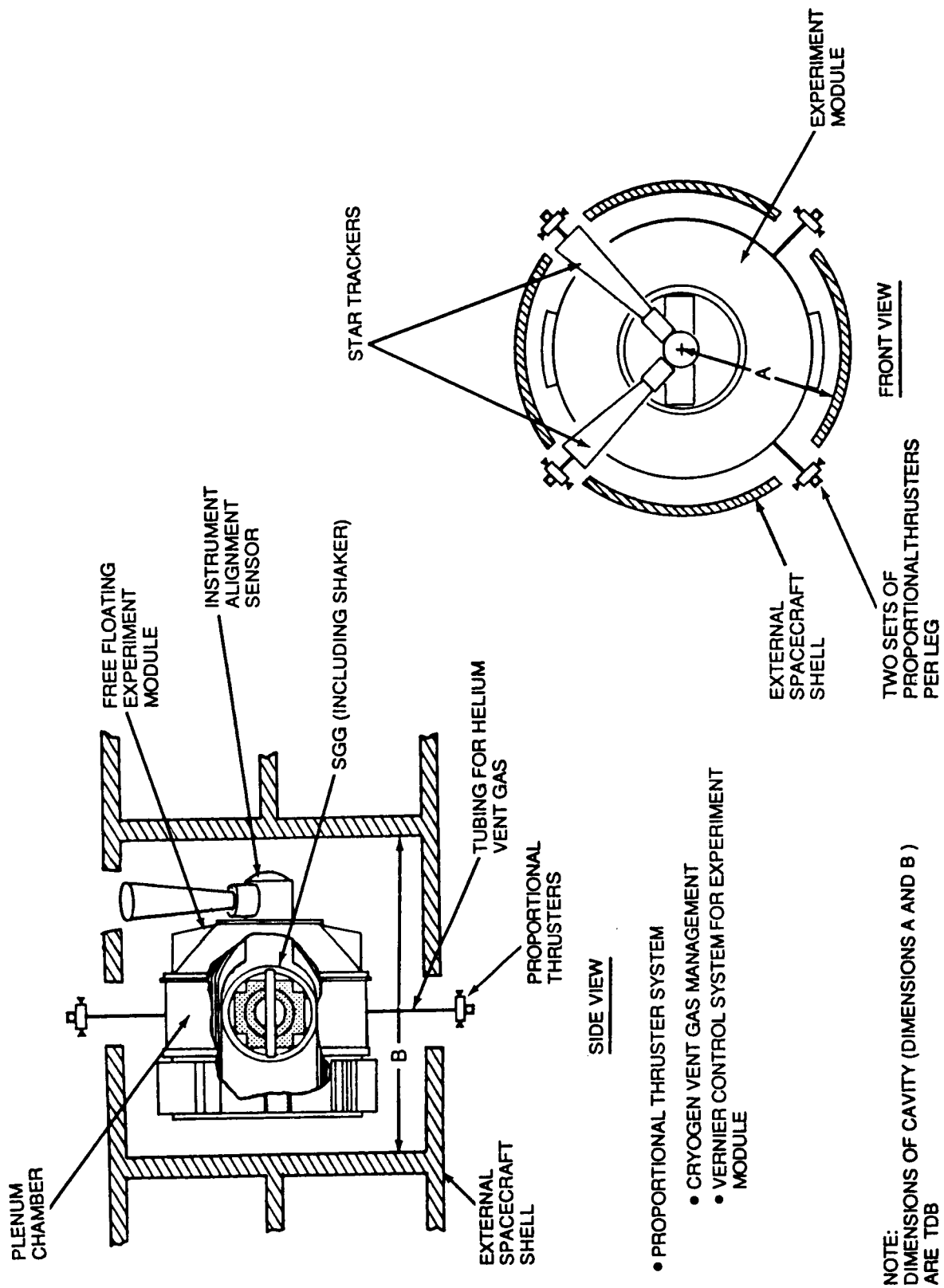


Figure 4-11. Experiment Module isolation utilizing cryogen vent gas for control.

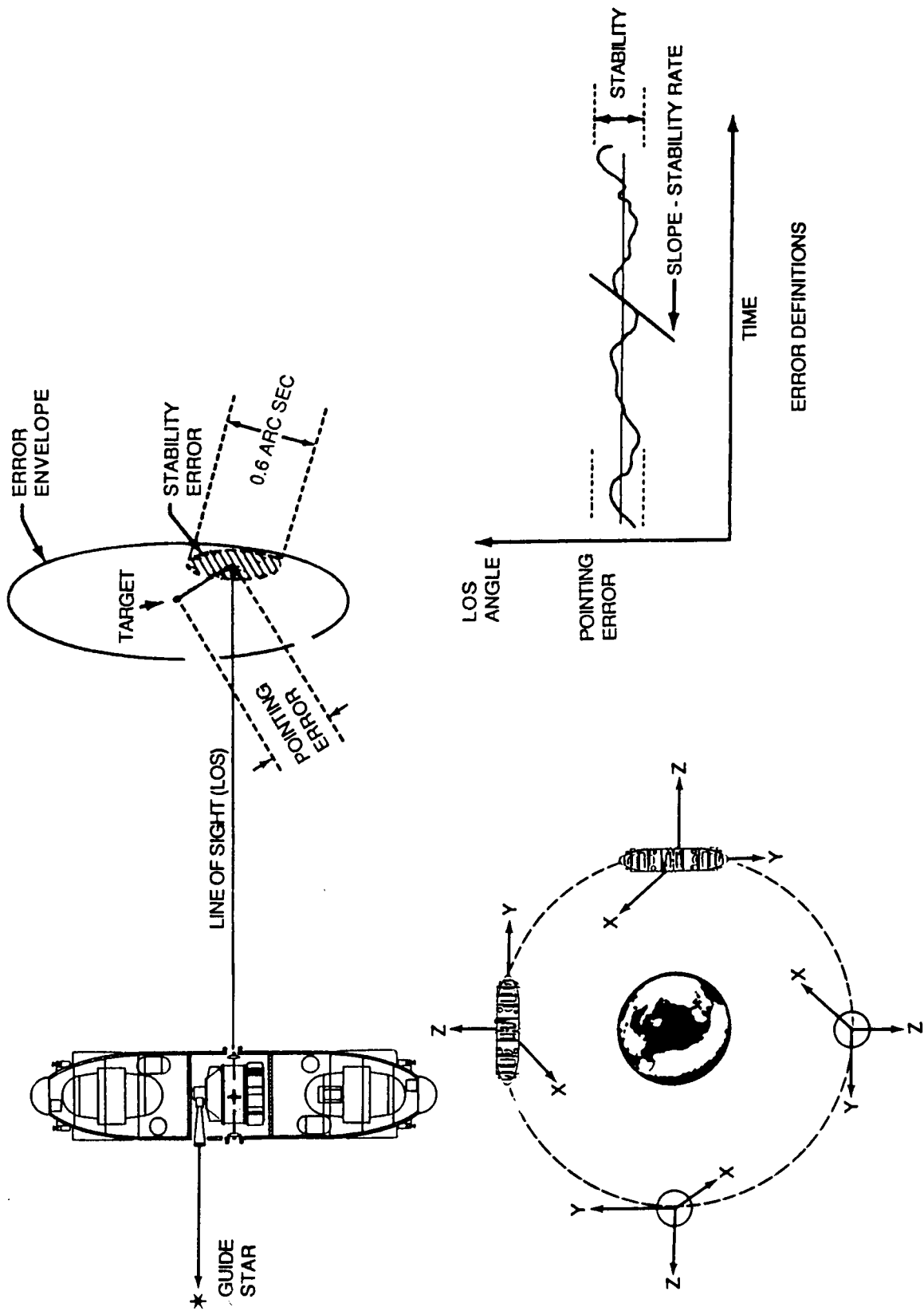


Figure 4-12. SSGM spacecraft pointing.

To develop an ACS, all spacecraft system components, including accelerometers, reaction wheels, thrusters, etc., must be characterized in detail. That is, the angular accelerometer must be defined according to bandwidth, frequency, and drift characteristics, and quantization. If unbalanced and bearing-induced accelerations from the reaction wheels prove to be a problem, then other means of producing control torques must be considered in the spacecraft design.

A technique for measuring the alignment of the outer navigation base (i.e., star tracker) with the gradiometer must be developed. Unless this alignment can be determined in real time to greater accuracy than the overall pointing requirement, the gradiometer attitude determination will not be adequate.

Existing and "off-the-shelf" spacecraft subsystems were considered, and utilized where appropriate. For example, the Multimission Modular Spacecraft (MMS) utilizes standard subsystem modules [e.g., power, communications and data handling (C&DH), and ACS] for a wide range of spacecraft applications. A modified MMS module was assumed as the baseline ACS for the analysis (Fig. 4-13) discussed in this section. The Inertial Reference Unit (IRU) will provide attitude information and will be updated with the navigation sensors. A magnetic torquer will be needed on the pitch axis for momentum management. Reaction wheels will be used for attitude control.

The block diagram of a preliminary control system for a free-floating Experiment Module is shown in Figure 4-14. The inner body control system consists of the dewar dynamics control, instrument accelerometer, integrators, controller/estimator, and proportional thrusters. As the inner body is controlled with minimum exterior disturbances, the outer body senses position with respect to the Experiment Module and maintains control. A minimum deadband system is required for the outer body (spacecraft) to reduce mass changes relative to the instrument.

An alignment sensor determines the position of the instrument with respect to the navigation base reference attached to the Experiment Module. The star trackers provide the inertial reference relative to selected guide stars.

A brief analysis of a linear acceleration controller was also made. A simplified block diagram is shown in Figure 4-15, which shows pertinent system parameters and disturbances. The outer loop controls the total spacecraft to some required level while the inner loop is indicative of the SGG accelerometer controller. F_d are external disturbance forces and F_e are forces from internal disturbances. The accelerometer noise is shown as a disturbance on the output of the accelerometer control loop. Preliminary estimates for some of the parameters are shown in the figure.

Observations are shown in the two graphs in the figure. It appears that, for frequencies near orbital rate, the spacecraft controller will maintain control forces at a low value. However, as the frequency increases, the controller will rapidly approach a one-to-one correspondence of control error, F_e , with respect to the external disturbance F_d . Also, the control error for very low frequencies will approach the accelerometer noise. The control performance in any control system is ultimately limited by the primary sensor noise. It is, therefore, critical that the accelerometers have a very low noise figure.

MMS ATTITUDE CONTROL SYSTEM MODULE

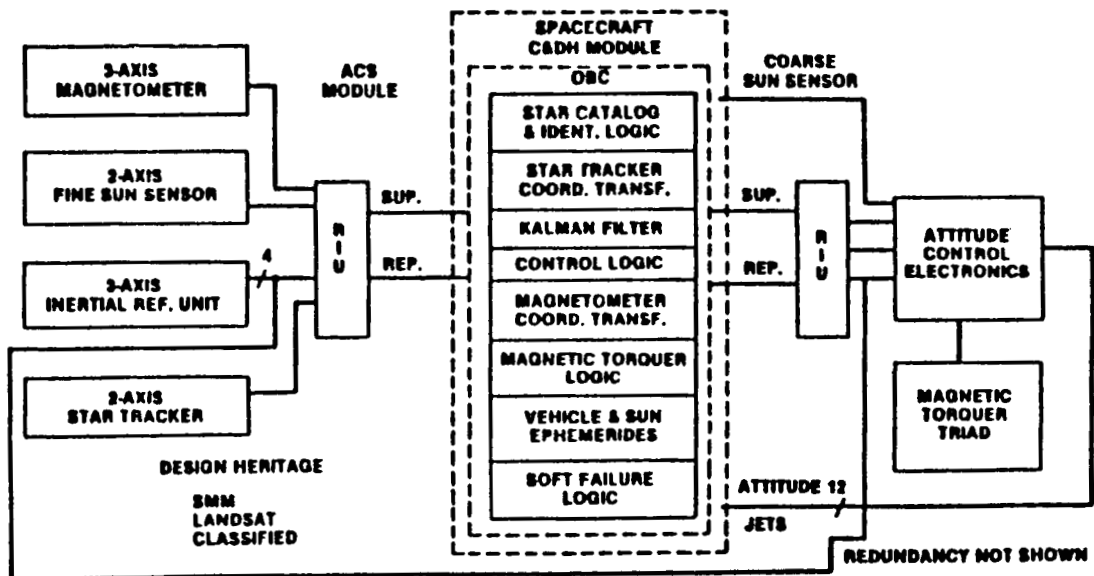
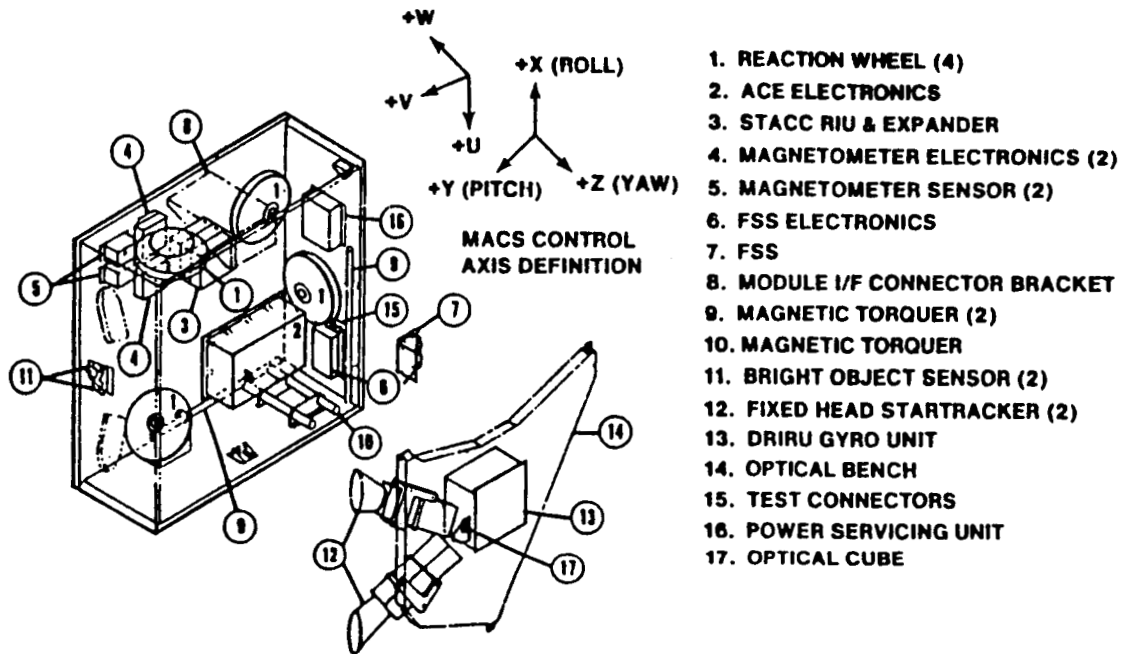


Figure 4-13. Attitude control module block diagram.

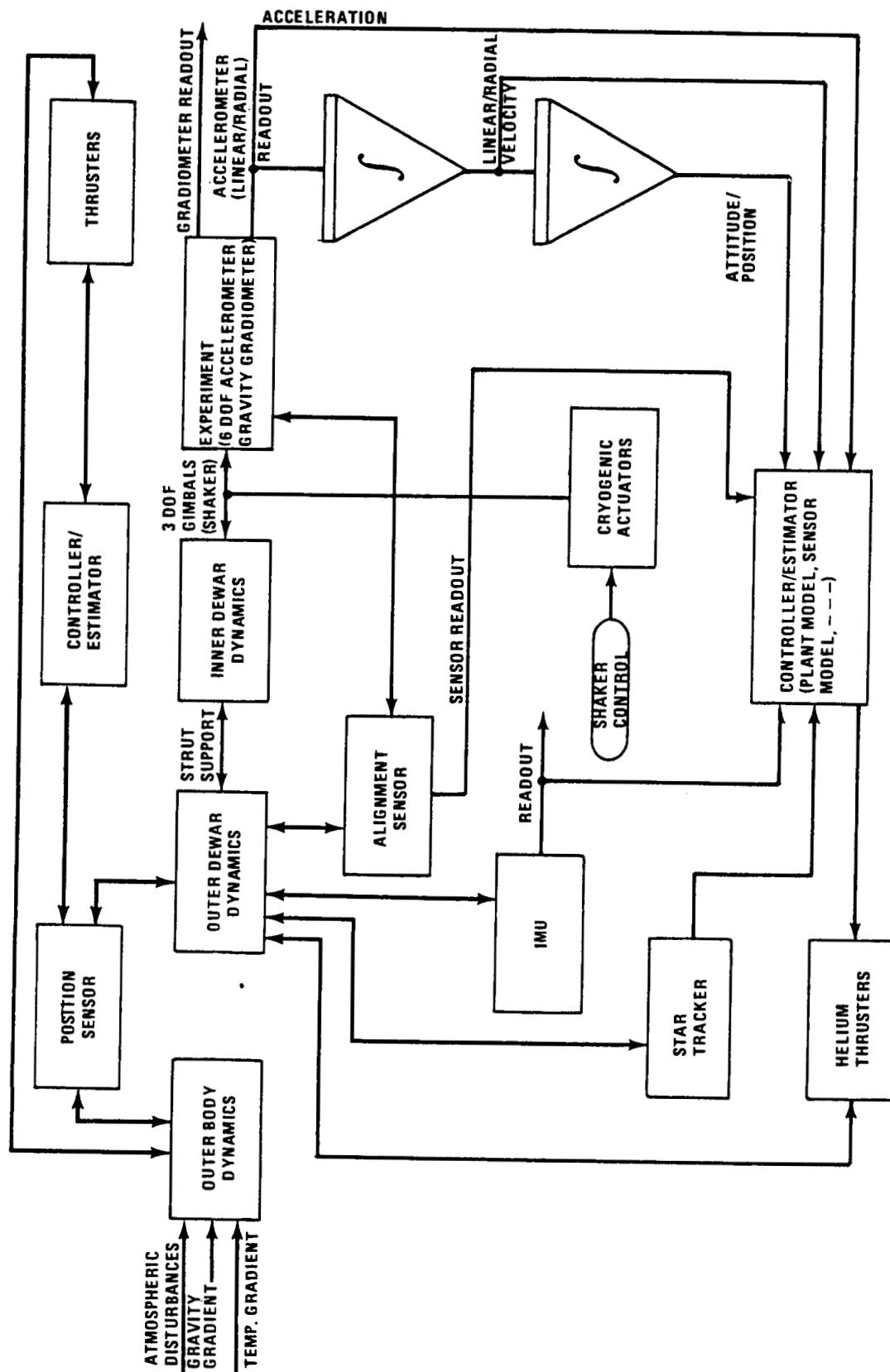


Figure 4-14. SGG control block diagram.

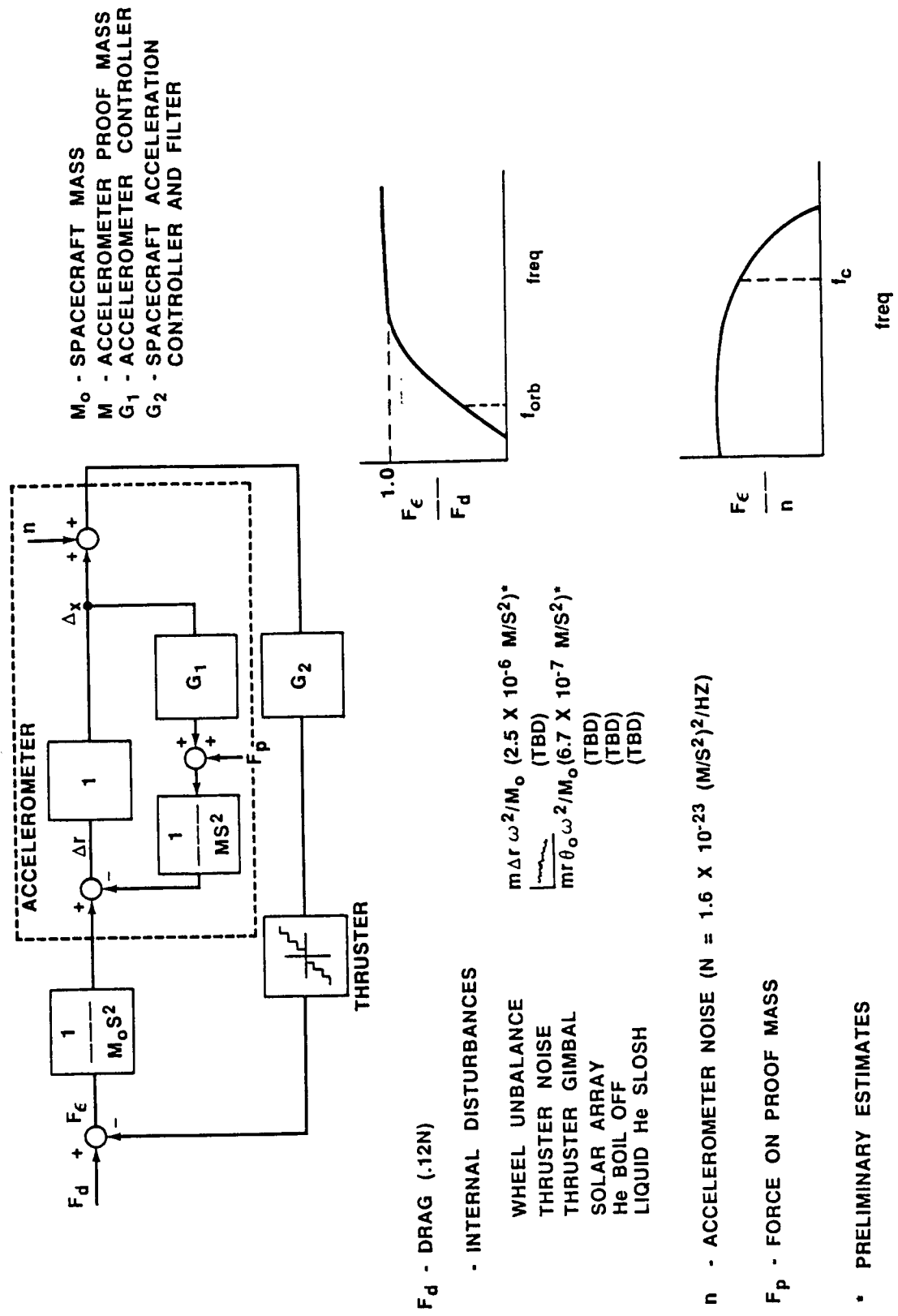


Figure 4-15. Linear acceleration controller.

4.2.3 Summary of Alternative Concepts

The alternative spacecraft concepts considered in this study are summarized in Figure 4-16 which lists major characteristics of each. In addition to the concepts analyzed, data for the GRM and GP-B spacecraft are shown for reference in the last two columns of the figure. These latter two concepts are included for comparison with spacecraft designs that have sensors which, like SGGM, impose demanding platform requirements. For example, a "near-perfect" gyroscope (drift rate less than $0.001 \text{ arcsec year}^{-1}$, seven orders of magnitude better than current inertial navigation gyroscopes) is integrated into the GP-B spacecraft to measure a very small gyroscope precession predicted by General Relativity [84]. This measurement is made with respect to the gyroscope spin axis, which must remain precisely pointed (0.003 arcsec) to an inertial reference. The required measurement is a cumulative gyroscope precession of 0.042 arcsec after one year in orbit! This measurement must be made in the presence of random noise and other disturbances such as some of those discussed in Section 4.2. For example, a drag free system is utilized to provide a low acceleration environment that must meet the 10^{-10} g requirements. Although drag disturbances are more severe at the lower altitude flown by SGGM, one can readily see that the requirements for SGGM are not as severe as the planned GP-B mission.

Four spacecraft concepts were considered in this study to provide a range of baseline references that included mission emphasis, technology requirements, and cost ranges upon which the mission requirements could then be compared. Systems and subsystems for these concepts were analyzed in some detail to assure that potential "show stoppers" were identified, and either resolved if within the scope of this study, or singled out for special consideration in future studies. The major spacecraft elements for all options were structured, where possible, in a modular manner, and existing subsystems or subsystem designs were selected if they could meet the requirements.

A spherical configuration was chosen as Option I so that either an inertial or Earth-fixed orientation would produce nearly the same atmospheric drag. This option was further divided into Option I-A, which utilized ion propulsion, and I-B, where monopropellant hydrazine was assumed. Ion propulsion, while it offers high performance, and lesser propulsion system weight and volume, requires large amounts of electrical power. This in turn necessitates large solar arrays [since Radioisotope Thermoelectric Generators (RTG) have been ruled out for this mission], which create additional drag, and possible perturbing mechanical vibrations. Both concepts would utilize the MMS modules where possible, thereby reducing cost.

Option II-A would rely heavily on the GRM spacecraft subsystems. Like GRM, it has a long, cylindrical envelope and produces less drag than Option I. However, it is limited to an Earth-fixed attitude. The GRM propulsion system would have to be modified, as well as portions of the ACS and the data management system.

Option II-B started with the GRM spacecraft design, and required that modifications to the GRM design be held to a minimum. This option thus addressed the question: Could the spacecraft designed for GRM accommodate the SGGM? To accomplish this, the SGGM Experiment Module, as discussed in Section 4.2.1, must fit within the 1.04-m diameter of the GRM spacecraft and would replace the Disturbance Compensation System (DISCOS) hardware. As discussed previously, there are also major problems involved in the design of the dewar within the constraints imposed by this spacecraft configuration.











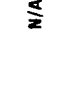



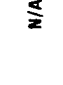
OPTION	(I) 3-M SPHERE	MINIMUM DRAG CONFIGURATIONS		(FOR REFERENCE ONLY)	
				GRM	GP-8
CONFIGURATION	 (I-A)  (I-B)	 (II-A) (1.7-M CYL)	 (II-B) (GRM DERIVED)		
CROSS SECTION					N/A
FEATURE					
ATTITUDE	EARTH-FIXED OR INERTIAL	EARTH-FIXED	EARTH-FIXED	EARTH-FIXED	INERTIAL
MINIMUM DURATION (MO)	6	6	6	6	24
ORBIT: ALTITUDE (km)	200	200	200	160	950
INCLINATION (DEG)	96.3	96.3	96.3	90 ± 0.1	90
TOTAL WEIGHT (kg)	2,524	4,072	3,377	2,734	1500
PROPELLANT WEIGHT (kg)	99 (XENON)	1400 (HYDRAZINE)	1400 (HYDRAZINE)	1400 (HYDRAZINE)	296 (HELIUM BOILOFF)
DIMENSIONS (LENGTH X DIAM.) (m)	3.05 (DIAM.) 20 W/SOLAR AR.	8.2 X 1.7	7.9 X 1.04	5.7 X 1.04 (10.1 X 1.04m/ MAG. 8000M)	4.3 X 4.3
POWER (W) (CONTINUOUS)	4,340	740	740	400	168
DATA HANDLING (kb/s)	43	43	43	4.6 34 (PLAYBACK)	0.256
CONTROL SYSTEM REQ.	EARTH-FIXED	EARTH-FIXED	EARTH-FIXED	EARTH-FIXED	ANG DISPL
-POINTING STAB (rad Hz ^{-1/2})	3 x 10 ⁻⁶	2 x 10 ⁻⁸	3 x 10 ⁻⁶	8.7 x 10 ⁻⁴ rad	ERRORS BETWEEN
-ATTITUDE RATE (rad s ⁻¹ Hz ^{-1/2})	3 x 10 ⁻⁷	3 x 10 ⁻⁷	3 x 10 ⁻⁷	5.2 x 10 ⁻⁵ rad s ⁻¹	TELESCOPE &
-GEOPHYSICS-	4 x 10 ⁻¹¹	4 x 10 ⁻¹¹	4 x 10 ⁻¹¹	~4.8 x 10 ⁻¹⁰ rad	INSTR.
-PHYSICS-	2 x 10 ⁻⁸	2 x 10 ⁻⁸	2 x 10 ⁻⁸	-	1 x 10 ⁻¹⁰ AVG.

Figure 4-16. Comparison of SGM spacecraft concepts.

In summary, unless the SGGM Experiment Module could be integrated into some type of inertial platform on the Earth-fixed spacecraft (Option II) that would decouple the SGG and spacecraft orientations, a spacecraft concept similar to Option I would be required if the inertial mode is preferred. The design of such a decoupling inertial platform is beyond the scope of this initial study. The details of the conceptual designs for Options I and II are discussed in Sections 4.3 and 4.4, respectively.

4.2.4 Other Potential Carriers

A brief examination of other potential platforms to accommodate the SGG was made. This was limited to the Space Station, the EOS platform, and the TSS. The accommodation of the SGG on any of these future systems does not appear promising.

Space Station: Performing the SGGM from the Space Station is not recommended. The Space Station orbit will be between 463 and 555 km, and at an inclination of 28.5 deg. This orbit altitude is too high to achieve the desired resolution; and the inclination is too low for the desired global coverage. In addition, the distribution and motion of large masses, crew, antenna and equipment slewing, solar array motion, and structural vibrations would create severe problems. Below 1 Hz, the predicted Space Station acceleration levels are around 10^{-5} g, three orders of magnitude above the SGGM tolerance. Thus, the SGGM as a Space Station attached payload is not a promising option.

Earth Observing System (EOS) Platform: The EOS will be a major element of the future Earth Systems Science Program. Large polar platforms are being considered to provide interdisciplinary, long-term Earth Science measurements. However, the high orbital altitude (~ 824 km) would not provide the required sensitivity for SGGM gravity gradient measurements.

Tethered Satellite System (TSS): Another possibility is to accommodate the SGGM on the TSS from the Shuttle or a platform. This would offer the advantage of providing a relatively inexpensive instrument carrier at the required low orbital altitude. For this to be a practical option, the TSS disturbance levels must be controlled to the required levels. Estimates of TSS disturbance levels are discussed in Appendix F.

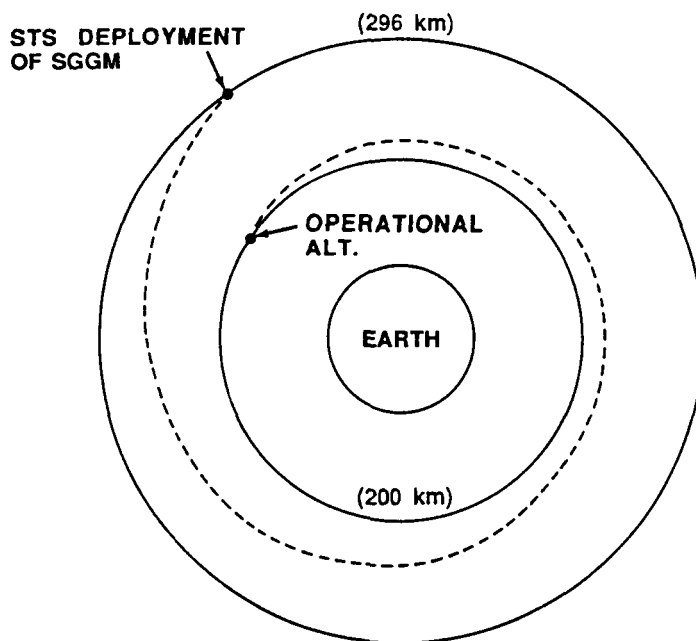
For two orbiting masses connected by a tether, there will be a resulting upward acceleration of the higher mass and a downward acceleration of the lower mass. This will give rise to a balancing tension in the tether. The attached masses will experience this tension as "artificial gravity." The magnitude of artificial gravity is proportional to the length of the tether from the system center of mass, and is given approximately by $4 \times 10^{-4} \text{ g km}^{-1}$. For example, a polar platform orbiting at 300 km with a mass attached to a 100-km tether would produce an acceleration level of approximately 0.04 g. Superimposed on this steady acceleration will be noise coupled from the platform. For example, if the Shuttle were used, crew motion, mechanical vibrations, and RCS disturbances would be coupled to the instrument. From an unmanned platform, station keeping motion, slewing, and vibrations would be coupled to the tethered spacecraft.

Although the vertical orientation of the tether system is stable, additional forces such as those from the Earth's oblateness, differential atmospheric drag, and other disturbances will cause the lower mass to oscillate about the vertical. This is explored in more detail in Appendix F.

In general, the Tether option introduces a system with complex dynamics into the already complex SGGM and it does not appear that an instrument with the severe low disturbance requirements of the SGG could be accommodated on the TSS.

4.2.5 Launch and Descent Phase

Launch aboard the STS has been assumed in this study; however, launch by an ELV is also considered to be a possibility. Since a polar orbit is required, the launch must be made from the Western Space and Missile Center at Vandenberg AFB, CA. After deployment by the STS, at approximately 300 km altitude, the SGGM is checked out for a period of about 24 hours. The SGGM then descends to 200 km in a spiral path with continuous thrusting. The times required for the descent phase and the estimated propellant expended are shown in Figure 4-17. The mission profile is only shown conceptually in the figure. For example, for Option I-A, the spacecraft would orbit the Earth approximately 155 times and, for Option I-B, 10 times before the spacecraft would reach the operational altitude.



OPTION	PROPELLANT REQUIRED (kg)	TIME REQUIRED FOR TRANSFER (HR)
OPTION I-A (ION)	4.8	233
OPTION I-B (HYDRAZINE)	109	14.8
OPTION II (HYDRAZINE)	135	18.4

Figure 4-17. SGGM descent to operational orbit - propellant requirements.

4.3 Option I: Earth-Fixed or Inertial Mode

This spacecraft may be placed in either an Earth-fixed or inertial orientation, and experience the same aerodynamic drag forces. Two alternatives for isolation of the Experiment Module were considered. In the first, the Experiment Module is protected from external disturbances by the outer spacecraft structure and floats free inside the spacecraft. The second alternative would isolate the Experiment Module by soft mounting it within the spacecraft. The detailed engineering for the soft mount was not pursued. Two alternative concepts were also developed within this option to analyze potential propulsion systems.

4.3.1 Option I-A: Ion Propulsion

Ion propulsion, which has very high performance characteristics ($I_{sp} \sim 3000$ sec) was considered in order to reduce spacecraft weight and volume, and to provide a low and even thrust for drag compensation. The large solar arrays that are required to provide the power for the ion thrusters are always oriented edge-on to the flight direction to minimize aerodynamic drag. However, as discussed in Appendix F, drag is still appreciable for this configuration. The weight summary, shown in Table 4-4, lists the individual elements of this concept, which is illustrated in Figure 4-18. MMS modules were assumed to provide power conditioning and distribution, major elements of the ACS, and the C&DH functions. A fourth MMS module is available for functions directly related to the SGG instrument that are not included as part of the Experiment Module.

A number of problems must be solved if the Experiment Module is freely floating within the spacecraft. First, the Experiment Module is not a homogeneous mass and, therefore, does not give an ideal orbit. Secondly, the helium boil-off introduces errors. To reduce these latter errors, the spacing between the spacecraft and the Experiment Module must be large enough to reduce helium gas plume impingement, and the helium must be exhausted through proportional thrusters. With these precautions, the errors and unknowns will still likely exceed the requirements imposed for linear acceleration and velocity. However, venting the helium boiloff gas outside the spacecraft and utilizing it to control the free-floating Experiment Module, as discussed in Section 4.2.1, may be a practical approach.

The analysis of the subsystems for this option indicated that the MMS modules could meet many of the requirements. The C&DH, Power Conditioning/Distribution, and an augmented and modified version of the ACS module could be utilized. Figure 4-19 shows the location and functions of the MMS modules. In the remainder of this section, the propulsion, power, thermal, and C&DH subsystems are discussed.

Propulsion Subsystem (Ion Propulsion): A propulsion system is required to provide orbit stability in the presence of atmospheric drag and other perturbations and to deboost from the nominal 300 km Shuttle insertion orbit to the 200 km operational altitude. Several candidate propulsion systems, such as monopropellant hydrazine, resistojet, colloid, and magnetoplasma dynamic arcjet are available. Power, thrust, and specific impulse make the ion system an attractive solution. For example, Figure 4-20 shows the propellant requirements as a function of drag for varying specific impulse values. Drag values for the different spacecraft configurations studied are indicated by dashed lines in the figure. One notes from the figure that a 3-m diameter spacecraft would require over 1800 kg of propellant per year if the specific impulse were around 200 sec, a typical monopropellant hydrazine I_{sp} value.

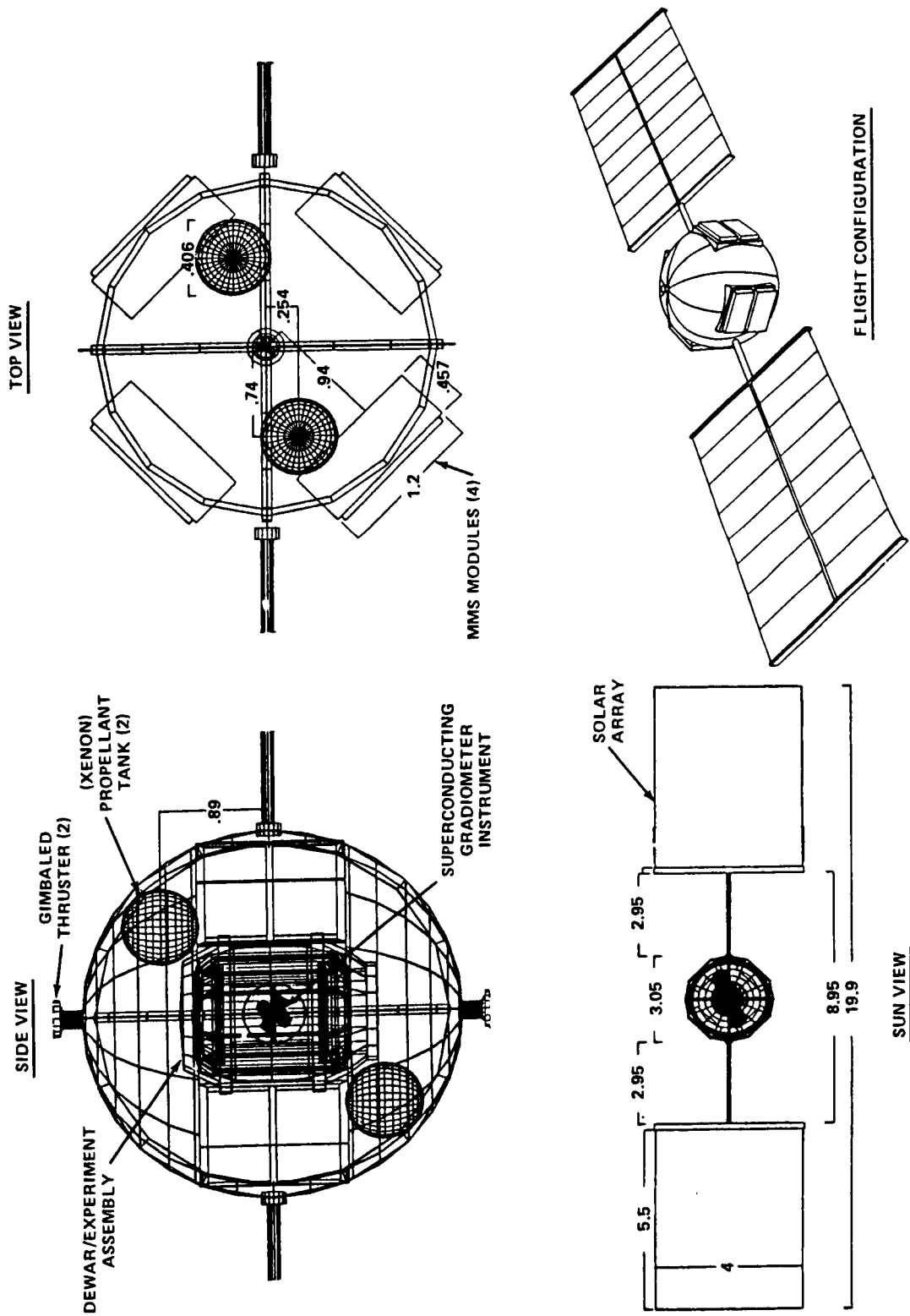


Figure 4-18. Free flyer spherical configuration - ion propulsion.

TABLE 4-4. OPTION I-A AND I-B WEIGHT SUMMARIES

	(kg)		
INSTRUMENT*	100		
DEWAR	176		
SPHERICAL STRUCTURE	393		
RINGS	68		
INSULATION/THERMAL CONTROL	113		
ATTACH STRUCTURE	186		
MISCEL. ELECTRONICS MODULE	125		
WIRE HARNESS	29		
INSULATORS & DISTRIBUTION	12		
EPS MODULE	164		
C&DH MODULE	135		
OMNI & H.G. ANT. & BOOMS	16		
RF COMBINER & HARNESS	5		
ACS MODULE	284		
DRIVE ASSY	10		
MECHANISMS	22		
SUBTOTAL	1838		
HELIUM	36		
SUBTOTAL	1874		
ADDITIONAL			
<u>OPTION IA</u>	(kg)	<u>OPTION IB</u>	(kg)
PROPULSION SYS	158	PROPULSION SYS	96
PROPELLANT (XENON)	99*	PROPELLANT (HYDRAZINE)*	1540
SOLAR ARRAYS	190	PRESSURANT (He)*	12
CONTINGENCY	203	SOLAR PANELS	20
		ADDITIONAL THERMAL INSUL.	14
TOTAL	2524	CONTINGENCY	171
		TOTAL	3727

NOTES:

* NO CONTINGENCY ON THESE ITEMS.

** 5% CONTINGENCY ON ALL AVIONICS, ELECTRICAL POWER, AND
PROPULSION SYSTEMS.
15% CONTINGENCY ON ALL NEW STRUCTURES AND THERMAL CONTROL.

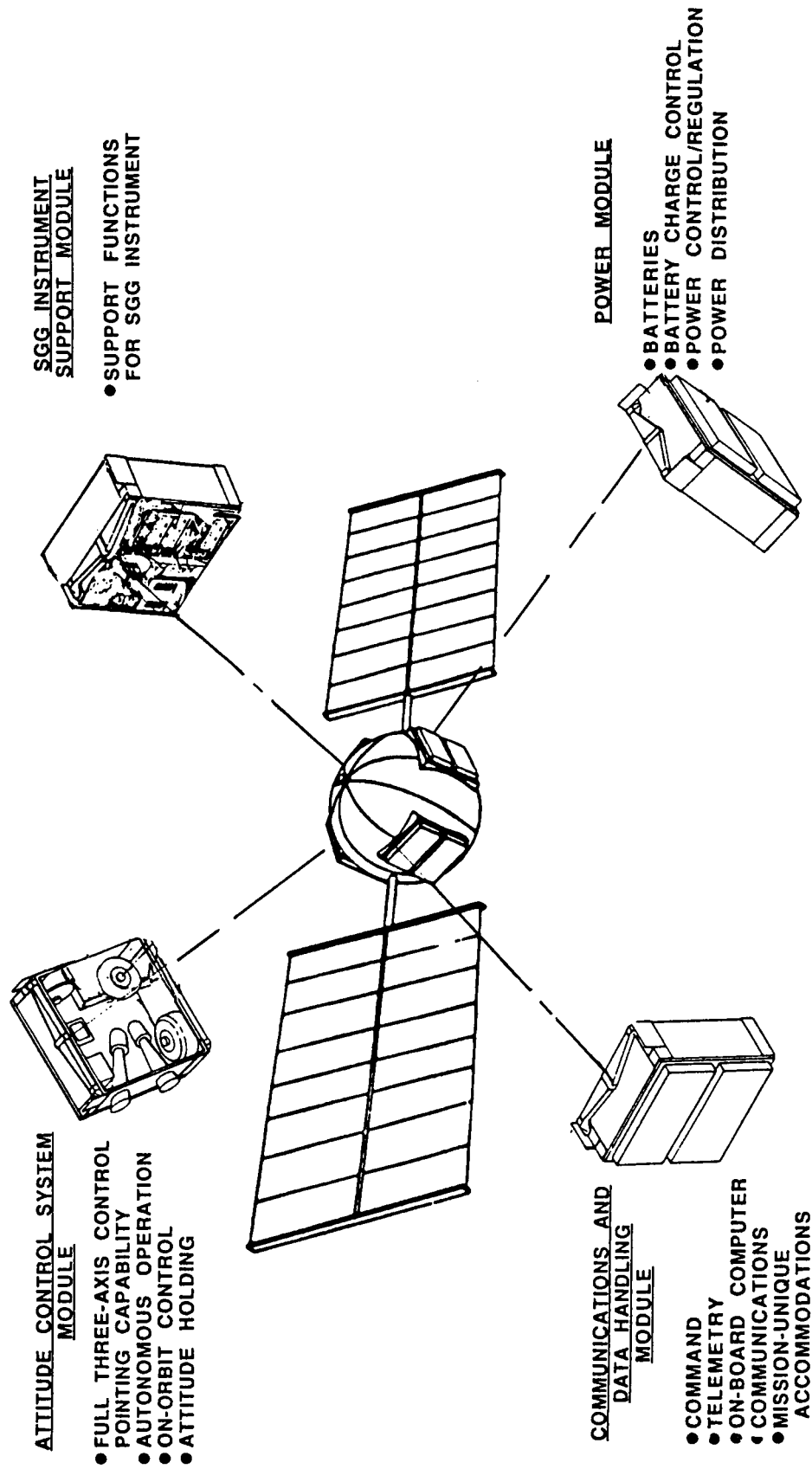


Figure 4-19. Multimission Modular Spacecraft module location.

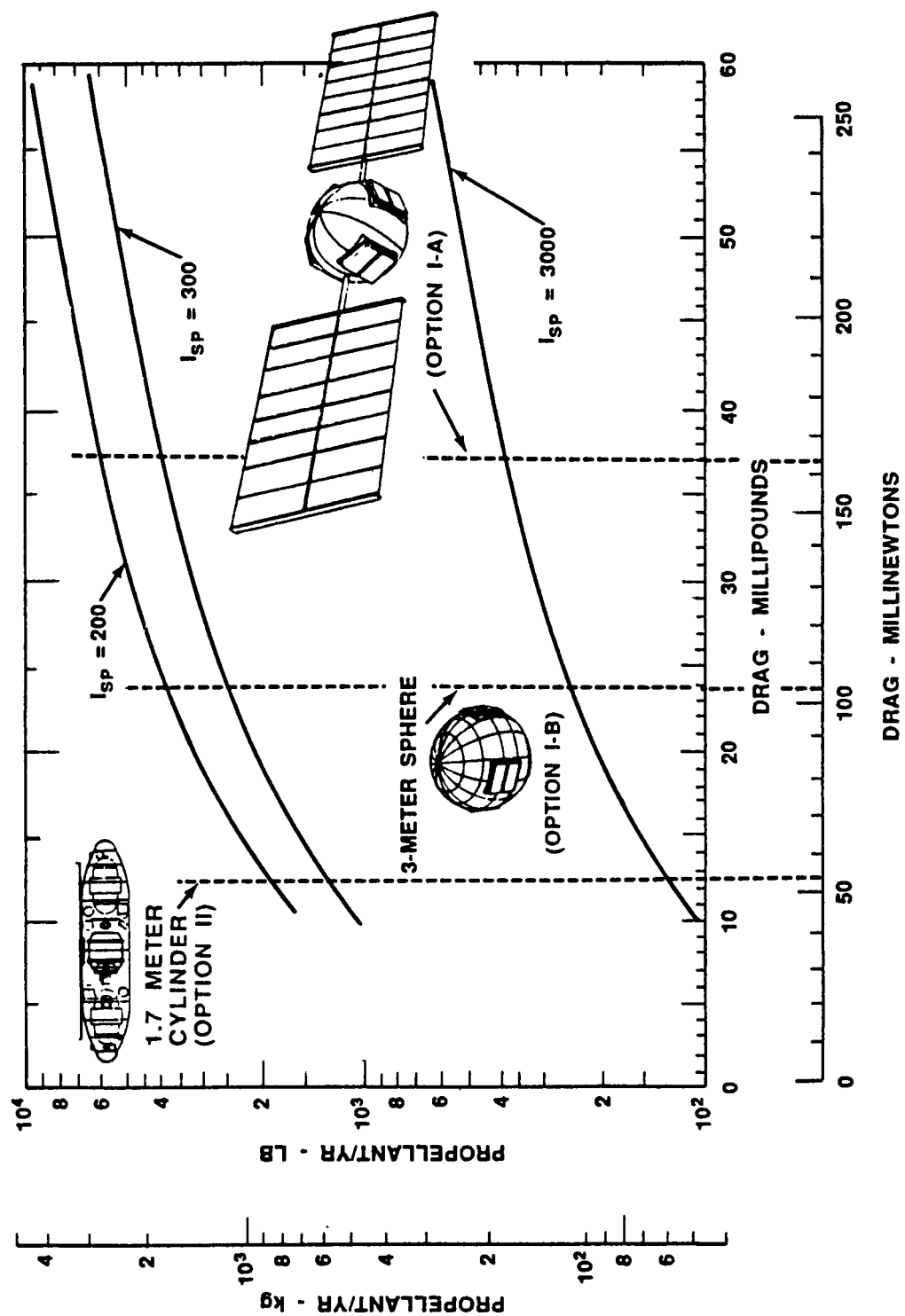


Figure 4-20. Propellant requirements as function of drag versus specific impulse.

However, for ion propulsion, with a nominal specific impulse around 3000 sec, the requirement is less than 140 kg year⁻¹. The figure dramatically illustrates that one pays a penalty in propellant required, both in weight and volume, for low performance.

A variety of working fluids are available but the selection was narrowed to argon or xenon since they are inert, readily available, and non-contaminating. Xenon was selected based on previous work with the Solar Electric Propulsion System (SEPS), which would use it as the working fluid [107]. The propulsion system consists of propellant tanks, distribution system, power processor, gimbal systems, and two ion thrusters. The gimbal system is assumed to be capable of a 45-deg square pattern and would allow the resultant thrust to act through the center of mass. This represents a first approximation of the system needs. Changes due to more refined drag estimates, atmospheric variation, or the like, could be taken into account by either increasing thrust or opening the gimbal angle. The nominal thrust was based on a drag force of 168 mN (see Appendix F). Each ion thruster is therefore sized at 0.085 N.

Figure 4-21 shows the required xenon propellant for a six-month mission and the volumetric penalty as a function of the thruster specific impulse. The data is based on an ideal gas, initial storage pressure of 24.15 MPa, and no residuals. As a first approximation, an I_{sp} of 3000 sec was assumed and results in two 0.41-m diameter tanks containing a total of 90 kg of xenon. The effect of the 45-deg thruster offset is included in the propellant requirements. Two tanks were used to maintain

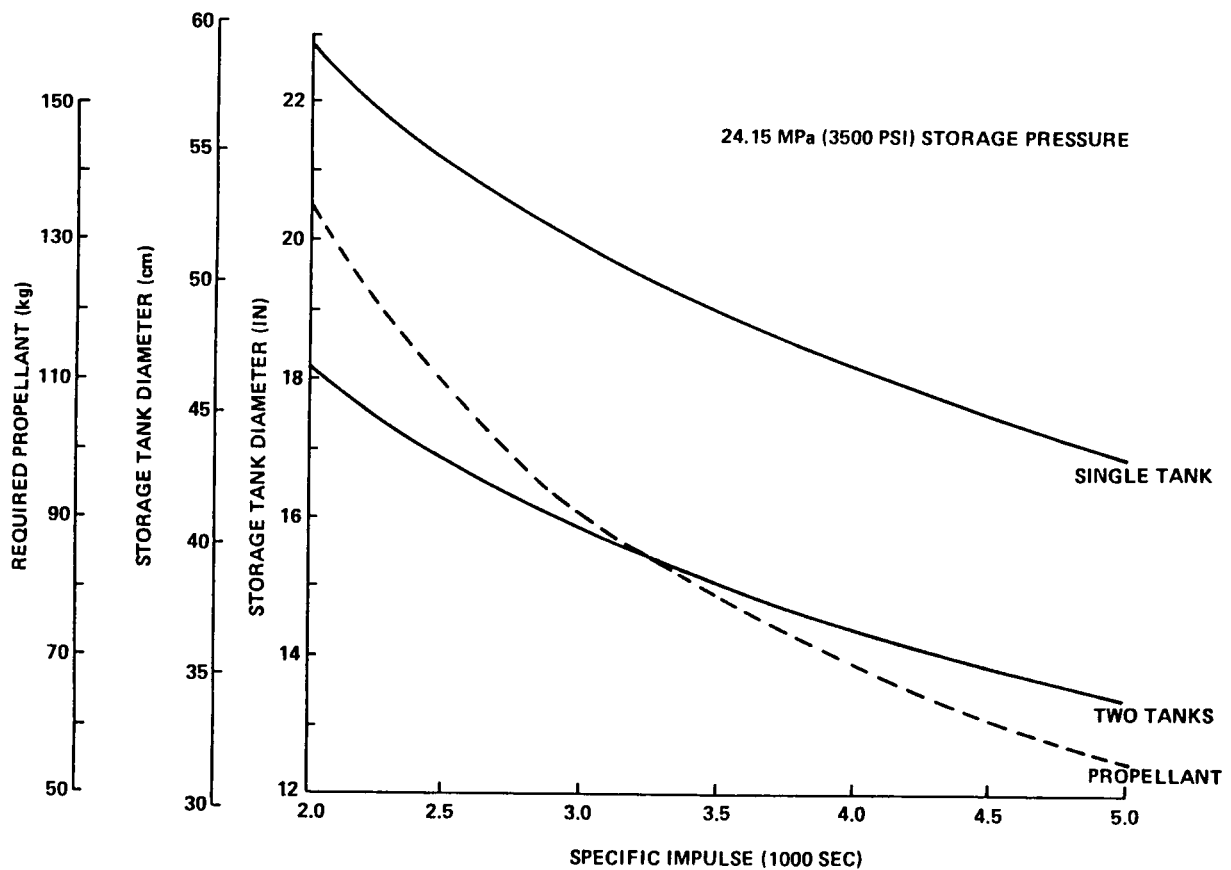


Figure 4-21. Required xenon propellant for six-month mission and volumetric penalty versus specific impulse.

equal mass distribution during depletion of the propellant. The xenon propellant is initially stored at 24.15 MPa and regulated to 68.9 kPa.

Only two ion thrusters were used in order to minimize the solar array size, and, with proper placement, it appears possible to compensate for drag for any of the spacecraft orientations postulated. Several ion thrusters, which would require modification to use xenon as the working fluid, now exist.

Power Subsystem: The two alternative methods considered in Option I to isolate the Experiment Module, the free-floating Experiment Module and the soft-mount approach, have different requirements for the power subsystem. The MMS power system module would be utilized for power conditioning and distribution in either case.

One of the major concerns in the free-floating Experiment Module alternative is the transmission of electric power to the Experiment Module. Three approaches were considered. The first utilized a microwave signal, which would require accurate positioning, along with dual transmitters and receivers to eliminate acceleration due to transmission.

The second approach would be to capture and latch the Experiment Module during one orbit every eight hours or so to recharge batteries, that would have to be mounted on the Experiment Module. This alternative has the disadvantages of requiring batteries mounted on the dewar shell, heat dissipation problems, and less scientific data. A block diagram of the Experiment Module to spacecraft interface for microwave power transmission and a summary of the power requirements for each alternative is shown in Figure 4-22.

The option of utilizing microwave transmission of power across the gap to the Experiment Module is complex and most likely costly. A third approach, and one that should be investigated in detail in future studies, would use a simple flexible cable system. However, this would require that the forces produced not saturate the control system. This should be studied as part of future control system simulation efforts (see Appendix G and section 7.1.3).

For the soft-mounted approach, the electrical power requirements for the SGG instrument and supporting subsystems, including losses, but not including the propulsion subsystem requirements, is estimated to be approximately 710 W. The power requirements for the propulsion subsystem is considered separately.

The xenon ion thruster performance is shown as a function of beam current and input voltage in Figure 4-23. The preliminary propulsion analysis indicated that a thrust level of about 0.085 N is desired. One must consider the specific impulse, beam current, and input voltage in order to optimize the system. Also included in Figure 4-23 are the beam current and maximum beam current for a 30-cm ion engine versus specific impulse. A design point at 60 percent maximum operating current has been selected. This corresponds to a power requirement of 1800 W per engine. Figure 4-24 is a simplified power flow diagram of the system. The portion enclosed by the dashed lines in the figure is an MMS provided power system used to process the power. Efficiencies associated with the generation, distribution, processing, and storage of energy are shown within parentheses in the flow diagram boxes.

Electrical power is obtained through solar arrays. To achieve the six-month mission at an altitude of 200 km, an end of life (EOL) solar array performance, capable of producing 5900 W, is required. Radiation degradation of the solar arrays at

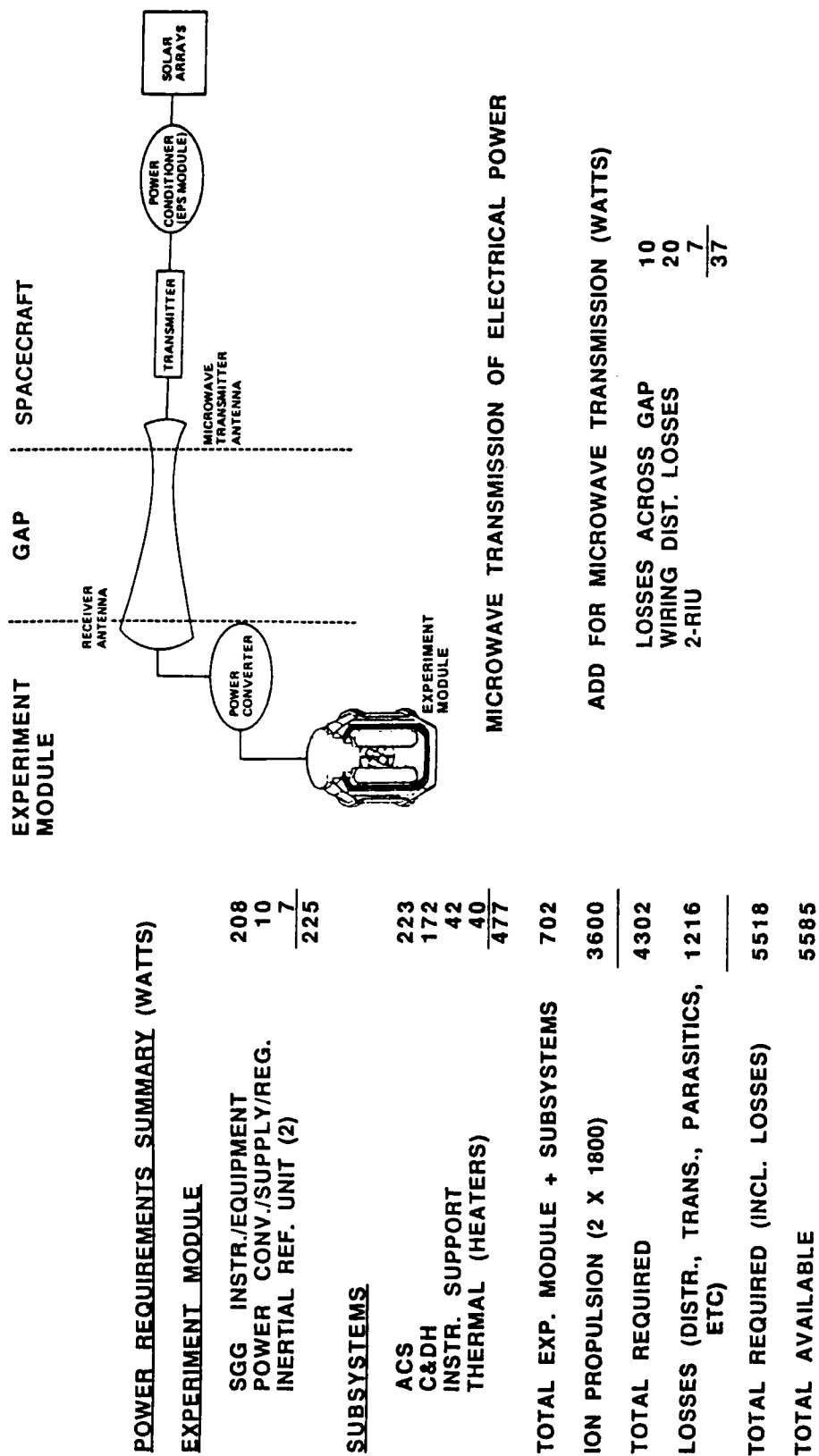
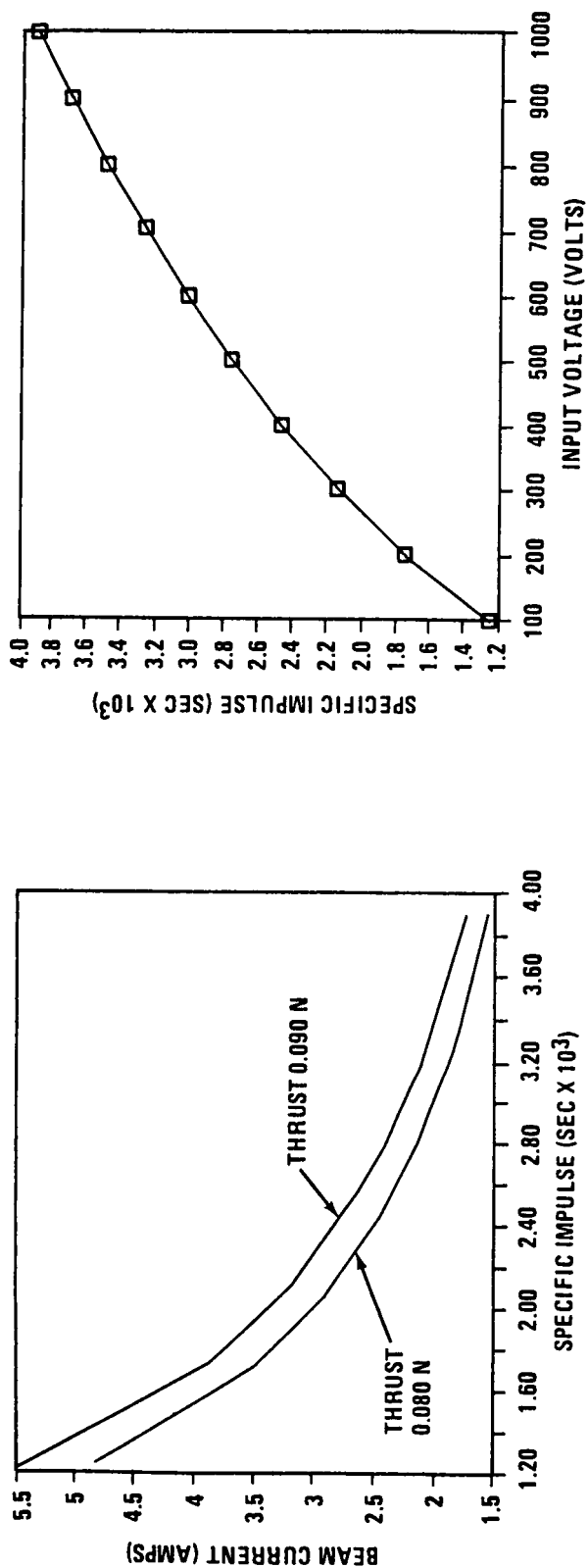


Figure 4-22. Power transmission block diagram and requirements for free-floating Experiment Module option.



(0.085 N THRUST LEVEL)

ISP (SEC)	POWER (WATTS)	BEAM CURRENT (J _B) (AMPS)	MAX BEAM CURRENT (J _B MAX) (AMPS)	J _B / (J _B MAX) (%)
3100	1600	2.06	2.15	96
3294	1700	1.94	2.58	75
3487	1800	1.83	3.07	60
3681	1900	1.74	3.61	48
3875	2000	1.65	4.21	40
4069	2100	1.57	4.87	32
4262	2200	1.5	5.60	27
4456	2300	1.44	6.40	22

Figure 4-23. Xenon ion thruster performance.

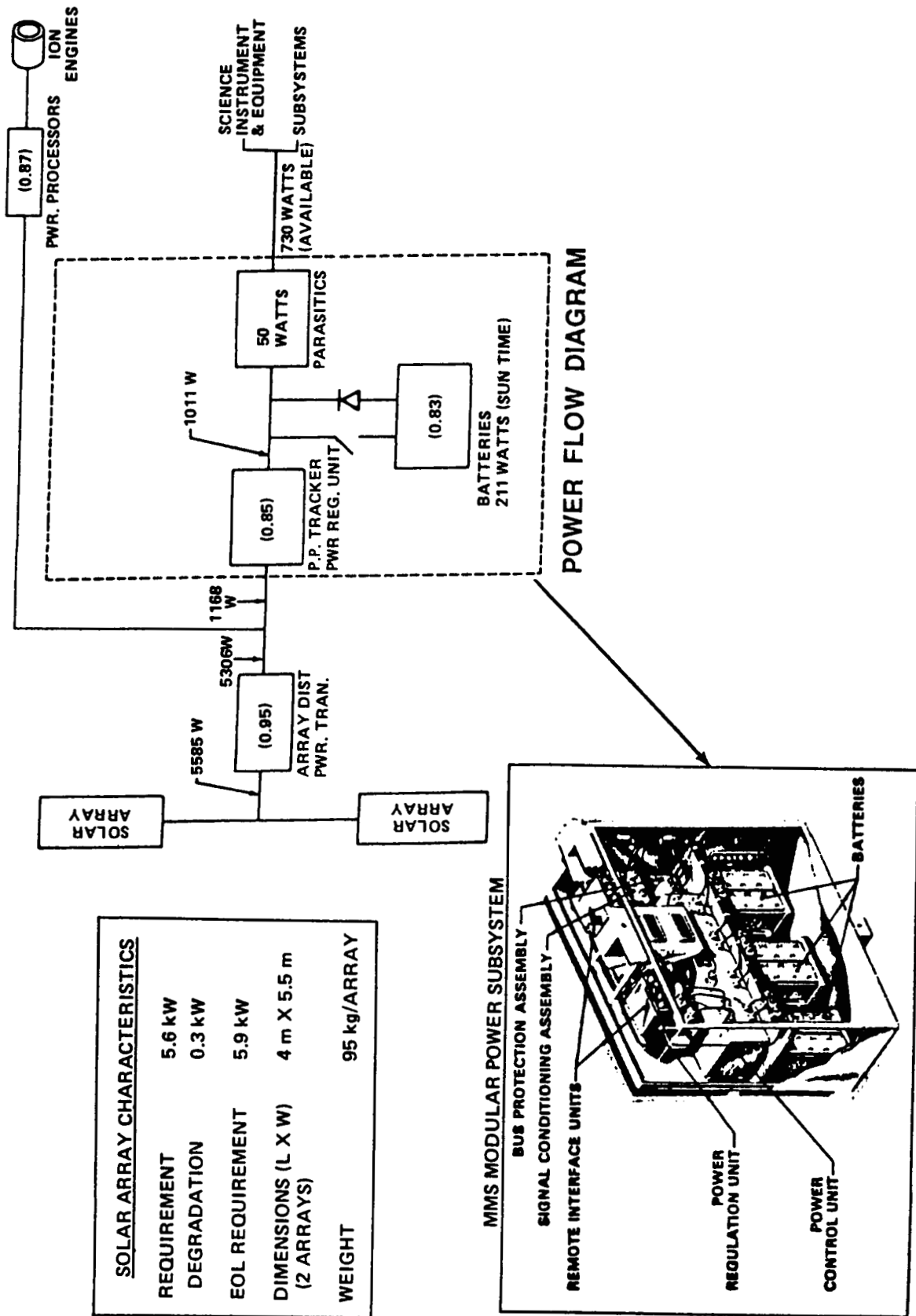


Figure 4-24. Option I-A power flow diagram and requirements.

200-km altitude was included. A solar array similar to the Solar Array Flight Experiment (SAFE) array, flown on the Shuttle, was used to estimate the size and weight of the array. Characteristics for this solar array are shown in Figure 4-24. One should note that the large arrays would introduce vibrations. This was not analyzed in this study, and must be considered if this option is pursued.

Thermal Control: The primary task in the thermal control design was to analyze a passively-controlled system, utilizing selective surface coatings, multilayer insulation (MLI), and strip heater elements. All heat generated on the Experiment Module, dewar dewar shell, and the spacecraft must be rejected with a minimum amount of soak-back to the dewar surface. This is necessary to minimize helium boiloff.

A computer model was used to determine the solar, albedo, and IR heat fluxes on the exterior surface of the spacecraft. The exterior module radiator panels are mounted parallel to the Sun's rays, thus enhancing the heat rejection capability, and to eliminate problems associated with Sun shadowing effects. The capacitance per unit area and the power per unit area were used for the transient orbital analysis of each module radiator panel, to determine the maximum and minimum temperatures of the panels. A cold bias design assures adequate margin in the hot case; however, it requires additional heater power. It was assumed that the MLI on the Sun side of the spacecraft would provide near adiabatic conditions.

Figure 4-25 lists the heat rejection requirements for the four MMS modules and for the SGG instrument. All subsystem components were designed to remain within an operating temperature range between 4° and 32°C.

Figure 4-25(a) shows a view of the spacecraft facing the Sun from behind the Experiment Module/spacecraft. Cold bias is achieved by mounting the modules on the vehicle parallel to the Sun, and through selective coating of the radiator surfaces. Symmetric mounting of the modules results in environmental heating loads that are the same for all modules over an entire orbit. By using either striped tape or optical paints, the radiator surfaces provide minimum heater power, while maintaining the module components within required temperature limits. The MLI on the interior surface of each module will minimize heat soak-back into the spacecraft.

Figure 4-25(b) illustrates the various factors associated with the Experiment Module thermal model. The spacecraft is influenced by the three external heat fluxes (solar, IR, and albedo) and the IR flux from the Experiment Module electronics. MLI with an external layer of beta cloth ($\alpha = 0.15$, $\epsilon = 0.8$, where α is the absorptivity and ϵ the emissivity, respectively) is placed on the Sun side of the spacecraft. The back exterior side of the spacecraft is coated with a high emissivity paint ($\epsilon = 0.9$). The interior spacecraft surface is coated with identical paint. With the back of the spacecraft radiating continuously to deep space, a cold sink temperature for the Experiment Module electronics can be provided.

The Experiment Module is shielded from incident environmental Earth and solar fluxes by the spacecraft. Heat generated by the Experiment Module electronics would be conducted to radiator panels, and radiated to the interior surface of the spacecraft.

Figure 4-25 lists the temperature ranges during one orbit, for the subsystem modules. The C&DH and ACS modules require low solar absorption and high IR emittance at all times, because of the 172 W and 223 W of heat generated, respectively. The EPS and Instrument Support Modules require a much lower emissivity due to the smaller heat loads.

<u>SUBSYSTEM MODULE</u>	<u>SELECTIVE COATING</u>	<u>RADIATOR PANEL</u> <u>TEMP. (CELSIUS)</u>
ABSORPTIVITY (α)	EMISSIVITY (ϵ)	
CDH	0.12	15-18
EPS	0.12 0.12	18-21 4-7
ACS	0.12	21-24
INSTRUMENT FUNCTIONS (MISC.)	0.12 0.12	18-24 4-7

Figure 4-25. Thermal control model and requirements.

Figure 4-26 is a plot of the heat flux through the front face of the MLI versus required thickness. The flux is based on an interior wall temperature of -42°C , and exterior equilibrium temperature of 49°C . The nominal MLI conductivity of $9 \times 10^{-4} \text{ W m}^{-1} \text{ }^{\circ}\text{C}^{-1}$ would require approximately 10 cm of insulation. This thickness would allow only 95 W m^{-2} to be conducted through the inside wall. The majority of the heat that reaches the interior surface would be radiated to the back wall of the spacecraft.

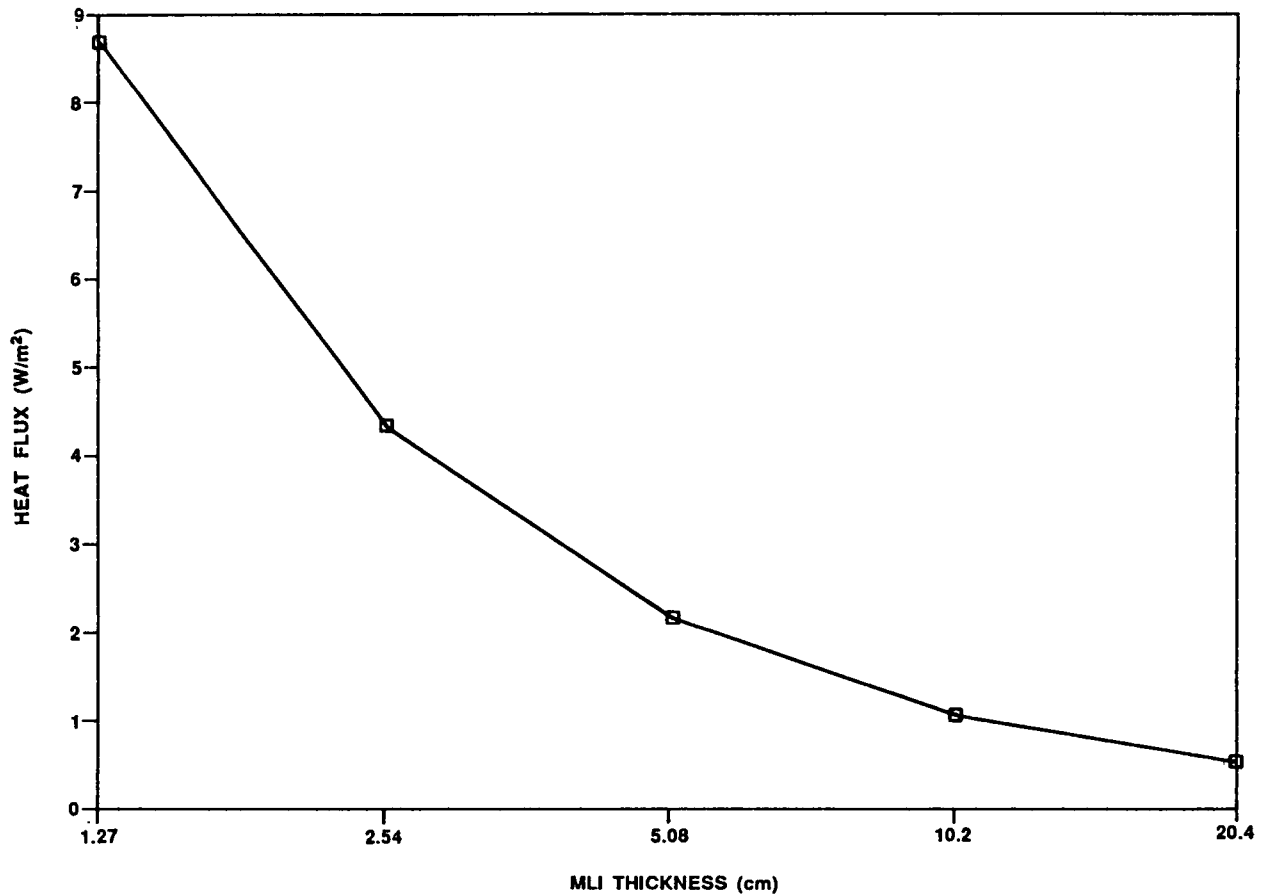


Figure 4-26. Heat flux through front face of MLI versus insulation thickness.

Figure 4-27 illustrates the required radiator area for the Experiment Module electronics as a function of the average spacecraft interior wall equilibrium temperature. With an average temperature of -42°C on the spacecraft interior surface and an average radiator temperature of 21°C , approximately 45.5 cm^2 surface area is required for each of the two panels.

Table 4-5 lists the weight and heater power requirements for this option. A total weight of 231 kg, including MLI, radiator panels, and liquid helium, will provide passive thermal control. The strip heater elements would require 42 W of peak power to maintain the electronics within the required temperature range.

The thermal analysis indicates that the thermal control is feasible and within available technology. Selective coatings of the Experiment Module will optimize

DEWAR ELECTRONICS CONTROL

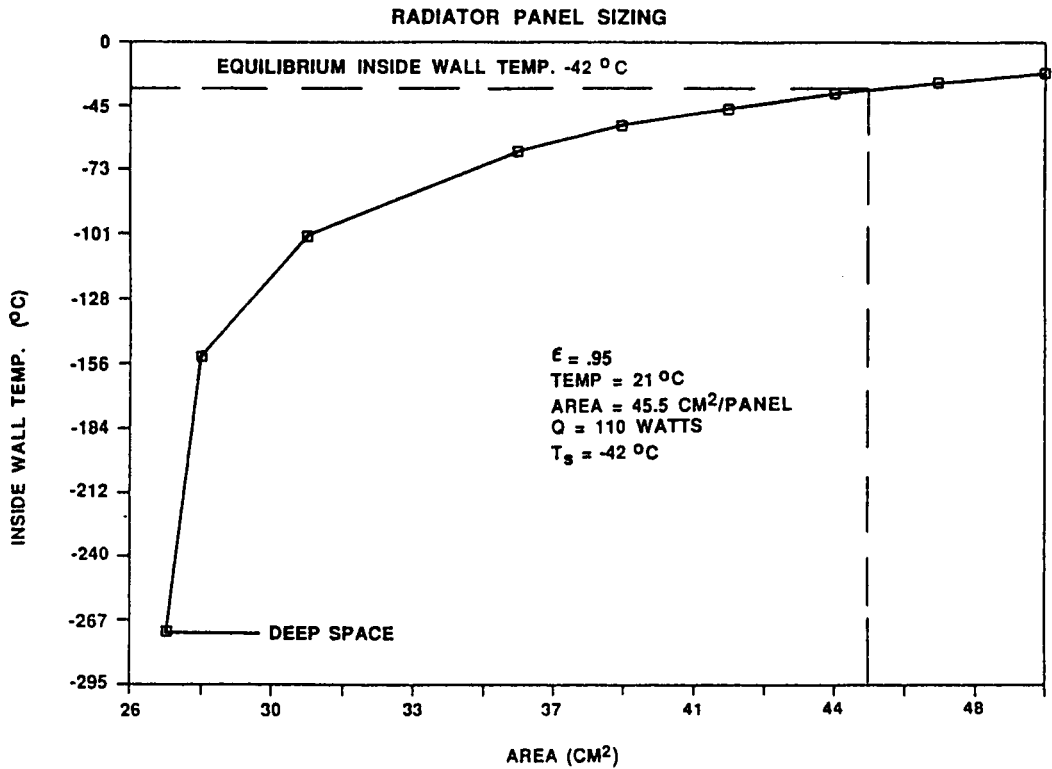


Figure 4-27. Required radiator area for removal of heat generated by Experiment Module electronics.

TABLE 4-5. WEIGHT AND POWER REQUIREMENTS FOR THERMAL CONTROL

	<u>WEIGHT (kg)</u>
FRONT FACE MLI (1.6 cm)	154
MODULES MLI	35
RADIATOR PANELS (DEWAR)	6
LIQUID HELIUM	36
TOTAL	360

	<u>POWER REQUIREMENT (WATTS)</u>
ACS	15
EPS	10
ACS	10
CDH	5
LOSSES (5%)	2
TOTAL	42

thermal control. The heat generated by the electronics mounted on the dewar shell can be removed radiatively to the interior wall of the spacecraft, and the heat generated within the dewar can be removed to allow the instrument to remain at superfluid helium temperature.

Communications and Data Handling Subsystem: An examination of the expected data requirements indicates that the highest data rates will be from the six accelerometer outputs. Temperature, pressures, and helium housekeeping measurements will only be a small percentage of the total data required, as shown in Table 4-6. The total anticipated rate of approximately 43 kb sec^{-1} is easily managed by the data system.

The C&DH subsystem, like the power subsystem, will require different designs for a free-floating or soft-mounted Experiment Module. The MMS module for C&DH is used as a central processor in both alternatives. Figure 4-28 shows a block diagram of the free-floating approach. A small, low-power unit would be mounted on the Experiment Module which gathers, formats, and transmits the data to an interface unit mounted nearby, via either an RF or optical link. The data would then be fed to the data bus of the C&DH module, and either recorded or downlinked through TDRSS. Commands for control would follow the reverse of this path. The elements within the dashed line in the figure would be contained in the MMS module.

For the soft-mounted approach, the elements within the double dashed lines of Figure 4-28 will not be required. Connection is made with the Experiment Module through an interface unit mounted near the dewar and linked through flexible conductors to the instrument. Table 4-6 also lists the equipment required for the C&DH subsystem. Note that redundancy is included for many of the components.

In general, the C&DH subsystem design is straightforward for the soft-mounted approach and no major problems were found. However, if the Experiment Module is to be floated within the spacecraft, additional analysis must be done.

4.3.2 Option I-B: Hydrazine Propulsion

This concept, illustrated in Figure 4-19, would utilize a hydrazine propulsion system similar to that designed for the GRM. One notes from the figure that the various components have been symmetrically placed since the center of mass must be located as near as possible to the SGG. For the actual design, however, additional mass compensation will most likely be required and movement of masses must be minimized.

Since hydrazine propulsion systems do not require high electrical power, the large solar arrays needed for the ion propulsion option are unnecessary. Instead, the power would be provided by body-mounted solar cells. In addition to the advantage of utilizing a propulsion system that enjoys a wealth of experience in space, elimination of the solar arrays significantly reduces atmospheric drag (see Appendix F) and eliminates problems associated with mechanical vibrations of the arrays.

Many of the subsystem requirements for this option are the same as those of Option I-A and will not be repeated here. The C&DH, ACS, and, to some extent, the EPS remain the same. The thermal environment is changed somewhat, because of the presence of the body-mounted solar cells, but can be readily controlled. The weight for this option is summarized in Table 4-4.

TABLE 4-6. C&DH REQUIREMENTS AND CHARACTERISTICS

DATA SYSTEM REQUIREMENTS

<u>SIGNAL NUMBER</u>	<u>FREQ. RANGE (Hz)</u>	<u>SAMPLE RATE/SEC.</u>	<u>BIT RATE/SAMPLE</u>	<u>TOTAL BITS/SEC</u>
DM OUTPUTS (3)	10	40	16	1920
CM OUTPUTS (3)	10	40	16	1920
ACC. OUTPUTS (6)	100	400	16	38400
TEMPERATURES (6)	1	4	16	384
PRESSURES (3)	1	4	16	192
HELIUM QUANTITY	1	4	16	64
HELIUM BOILOFF	1	4	16	64
HELIUM SLOSHING	1	4	16	64
				<hr/>
				43008
INSTRUMENT COMMANDS (10)	DISCRETE	-	-	-
SUBSYSTEM COMMANDS (15)	DISCRETE	-	-	-

COMMUNICATIONS AND DATA HANDLING
EQUIPMENT LIST

<u>C&DH MODULE COMPONENTS</u>	<u>QUANTITY</u>	<u>WEIGHT kg</u>	<u>AVG. POWER (WATTS)</u>	<u>VOLUME (cm)</u>
TRANSPONDER	2	12.8	36	
COMPUTER	1	17.1	103.6	
PRE-MOD PROCESSOR (PMP)	1	6.7	7.5	
CENTRAL UNIT	2	7.0	26.3	
RIU	2	5.0	7.5	
EXPANDER UNIT	1	1.1		
POWER CONTROL UNIT (PCU)	1	5.8	7	
BAND-PASS FILTER	2	0.5		
DIPLEXER	2	0.8		
R.F. SWITCH	3	0.7		
BUS COUPLER UNIT	1	0.2		
TAPE RECORDER	2	13.8	15.3	
TIME TRANSFER UNIT	2	4.5	7	
EXTERNAL OSCILLATOR	2	2.7	15.6	
THERMAL CONTROL	1 SET	16.7		
STRUCTURE & ELECT HARNESS	1 SET	61.2		
SUBTOTAL (MODULE)		156.6	225.8	122 X 122 X 46
<u>EXTERNAL COMPONENTS</u>				
RF POWER AMP	2	10.8	3	20 X 18 X 5 (EA)
OMNI ANTENNA	2	0.5		15 X 10 X 8 (EA)
H.G. ANTENNA (ESSA)	2	59.4		76 cm DIA SPHERE
ANTENNA CONTROLLER	2	9.0	40	31 X 23 X 23 (EA)
EXP. COMPUTER/MPX	1	4.5	10	15 X 10 X 5
INTERFACE UNIT	1	2.2	4	15 X 25 X 8
EXP. XMTR/RCVR	4	0.9	3	8 X 13 X 5 (EA)
TOTALS		243.9	285	

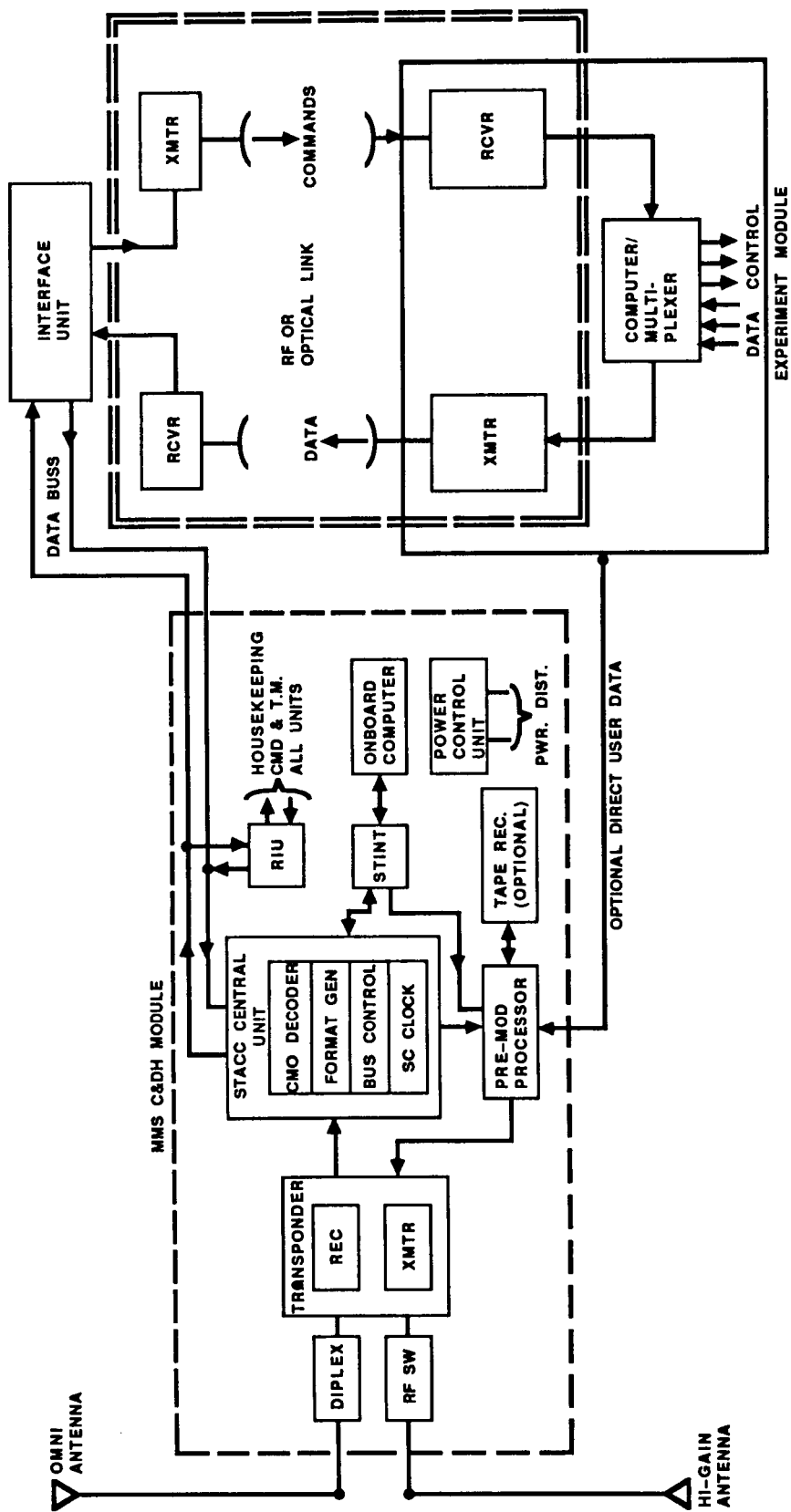


Figure 4-28. C&DH management system using MMS.

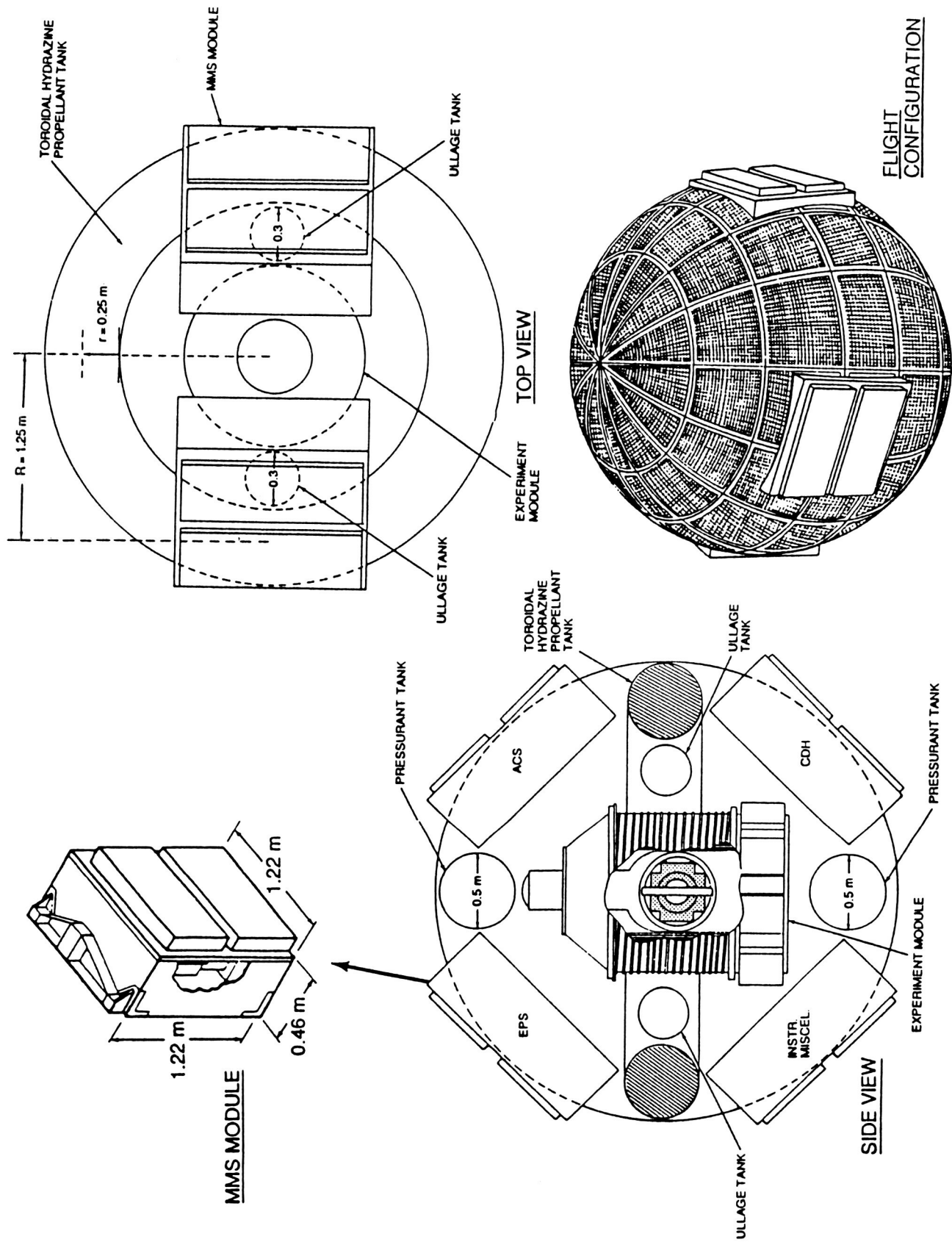


Figure 4-29. Option I-B (hydrazine propulsion) spacecraft configuration.

Propulsion Subsystem (Hydrazine): Although the propulsion subsystem is similar to GRM, the thrusters would have to be smaller. Moreover, and most importantly, an analysis must be made to determine if a steady-state or pulsing mode can meet the SGGM requirements. From Figure 4-20, one notes that the hydrazine propellant ($I_{sp} \sim 200$ sec) required for a 3-m sphere (which has a nominal drag force of 100 mN) would be a little less than 1000 kg for a six-month mission. To provide adequate margin, a propellant capacity of 1500 kg was selected. A toroidal tank with a diaphragm or flexible bag inside the metal tank could be utilized to equalize propellant throughout the tank, as the propellant is consumed. Spherical propellant tanks were considered, but were rejected, since this would have required enlarging the spacecraft diameter to about 4 m. A toroidal tank tends to distort into a "figure-eight" configuration when pressurized. However, this can be easily overcome by judiciously selecting the location of the attach points for the structural members that secure the tank to the spacecraft. Two 0.5-m pressurant tanks (2000 kPa) are included to pressurize the fuel and two 95-kg ullage tanks are added to accommodate any fuel overflow caused by thermal expansion. The GRM propulsion system, and its possible adaptation to the SGGM, is discussed in more detail in Section 4.4.1.

Power Subsystem: Electrical power is provided by body-mounted solar cells. Since, for a spherical surface, the effectiveness of the cells in converting the solar energy to electrical power will vary as the cosine of the angle to the Sun. Only about 25 percent of the cells covering the spacecraft will be effective, i.e., about an area of about 7 m^2 for the 3-m diameter spacecraft. Gallium arsenide cells would provide about 1250 W and would meet the 1100-W requirement (including losses) for this concept.

4.3.3 Summary

The advantages and disadvantages of Options I-A and I-B are summarized in Table 4-7. The two concepts differ primarily in the propulsion system assumed and the electrical power required. The spacecraft cross sections are quite different, resulting in vastly different atmospheric drag forces, even when the solar arrays in Option I-A are flown "edge-on." This problem, and the potential for vibrations from the large solar arrays, make the ion propulsion concept (Option I-A) less attractive. For Option I-B to be considered as a viable candidate, more detailed analyses must be done to demonstrate that the hydrazine propulsion system can meet the SGGM requirements. If this problem is favorably resolved, then it would appear that Option I-B is the best approach to a spherical spacecraft configuration. This appears to be true even with the attendant weight and volume penalties.

4.4 Option II: Earth-Fixed Mode

Since this option is designed only for an Earth-fixed orbital attitude, a long cylindrical envelope would be utilized to minimize atmospheric drag. The Experiment Module that was assumed in Option I was included in this option, and established the minimum diameter of the spacecraft. After an investigation of the GRM propulsion system, it was concluded that some propulsion changes would be required, and several areas were identified for further study. The spacecraft requirements would also exceed the ACS, power, and data handling capabilities of the GRM design.

TABLE 4-7. COMPARISON OF ION AND HYDRAZINE PROPULSION SYSTEMS FOR SGGM

PROPULSION SYSTEM	HYDRAZINE	ION
<u>ADVANTAGES</u>	<ul style="list-style-type: none"> ● CURRENT STANDARD FOR SPACECRAFT AUXILLIARY PROPULSION —STATE OF ART >14 YEARS ● LOW EXTERNAL POWER REQUIRED 	<ul style="list-style-type: none"> ● HIGH PERFORMANCE —I_{sp} ~1000-3000 SEC ● LOW PROPELLANT MASS AND VOLUME REQUIREMENTS ● LOW, CONTROLLABLE THRUST LEVELS ● INERT GAS PROPELLANT
<u>DISADVANTAGES</u>	<ul style="list-style-type: none"> ● RELATIVELY LARGE PROPELLANT MASS AND VOLUME REQUIRED ● LOW PERFORMANCE —I_{sp} ~300 SEC ● NOT CLEAR THAT THRUST CAN BE CONTROLLED AT LEVELS REQUIRED BY SGGM 	<ul style="list-style-type: none"> ● MASSIVE EXTERNAL POWER REQUIRED (~FACTOR OF 6 OVER HYDRAZINE FOR SGGM) ● LARGE SOLAR ARRAYS —INDUCED VIBRATIONS —ADDITIONAL ATMOSPHERIC DRAG ● APPLICATIONS HAVE BEEN MINIMAL —FLOWN AS EXPERIMENTS EXCEPT TWO US PRODUCED OPERATIONAL SPACECRAFT (NOVA AND INTELSAT V) ● TECHNOLOGY ADVANCES REQUIRED

4.4.1 Option II-A: Cylindrical Spacecraft

The spacecraft configuration, shown in Figure 4-30, is that of a 1.7-m diameter cylinder, 8.2 m in length. This cross section has an average atmospheric drag about a factor of 3 lower than Option I-A. The configuration shown in the figure includes a schematic representation of the instrument isolation technique, utilizing the free-floating Experiment Module, as discussed in Section 4.2.1. On the Sun side of the spacecraft, a 1.7-m x 6.6-m x 0.025-m solar array provides the electrical power. At each end of the spacecraft, 76-cm antennas are attached. The weight summary for this option is tabulated in Table 4-8. The moments of inertia shown in the Table were referenced from the center of the shell structure.

The major concern in this configuraiton, like that of Option I, is the ACS. The thermal, power, and C&DH designs are straightforward, and no problems in developing these subsystems are anticipated.

Spacecraft Control: The ACS system was discussed in Section 4.2.2. The IRU will provide attitude information and will be updated with the navigation sensors. Magnetic torquers along with the magnetometer will provide momentum management.

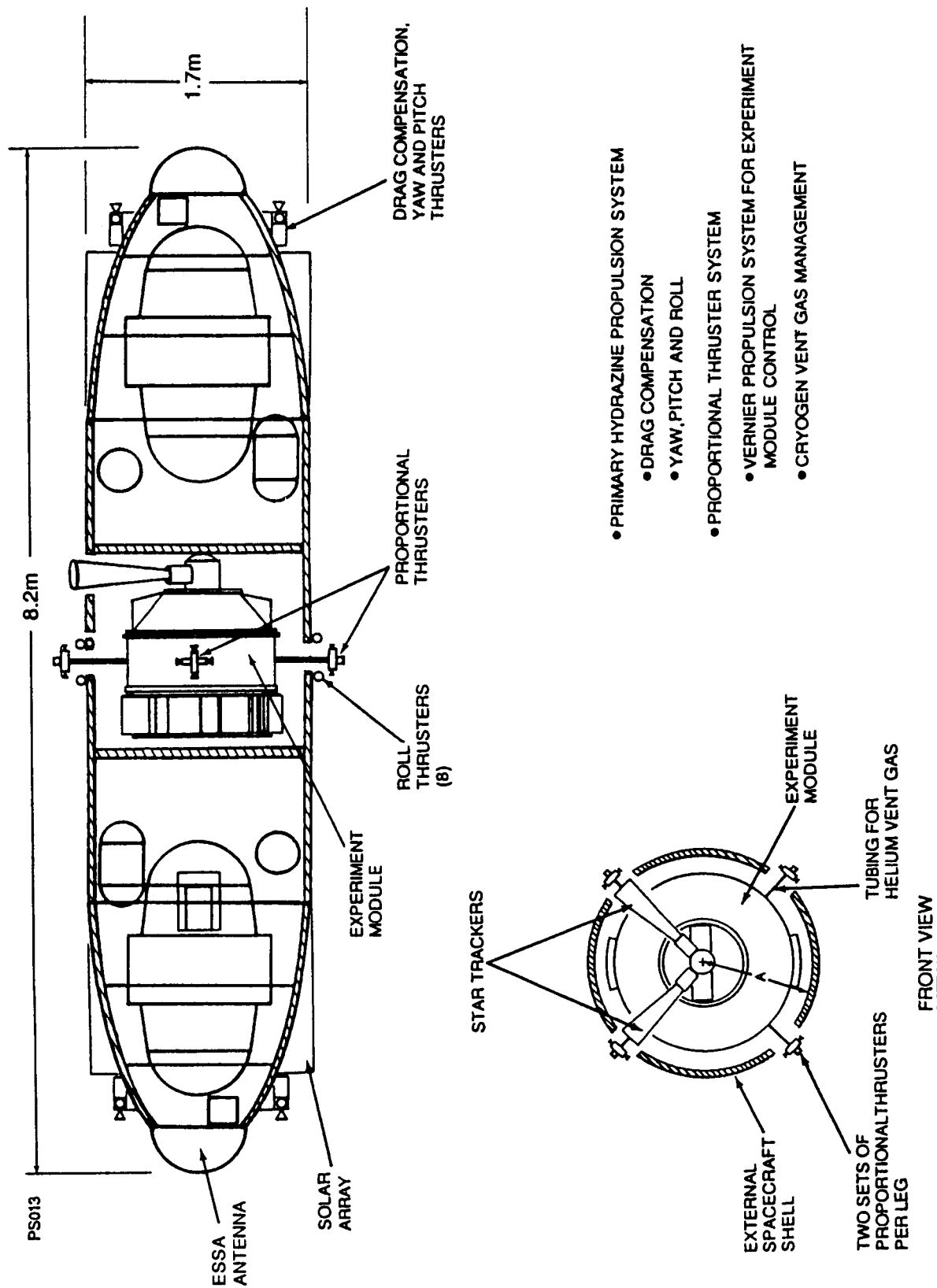


Figure 4-30. Option II-A (Earth-fixed only) spacecraft configuration.

TABLE 4-8. OPTION II-A WEIGHT SUMMARY

	(kg)
SGG INSTRUMENT*	100
DEWAR	176
INSULATION/THERMAL CONTROL	113
OUTER SHELL STRUCTURE	998
ATCH. STRUCTURE/BRKTS & HARDWARE	172
SOLAR ARRAY	58
EPS	56
WIRE HARNESS	25
INSULATORS & DISTRIBUTION	12
C&DH	36
C&DH EXT. (ANT, CNTRL, & PWR AMP)	88
R.F. CONTAINER & HARNESS	6
PROPULSION SYS. (DRY)	307
ACS	200
MECHANISMS	22
GROWTH/CONTINGENCY (5% & 15%)**	259
SUBTOTAL DRY	2628
PROPELLANT*	1397
PRESSURANT (He)*	11
HELIUM (DEWAR)*	36
TOTAL	<hr/> 4072

NOTES:

* NO CONTINGENCY ON THESE ITEMS.

** 5% CONTINGENCY ON ALL AVIONICS, ELECTRICAL POWER, AND PROPULSION SYSTEMS.

15% CONTINGENCY ON ALL NEW STRUCTURES AND THERMAL CONTROL.

Reaction wheels will be used for attitude control. Alignment is required between the external navigation base and the SGG, to maintain the strict pointing required for the instrument.

An analysis was made to examine the expected response of the spacecraft to an on-off Reaction Control System (RCS) using hydrazine thrusters. The plots shown in Figure 4-31 illustrate, to first order, the spacecraft translation and attitude acceleration per RCS firing, and the incremental angular rate for a given minimum "thruster-on" time. Existing hydrazine thrusters have a minimum thrust level capability of about 178 mN. Based on average aerodynamic forces, the drag compensation thrust required is about 53 mN (see Appendix F), which is less than the minimum RCS thrust. The GRM thrusters were designed for a thrust level of 1.11 N. The translational acceleration curve shows that, at this thrust level, the spacecraft will experience acceleration levels between 10^{-5} and 10^{-6} g. The corresponding angular acceleration levels would be between 1 to tens of arcsec sec^{-2} , respectively. Finally, for a minimum of 40 msec with the thrusters on, the body rate would be between 0.1 to several arcsec sec^{-2} .

In summary, additional refinements will have to be made through more thorough analyses to determine whether the performance of the baseline ACS is adequate. These analyses should consider reaction control wheels, magnetic torquers, and possibly other means for control; an analysis of the vehicle controllability with respect to control bandwidth; closed-loop control simulations; and refined sensor requirements.

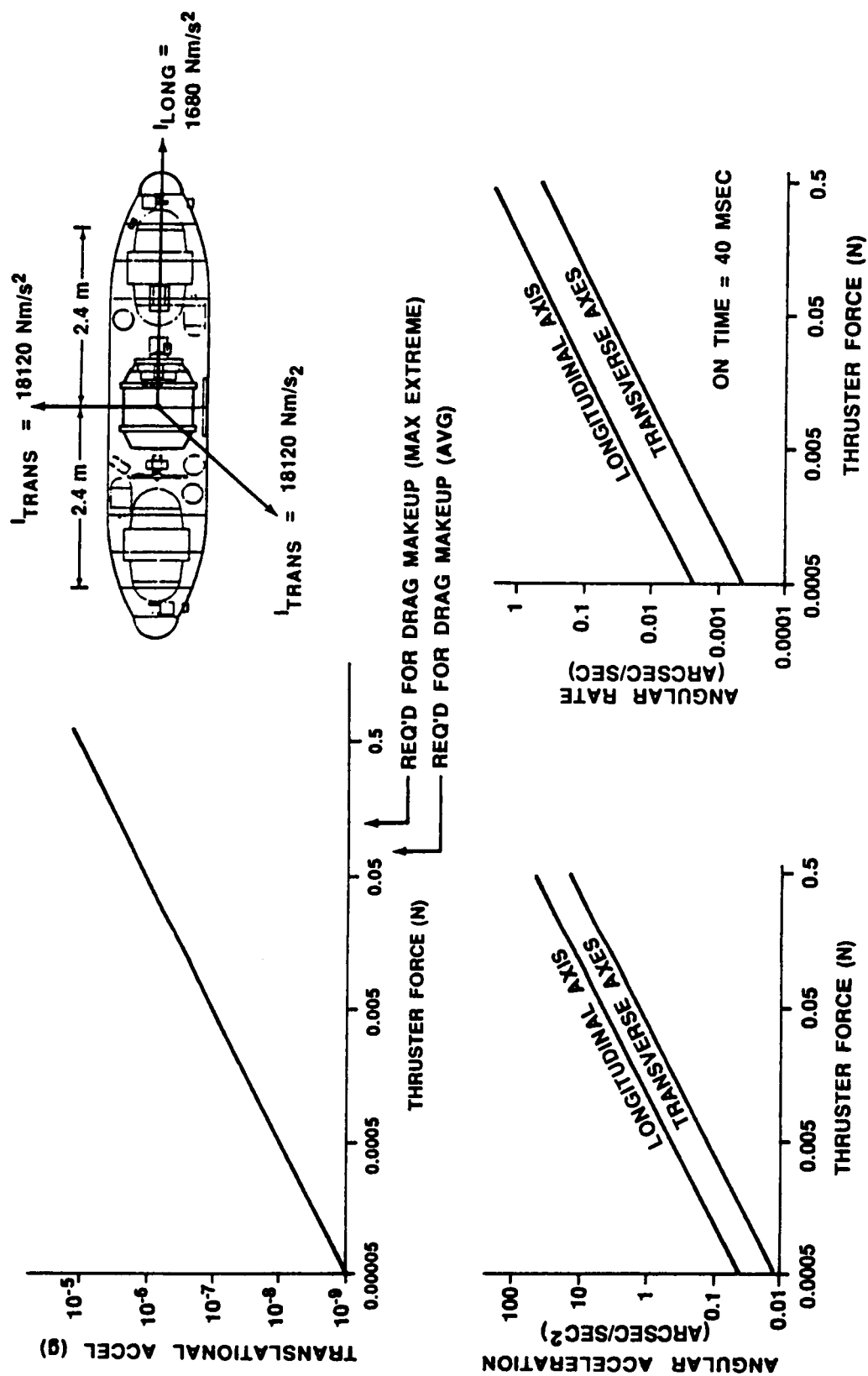


Figure 4-31. Thruster sizing impact on translational and attitude stability.

Propulsion Subsystem: An investigation was made to determine whether the GRM propulsion system was adequate, or could be readily adapted for this option. The basic GRM propulsion schematic is shown in Figure 4-32 [101]. As pointed out in the discussion above, the thrust levels of the GRM drag compensation thrusters are too high. If one replaces these nominal 4 N thrusters with 1 N thrusters, the thrust levels would be more nearly acceptable.

By considering a pulsing mode, a 0.045 N sec total impulse operation could be achieved. An 8 to 20 msec pulse width can be obtained depending on the valving selected. It remains to be determined if a pulsing mode can be used.

The main propulsion tanks have metal diaphragms which will tend to minimize sloshing and permit balancing the propellant in the tanks. In addition, the location of the tanks must be equidistant from the center of mass to minimize any gravity imbalance.

Power Subsystem: Electrical power is provided by a solar array/battery system. The solar array characteristics are illustrated in Figure 4-33. The orbital beta angle varies between -90 deg and -60 deg and the maximum dark period can be limited to 16 min for a six-month mission, if the launch date is properly selected (see Section 4.1). A launch between early March and mid-October would increase the dark period and require increased battery capabilities and a larger solar array.

The array would consist of an aluminum honeycomb substrate and either advanced, high efficiency solar cells, or current technology gallium arsenide cells. Figure 4-34 includes a simplified block diagram of the power system, with efficiencies shown in parentheses, and a summary of the power requirements for this option.

C&DH Subsystem: The C&DH requirements are the same as those of Option I, summarized earlier in Table 4-6. Two 76-cm Electrically Steerable Spherical Array (ESSA) antennas are mounted at each end of the spacecraft. The ESSA antennas provide omni modes as well as several high gain modes. These antennas, which will be flown on COBE, provide full 4π Sr spatial coverage and can electronically direct a beam within a hemisphere, and thus produce no mechanical motion.

4.4.2 Option II-B: Modified GRM Spacecraft

This option was considered in order to determine if the GRM spacecraft design could be modified to accommodate the SGGM. The primary modification to the GRM spacecraft is to remove the DISCOS, which occupies a 0.5- by 1.0-m cylindrical volume and weighs about 15 kg, and replace it with the SGGM Experiment Module. The GRM subsystems were then analyzed to determine what, if any, subsystem modifications would be required.

A major constraint of this option was an Experiment Module design that would fit within the GRM spacecraft envelope. This would require a long, relatively thin (and very inefficient) dewar, as discussed in Section 4.2.1. This is the major difficulty of this option.

It was assumed that the GRM spacecraft length could be changed to accommodate the SGGM Experiment Module, but not the diameter. (To change both dimensions would essentially repeat Option II-A, a new spacecraft design.) To include the Experiment

ORBIT

96.3 DEG INCLINATION
200 km ALT.
6 AM CROSSING

ARRAY SIZING BASED ON:

89 MIN. ORBITAL PERIOD
MAX. DARKNESS OF 16 MIN.
6 MONTH LIFE
BETA ANGLE BETWEEN -90 DEG AND -60 DEG
739 W CONTINUOUS BUS LOAD

REQUIRED AREA:

11.2 M²

DIMENSIONS (W X L X THICKNESS):

1.7 M X 6.6 M X .025 M

WEIGHT:

58 KG

BY LIMITING FLIGHT BETWEEN 3/1 AND 10/15 -
MAX. DARK APPROX. 16 MIN.

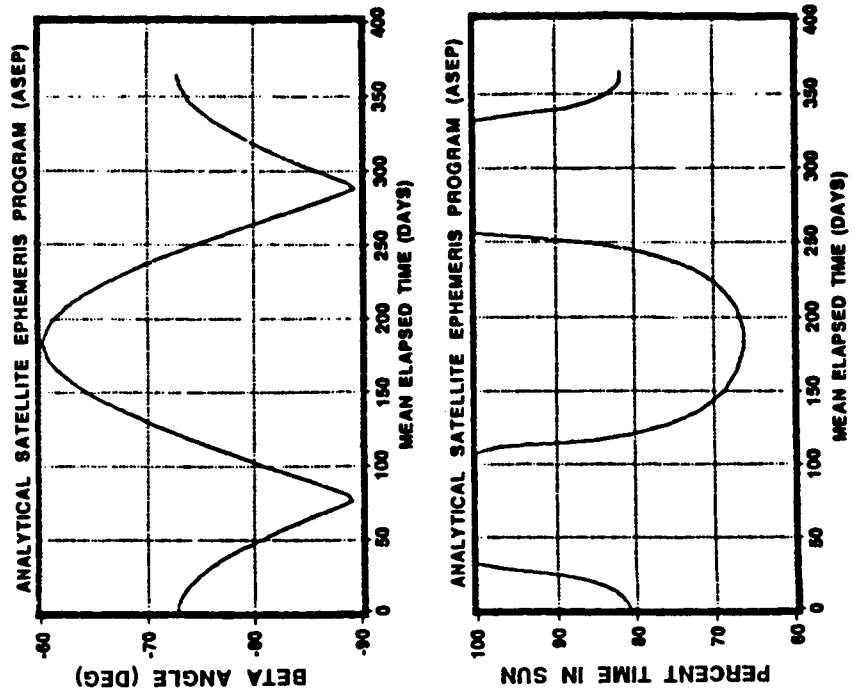
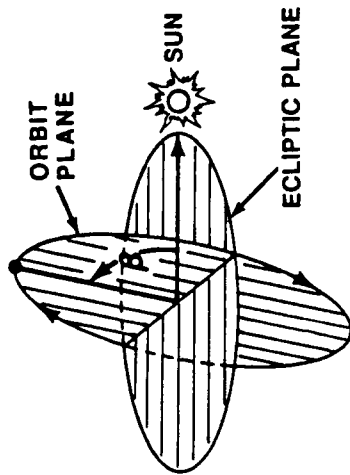


Figure 4-33. Option II-A solar array characteristics.

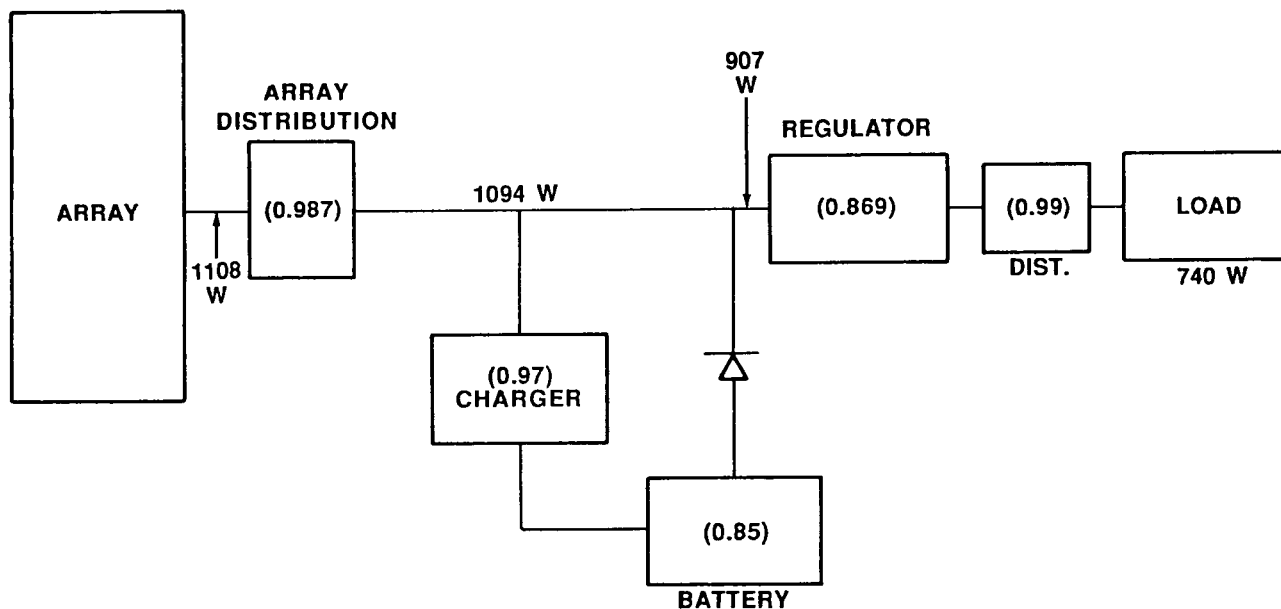


Figure 4-34. Option II-A power flow diagram.

Module and other equipment changes, the GRM spacecraft would have to be lengthened by about 2.5 m, as illustrated in Figure 4-35. Additional data handling, power, and GNC equipment would have to be included. Even with the GRM gravity and magnetic instrumentation removed, the power supplied is not sufficient for SGGM, and the solar arrays would have to be extended.

Although no detailed atmospheric drag analysis was made, drag would be increased since the cylinder lateral surface area would increase from 13 to 19 m² and the solar array surfaces would become larger. Thus, the propellant capacity would have to be increased over that designed for GRM. In addition, as discussed in Section 4.4.1, the GRM propulsion system is not adequate for SGGM.

4.4.3 Summary

For geophysics applications, either an Earth-fixed or inertial orientation would be acceptable, and Option II-A appears to be a viable option if the Earth-fixed orientation is selected. Like GRM, the cylindrical cross section, which is based on the diameter of the Experiment Module, offers a low drag profile. Isolation of the SGG by free floating the Experiment Module, in conjunction with utilizing the helium boiloff gas for vernier control of the Experiment Module, and using the six-axis accelerometer to control the spacecraft, is an attractive approach at this time.

Critical subsystems that need further study include the ACS and the hydrazine RCS. Isolation of the Experiment Module must also be studied in more detail. In-depth analyses, including a high-fidelity simulation of the control system, should be initiated. Since the spacecraft attitude rate and acceleration, altitude stability, pointing stability, and linear acceleration must all be satisfied simultaneously, a simulation is a critical element in assessing overall mission feasibility.

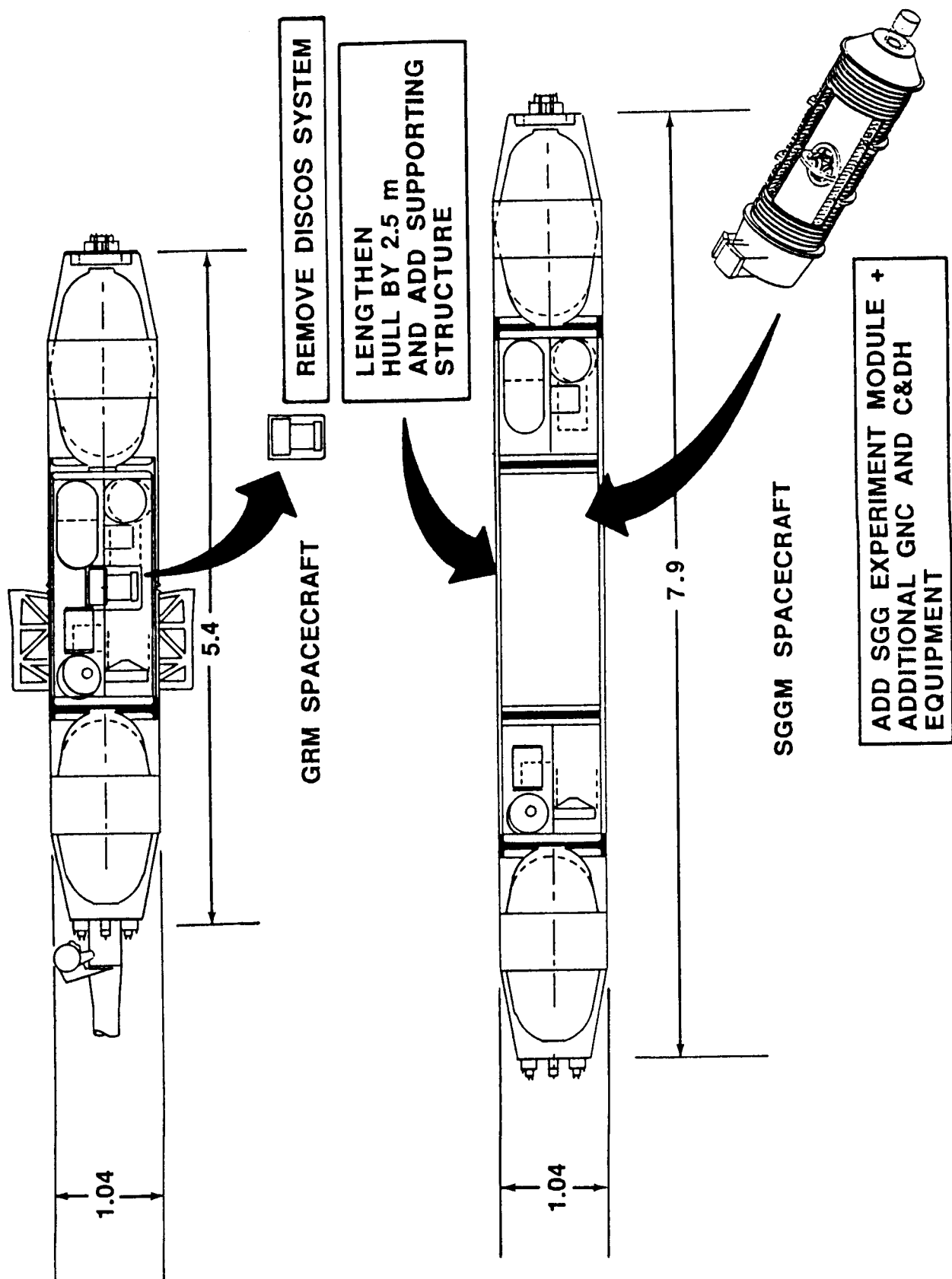
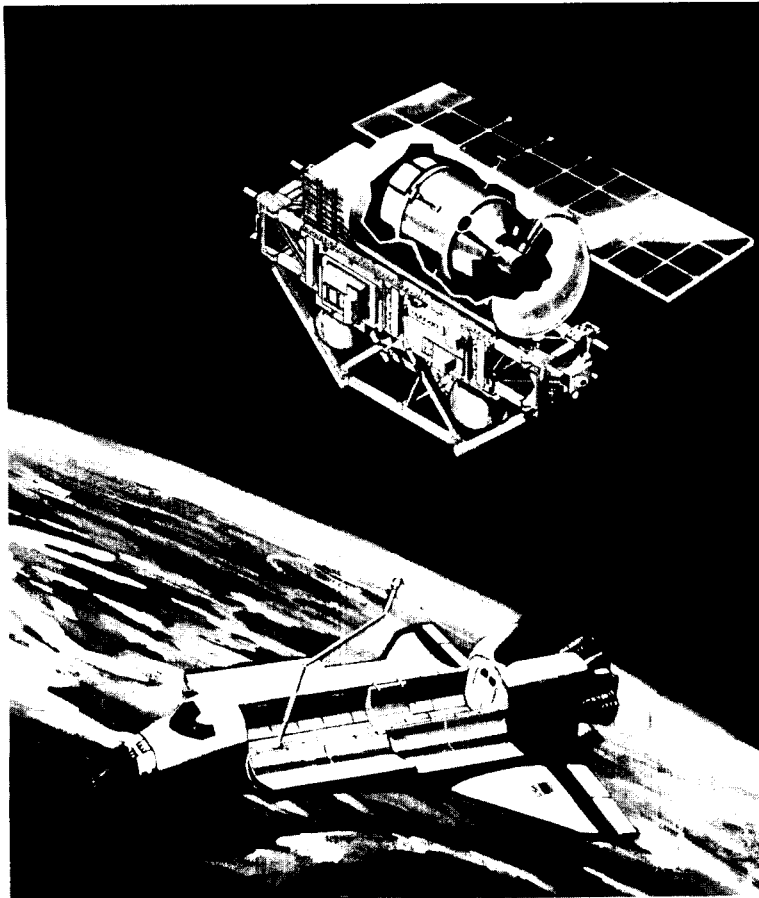


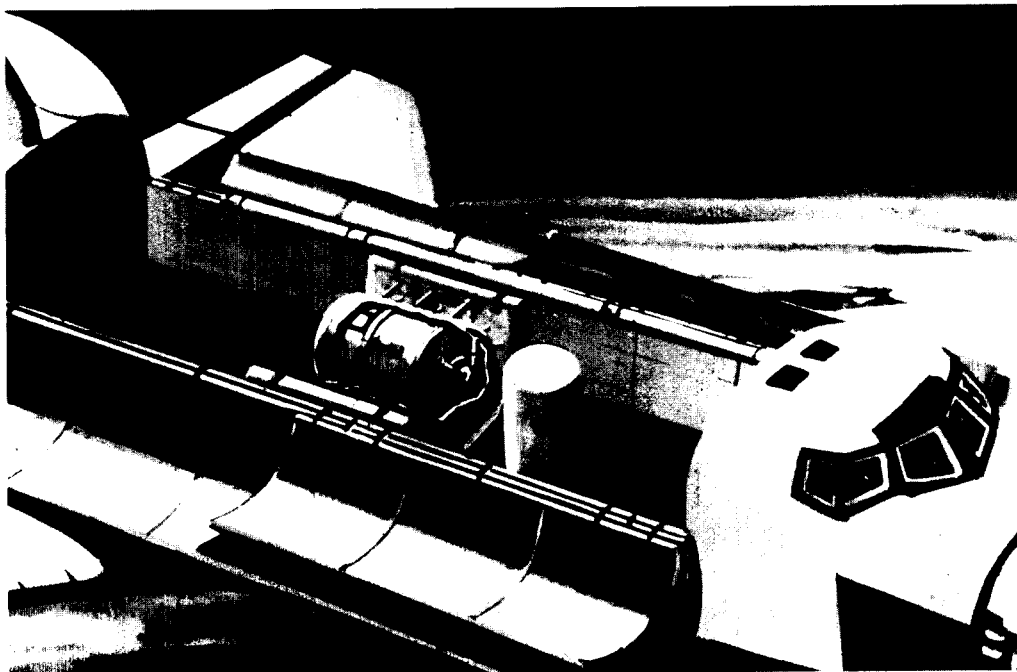
Figure 4-35. Option II-B, modified GRM concept.

The RCS will also have to be analyzed further to determine whether a pulsed hydrazine system can adequately provide the necessary compensation for relatively large drag forces and yet offer control which is gentle enough to meet the severe spacecraft acceleration requirements.

Based on the considerations above, and those GRM subsystem modifications discussed previously, the changes to the GRM spacecraft design to conduct the SGGM are extensive. Furthermore, the constraints on the dewar configuration lead to a risky design of the Experiment Module. Therefore, Option II-B is not recommended for further study.



DETACHED (FREE FLYING) MODE



SHUTTLE ATTACHED MODE

Figure 5-1. SGG Flight Test modes.

5.0 FLIGHT TEST PROGRAM (Fig. 5-1)

The SGGM represents a significant investment to obtain important scientific data. Moreover, a very sensitive instrument, and demanding spacecraft performance, are necessary to meet the scientific requirements. Risks should thus be reduced to the greatest extent possible. With a very sensitive instrument like SGG, it is virtually impossible to verify the instrument flight performance unambiguously, under the full gravitational acceleration and ambient disturbances existing in an Earth laboratory: the ground accelerations are several orders of magnitude greater than the gravity gradient signals that are to be measured. There are also unknowns concerning the effects of the orbital and platform environments on the instrument performance that can only be determined through an orbital test. Therefore, it is prudent to conduct an orbital test prior to the full duration science mission.

Since the primary objective of a flight test is to obtain technical and engineering data, it is not expected that a Shuttle flight of the SGG would provide significant geophysics or physics data. However, one option, that of utilizing a limited duration free flyer, could result in useful scientific results.

The objectives of the flight test and potential options for accomplishing it are discussed below. To establish the lowest baseline cost, an option that would utilize existing space-qualified hardware was analyzed. This option, although it requires minimum resources, would not provide all of the desired results. Furthermore, new development items, except for the SGG flight instrument, would not be used for the later SGG free-flying science mission. An option to soft-mount the Experiment Module in the Shuttle's cargo bay was next analyzed. This was followed by an option to freely float the Experiment Module within a protective structure, which would be fixed within the cargo bay. Finally, placing the Experiment Module on a carrier, setting it free from the Shuttle, and then recovering it, was briefly considered. The various Flight Test options that should be considered in detailed subsequent studies are summarized in Table 5-1.

TABLE 5-1. SUMMARY OF FLIGHT TEST OPTIONS

OPTION	SHUTTLE HARD-MOUNT	FLOATED IN SHUTTLE BAY	5-DAY FREE-FLIGHT	30-DAY FREE-FLIGHT
10 E SENSITIVITY ACHIEVABLE+	NO	YES	YES	YES
USEFUL GEOPHYSICS SCIENCE DATA I = 28.5 DEG I = 90 DEG	NO NO	NO NO	NO YES	NO YES
DURATION OF DATA ACQUISITION	10 HRS	10 HRS	100 HRS	500 HRS+
FUNDAMENTAL PHYSICS DATA POSSIBLE	NO	NO	YES (I = 90 DEG)	YES (I = 90 DEG)

+ ESTIMATE. FURTHER ANALYSIS REQUIRED.

5.1 Flight Test Objectives

The objectives of the Flight Test are listed below in roughly descending order of importance. However, many of the objectives are interrelated and all are considered vital to the program.

1. Validate the flight performance of the SGG instrument.

(a) Evaluate the operational characteristics of the instrument, including sensitivity, stability, noise spectrum, and bandwidth in a low-g environment.

(b) By using either a six-axis shaker or by moving the Experiment Module and/or carrier, validate the common mode balance.

(c) Determine the full instrument sensitivity of $3 \times 10^{-4} \text{ E Hz}^{-1/2}$ for brief periods.

(d) Determine if the noise figure of the accelerometer would permit its use to control the SGGM spacecraft during the subsequent science mission.

2. Validate the design and operation of the Experiment Module.

(a) Determine whether it will be possible to soft-mount the Experiment Module to the spacecraft. Examine the vibration levels coupled to the instrument. Can these be compensated for or suppressed?

(b) Determine the effect of liquid helium at low-g for this particular design, including thermal isolation and control, and force and torque balancing of the helium vents. Validate helium boiloff management techniques.

3. Validate alignment and attitude control of the Experiment Module.

(a) Investigate alignment of the instrument with the external navigation base. What is the performance of the alignment system?

(b) How well can the instrument be pointed and controlled?

4. Determine the noise spectrum of the carrier.

(a) Evaluate orbital aberrations (drag, gravity gradients, thermal).

(b) Evaluate platform noise: linear and angular accelerations, self-gravity noise, and electromagnetic disturbances.

(One should note that, by flying the SGG instrument aboard the Shuttle, one would obtain the Shuttle acceleration levels in six degrees-of-freedom, using the most sensitive accelerometer in existence. This could benefit other disciplines that utilize microgravity.)

5. Validate the analytic predictions of the instrument error model.

6. Assess the performance of automated instrument control. Validate algorithms that will be used.

7. Data Handling and Analysis: validate the techniques for processing the data.

5.2 Instrument Calibration

There is a close relationship between the ground test program and orbital flight test. The relationships between ground measurements made on Earth and those made in zero-g must be understood. Ground tests should cover scale factor variations, nullshifts, and interaxis coupling on both the accelerometer and gradiometer, and should explore any possible coupling, between the two instruments. One of the most important goals of the ground test program is calibration of the SGG. All of the error sources must be identified and understood to the extent that the instrument calibration, done as part of the flight test, will cover all pertinent parameters. This is also vital for an understanding of the in-flight data during the flight test and to allow modification of the instrument tests, if necessary.

Accelerometer Calibration: One of the major challenges is to calibrate an instrument that is more sensitive than any other instrument of its type. Thus, since an instrument with comparable sensitivity is unlikely to exist at the time of the flight test, some combination of indirect measurements, calibrated mass motions, and semi-bootstrap techniques will be useful. Some direct measurements using horizon scanners, gyros, star trackers, drag free systems, etc., will be extremely beneficial.

It will probably be necessary to test the accelerometer first and then use it to test the gradiometer. Using the above system, the linear and angular accelerometer nulls could be determined. The scale factors and interaxis couplings could be measured using calibrated rotational mass motions. Simple wheels may be adequate.

The accelerometer is relatively simple, compared to the gradiometer, and is expected to behave much the same in zero-g as on Earth. Because of its simplicity, it may be reasonable to extrapolate some aspects of the ground calibrations.

The spacecraft drag and disturbance torques will appear as "noise" to the calibration. Flying at a relatively high orbital altitude would minimize both effects. A drag-free system could be used to null the drag. The gyros and/or star trackers could be used to measure angular motion. Flying in an equatorial or near-equatorial, repetitive orbit would result in a fairly repetitive environment and would thus permit some filtering of these disturbances.

Gradiometer Calibration: The gradiometer is expected to behave quite differently in zero-g compared to the laboratory. The proof masses are supported by soft "springs." In one-g they depend on magnetic levitation to simulate their zero-g alignments. This simulation, however, may not be absolutely correct. The proof masses and their position sensors are also more spread out and have a more complicated geometry than the accelerometer sensitive elements. The elaborate feedback decoupling system may also operate quite differently in the orbital environment. While ground calibrations at different orientations and analytic results will help to approximate zero-g, it may not be adequate to permit an extrapolation of the ground calibrations. It would be highly desirable to perform a completely independent orbital calibration.

The use of mass motions to calibrate the gradiometer would be somewhat more involved than the accelerometer because either translational motion or rotating masses in the form of a dumbbell will be necessary. These masses must not be too close to the gradiometer because the instrument positional control may then become critical.

Shuttle Attached versus Detached Mode: The amplitude and frequency range requirements for calibration will determine if the Shuttle attached option will be adequate for calibration tasks. If ground tests and analyses can give sufficient confidence

that the amplitude and frequency response characteristics and intercouplings are stable, and well understood, the Shuttle attached option may be possible. Amplitude levels will have to be above the noise levels due to crew motion, ACS, mechanical, drag, and thermal disturbances.

5.3 Shuttle Attached Options

During data taking, other Orbiter activities must be curtailed. This would limit SGG operations to either a dedicated Shuttle flight, flights which deploy free-flying satellites, or dedicated portions of shared flights. In addition, the SGG instrument must be located as close as possible to the Orbiter's center of mass. The Shuttle environment, as discussed in Appendix F, is relatively severe for an instrument that is very sensitive to linear and angular accelerations. A major question to be resolved is whether the SGG can be adequately isolated from Orbiter disturbances. Crew or Shuttle RCS disturbances produce the most significant accelerations.

Overall Shuttle acceleration levels of 10^{-3} to 10^{-4} g are common. The measured power spectrum shows peaks above 1 Hz (see Appendix F). Acceleration levels at very low frequencies seem to reach 10^{-6} g or better during unpredictable periods. However, this region has been very difficult to measure and no assurances can be made for low frequency disturbances at this time. Moreover, the attitude may be uncertain to the order of arcminutes.

Typical acceleration environments for the Orbiter under control of the vernier thrusters are between 10^{-3} and 10^{-4} g. If the Orbiter is in the gravity gradient stabilized attitude, thruster disturbances are eliminated for periods of time, reducing the accelerations by about an order of magnitude (see Appendix F). Aerodynamic drag will be in the 10^{-6} to 10^{-7} g range, depending on orbital altitude and attitude (see Appendix F). Obviously, some type of instrument isolation is required if the SGG instrument is to be tested at its full sensitivity of 10^{-4} E Hz $^{-1/2}$.

Pointing is also an important consideration. For Orbiter payloads, pointing and stabilization are limited by the Orbiter ACS, by Orbiter structural distortions, and misalignments between the Inertial Measuring Unit (IMU) and the instrument (Fig. 5-2). By providing attitude sensors between the Orbiter and SGG, absolute pointing accuracy can be improved.

5.3.1 Low Cost Approach

The approach requiring the minimum of new developments (and lowest cost) would be to utilize available flight hardware and existing standard Orbiter, Spacelab, and Igloo accommodations. A concept based on this approach is shown in Figure 5-3. The dewar, helium control system, structures, and pumps from the Spacelab IRT mission would be used [104]. A new cryostat to accommodate the SGG and attitude measuring equipment would be added. The experiment assembly would be mounted on a standard ESA pallet near the Orbiter center of mass. The pallet could be suspended as discussed in Section 5.3.2. Power and data requirements could be easily met by standard Spacelab subsystems. A weight summary for this approach is shown in Table 5-2.

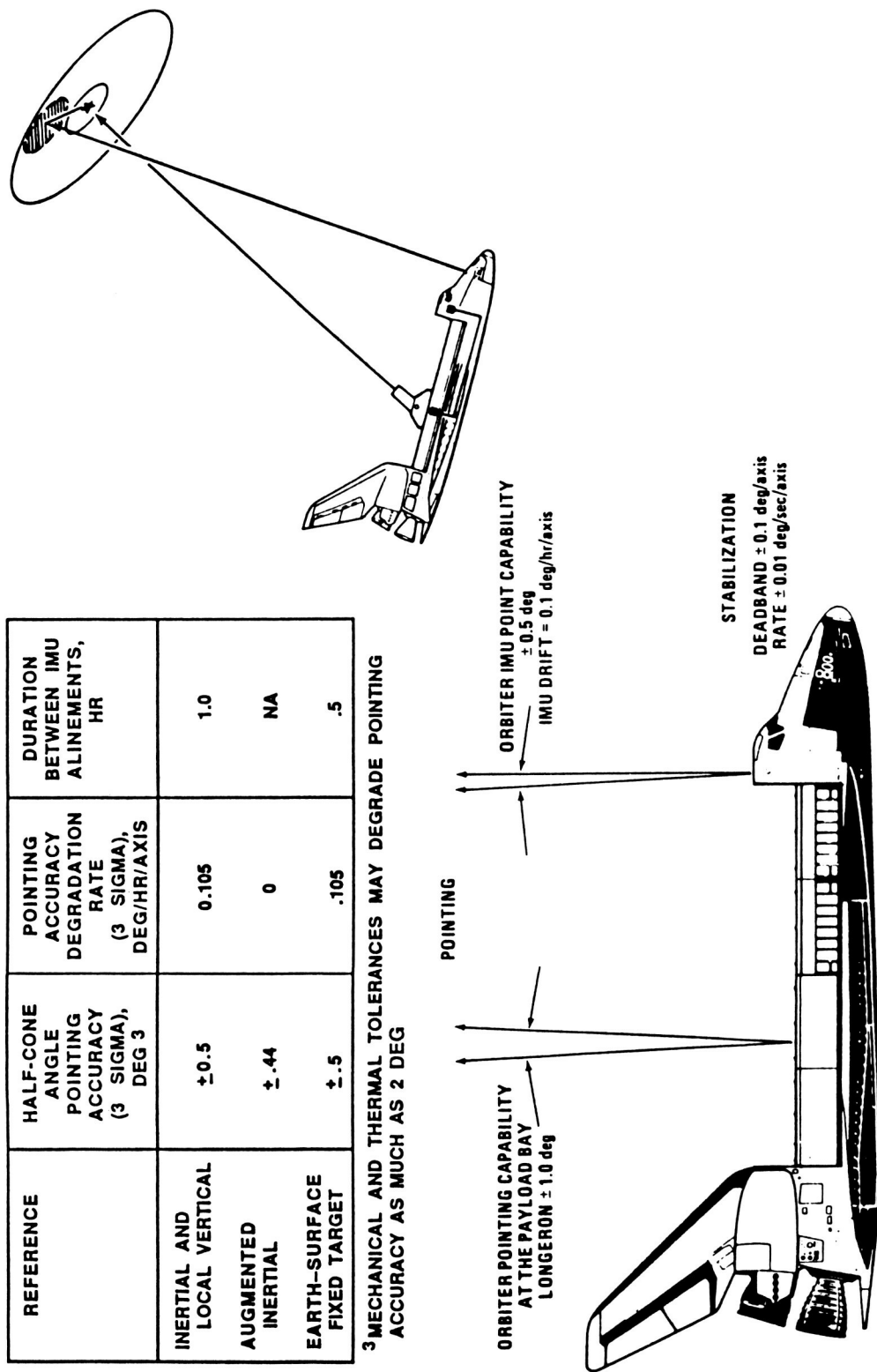


Figure 5-2. Orbiter pointing capability.

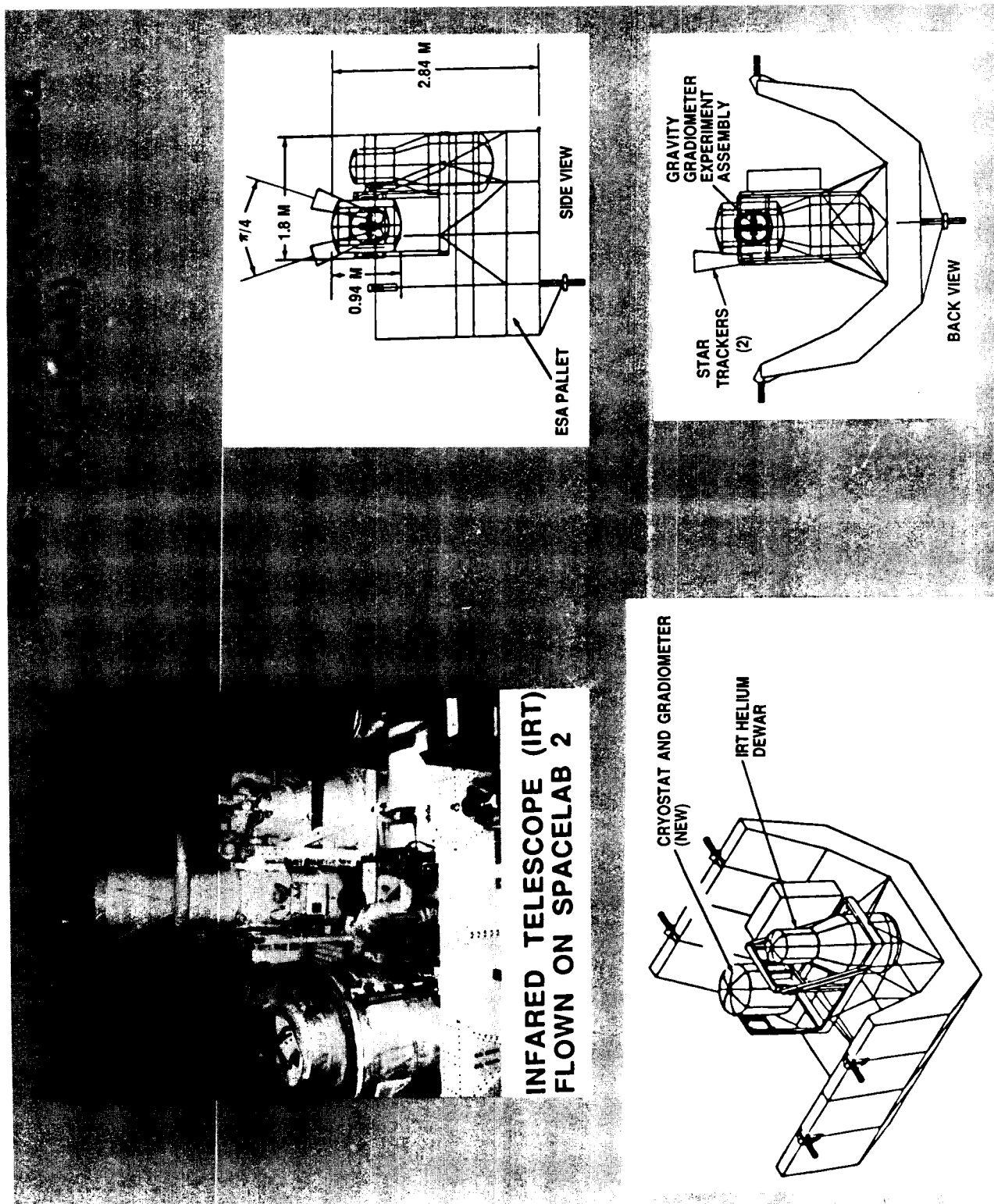


Figure 5-3. SGG Flight Test configuration - modified IRT hardware (dimensions are in meters).

**TABLE 5-2. WEIGHT SUMMARY FOR SGG FLIGHT TEST
UTILIZING IRT HARDWARE**

	(LBS)	(kg)
INSTRUMENT CONTAINER	238	108
INSTRUMENT	220	100
HELIUM DEWAR	440	200
HELIUM	60	27
PUMPS AND MOTOR	148	67
THERMAL CONTROL BOX INCL. VALVES (1)	143	65
CABLE AND HOSES	126	57
PALLET MNTG. STR.	238	108
GSE STRUCTURE (2)	43	19
INSTRUMENT CONTAINER ATTCH. STR.	36	16
MOUNTING STR. ELECTRONICS	24	11
INSULATION	6	3
STAR TRACKERS (2 REQ'D)	34	15
ELECTRONIC BOX SIGNAL CONDITION	35	16
POWER SUPPLY	15	7
INSTRUMENT ALIGNMENT UNIT	15	7
SUB-TOTAL	1821	826
CONTINGENCY 5%	91	41
TOTAL	1912	867

NOTES: (1) WEIGHT MAY BE REDUCED APPROXIMATELY 18 kg BY REDUCING THE SIZE OF THE THERMAL CONTROL BOX AND NUMBER OF VALVES.

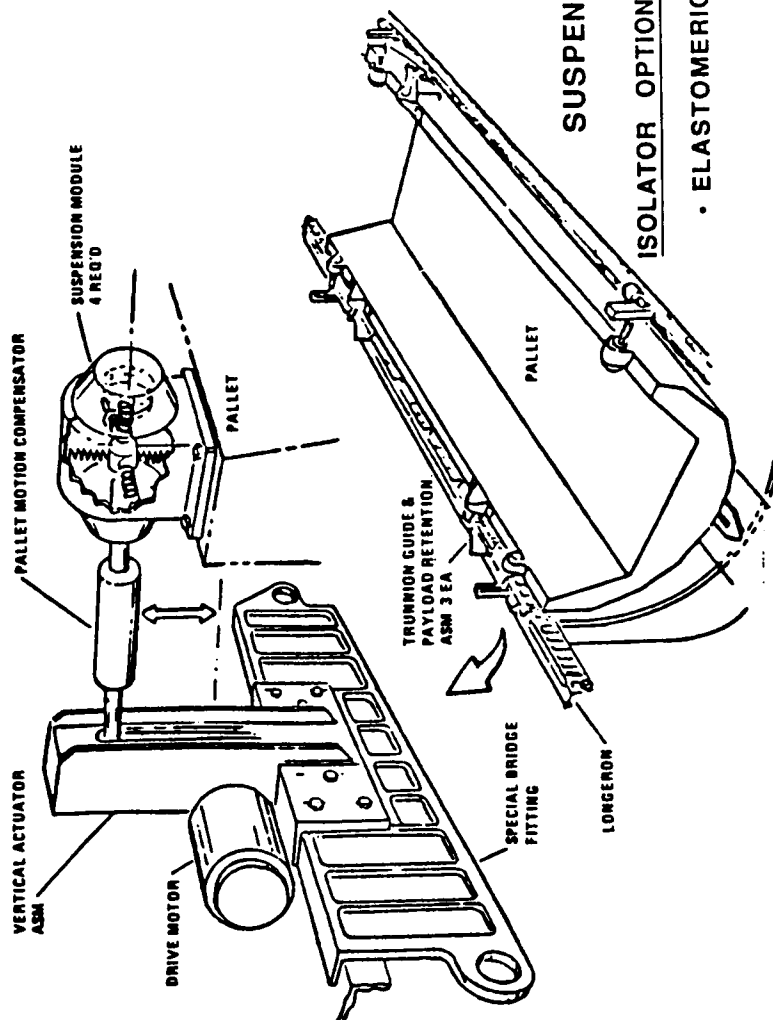
(2) GSE STRUCTURE IS USED FOR HANDLING EXPERIMENT.

Attitude knowledge would be provided by two star trackers mounted on the cryostat. An inertial alignment system would also be needed to determine the attitude of the SGG instrument inside the cryostat relative to the star tracker. This could be accomplished by directing a light beam through a port in the cryostat to a mirror. A plane mirror would then reflect the light to the detector to give two-axis knowledge. A second light beam could be used to provide knowledge of the third axis attitude. Two star trackers mounted on the cryostat, positioned 45 deg from the mounting surface and 90 deg from each other, would provide three-axis orientation knowledge.

This option, utilizing previously flown hardware, is straightforward and no obstacles to its development were identified. However, a separate development and integration for the SGG science mission, with the exception of the SGG instrument package, would be required. An option to utilize the SGG Experiment Module was also considered and most of the analysis for the IRT approach can be directly applied.

5.3.2 Soft-Mounted Mode

Studies have been made of a Suspended Experiment Mount (SEM) to provide some isolation from accelerations and to stabilize the viewing direction of Shuttle attached payloads [108]. A flexible suspension system has been considered which would be rigidly locked for ascent and descent (Fig. 5-4). Figure 5-4 also lists the isolation techniques that have been considered. Analysis has shown that about an order of magnitude attenuation of the disturbances can be expected from a fairly straightforward SEM design.



SUSPENSION/ISOLATION CONCEPTS

ISOLATOR OPTIONS

- ELASTOMERIC

CHARACTERISTICS

- NON-LINEAR LOAD VS. DEFLECTION
- HYSTERETIC DAMPING (5% TO 15%)
- TEMPERATURE SENSITIVE REQUIRING THERMAL CONTROL
- NON-LINEAR LOAD VS. DEFLECTION
- FRICTION DAMPING 15% TO 20%
- LINEAR LOAD VS. DEFLECTION
- HYSTERETIC DAMPING 0.5%
- REQUIRES ADDITIONAL DAMPING
- LINEAR LOAD VS. DEFLECTION
- VISCOUS DAMPING 10% (BASED ON GAS FLOW)
- INSENSITIVE TO TEMPERATURE RANGE
- SIMPLE SPRING/DAMPER INTEGRAL DESIGN

- WIRE ROPE HELICAL SPRING

- SOLID WIRE HELICAL SPRING

- GAS FILLED BELLOWS

Figure 5-4. Suspended experiment mount concepts for soft-mounting.

Passive isolation mounts, by attenuating the higher frequencies, act as low pass filters. Above 0.1 Hz, with proper tuning levels, around 10^{-6} g could probably be reached (with a 10^{-4} g disturbance input). In general, the suspended mount is better than hard-mounting the instrument, but probably not good enough if one must demonstrate the full instrument performance. An active isolation system could perhaps be pursued, and is briefly discussed below.

5.3.3 Free-Floating Mode

A possible instrument isolation approach would be to float the Experiment Module in zero-g and essentially operate the Shuttle as a drag-free satellite. An experiment provided drag-free package would control the Shuttle's vernier thrusters to provide drag compensation. This approach, however, does not appear feasible since it would relinquish control of the Shuttle to the experiment. Moreover, the Shuttle's RCS is probably too coarse to provide the precise control needed to compensate for drag levels around 10^{-6} g. Therefore, this approach was not seriously considered. However a related approach (Fig. 5-5) and one that is currently under investigation, would use magnetic suspension or the helium boiloff to actively position the Experiment Module, as discussed in Section 4.2.1.

Two options are possible. One is a "quasi drag-free" operation. In this mode, the Experiment Module is permitted to follow a drag-free orbit within the Shuttle bay for brief periods (~ 20 sec) which are interrupted by the firing of a magnetic suspension system to reposition the instrument package. The other option is an active vibration isolation mode in which only AC vibrations are attenuated and a DC force is applied by the helium boiloff gas or the magnetic suspension so that the instrument package follows the Shuttle orbit on the average. Since the SGG may not be able to stabilize within the short drag-free time, the first option may not be viable.

The active vibration isolation option appears promising since the DC accelerations of 10^{-5} to 10^{-6} g are not expected to present problems for the operation of the SGG. Two stage control loops can be provided. The first stage constitutes a feedback loop within the dewar, between the six-axis accelerometer and the six-axis shaker. The second stage is the control loop between the conventional accelerometers and gyros mounted on the dewar and the magnetic suspension coils or the proportional thrusters for helium gas.

Figure 5-5 illustrates this general concept. During orbital operations, the Experiment Module would be free-floating within a surrounding outer structure that is mounted to a pallet in the Shuttle cargo bay. This outer body simulates the spacecraft outer surface, as discussed in Section 4.4.1. During launch, ascent, and descent of the Shuttle, the Experiment Module would be rigidly locked by a latching mechanism (not shown in the figure). The particular concept shown in the figure would use the helium vent gas for vernier control of the Experiment Module.

5.4 Shuttle Detached Option

This option would accommodate the Experiment Module on a carrier in the Shuttle cargo bay, which would be deployed from the Shuttle. The SGG experiment would then be a nearly autonomous, subsatellite of the Shuttle. The flight experiment could

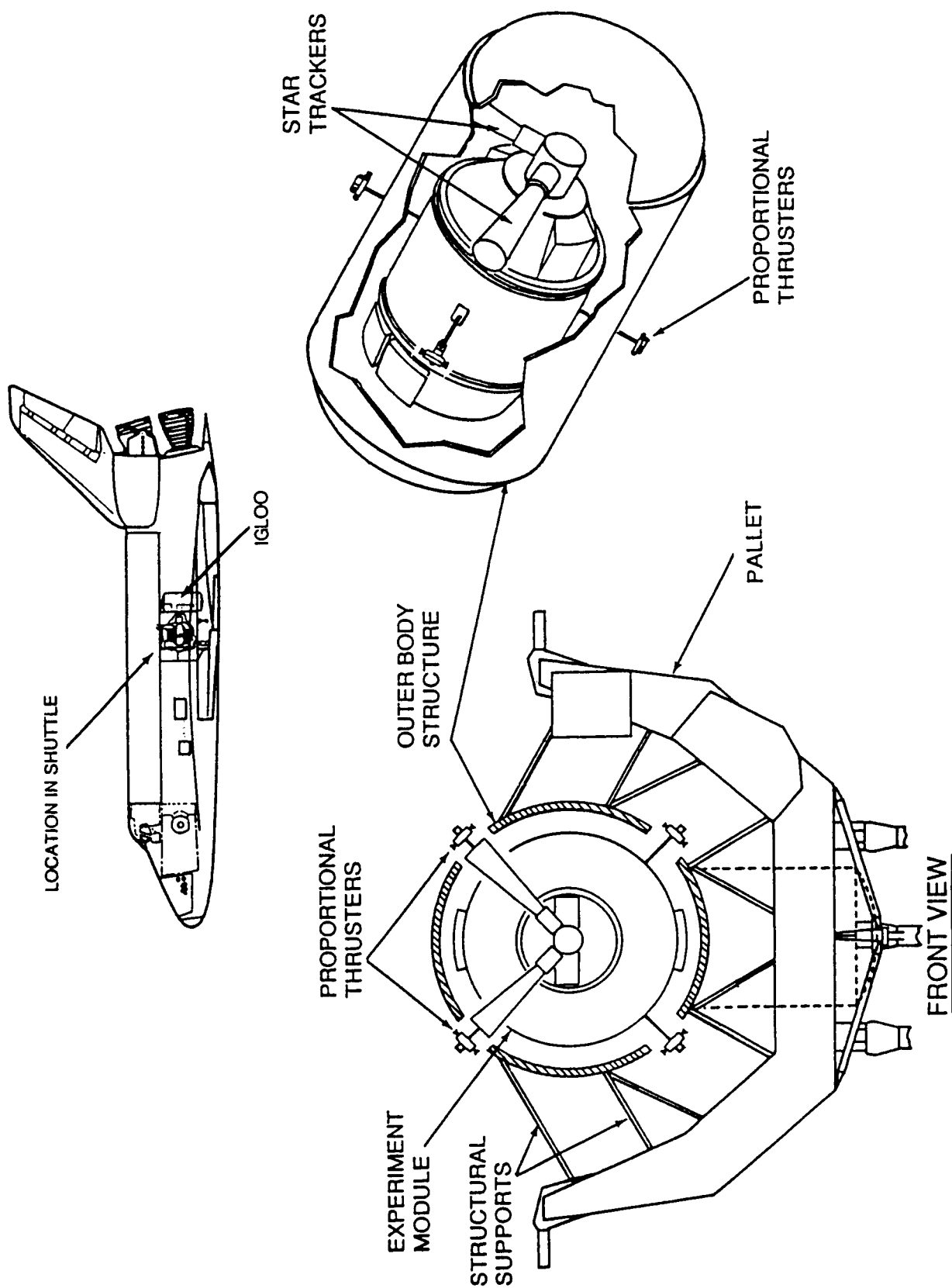


Figure 5-5. SGG Flight Test - free-floating mode concept.

be left in orbit and retrieved during a later Shuttle mission, if the experiment carrier were designed to provide sufficient utilities.

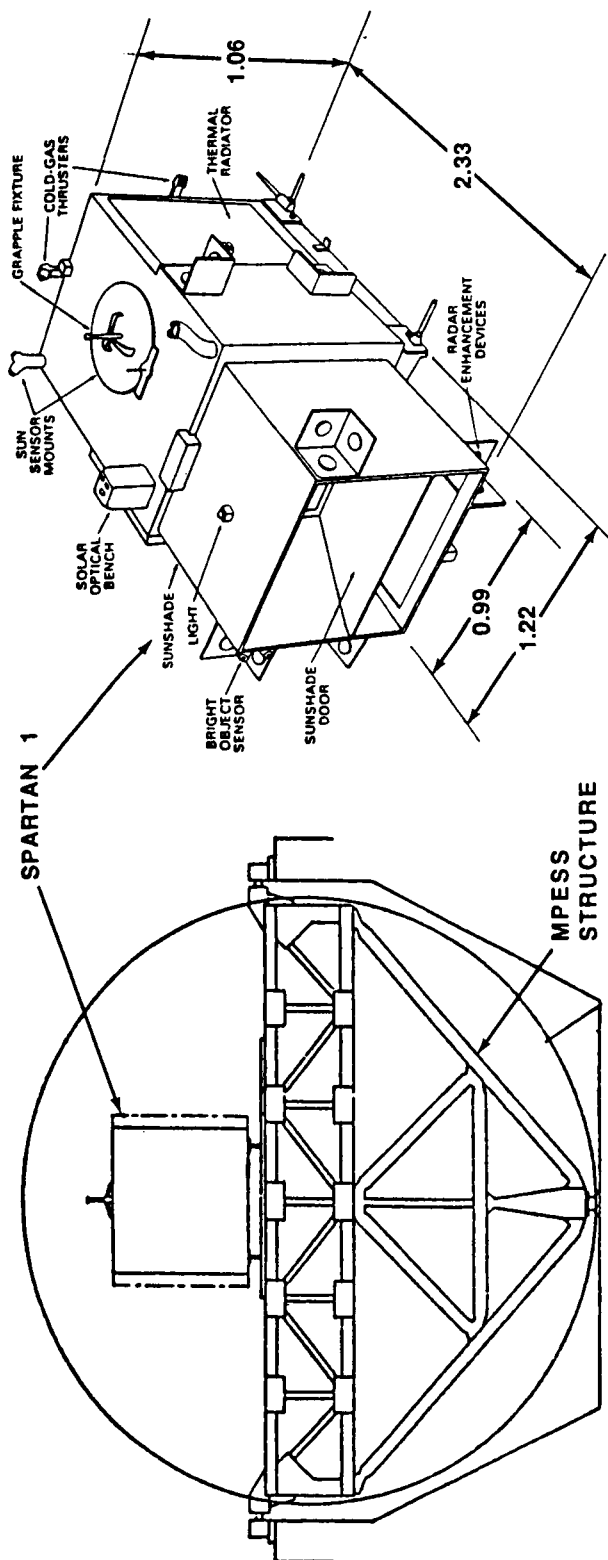
One concept would use the Spartan as the carrier [109]. The Spartan is an experiment carrier that is placed in the cargo bay on a modified Multi-Purpose Experiment Support Structure (MPRESS) carrier and released from the Shuttle during an orbital mission. This carrier was initially intended as a means of flying sounding rocket-type experiments aboard the STS. The primary emphases are simplicity, low cost, and reusability. The baseline Spartan program included three separate configurations, and enhancements to the basic Spartan capabilities have been proposed.

Power, C&DH, ACS, and thermal control capabilities of Spartan are quite limited for a mission as demanding as the SGG Flight Test. The existing Spartan capabilities and proposed enhancements are shown in Figure 5-6. Power is provided by batteries, data storage by tape recorders, and ACS by cold gas thrusters. These subsystems rely heavily on existing sounding rocket and Get Away Special Programs, and consequently limit the mission life of the current Spartan to about 40 hours.

The current Spartan carrier would not accommodate the SGG Flight Test. For example, only payloads less than 0.56 m in diameter and weighing less than 225 kg can now be used [109]. The power, pointing, and data handling are also not sufficient for the SGG Flight Test. Since no RF link exists for Spartan, no real time experiment control is possible. The experiment would essentially be passive and of very short duration.

Possible future Spartan enhancements include solar panels, a momentum exchange system, and possibly RF uplink and/or downlink capability. If the Spartan carrier is indeed enhanced as proposed, then it should be examined further as a potential carrier. Otherwise, if one had to greatly augment or supply the necessary utilities and/or capabilities, the best approach would likely be to build the experiment carrier specifically for the SGG Flight Test.

In summary, to conduct an SGG Flight Test in the Shuttle detached mode, no existing experiment carrier was found that would adequately support the mission. In the future, some carriers, like an enhanced Spartan, may be developed. However, if this option is pursued, given the timing of the mission and the uncertainty of availability, one should plan for the development of an SGG experiment carrier. One approach might be to start with an existing flight structure, such as the MPRESS carrier, and build from there. This is shown conceptually in Figure 5-7. The concept shown in the figure also includes the SGG isolation techniques discussed in Section 4.2.1. Studies should also include extended mission life (e.g., ~30 days) beyond the nominal seven day mission with retrieval during a subsequent mission.



SUBSYSTEM	SPARTAN	ENHANCED SPARTAN (PROPOSED)	SGG REQUIREMENTS
POWER	2-8 kw-HRS (BATTERIES)	TBD (SOLAR ARRAYS/ RECH. BATTERIES)	30 kw-HRS (100 HOURS OPERATION)
DATA RATE	12.5 kb/s (TAPE)	INCREASED - TBD (RF - SHUTTLE, GROUND)	43 kb/s
ACS	15 ARC SEC POINTING DRIFT 0.1 ARC SEC/SEC JITTER 10 ARC SEC PP (COLD GAS)	IMPROVED (TBD) TBD JITTER 1 ARC SEC PP IMPROVED, MOMENTUM MGT.	ANGULAR POSITION - 0.2 ARC SEC Hz ^{-1/2}
PAYLOAD SIZE	0.6m DIA. X 3mL 225 kg	1.1m DIA. X 3mL 680 kg	1.5m DIA. X 2mL
OPER. LIFE	40 HRS	200 HRS	- 100 HRS

Figure 5-6. Comparison of Spartan capabilities and SGG flight experiment requirements.

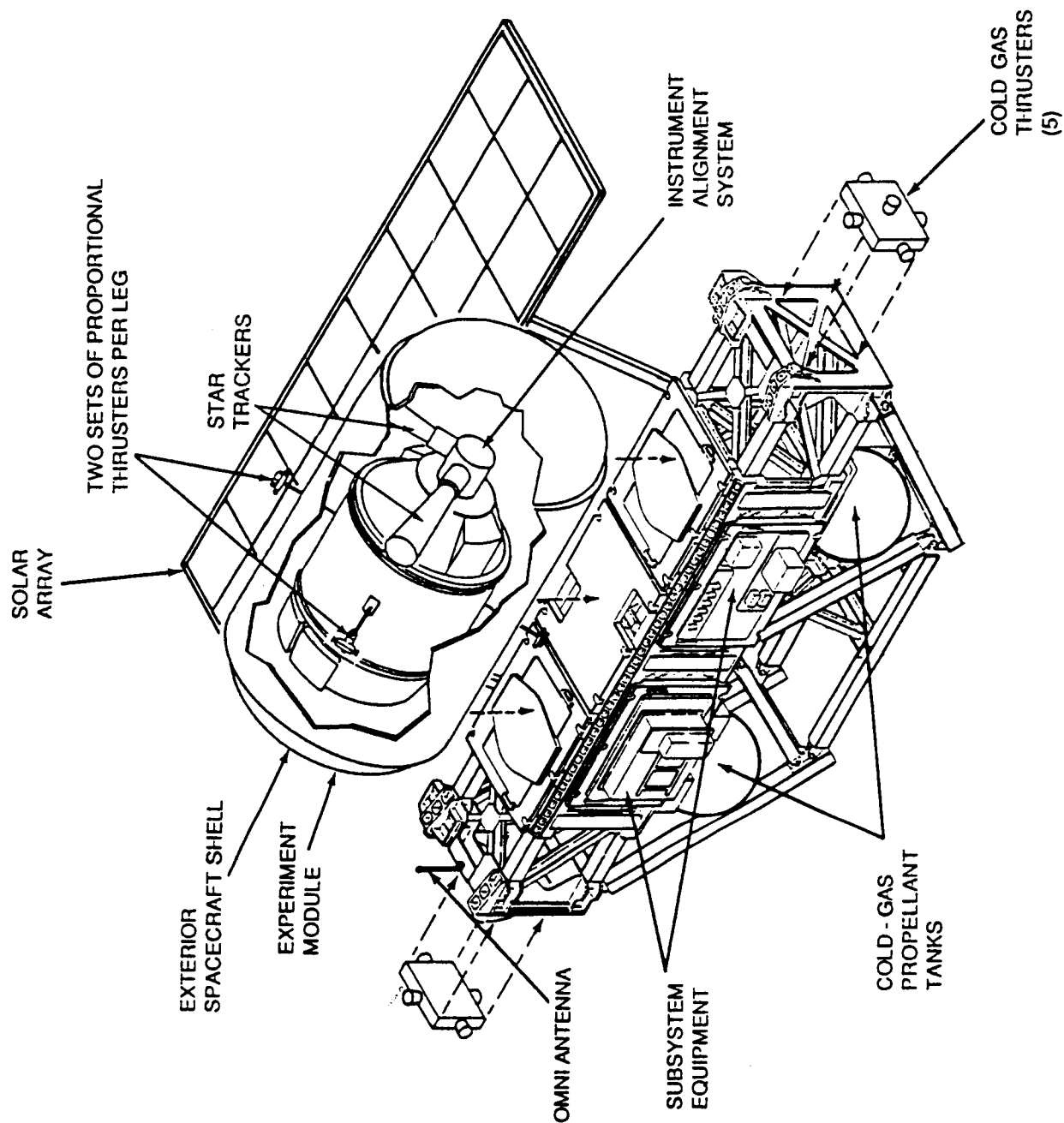


Figure 5-7. SGG Flight Test - detached mode concept.

6.0 STATUS AND POTENTIAL OF TECHNOLOGY ADVANCES

Advances in technology and developments in several areas could benefit the SGGM. Included among these are developments associated with guidance, navigation, and control; instrument cooling; high-temperature superconductivity; and spacecraft auxiliary propulsion systems. The status and potential advances of these subsystem elements are summarized below. Additional details can be found in Reference 103.

6.1 Guidance, Navigation, and Control (GNC)

Modern GNC systems utilizing digital control techniques greatly enhance the stability and accuracy of present day spacecraft. Primarily, the control system will be governed by the sensors and control (forcing) elements such as reaction control thrusters, momentum wheels, control moment gyros, and magnetic torquers. Existing sensors consist of gyroscopes (both mechanical and optical), accelerometers, star trackers, star scanners, horizon scanners, Sun sensors, and magnetometers. Based on the requirements for SGGM, only star trackers and the superconducting accelerometer have the required accuracy. The most accurate existing solid-state star trackers are in the 5×10^{-6} rad range, with a projected accuracy near 0.5×10^{-6} rad within five years.

If the superconducting accelerometer is used for control of the SGGM, a conventional gyro or rate gyro system is still required to complete the system. Gyro noise must be reduced to make them acceptable.

Momentum wheels should be considered for spacecraft fine pointing. Noise from existing wheels must be included in analytic simulations. Great reductions of wheel noise are not anticipated within the next five years. One method of stabilizing the Experiment Module consists of proportional thrusters being developed for the GP-B spacecraft. Small levels of thrust, generated by using the helium boiloff gas, will allow extremely fine control. If this technology is perfected for GP-B, it could be used for vernier control of the Experiment Module.

6.2 Instrument Cooling

Instrument cooling load, mission life, required operational temperature, power, and orbit constraints must be considered in selecting the SGG cooling system. Stored liquid helium coolers are state-of-the-art and have been considered for this mission. A superfluid helium dewar would provide the necessary thermal and vibration-free environment for the required mission life. Moreover, flight experience has been obtained with these dewars.

The major technology need for liquid helium systems is to improve the system operating lifetime. Advances are needed in cryogen tank support material and design of multilayer insulation. For IRAS, about 67 percent of the parasitic heat leak came through the tank support straps. Other advances could be made in more efficient wire feedthrough design, plumbing penetrations, and vapor cooling of multilayer insulation.

The use of solid cryogenics would offer distinct advantages over liquid systems (Table 6-1) [110]. Because the heat of sublimation is 10 to 15 percent higher than

TABLE 6-1. CRYOGENIC COOLING TECHNIQUES (FROM REFERENCE 110)

COOLING TECHNIQUE	TEMP. RANGE, ^a K	USABLE REFRIGERATION LOAD FOR 1 YEAR MISSION
RADIANT COOLERS	70-100	0-90 mW TO DATE; HIGHER CAPACITY POSSIBLE IN FUTURE
STORED SOLID CRYOGEN COOLERS	8-125	0-800 mW ^b PLUS VENT GAS COOLING
STORED LIQUID-HELIUM COOLERS	1.5-5.2	0-100 mW ^b
MECHANICAL COOLERS	4-100	0-300 W
He ³ COOLERS	0.3	0-100 μW
ADIABATIC DEMAGNETIZATION REFRIGERATION	0.001-0.3	0-100 μW

^a THESE VALUES ARE NOT THEORETICAL LIMITS, BUT ARE ESTIMATES OF TEMPERATURES AND LOADS BASED ON THE DESIGNS AS THEY APPEAR TO BE EVOLVING.

^b FOR MISSIONS OF SHORTER DURATION (e.g., 7-30 DAY SHUTTLE SORTIE), HIGHER COOLING LOADS COULD BE ACCOMPLISHED.

the heat of vaporization, and the solid cryogen has a 10 to 15 percent higher density than the liquid, the construction of a lighter, smaller system with larger cooling capacity could be achieved. In addition, stored liquid introduces sloshing, which must be minimized for SGGM. Moreover, the SGGM requires cooling to liquid helium temperatures (1.5 to 4.2 K) which is lower than the solid systems allow. For example, the DOD Teal Ruby System would use solid neon as the primary cryogen and methane as the secondary cryogen. The cooler system weight is about 159 kg and its projected lifetime is around 17 months. However, the operating temperature is between 13.5 and 24.5 K, too high for SGGM. The lowest projected operating range for a solid system is 8.3 to 13.8 K with solid hydrogen. This is still too high for SGGM.

A closed-loop superfluid helium refrigeration system, which could offer several advantages for the SGGM, will probably not be practical for some time to come. There are several developments underway to achieve closed-loop refrigerators at liquid nitrogen temperature (66 K), and down to 10 to 15 K (magnetic refrigeration).

In principle, such a system could be used to cool the heat shield of a superfluid helium dewar. A detailed analysis would be needed to determine if such a solution would offer technical or cost advantages, compared to a superfluid helium boiloff dewar. Present closed-loop cooling systems use either moving parts or strong magnetic fields, which will probably prevent their application for the SGGM.

6.3 High-Temperature Superconductivity

The recent discovery of new superconducting materials with high transition temperatures (T_c) adds a completely new outlook for the application of SGG technology. Yttrium-barium-copper-oxide and its isostructural rare Earth analogs have been shown to have T_c 's in excess of 90 K. There are preliminary reports that some variations of these compounds may be superconducting at around 240 K or higher. Rapid progress is being made in forming these compounds into useful shapes such as wires, thin films, and bulk materials. A high- T_c rf SQUID has been successfully demonstrated.

In order for these materials to find useful applications in gravity gradiometers and accelerometers, it is important that the high- T_c superconductors have a reasonably high critical field (first critical field, $H_{c1} \geq 100$ Oersted) and a low damping coefficient (decrement, $\Delta \leq 10^{-5}$). The high critical field would allow a strong electromagnetic coupling, and the low damping is needed to minimize the Johnson noise of the instrument. It is also important that a high- T_c SQUID with a low noise characteristic be developed. In view of the enormous enthusiasm and extent of the ongoing research activity in this field, it is reasonable to expect the useful high- T_c superconductors will become available for applications within the next decade. It appears, however, that high temperature versions of the SGG and the superconducting accelerometer will not be able to compete in sensitivity with the current niobium devices operating at liquid helium temperatures. This is because the Brownian motion noise of the proof masses and the Johnson noise in the SQUIDS, which limit the ultimate sensitivity of the superconducting inertial instruments, scale with temperature. It is therefore safe to remain with conventional superconductivity for the time being.

A high- T_c SGG would make future gravity survey missions to other planets much more feasible. Here the sensitivity requirement is not as severe as in the Earth-orbit applications. The spacecraft could carry a liquid nitrogen dewar, which can have a hold-time of many years in space, or radiation cooling might be sufficient to keep the sensors in the superconducting state. If the dewar could be eliminated, an Earth-orbit mission with a high- T_c SGG might be conceivable. Without the dewar, the spacecraft could be made with a much smaller cross section, reducing the drag coefficient, and thus permitting a lower altitude orbit. The loss of gradiometer sensitivity, caused by the higher operating temperature, might then be offset by the increased gravity signal in the lower orbit. High-temperature superconductivity, therefore, presents interesting possibilities for extending SGG technology to future Earth-orbit and planetary missions.

6.4 Propulsion

Monopropellant hydrazine is the current standard for spacecraft auxiliary propulsion. Since this type of system has been state-of-the-art for more than 12 years, improvements are becoming more difficult. The development of a new catalyst, or a new monopropellant, does not appear likely. However, several technologies, including improved heaters for catalyst beds, valves, lines, and tanks are needed.

In a continuous thrusting mode, the I_{sp} produced is around 235 sec. For a pulsed mode, the performance drops to about 180 sec. The specific impulse can be improved by the introduction of a thrust chamber heater, which could increase the steady state I_{sp} to approximately 300 sec. This would require about 1.4 W of electrical power per mN of thrust [110].

Ion propulsion is ideally suited for missions like SGGM, which demand low acceleration levels. The potential for electric propulsion has been known for many years, however, applications have been minimal. Ion thrusters have been flown as experiments, and technology work has been carried out for proposed future planetary missions. The critical technology component program for the baseline 30-cm ion thruster was developed for missions such as a Comet Rendezvous Mission. Current technology efforts are directed towards an increase in performance, higher reliability, and reduction in cost. Major directions are toward an increase in thrust-to-power, reductions in mass, and simplifications of the thruster system.

For inert gas ion thrusters, efforts are underway on analyses and component level R&D for thrusters and power processors. Studies have been initiated to provide technology direction for orbital use of inert gas ion propulsion systems.

Ion propulsion is power limited, since the performance depends on the available electric power. Thus, propulsion technologies are tied to advances in energy conversion and power processing. Present research and technology work on ion thrusters is directed toward 8-, 12-, and 30-cm thrusters, using both mercury and inert gases. Baseline thrusters have thus far been operated up to 200 mN with inert gases.

7.0 CONCLUSIONS AND RECOMMENDATIONS

7.1 Conclusions

7.1.1 Program

1. The SGG is a substantial advance over present technology. Progress is being made in the development of the instrument, and no fundamental barriers to the delivery of an instrument with the required sensitivity were found. However, instruments of the SGG class present particular problems. For example, a more demanding instrument, but of the same general class, the GP-B, has been under development for over 20 years. In general, instruments of the SGG class present quite long development times, and high technical risks. The program must take care to minimize these risks to the greatest extent possible.

2. While the primary (geophysics) and secondary (physics) mission objectives are not mutually exclusive from a mission standpoint, the more severe requirements for the secondary mission objectives indicate that a separate mission may be necessary to accomplish the physics experiments.

3. A precursor flight test of the SGG aboard the STS, while adding more expense to the program, is nevertheless vitally important in order to verify that the key elements of the science payload will meet the mission requirements, and to reduce overall mission risks.

7.1.2 Instrument

1. The SGG and the SSA under development at the University of Maryland should meet the sensitivity requirement for SGGM. While the SGG is the primary instrument which measures gravity signals, the SSA will also be a necessary component of the instrument since its outputs will likely be used to control the attitude of the Experiment Module and the spacecraft drag compensation.

2. While the primary (geophysics) mission objective requires measurement of any single component of the gravity gradient, redundancy in measurement is desirable. The secondary (physics) mission objectives require measurement of three orthogonal inline component gradients.

3. Common-mode acceleration balance of the gradiometer and attitude control of the instrument are among the most demanding requirements for SGGM. By isolating the Experiment Module from the spacecraft, one should be able to decouple the instrument from the expected high mechanical noise level of the carrier. Helium boil-off gas could be used to obtain fine control of the attitude and position of the Experiment Module within the outer spacecraft. Transmitting power and signals between the outer spacecraft and Experiment Module with minimum mechanical coupling needs further investigation.

7.1.3 Mission

1. For geophysics applications, either an Earth-fixed or inertial orientation appears acceptable at this time. Refined future analyses will determine which of the

two orientations offers definitive advantages. Likewise, further studies are needed to decide which orientation will give best resolutions for tests of laws of physics.

2. A Shuttle attached flight test, even with some type of soft mounting, probably will not meet all the desired objectives of the flight test. A free-flying mode would be ideal scientifically, but would likely be considerably more expensive. A controlled, free-floating mode inside the Shuttle cargo bay may be an acceptable alternative, and appears feasible.

3. In these initial studies, an orbital altitude of 200 km is a reasonable compromise between the desired high resolution and minimum aerodynamic drag.

4. Other potential carriers that were examined, i.e., Space Station, EOS platform, and TSS, are not viable options.

Spacecraft Systems: The SGGM imposes severe requirements on control of spacecraft dynamics, attitude, and acceleration levels. Moreover, all requirements must be satisfied simultaneously. This places severe requirements on the spacecraft control systems, and for isolation of the SGG.

The limited analysis of the ACS, performed thus far, uncovered no "show stoppers" to the development of an ACS to meet the SGGM requirements. Included among these analyses was a computer simulation of the SGGM control system, which is discussed in Appendix G. This simulation modeled the major environmental disturbances along with a preliminary control system configuration. Preliminary results did not indicate any behaviors of the system that would preclude the feasibility of the SGGM. This conclusion, however, must be qualified by a listing of those potentially important effects which have not yet been investigated. Effects due to sensor noise or dynamic characteristics have not yet been included. Neither have self and mutual gravity effects. No sensor complement, which is necessary to define ways in which accelerometers, rate gyros, star trackers, and perhaps the GPS may be used together to control the system to the required levels of accuracy, has been established.

Other interaction forces and moments such as those due to fluid, data, and power transfer cables and tubing between the Experiment Module and outer spacecraft may be significant disturbance sources. Controller effects such as ampling and quantization need to be investigated. Higher order gravity effects may also be significant error sources.

In order to provide a gentle RCS for drag compensation, ion propulsion offers many advantages. However, serious disadvantages such as large power requirements and the attendant requirement for large solar arrays, make this approach less attractive. On the other hand, it is not clear that a hydrazine system can provide the thrust levels necessary to compensate for the drag imposed at the low mission altitude, and yet be gentle and controllable enough to meet the low instrument acceleration requirements. This area is closely related to instrument isolation. Primary RCS by helium boil-off, as utilized by GP-B, is not feasible since the drag forces for SGGM are much higher than GP-B which will orbit at a lower drag (450 km higher) altitude. However, vernier control of the Experiment Module appears to be feasible. Cold gas is not recommended, due to its low performance characteristics.

Although several candidate techniques are being considered, no definitive instrument isolation technique has been arrived at. The most promising approach identified, would float the Experiment Module, and utilize the cryogen vent gas for vernier control of the Experiment Module.

Spacecraft dynamics have not yet been examined in detail, and can only be approximated until a preliminary spacecraft design is produced.

Successful experiences with cryogenic systems flown in space and under development indicates that no major barriers exist to the development of an acceptable dewar system.

The SGGM power, thermal control, and C&DH system requirements can be met with state-of-the-art systems.

Modification of the GRM spacecraft design to accommodate SGGM does not appear to be a viable option. A new spacecraft design, with some of the subsystems similar to the GRM, is required for the SGGM.

7.2 Recommendations

7.2.1 Program

1. A detailed Phase A study of the flight test mission should be initiated as soon as possible to resolve issues beyond the scope of the current study, to further refine a preliminary design of the systems, and to provide preliminary schedules and cost estimates.

2. The physics objectives would provide important contributions to knowledge, and should be actively pursued through the physics community and the NASA program organizations having responsibility for this area.

7.2.2 Instrument

1. Development of the SGG, SSA, and associated electronics should be accelerated. The operation of these instruments should be brought under computer control and be automated.

2. Instrument error analysis, including dynamic error analysis, should be continued. Error compensation techniques should be developed.

3. Details of ground test requirements should be formulated.

7.2.3 Mission

1. Analyses of the flight test mission in detail, including, but not limited to isolation techniques (attached, suspended, or free flyer); measurements required; calibration, alignment, and pointing techniques/requirements; time history in orbit; environmental monitoring; and Shuttle/Spacelab integration required, should be conducted. An upgraded version of the laboratory SGG should be considered as the flight test instrument.

2. A Phase B study of the SGGM should be initiated, following the Phase A and B studies of the flight test, as soon as the availability of resources permits.

3. Detailed trade studies of mission altitude, inclination, ground retrace pattern, and duration, versus science return should be made.

4. Simulation of the control system should be continued. This should involve a high fidelity model of the spacecraft dynamics, external and internal disturbances, and instrument noise, to generate power spectral densities for the various attitude and linear velocities and accelerations, orbit variations, and other disturbances. These should then be iterated with the mission requirements to determine feasibility of controlling the spacecraft to the required levels. The first task of follow-up studies should be the selection of a complement of sensors for the SGGM and the development of concepts for combining the outputs of these sensors in the most optimal way. The sensors selected should be modeled to sufficient fidelity to include their significant error sources and operating characteristics. Controller effects such as sampling and quantization should also be included.

5. A detailed analysis of instrument isolation techniques should be completed. This should include, among other possibilities, eddy current forcing and helium boil-off control of a free-floating Experiment Module, as well as various soft-mounting approaches.

6. Total error analysis, including the instrument, internal and external disturbances, and all spacecraft systems should be developed as soon as possible. Typical error sources to be considered are listed in Table 7-1.

7. Techniques for utilizing and controlling helium boil-off should be investigated further. This technology, now being developed for GP-B, should be closely followed.

TABLE 7-1. TYPICAL SGGM ERROR SOURCES

ERROR SOURCE

1. INSTRUMENT

2. INTERNAL DISTURBANCES

THERMAL
STRUCTURAL VIBRATIONS
INSTRUMENT SUSPENSION
WHEEL IMBALANCE
THRUSTER NOISE
THRUSTER GIMBAL
SOLAR ARRAY DISTURBANCES
He BOIL-OFF/VENTING
SUPERFLUID He SLOSH
PROPELLANT SLOSH
ACCELEROMETER NOISE
MASS DISTRIBUTION IMBALANCE

3. EXTERNAL DISTURBANCES

ATMOSPHERIC DRAG
GRAVITY GRADIENT TORQUES
ELECTROMAGNETIC DISTURBANCES

4. OTHER

STAR TRACKER
ALTITUDE DETERMINATION
INSTRUMENT-BASE ALIGNMENT
DATA REDUCTION

REFERENCES

1. McNutt, M. K. and Flinn, E. A. (editors): Geophysical and Geodetic Requirements for Global Gravity Field Measurements 1987-2000, Report of a Gravity Workshop. NASA, Colorado Springs, CO, February 1987.
2. Committee on Earth Sciences: A Strategy for Earth Science from Space in the 1980s; Part I: Solid Earth and Oceans. National Academy of Sciences, National Academy Press, Washington, D.C., 1982.
3. Taylor, P. T., Keating, T., Kahn, W. D., Langel, R. A., Smith, D. E., and Schnetzler, C. C.: GRM: Observing the Terrestrial Gravity and Magnetic Fields in the 1990s. EOS, Vol. 64, No. 43, 1983, pp. 609-611.
4. Metzger, E. H. and Allen, D. R., Bell Aerospace Company Report 9500-92044, 1972.
5. Wells, W. C. (editor): Spaceborne Gravity Gradiometers. NASA Conference Publication 2305, Greenbelt, MD, 1983.
6. Paik, H. J., Mapoles, E. R., and Wang, K. Y.: Superconducting Gravity Gradiometers. In Future Trends in Superconductive Electronics, AIP Conference Proceedings No. 44, edited by B. S. Deaver, Jr., C. M. Falco, J. H. Harris, and S. A. Wolf, AIP, New York, NY, 1978, pp. 166-170.
7. Space Science Board, National Research Council: Space Science in the Twenty-First Century: Imperatives for the Decades 1995 to 2015; Vol. I, Earth Sciences. National Academy Press, Washington, D.C., 1988.
8. Watts, A. B. and Talwani, M.: Gravity Anomalies Seaward of Deep-Sea Trenches and Their Tectonic Implications. Geophys. J. Roy. Astron. Soc., Vol. 36, 1974, pp. 57-90.
9. McAdoo, D. C. and Martin, C. F.: SEASAT Observations of Lithospheric Flexure Seaward of Trenches. J. Geophys. Res., Vol. 89, 1984, pp. 3201-3210.
10. Isacks, B. and Barazangi, M.: Geometry of Benioff Zones: Lateral Segmentation and Downwards Bending of the Subducted Lithosphere. In Island Arcs, Deep Sea Trenches, and Back-Arc Basins, Maurice Ewing Ser., Vol. 1, edited by M. Talwani and W. C. Pitman, III, AGU, Washington, D.C., 1977, pp. 99-114.
11. Creager, K. C. and Jordan, T. H.: Slab Penetration Into the Lower Mantle Beneath the Mariana and Other Island Arcs of the Northwest Pacific. J. Geophys. Res., Vol. 91, 1986, pp. 3573-3589.
12. Toksoz, M. N., Minear, J. W., and Julian, B. R.: Temperature Field and Geophysical Effects of a Downgoing Slab. J. Geophys. Res., Vol. 76, 1971, pp. 1113-1138.
13. Ocola, L. C. and Meyer, R. P.: Central North American Rift System, 1. Structure of the Axial Zone from Seismic and Gravity Data. J. Geophys. Res., Vol. 78, 1973, pp. 5173-5194.

14. King, E. R. and Zietz, I.: Aeromagnetic Study of the Midcontinent Gravity High of Central United States. *Geol. Soc. Amer. Bull.*, Vol. 82, 1971, pp. 2187-2208.
15. Bryan, K.: Geology and Groundwater Conditions of the Rio Grande Depression in Colorado and New Mexico. In Rio Grande Joint Investigations in the Upper Rio Grande Basin in Colorado, New Mexico, and Texas, National Resources Commission, Regional Planning, Part 6, Washington, D.C., 1938, pp. 196-225.
16. Cordell, L.: Regional Geophysical Setting of the Rio Grande Rift. *Geol. Soc. Amer. Bull.*, Vol. 89, 1978, pp. 1073-1090.
17. Ervin, C. P. and McGinnis, L. D.: Reelfoot Rift - Reactivated Precursor to the Mississippi Embayment. *Geol. Soc. Amer. Bull.*, Vol. 86, 1975, pp. 1287-1395.
18. Hildenbrand, T. G.: Rift Structure of the Northern Mississippi Embayment from Analyses of Gravity and Magnetic Data. *J. Geophys. Res.*, Vol. 90, 1985, pp. 12607-12622.
19. Linser, H.: Interpretation of Regional Gravity Anomalies in the Amazonas Areas, Brazil. Petrobras DEPEX Report No. 3250, Rio de Janeiro, 1958.
20. Cordell, L.: Extension in the Rio Grande Rift. *J. Geophys. Res.*, Vol. 87, 1982, pp. 8561-8569.
21. Cochran, J. R., Martinez, F., Stekcler, M. S., and Hobart, M. A.: Conrad Deep, a New Northern Red Sea Deep: Origin and Implications for Continental Rifting. *Earth Planet. Sci. Lett.*, Vol. 78, 1986, pp. 18-32.
22. Plouff, D. and Pakiser, L. C.: Gravity Study of the San Juan Mountains, Colorado. U.S. Geological Survey Professional Paper 800-B, 1972, pp. B183-B190.
23. Cordell, L., Long, C. L., and Jones, D. W.: Geophysical Expression of the Batholith Beneath Questa Caldera, New Mexico. *J. Geophys. Res.*, Vol. 90, 1986, pp. 11263-11269.
24. Haxby, W. F., Turcotte, D. L., and Bird, J. M.: Thermal and Mechanical Evolution fo the Michigan Basin. *Tectonophysics*, Vol. 36, 1976, pp. 57-75.
25. Karner, G. D. and Watts, A. B.: Gravity Anomalies and Flexure of the Lithosphere at Mountain Ranges. *J. Geophys. Res.*, Vol. 88, 1983, pp. 10449-10477.
26. Sheffels, B. and McNutt, M.: Role of Subsurface Loads and Regional Compensation in the Isostatic Balance of the Transverse Ranges, California: Evidence for Intracontinental Subduction. *J. Geophys. Res.*, Vol. 91, 1986, pp. 6419-6431.
27. Lyon-Caen, H. and Molnar, P.: Constraints on the Structure of the Himalaya from an Analysis of Gravity and Flexural Model of the Lithosphere. *J. Geophys. Res.*, Vol. 88, 1983, pp. 8171-8192.

28. McNutt, M. K. and Kogan, M. G.: Isostasy in the USSR II, Interpretation of Admittance Data. In The Composition, Structure and Dynamics of the Lithosphere-Astenosphere System, Geodyn. Ser., edited by K. Fuchs and C. Froidevaux, AGU, Washington, D.C., in press, 1987.
29. Anderson, D. L.: The Deep Structure of Continents. J. Geophys. Res., Vol. 84, 1979, pp. 7555-7560.
30. Jordan, T. H.: The Deep Structure of Continents. Sci. Amer., Vol. 240, 1979, pp. 92-107.
31. Jordan, T. H.: Mineralogies, Densities, and Seismic Velocities of Garnet Lherzolites and Their Geophysical Implications. In The Mantle Sample: Inclusions of Kimberlites and Other Volcanics, edited by F. R. Boyd and H. O. A. Meyer, AGU, Washington, D.C., 1979.
32. Richards, M. A. and Hager, B. H.: Geoid Anomalies in a Dynamic Earth. J. Geophys. Res., Vol. 89, 1984, pp. 5987-6002.
33. Hager, B. H., Clayton, R. W., Richards, M. A., Comer, R. P., and Dziewonski, A. M.: Lower Mantle Heterogeneity, Dynamic Topography and the Geoid. Nature, Vol. 313, 1985, pp. 541-545.
34. Hager, B. H.: Subducted Slabs and the Geoid: Constraints on Mantle Rheology and Flow. J. Geophys. Res., Vol. 89, 1984, pp. 6003-6105.
35. Ho-Liu, P., Kanamori, H., and Clayton, R. W.: Applications of Attenuation Tomography to Imperial Valley and Coso-Indian Wells Region, Southern California. J. Geophys. Res., submitted for publication.
36. Hearn, T. M. and Clayton, R. W.: Lateral Velocity Variations in Southern California, I. Results for the Upper Crust From P Waves; II. Results for the Lower Crust from P Waves. Bull. Seismo. Soc. Am., Vol. 76, 1986, pp. 495-520.
37. Humphreys, E., Clayton, R. W., and Hager, B. H.: A Tomographic Image of Mantle Structure Beneath Southern California. Geophys. Res. Lett., Vol. 11, 1984, pp. 625-627.
38. Grand, S. P. and Helmberger, D. V.: Upper Mantle Shear Structure of North America. Geophys. J. Roy. Astr. Soc., Vol. 76, 1984, pp. 11465-11475.
39. Grand, S. P.: Shear Velocity Structure of the Mantle Beneath the North American Plate. Ph.D. Thesis, 228 pp., California Institute of Technology, Pasadena, CA, 1986.
40. Dziewonski, A. M.: Mapping the Lower Mantle: Determination of Lateral Heterogeneity in P-Velocity Up to Degree and Order 6. J. Geophys. Res., Vol. 89, 1984, pp. 5929-5952.
41. Woodhouse, J. H. and Dziewonski, A. M.: Mapping the Upper Mantle: Three-Dimensional Modeling of Earth Structure by Inversion of Seismic Waveforms. J. Geophys. Res., Vol. 89, 1984, pp. 5953-5986.

42. Nataf, H. C., Nakanishi, I., and Anderson, D. L.: Anisotropy and Shear-Velocity Heterogeneities in the Upper Mantle. *Geophys. Res. Lett.*, Vol. 11, 1984, pp. 109-112.
43. Nataf, H. C., Nakanishi, I., and Anderson, D. L.: Measurements of Mantle Wave Velocities and Inversion for Lateral Heterogeneities and Anisotropy, Part III. Inversion. *J. Geophys. Res.*, Vol. 91, 1986, pp. 7261-7307.
44. Tanimoto, T.: The Backus-Gilbert Approach to Three-Dimensional Structure in The Upper Mantle: II. SH and SV Velocity. *Geophys. J. Roy. Astron. Soc.*, Vol. 84, 1986, pp. 49-69.
45. Hager, B. H. and Clayton, R. W.: Constraints on the Structure of Mantle Convection Using Seismic Observations, Flow Models, and the Geoid. In Mantle Convection, W. R. Peltier, Ed., in press, 1987.
46. Kohlstedt, D. T. and Hornack, P.: Effect of Oxygen Partial Pressure on the Creep of Olivine. In Anelasticity in the Earth, edited by F. D. Stacey, M. S. Paterson, and A. Nicholas, *Geodynamics Ser.*, Vol. 4, 1981, pp. 101-107.
47. Peltier, W. R. and Wu, P.: Mantle Phase Transition and the Free Air Gravity Anomalies Over Fennoscandia and Laurentia. *Geophys. Res. Lett.*, Vol. 9, 1982, pp. 731-734.
48. Wu, P. and Peltier, W. R.: Glacial Isostatic Adjustment and the Free Air Gravity Anomaly as a Constraint Upon Deep Mantle Viscosity. *Geophys. J. Roy. Astro. Soc.*, Vol. 74, 1983, pp. 377-449.
49. Karato, S.: Rheology of the Lower Mantle. *Phys. Earth. Planet. Int.*, Vol. 24, 1981, pp. 1-14.
50. McAdoo, D. C.: On the Compensation of Geoid Anomalies Due to Subducting Slabs. *J. Geophys. Res.*, Vol. 87, 1982, pp. 8684-8692.
51. Jacobsen, S. B. and Wasserburg, G. J.: Transport Models for Crust and Mantle Evolution. *Tectonophysics*, Vol. 75, 1981, pp. 163-179.
52. Spohn, T. and Schubert, G.: Modes of Mantle Convection and the Removal of Heat from the Earth's Interior. *J. Geophys. Res.*, Vol. 87, 1982, pp. 4682-4696.
53. Christense, U. R. and Yuen, D. A.: The Interaction of a Subducting Lithospheric Slab with a Chemical or Phase Boundary. *J. Geophys. Res.*, Vol. 89, 1984, pp. 4389-4402.
54. Busse, F. H.: On the Aspect Ratios of Two-Layer Mantle Convection. *Phys. Earth Planet. Int.*, Vol. 24, 1981, pp. 320-324.
55. Creager, K. C. and Jordan, T. H.: Slab Penetration into the Lower Mantle. *J. Geophys. Res.*, Vol. 89, 1984, pp. 3031-3049.
56. Richter, F. M. and Parsons, B.: On the Interaction of Two Scales of Convection in the Mantle. *J. Geophys. Res.*, Vol. 80, 1975, pp. 2529-2541.

57. Yuenm, D. A., Peltier, W. R., and Schubert, G.: On the Existence of a Second Scale of Convection in the Upper Mantle. *Geophys. J. Roy. Astro. Soc.*, Vol. 65, 1981, pp. 171-190.
58. Buck, W. R.: When Does Small Scale Convection Begin Beneath Oceanic Lithospheres? *Nature*, Vol. 313, 1985, pp. 775-777.
59. Haxby, W. F. and Weissel, J. K.: Evidence for Small-Scale Mantle Convection from SEASAT Altimeter Data. *J. Geophys. Res.*, Vol. 91, 1986, pp. 3507-3520.
60. Weissel, J. K., Anderson, R. N., and Geller, C. A.: Deformation of the Indo-Australian Plate, *Nature*, Vol. 287, 1980, pp. 284-291.
61. McAdoo, D. C. and Sandwell, D. T.: Folding of the Oceanic Lithosphere. *J. Geophys. Res.*, Vol. 90, 1985, pp. 8563-8569.
62. Froidevaux, C.: Basin and Range Large Scale Tectonic: Constraints From Gravity and Reflection Seismology. *J. Geophys. Res.*, Vol. 91, 1986, pp. 3625-3632.
63. Morgan, W. J.: Deep Mantle Convection: Plumes and Plate Motions. *Amer. Assoc. Petrol. Geol. Bull.*, Vol. 56, 1972, pp. 203-213.
64. Olson, P. and Nam, I. S.: The Formation of Sea Floor Swells by Mantle Plumes. *J. Geophys. Res.*, Vol. 91, 1986, pp. 7181-7191.
65. Richards, M. A., Hager, B. H., and Sleep, N. H.: Dynamically Supported Geoid Highes Over Hotspots: Observations and Theory. *J. Geophys. Res.*, in press, 1987.
66. Wagner, C. A. and McAdoo, D. C.: Time Variations in the Earth's Gravity Field Detectable with Geopotential Research Mission Intersatellite Tracking. *J. Geophys. Res.*, Vol. 91, 1986, pp. 8373-8386.
67. Yoder, C. F., Williams, J. G., Dickey, J. O., Schutz, B. E., Eanes, R. J., and Tapley, B. D.: Secular Variation of Earth's Gravitational Harmonic J from LAGEOS and the Nontidal Acceleration of Earth Rotation. *Nature*, Vol. 303, 1983, pp. 757-762.
68. Meier, M. F.: Contributions of Small Glaciers to Global Sea Level Change. *Science*, Vol. 226, 1984, pp. 1418-1421.
69. Hinnov, L. A. and Wilson, C. R.: An Estimation of the Water Storage Contribution to the Excitation of Polar Motion. *Geophys. J. Roy. Astron. Soc.*, Vol. 88, 1987, pp. 437-459.
70. Wahr, J. M.: Effects of the Atmosphere and Oceans on the Earth's Wobble. *Geophys. J. Roy. Astro. Soc.*, Vol. 70, 1982, pp. 349-372.
71. Rundle, J. B.: Deformation, Gravity, and Potential Changes Due to Volcanic Loading of the Crust. *J. Geophys. Res.*, Vol. 87, 1982, pp. 10729-10744.

72. Dzurisin, D., Anderson, L. A., Eaton, G. P., Koyanagi, R. Y., Lipman, P. W., Lockwood, J. P., Okahura, R. T., Puniwai, G. S., Sako, M. K., and Yamashita, K. E.: Geophysical Observations of Kilauea Volcano, Hawaii, 2. Constraints on the Magma Supply During November 1975 - September 1977. *J. Volcan. Geotherm. Res.*, Vol. 7, 1980, pp. 241-269.
73. Jachens, R. C., Spydell, D. R., Pitts, G. S., Dzurisin, D., and Roberts, C. W.: Temporal Gravity Variations at Mount St. Helens, March-May, 1980. In *The 1980 Eruptions of Mount St. Helens*, Washington, U.S. Geological Survey Professional Paper No. 1250, 1981, pp. 175-181.
74. Walsh, J. B. and Rice, J. R.: Local Changes in Gravity Resulting from Deformation. *J. Geophys. Res.*, Vol. 84, 1979, pp. 165-170.
75. Savage, J. C.: Local Gravity Anomalies Produced by Dislocation Sources. *J. Geophys. Res.*, Vol. 89, 1984, pp. 1945-1952.
76. "Reanalysis of Old Eötvös Data Suggests 5th Force...to Some," *Physics Today*, October 1986, pp. 17-20.
77. Stacey, F. D. and Tuck, G. J.: Geophysical Evidence for non-Newtonian Gravity. *Nature*, Vol. 292, 1981, pp. 230-232.
78. Fishbach, E., Sudarsky, D., Szafer, A., Talmadge, C., and Aronson, H.: Reanalysis of the Eötvös Experiment. *Phys. Rev. Lett.*, Vol. 56, 1986, pp. 3-6.
79. Paik, H. J.: New Null Experiment to Test the Inverse Square Law of Gravitation. *Phys. Rev. D.*, Vol. 19, 1979, pp. 2320-2324.
80. Rapp, R. H.: Current Estimates of Mean Earth Ellipsoid Parameters. *Geophys. Res. Lett.*, Vol. 1, 1974, pp. 35-38.
81. Lerch, F. J., Laubscher, R. E., Klosko, S. M., Smith, D. E., Kolenkiewics, R., Putney, B. H., Marsh, J. G., and Brownd, J. E.: Determination of the Geocentric Gravitational Constant from Laser Ranging on Near-Earth Satellites. *Geophys. Res. Lett.*, Vol. 5, 1978, pp. 1031-1034.
82. Ferrari, A. J., Sinclair, W. C., Sjogren, W. J., Williams, J. G., and Yoder, C. F.: Geophysical Parameters of the Earth-Moon System. *J. Geophys. Res.*, Vol. 85, 1980, pp. 3939-3951.
83. Misner, C. W., Thorne, K. S., and Wheeler, J. A.: Gravitation. Freeman, Parts VIII and IX, San Francisco, 1973.
84. Everitt, C. W. F.: The Stanford Relativity Gyroscope Experiment: History and Overview. In *Near Zero: New Frontiers of Physics - Papers in Honor of William M. Fairbank*, edited by B. Deaver, C. W. F. Everitt, J. Fairbank, and P. M. Michelson, W. H. Freeman Co., New York, 1986.
85. Braginsky, V. B. and Polnarev, A. G.: Relativistic Spin-Quadrupole Gravitational Effect. *Sov. Phys. JETP Lett.*, Vol. 31, 1980, pp. 415-418.
86. Mashhoon, B. and Theiss, D. S.: Relativistic Tidal Forces and the Possibility of Measuring Them. *Phys. Rev. Lett.*, Vol. 49, 1982, pp. 1542-1545.

87. Paik, H. J., Mashhoon, B., and Will, C. M.: Detection of Gravitomagnetic Field Using an Orbiting Superconducting Gravity Gradiometer. In Proceedings of the International Symposium on Experimental Gravitational Physics, edited by P. Michelson, Guangzhou, China, August 1987.
88. Paik, H. J.: Superconducting Tunable-Diaphragm Transducer for Sensitive Acceleration Measurements. *J. Appl. Phys.*, Vol. 47, 1976, pp. 1168-1178.
89. Hopkins, R. A. and Books, W. F.: Orbital Performance of a One-Year Lifetime Superfluid Helium Dewar Based on Ground Testing and Computer Modeling. In *Advances in Cryogenics Engineering*, Vol. 27, 1982.
90. Reed, G. B.: Application of Kinematic Geodesy for Determining the Short Wavelength Components of the Gravity Field by Satellite Gradiometry. Report No. 2101, Department of Geodetic Science, Ohio State University, Columbus, OH, 1973.
91. Breakwell, J. V.: Satellite Determination of Short Wavelength Gravity Variations. *J. of Astronaut. Sci.*, Vol. 27, 1979, pp. 329-344.
92. Kahn, W. D. and VonBun, F. O.: Error Analysis for a Gravity Gradiometer Mission. *IEEE Trans. on Geoscience and Remote Sensing*, Vol. GE-25, 1985, pp. 527-530.
93. Colombo, O. L. and Kleusberg, A.: Applications of an Orbiting Gravity Gradiometer. *Bull. Geod.*, Vol. 57, 1983, pp. 83-101.
94. Paik, H. J. and Richard, J.-P.: Development of a Sensitive Superconducting Gravity Gradiometer for Geological and Navigational Applications. NASA Contractor Report 4011, NASA, 1986.
95. Chan, H. A. and Paik, H. J.: Superconducting Gravity Gradiometer for Sensitive Gravity Measurements, I. Theory. *Phys. Rev. D.*, Vol. 35, 1987, pp. 3551-3571.
96. Moody, V., Chan, H. A., and Paik, H. J.: Superconducting Gravity Gradiometer for Terrestrial and Space Applications. *J. of Appl. Phys.*, Vol. 60, 1986, pp. 4308-4315.
97. Chan, H. A.: Null Test of the Gravitational Inverse Square Law with a Superconducting Gravity Gradiometer. Ph.D. Thesis, University of Maryland, College Park, MD, 1982.
98. Chan, H. A., Moody, M. V., and Paik, H. J.: Superconducting Gravity Gradiometer for Sensitive Gravity Measurements, II. Experiment. *Phys. Rev. D.*, Vol. 35, 1987, pp. 3572-3597.
99. Chan, H. A., Paik, H. J., Moody, M. V., and Parke, J. W.: Superconducting Techniques for Gravity Survey and Inertial Navigation. *IEEE Transactions on Magnetism*, Vol. MAG-21, 1985, pp. 411-414.
100. Chan, H. A., Moody, M. V., and Paik, H. J.: Null Test of the Gravitational Inverse Square Law. *Phys. Rev. Lett.*, Vol. 49, 1982, pp. 1745-1748.

101. Keating, T., Kahn, W., and Lerch, F. (editors): Geopotential Research Mission: Science, Engineering, and Program Summary. NASA TM 86240, 1986.
102. Bardas, D., Cheung, W. S., Gill, D., Hacker, R., Keiser, G. M., Lipa, J. A., Macgirvin, M., Saldinger, T., Turneure, J. P., Wooding, W. S., and Lockhart, J. M.: Hardware Development for Gravity Probe-B. SPIE Proceedings, Vol. 619, 1986, pp. 29-45. See also: Gravity Probe-B Phase B Final Report, George C. Marshall Space Flight Center, Huntsville, AL, February 1983.
103. Hopkins, R. A. and Castles, S. H.: Design of the Superfluid Helium Dewar for the Cosmic Background Explorer (COBE). SPIE Proceedings, Vol. 509, 1984, pp. 207-215.
104. Urban, E. W. and Ladner, D. R.: Infrared Telescope (IRT) System Cryogenic Performance. SPIE Proceedings, Vol. 509, 1984, pp. 216-232.
105. Fairbank, W. M., Everitt, C. W. F., and DeBra, D. B.: Final Report on NASA Grant 05-020-019 to Perform a Gyro Test of General Relativity in a Satellite and Develop Associated Control Technology. Stanford University, Stanford, CA, July 1977, pp. 271-272.
106. Seaman, C. H. and Sonnabend, D.: Semi-Drag Free Gravity Gradiometry. J. Astronaut. Sci., Vol. 33, No. 4, 1985.
107. "Advanced Propulsion Systems Concepts for Orbital Transfer Study," Final Report NAS8-33935, Vol. 1, D180-2668-1, Boeing Aerospace Company, Seattle, WA, 1981.
108. Bailey, W. L., De Sanctis, C. E., Nicaise, P. D., and Schultz, D. E.: "Payload Isolation and Stabilization by a Suspended Experiment Mount (SEM)," Space Shuttle Experiment and Environment Workshop, New England College, Henniker, NH, 1984.
109. Shrewsberry, D. J. and Olney, D. J.: Development of an Experiment of Opportunity Test Payload for the Space Transportation System. Seventeenth Space Congress, Cocoa Beach, FL, May 1980. See also: "Spartan in the Space Station Era," Contract NAS5-28057, OAO Corporation, Greenbelt, MD, July 1984.
110. NASA Space Systems Technology Model, Vol. II-A: Space Technology Trends and Forecasts, NASA, Washington, D.C., January 1984.

APPENDIX A

BACKGROUND ON GRAVITY

A.1 Units and Numbers

The gravity field is the vector sum of gravitational acceleration due to the mass of the Earth and the centrifugal acceleration associated with the rotation of the Earth. Since gravity is an acceleration, the appropriate SI unit is m sec^{-2} . Since gravity is a vector, one can discuss gravity in specified directions and in terms of magnitude. This report emphasizes the magnitude of gravity. The unit still widely used for gravity studies is the "gal" which is $10^{-2} \text{ m sec}^{-2}$. A sub-unit is the mgal which is 10^{-3} gal or $10^{-5} \text{ m sec}^{-2}$. The SI unit for density is kg m^{-3} , which is equivalent to $10^{-3} \text{ g cm}^{-3}$.

The average gravity on the surface of the Earth at the equator is approximately 980 gal. Gravity varies from the equator to the pole because the Earth's shape is flattened toward the poles and because of the reduction of centrifugal acceleration in going from the equator to the pole. Gravity also changes due to the variation in topography, lateral variations in internal mass, and to a much lesser extent by time variations associated with a variable rotation rate and changing internal mass distribution. Tidal variations in gravity are also caused by the attraction of the Sun, Moon, and planets. The variation of greatest interest for this discussion is that associated with internal density variations. The specific problem is known as the inverse problem which is the determination of the distribution of masses inside the Earth from gravity observations. It is a key area of research in geophysics and geodesy. The observed variations of gravity due to mass inhomogeneity are of the order of 10^{-6} to 10^{-4} of the average value of gravity, so that a convenient unit for discussing the gravity variations is the milligal, defined above.

Also of interest here is the linear gradient of gravity. The most commonly used unit is the Eötvös unit defined by $1 \text{ E} = 0.1 \text{ mgal/km}$ or 10^{-9} sec^{-2} . The vertical gradient of gravity at the surface of the Earth is about 3100 E.

A.2 Gravity and Its Relatives

Descriptions of the Earth's gravity field are given in terms of the gravity potential, from which gravity can be obtained by computing the spatial derivatives (see Table A-1). Normally, gravitational potential ϕ and its derivatives are discussed after the removal of a reference potential ϕ_{ref} associated with an ellipsoid whose shape (flattening) corresponds to the Earth, either as it now exists (the "spheroid"), or as it would be if it were a fluid affected only by gravitation and centrifugal acceleration (the "hydrostatic figure"). The net values $\delta\phi = \phi - \phi_{\text{ref}}$ can be used to calculate undulations in geoid height δN , gravity disturbances or anomalies δg , and various gravity gradients $\delta\Gamma_{ij}$. The relationships among some of these quantities are shown in Table A-1.

TABLE A-1. DEFINITIONS AND EXAMPLES OF EARTH'S GRAVITY PARAMETERS

<u>GRAVITY PARAMETER</u>	<u>DEFINITION</u>	<u>EXAMPLE (point mass)</u>
ANOMALOUS POTENTIAL	$\delta\Phi(\vec{r}) = - \int \frac{G \Delta\rho(\vec{r}_0)}{ \vec{r} - \vec{r}_0 } d\vec{r}_0$	$\delta\Phi = - \frac{G \Delta m}{r}$
GEOID HEIGHT UNDULATION	$\delta N = \frac{\delta\Phi}{g_0}$	$\delta N = \frac{\Delta m a^2}{r M_E}$
GRAVITY ANOMALY	$\delta\vec{g} = - \vec{\nabla} \delta\Phi$	$\delta g_r = - \frac{\partial\Phi}{\partial r} = - \frac{G \Delta m}{r^2}$
GRAVITY GRADIENT ANOMALY	$\delta\vec{\Gamma} = - \vec{\nabla} (\vec{\nabla} \delta\Phi)$	$\delta\Gamma_\pi = - \frac{\partial^2\Phi}{\partial r^2} = \frac{2G \Delta m}{r^3}$

G = Newton's gravitational constant; $\Delta\rho$ = density anomaly; \vec{r}, \vec{r}_0 = position vectors; Δm = mass anomaly; g_0 = average surface gravity; a = radius of the Earth; M_E = Mass of the Earth.

A.3 Spherical Harmonic Expansion

Spatial variations in these measures of the Earth's gravity field result from density contrasts distributed on and within the Earth. For density contrasts varying with horizontal length scales of thousands of kilometers, the density contrasts are commonly expressed in terms of spherical harmonics of degree ℓ and order m . For a given harmonic component of a density contrast $\Delta \rho_{\ell m}$, distributed over a thickness h at a depth z below the Earth's surface, the geoid anomaly $\delta N_{\ell, m}$, gravity anomaly $\delta g_{\ell m}$, and gravity gradient anomaly $\delta \Gamma_{\ell m}$ as evaluated at the Earth's surface ($r = a$) are given by

$$\delta N_{\ell m} = \frac{4\pi G a}{g_0(2\ell+1)} \left(\frac{a-z}{a} \right)^{\ell+1} \Delta \rho_{\ell m} h, \quad (A-1)$$

$$\delta g_{\ell m} = \frac{2\pi(\ell+1)G}{\left(\ell + \frac{1}{2}\right)} \left(\frac{a-z}{a} \right)^{\ell+2} \Delta \rho_{\ell m} h, \quad (A-2)$$

$$\delta \Gamma_{\ell m} = \frac{2\pi(\ell+1)(\ell+2)G}{\left(\ell + \frac{1}{2}\right) a} \left(\frac{a-z}{a} \right)^{\ell+3} \Delta \rho_{\ell m} h. \quad (A-3)$$

The approximate wavelength λ of a spherical harmonic of degree ℓ is

$$\lambda \approx \frac{2\pi a}{\ell + \frac{1}{2}}. \quad (A-4)$$

when $\lambda \ll a$ ($\ell \gg 10$), the following asymptotic Cartesian relations are valid:

$$\delta N(\lambda) = \frac{G \lambda \Delta \rho(\lambda) h}{g_0} \exp(-2\pi z/\lambda), \quad (A-5)$$

$$\delta g(\lambda) = 2\pi G \Delta \rho(\lambda) h \exp(-2\pi z/\lambda), \quad (A-6)$$

$$\delta \Gamma(\lambda) = \frac{4\pi^2 G \Delta \rho(\lambda) h}{\lambda} \exp(-2\pi z/\lambda). \quad (A-7)$$

A.4 Effects of Satellite Altitude and Source Depth

The above expressions quantify two important considerations which must be kept in mind in designing any program to measure the geopotential. The first is the inescapable attenuation by the factor $\exp(-2\pi z/\lambda)$ of the gravity signal with distance from its source (or, equivalently, height of observation). The amplitude is reduced by a factor of 0.1 for $z = 0.37 \lambda$, by a factor of 0.01 for $z = 0.74 \lambda$, and by a factor of 0.001 for $z = 1.1 \lambda$. At the satellite altitude of 200 km, surface gravity anomalies of 1000, 500, 200, 100, and 50 km wavelengths are attenuated by factors of 0.3, 0.08, 0.002, 3×10^{-6} , and 10^{-11} , respectively. Clearly, once $z > \lambda$, most gravitational signal is lost. Quoted here is the spatial resolution and accuracy necessary for gravity observations in order to address certain problems. We evaluate these requirements at the Earth's surface and consider the resolution to be one-half the shortest wavelength λ sampled by the data. The more severe accuracy requirements at satellite altitude can be calculated from these relations given the height above the Earth's surface and the desired resolution.

The second consideration is the fact that short wavelength gravity signals are dominated by the largest, shallowest density contrast, namely, the surface topography. For example, all of the following produce a 1 mgal gravity anomaly at the Earth's surface: a 10-m layer of crustal rock; a 1-km deflection of the Moho at depth $z = 0.7 \lambda$; a 4-km deflection of the Moho at $z = 0.5 \lambda$; a thermal anomaly of 100°C at the top of the mantle extending over a thickness of 80 km; a surface layer of water 25-m thick. The bottom line is that, if we wish to interpret gravity data accurately to x mgals in terms of crustal structure, thermal anomalies in the mantle, or dynamic sea surface, we must at the same time have measured the topography of the Earth's surface to within $10x$ m.

APPENDIX B

GRADIOMETRY FUNDAMENTALS

B.1 Introduction

This Appendix provides a basic discussion of the ideas involved in gravity gradiometry. A general description of the instrument is given, followed by a discussion of what they do and do not measure. Problems arising from rotation, self gravity, and scale factor errors are discussed, and the theory is applied to Earth-bound and orbital gradiometers.

B.2 Instrument Definitions

Most existing gradiometers are derived from accelerometers. So it is best to discuss them first. Accelerometers consist of a mass, spring restraints, and some kind of damping device. The springs are often magnetic or electrostatic, rather than mechanical. In response to either acceleration or gravity (the external field), the mass distorts the spring, yielding a measure of the field. Quality instruments apply an extra internal force to recenter the mass; the force applied is then a measure of the field. These are called "rebalance" accelerometers. An accelerometer in free fall sees the combination of acceleration and gravity, and measures nothing. This is intrinsic — Einstein's Principle of Equivalence states that purely inertial point measurements cannot distinguish between acceleration and gravity.

A number of these instruments are used solely for gravity measurements. They are designed to be used in a fixed location, and have high sensitivity and sluggish response. Such instruments are generally called "gravimeters." Of course, they too are sensitive to acceleration, and must generally be corrected for Earth rotation.

Most accelerometers have a single sensitive axis; i.e., they measure the components of the field vector along that axis. Some, such as spherical or cubical electrostatically supported types, are intrinsically three-axis. Three single-axis types can be combined to produce a full vector instrument. In this Appendix, it is assumed that any accelerometer is a vector instrument, although this is not always the case in practice.

The most common way to build a gradiometer is to connect two accelerometers rigidly, separated by some baseline vector $\vec{\ell}$, and subtract their outputs. This yields the component of the gradient (space rate of change) of the field vector along $\vec{\ell}$. With additional accelerometers and baselines, one may construct the full nine element tensor gradiometer; i.e., the rate of change of each field vector component along each spatial axis. Most existing and planned gradiometers consist of some variation on this simple notion.

An instrument built by R. L. Forward of Hughes Research Laboratories uses no accelerometers, but measures the gradient directly by means of a rotating, spring coupled, cross [B-1]. A variation of the Forward design has recently been constructed by A. Čadež of the University of Lyublyana. Another device, built by M. B. Trageser of Draper Laboratories, uses a spherical floated dumbell to measure the gradient,

somewhat akin to gravity gradient stabilized satellites [B-2]. While the theoretical treatment below is based on separated accelerometers, the results apply equally to direct gradient measurements.

Calculation needs coordinates, starting with a reference (inertial) coordinate system E^R . An arbitrary location in this system is given by \vec{r} , with components x_i : $i = 1, 2$, or 3 . Within this, assume that the first accelerometer is at location \vec{R} ; and the second is at location $\vec{R} + \vec{\ell}$. There are also instrument axes E^I . The origin is at \vec{R} , and the orientation is such that $\vec{\ell}$ lies along E_1^I . Thus, in E^I , the second accelerometer is located at $(\ell, 0, 0)$.

B.3 Gravity

A central tenet of gravitational physics is that the vector gravitational field is derivable from a scalar potential $\phi(\vec{r})$. That is, the acceleration of a test mass in this field is given by

$$\vec{a} = -\vec{\nabla} \phi(\vec{r}) \quad , \quad (B-1)$$

or, in components

$$a_i = -\partial_i \phi(\vec{r}) \quad , \quad (B-2)$$

where $\partial_i \equiv \partial x_i$. The gradient, or space rate of change of \vec{a} may be written as

$$\vec{\Gamma} = \vec{\nabla} \vec{a} = -\vec{\nabla} \vec{\nabla} \phi(\vec{r}) \quad , \quad (B-3)$$

or, in components,

$$\Gamma_{ij} = -\partial_i \partial_j \phi(\vec{r}) \quad . \quad (B-4)$$

Observe that, as the derivatives commute, the gravity gradient tensor is always symmetric. In addition, a well-known result of potential theory is that $\phi(\vec{r})$, due to all mass not at \vec{r} , must obey the Laplacian equation:

$$\nabla^2 \phi(\vec{r}) = 0 \quad . \quad (B-5)$$

From equation (B-4), this immediately shows that the trace of the tensor $\overleftrightarrow{\Gamma}$ must vanish.

It is useful to carry out these calculations for the field due to a point mass, or a spherically symmetric body. Assuming the body to be at the origin, the potential is generally taken to be

$$\phi(\vec{r}) = -GM/r \quad , \quad (B-6)$$

where M is the mass of the body, and $G = 6.670 \times 10^{-11} \text{ m}^3 \text{ kg}^{-1} \text{ sec}^{-2}$ is the universal gravitational constant. Putting this into equation (B-1) gives the well-known force law:

$$\vec{a} = -GM\vec{r}/r^3 \quad . \quad (B-7)$$

Then, from equation (B-3), the gradient works out to be

$$\overleftrightarrow{\Gamma} = \frac{GM}{r^3} \left(\frac{3}{r^2} \vec{r} \vec{r} - \overleftrightarrow{I} \right) \quad . \quad (B-8)$$

Here, \overleftrightarrow{I} is the 3×3 identity tensor, and $\vec{r} \vec{r}$ may be thought of as an outer product, or as a dyadic, rather than as a tensor. The symmetry of $\overleftrightarrow{\Gamma}$ is obvious, and it is not hard to show that it is trace-free.

So, what does the instrument read? To first order, the field at the second accelerometer is

$$\vec{a}(\vec{R} + \vec{\ell}) = \vec{a}(\vec{R}) + \vec{\ell} \cdot \vec{\nabla} \vec{a} \quad . \quad (B-9)$$

As the instrument reads the difference of the two accelerometers, this measurement is, from equation (B-3),

$$\vec{Z}_g = \vec{\ell} \cdot \overleftrightarrow{\Gamma} = -\vec{\ell} \cdot \vec{\nabla} \vec{\nabla} \phi(\vec{R}) \quad , \quad (B-10)$$

which, for a spherical or point mass, becomes

$$\vec{Z}_g = \frac{GM}{R^3} \left[\frac{3(\vec{\ell} \cdot \vec{R})}{R^2} \vec{R} - \vec{\ell} \right] \quad , \quad (B-11)$$

from equation (B-8). These expressions will be used in Sections B.5 and B.6 to see what is measured under various conditions, on Earth and in orbit.

The units of gradient are readily seen to be sec^{-2} . As real gradients are nowhere near this large, the Eötvös unit is now widely used. By definition, $1 \text{ E} = 10^{-9} \text{ sec}^{-2}$ (Appendix A).

B.4 Rotation

If two perfect, rigidly connected accelerometers are subtracted, neither linear acceleration nor uniform gravity will produce any output. Rotation, however, is another matter, requiring some fairly careful analysis. Suppose E^1 to be rotating at angular velocity $\vec{\Omega}$ relative to E^R . Then, by arbitrarily choosing the origin of E^1 to be the fixed center of rotation, the velocity of the first accelerometer can always be expressed as

$$\dot{\vec{R}} = \dot{\vec{R}}_0 + \vec{\Omega} \times \vec{R} \quad , \quad (\text{B-12})$$

where \vec{R}_0 is the position vector in an inertial reference frame.

Here and below, the time derivatives are inertial. Thus, the acceleration perceived by the first accelerometer is

$$\vec{Z}_1 = \ddot{\vec{R}} = \ddot{\vec{R}}_0 + \vec{\Omega} \times \vec{R} + \dot{\vec{\Omega}} \times \vec{R}_0 + \vec{\Omega} \times (\vec{\Omega} \times \vec{R}) \quad . \quad (\text{B-13})$$

The corresponding analysis for the second accelerometer merely replaces \vec{R} by $\vec{R} + \vec{\ell}$. Since $\vec{\ell}$ is invariant in E^1 , we may write

$$\dot{\vec{\ell}} = \vec{\Omega} \times \vec{\ell} \quad , \quad (\text{B-14})$$

after which the second accelerometer output is

$$\vec{Z}_2 = \frac{d}{dt} [\dot{\vec{R}} + \vec{\Omega} \times \vec{\ell}] = \vec{Z}_1 + \dot{\vec{\Omega}} \times \vec{\ell} + \vec{\Omega} \times (\vec{\Omega} \times \vec{\ell}) \quad . \quad (\text{B-15})$$

Now, if the output of an accelerometer is taken to be positive for a gravity field in a particular direction, then an acceleration in the same direction will yield a negative output, as may be seen by examining the displacement of the mass inside the accelerometer. Thus, by subtracting the two perceived accelerations, and including a gradient $\vec{\Gamma}$, the overall instrument output is

$$\vec{z} = \vec{\Gamma} \cdot \vec{\ell} - \dot{\vec{\Omega}} \times \vec{\ell} - \vec{\Omega} \times (\vec{\Omega} \times \vec{\ell}) \quad . \quad (\text{B-16})$$

The overall sign of z is arbitrarily chosen.

Examination of equation (B-16) shows that it is a linear homogeneous function of the elements of $\vec{\ell}$. Thus, it may be factored into the form:

$$\vec{z} = (\vec{\Gamma} + \Omega^2 \vec{\Gamma} - \vec{\Omega} \vec{\Omega} - \dot{\vec{\Omega}}) \cdot \vec{\ell} \quad (B-17)$$

Here, the $\vec{\Gamma}$ and $\vec{\Omega} \vec{\Omega}$ terms are symmetric, while

$$\vec{\Omega} = \begin{bmatrix} 0 & -\Omega_3 & \Omega_2 \\ \Omega_3 & 0 & -\Omega_1 \\ -\Omega_2 & \Omega_1 & 0 \end{bmatrix} \quad (B-18)$$

contributes the only skew-symmetric terms. Components may be taken in any coordinate system, but E^I is usually the most convenient.

The rotation modified gradient tensor in equation (B-17) is neither symmetric nor traceless. Moreover, it is intrinsic in that, as $\vec{\ell}$ factors out, it is independent of the design of the instrument. Thus, extracting $\vec{\Gamma}$ from sets of measurements \vec{z} requires some combination of attitude acceleration and rate sensors, together with some form of dynamical estimator.

Measuring $\vec{\Omega}$ to the accuracy required for gradiometric corrections is not routine. If the measurement error in some gyro axis is $\delta \Omega$, then the corresponding error in correcting a gradient component is of order $\Omega \delta \Omega$. For example, consider an inertial-grade gyro with an uncompensated drift rate of 10^{-8} rad sec $^{-1}$. Then, to keep correction errors below, say, 0.1 E, consistent with conventional ground instruments of around 1 E sensitivity, requires that rotation rates be kept below about 0.01 rad sec $^{-1}$ — a significant constraint in many applications. For orbital applications, intended to reach 0.001 E, keeping the rotation correction error below 10 percent of this would require rates below about 10^{-5} rad sec $^{-1}$, or well below orbital rate, for the same gyro. Even in the laboratory, it would be necessary to mount these instruments on a rate table to remove the Earth's spin rate.

Estimating the $\dot{\vec{\Omega}}$ terms to adequate accuracy is not routine either. For the Earth and orbital examples above, determination errors of 10^{-10} and 10^{-12} rad sec $^{-2}$, respectively, would be about the limit of our tolerance. Note, however, that recovering the trace of $\vec{\Gamma}$ is not affected by $\dot{\vec{\Omega}}$ errors.

B.5 On Earth

The general size of the gradient due to a spherically symmetric mass is given by the coefficient in equation (B-8):

$$\Gamma_0 = GM/r^3 \quad . \quad (B-19)$$

For the Earth, at mean sea level, this amounts to 1540 E. From the rest of equation (B-8), components range from $-\Gamma_0$ (horizontal-horizontal) to $2 \Gamma_0$ (up-up).

If the gradiometer is fixed, then rotation is that of the Earth, 7.29×10^{-5} rad sec^{-1} . Thus, the rotation corrections are of order 5.3 E, which can be a serious nuisance, as just shown.

The main application of gradiometry on Earth is gravity surveys from moving vehicles, because of the great difficulty of removing dynamic effects for gravimeters. However, even fixed-base gravimeters are affected by seismics, to which rotation corrected gradiometers are essentially immune [B-3] (see Section VI of Appendix E for vibration effects in a practical gradiometer). However, another potential use of the gradiometer technology is in inertial navigation of air or land vehicles, in which measurement of $\vec{\Gamma}$ may be used to correct for unknown local gravity variations. For this, if the vehicle follows some path C, then the running gravity vector may be expressed as

$$\vec{g}(t) = \vec{g}_0 + \int_C \vec{\Gamma} \cdot d\vec{S} = \vec{g}_0 + \int_0^t \vec{\Gamma} \cdot \vec{v} dt \quad . \quad (B-20)$$

As \vec{v} is measured by the inertial navigator, the \vec{g} corrections may be determined if $\vec{\Gamma}$ is measured en route, and if the starting value \vec{g}_0 is known.

It is of interest to see what effect nearby objects have. Table B-1 lists Γ_0 for several common disturbing objects. This idea is extended in Figure B-1. If the tolerance for disturbance corresponds to some Γ_0 line, then the mass-distance coordinates of all unknown objects must be kept above that line. Some of the examples in Table B-1 are plotted in Figure B-1 to get a better feeling for how much trouble they can cause. As gradiometers now under development are promising sensitivities well below 1 E, they are definitely not "hands on" instruments.

Next, consider what a gradiometer would read, if fixed to the Earth. Suppose the reference coordinates have their origin at the center of the Earth, and that E_1^R passes through the instrument at the surface, then $\vec{R} = (R_E, 0, 0)$, and from equation (B-8), the gradient is essentially given by

$$\vec{\Gamma} = \Gamma_0 \begin{bmatrix} 2 & 0 & 0 \\ 0 & -1 & 0 \\ 0 & 0 & -1 \end{bmatrix} \quad . \quad (B-21)$$

An instrument with a vertical baseline $\vec{\ell} = (\ell, 0, 0)$ would then actually measure $\vec{z} = (2\ell\Gamma_0, 0, 0)$, ignoring the rotation correction. What would this instrument read if it were tipped over? Specifically, suppose $\vec{\ell}$ is rotated about E_2^R through some angle θ . Applying this rotation as a symmetry transformation to $\vec{\Gamma}$ yields the instrument axis tensor components:

$$\vec{\Gamma} = \frac{\Gamma_0}{2} \begin{bmatrix} 1 + 3 \cos 2\theta & 0 & 3 \sin 2\theta \\ 0 & -2 & 0 \\ 3 \sin 2\theta & 0 & 1 - 3 \cos 2\theta \end{bmatrix}, \quad (\text{B-22})$$

from which the measurement is $\vec{\ell}$ times the first row. Here, the measurement z_1 would arise from an accelerometer pair with sensitive axes aligned along $\vec{\ell}$; the null reading z_2 when the sensitive axes are along E_2^R ; and z_3 when the sensitive axes are orthogonal to $\vec{\ell}$ and in the plane of rotation. Note that both z_1 and z_3 vary sinusoidally, with the same amplitude, and with two cycles per rotation. Of course, the remaining components of $\vec{\Gamma}$ could be revealed, if a more general $\vec{\ell}$ were considered. Increasing the reality, by including the effects of a non-spherical Earth, the Earth's rotation, and instrument noise and bias, would add greatly to the algebra, but not much to our understanding.

One instrument problem, scale factor error, should be discussed here. In gradiometers, the main source of scale factor error is mismatch of the input-output curves of the two accelerometers; i.e., volts (or whatever) out versus acceleration input. For a simple illustration, suppose the instrument is exposed to an acceleration field A , plus a gradient field Γ . Moreover, suppose the second accelerometer has output gain K , and the first has $K(1+\epsilon)$. Then, the measurement is (again neglecting rotation)

$$z = K (A + \ell \Gamma) - K (1 + \epsilon) A = K (\ell \Gamma - \epsilon A) . \quad (\text{B-23})$$

Interpreting this output as purely due to gradient leads to an error:

$$\delta \Gamma = \epsilon A / \ell . \quad (\text{B-24})$$

Note that this error is proportional to the common acceleration field A . On Earth, this could be as bad as $1g$, if the accelerometer input axes are vertical. For example, if gains are matched to 1 part in 10^4 , the residual mismatch is calibrated to 1 part in 10^4 , and the sensitive axes are within 1 mrad of the horizontal, then a baseline $\ell = 0.2$ m would result in errors of order $0.5 E$. Since longer baselines can lead to serious vibration problems, scale factor errors have led to severe design restraints in Earth-bound instruments.

B.6 In Orbit

Matters are not essentially different in orbit. Imagine a free-falling accelerometer in space. A gravity field will affect the proof mass and case equally, causing a common acceleration, but no deflection of the spring. Thus, it will read zero. Imagine a gradiometer aboard some inertially oriented satellite. Now, the only point in the satellite where an accelerometer would read zero is the center of mass. If the reference coordinate system is centered there, then the first accelerometer would read $\vec{r} \cdot \vec{R}$; while the second would read $\vec{r} \cdot (\vec{R} + \vec{\ell})$. Thus, the gradiometer would read $\vec{r} \cdot \vec{\ell}$, as on Earth. The practical difference is that much weaker and more sensitive springs can be used, and that the common acceleration is reduced to the drag level, which lowers the scale factor error by several orders of magnitude.

Finally, what happens in a satellite in a circular orbit, maintaining a constant Earth-fixed attitude, will be examined. First, for a spherical Earth, Keplerian orbit theory shows that

$$\Gamma_O = G M / r^3 = \Omega_O^2, \quad (B-25)$$

where Ω_O is the magnitude of $\vec{\Omega}$, the orbital angular velocity. The same reference coordinates as used on the Earth, where E_1^R continues to be up, are adopted here; E_3^R is now the orbit normal, so that E_2^R is forward. In this system, $\vec{\Omega}_O = (0, 0, \Omega_O)$; so, for a spherical Earth, the measurement equation (B-17) can be calculated from the gradient equation (B-21), resulting in

$$\vec{z} = \Omega_O^2 \begin{bmatrix} 3 & 0 & 0 \\ 0 & 0 & 0 \\ 0 & 0 & -1 \end{bmatrix} \cdot \vec{\ell}. \quad (B-26)$$

This curious result comes about because the rotation is tied to gravity. It is interesting to note that, except for the $\vec{\ell}$ term, equation (B-26) is just the stress tensor seen by a gravity stabilized satellite, with tension along the yaw axis and compression along the pitch axis. Of course, in the real world, \vec{z} would be complicated by the Earth's asphericity, orbital eccentricity, and attitude motions.

REFERENCES

- B-1. Forward, R. L., Hughes Research Laboratories, Research Report 469, 1973.
- B-2. Trageser, M. B., in Proceedings of the 2nd International Symposium on Inertial Technology for Surveying and Geodesy, edited by K. Schwartz, Canadian Institute of Surveying, Ottawa, 1981.
- B-3. Moody, M. V., Chan, H. A., and Paik, H. J.: Superconducting Gravity Gradiometer for Terrestrial and Space Applications. J. of Appl. Phys., Vol. 60, 1986, pp. 4308-4315. Reproduced as Appendix E of this report.

TABLE B-1. DISTURBING FIELDS

<u>Number</u>	<u>Object</u>	<u>Mass (kg)</u>	<u>Distance (m)</u>	<u>Γ_o (E)</u>
1	Whole Earth	5.98×10^{24}	6.37×10^6	1540
2	Equivalent Earth	1	0.035	1540
3	Equivalent Earth	2.31×10^4	1	1540
4	1 km ³ Mountain	3×10^{12}	10^3	200
5	Building	3×10^4	10	2.0
6	Boulder	10^4	4	10.4
7	Small car	10^3	2	8.3
8	Calibrated Disturbance	15	1	1.0
9	Standard object	1	1	0.067
10	Man next to instrument	70	0.7	14
11	Battery next to instrument	0.3	0.1	20
12	Internal component	0.1	0.03	250

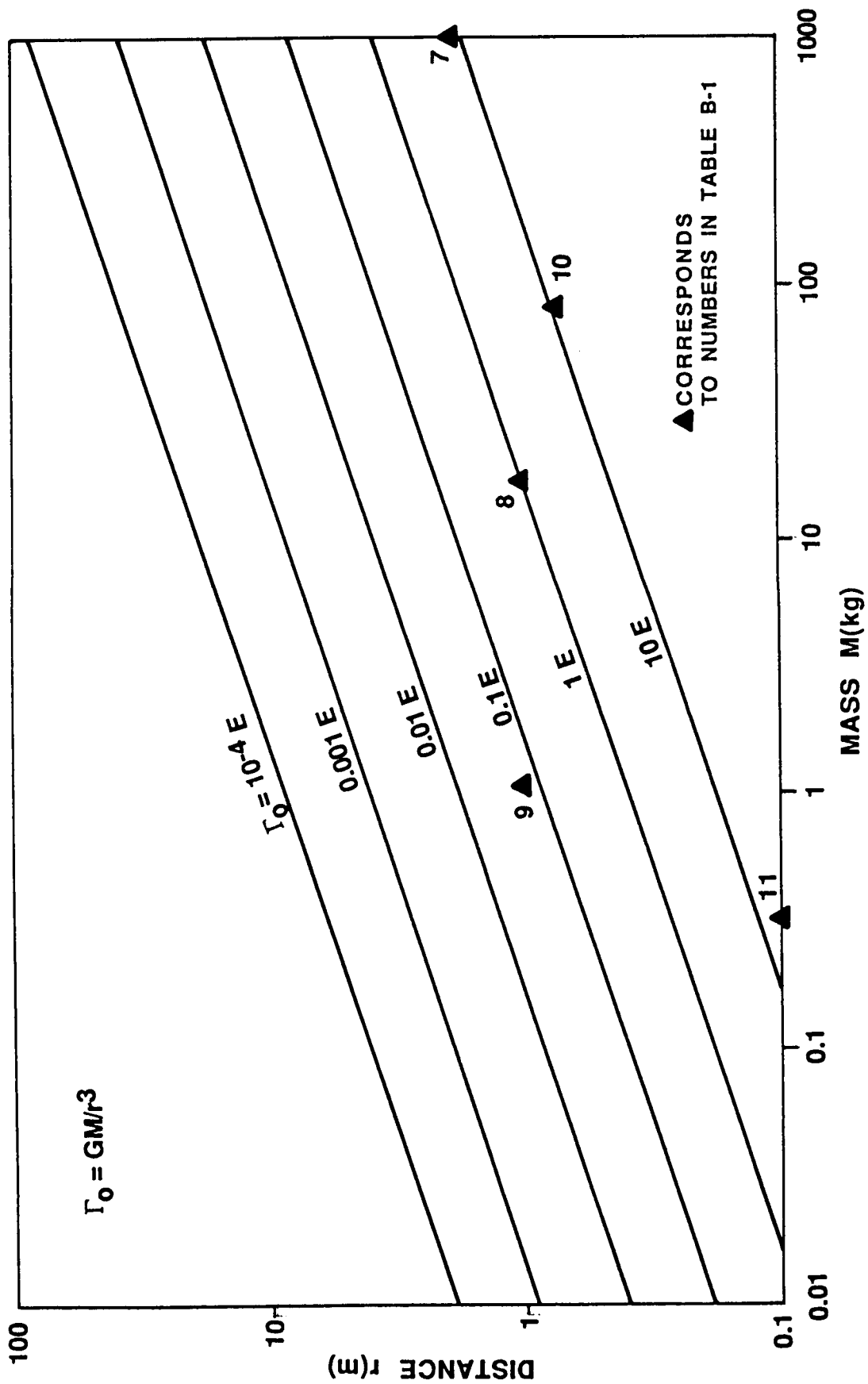


Figure B-1. Gradient sensitivity levels.

APPENDIX C

ERROR ANALYSES AND SIMULATION STUDIES OF A GRADIOMETER MISSION

Error analysis studies of satellite gradiometry fall into two categories: regional gravity field mapping and global gravity field mapping. The regional approach is limited in the spectral information by the size of the regional area. Global approaches, on the other hand, provide general information about the average gravity at all wavelengths. In both cases, the effect of instrument precision, satellite altitude, orbit error, and spacecraft dynamics puts a limit on the harmonic coefficients, or mean anomaly block sizes, that can be recovered from a gradiometry mission.

In this Appendix, some of the error analysis studies are summarized. Figures C-1 and C-2 display the results of these studies in terms of the recovery errors for $1/2$ deg x $1/2$ deg and 1 deg x 1 deg mean anomaly blocks. Instrument precision levels are 10^{-2} , 10^{-3} , 10^{-4} E with a 4-sec measurement sampling at 160 and 200 km altitudes for a six-month mission duration. The methods included do not necessarily reflect an exhaustive list, but are representative of the alternative techniques which may be used in analyzing gravity gradiometer data.

C-1. Regional Analyses

Kahn et al. [C-1] employs the Stokes-Pizetti form, which gives the anomalous potential at altitude, to relate mean gravity anomalies in the surface of the Earth to the second derivatives of the gravitational potential (the output of the gradiometer). A covariance matrix of a group of $1/2$ deg x $1/2$ deg mean anomaly blocks are derived in a 7.5 deg x 7.5 deg region. They assume that prior information about the mean anomalies exists with a 30-mgal uncertainty, and this information is introduced into the covariance matrix computations. They calculate the uncertainty of a 1 deg x 1 deg block centered in the region using a $1/2$ deg block full covariance matrix. Results displayed in Figures C-1 and C-2 are for a three-axis gravity gradiometer.

Tscherning [C-2] gives results based on the application of the least-squares collocation method to 400 gradient data points of a 3-axis gravity gradiometer with 0.125 deg x 0.25 deg spacing, using a spherical harmonic solution complete to degree and order 360 of Rapp and Cruz [C-3]. He assumes potential coefficients up to degree 60 are well known. He reports sensitivity due to the altitude.

Robbins' analysis [C-4] is also based on the least-squares collocation technique. A radial-axis gradiometer data is centered using a high degree and order reference field to meet the requirement of the collocation method. The degree variance model of Tscherning and Rapp is used in generating the error covariance matrices for the mean gravity anomalies. Results given in Figures C-1 and C-2 are for 15' data spacing in a 2.5 deg x 2.5 deg area.

Ilk's [C-5] results are byproducts of a Satellite-to-Satellite Tracking (SST) simulation analysis. In a differential mode, two satellites with a 50-cm separation is radial, along the cross tracks emulate a three-axis satellite gradiometer. In a simulation, he generates residual 1 deg x 1 deg mean gravity anomalies using the difference

of a spherical harmonic representation of the Earth's gravity field up to degree 180 of Rapp [C-6] and spherical harmonic representation up to degree 36 of GRIM 3-L1 (Reigber et al., [C-7]). Range rate observations between two satellites are generated over a 6-month period over a test area for two satellites at 160-km polar orbit. These results are reduced by Fourier expansion using numerical quadrature. A regularized solution describing the downward continuation process from satellite altitude to the Earth's surface is then performed. Recovered residual mean gravity anomalies are compared with the simulated original values and different norms of the simulated-recovered mean anomalies are computed. Relative and absolute position errors and relative velocity errors are presented in the orbit determination process. Ilk reports low sensitivity to the instrument noise and orbital error for a three-axis gradiometer.

C.2 Global Analyses

Jekeli and Rapp [C-8] and Rapp [C-9] develop a global radial-axis gradiometry data error analysis method, using a degree variance model for the harmonic coefficients. In this approach, the degree at which the gradient signal is equivalent to white instrument noise is determined in the power spectrum. Mean gravity anomaly uncertainties are computed using covariance propagation (in Moritz sense) up to the maximum degree variance implied by the harmonic degree at which signal-to-noise ratio equals one (commission error). The effect of higher degree harmonics (omission error) are then added into the error estimates resulting in a total rms error budget. Rapp [C-9] calculates 315, 406, and 497 highest degree estimates at which signal-to-noise ratio is unity at 160 km altitude for 10^{-2} , 10^{-3} , 10^{-4} E instrument precision. These estimates reduce to 253, 326, 399 at 200 km altitude, indicating the dependency of the harmonic coefficient recovery uncertainties on the altitude.

Colombo [C-10, C-11] carried out an error analysis study including the effect of orbit, instrument drift, and satellite attitude errors. The analysis consists of constructing and inverting the normal matrix of a least-squares adjustment of all coefficients of degrees between $3 < n < 360$. Full tensor elements are first represented in spherical harmonics and then transformed to a time series using Kaula's formulation for the gravitational potential. Orbit errors, rotation of the instrument, and instrument drift are assumed to be contained in a low-frequency band below 3 cycles per revolution. Normal matrix of the potential coefficients are constructed up to the degree and order 360. Mean anomaly block rms errors are calculated from the estimated potential coefficient uncertainties. Colombo gives an empirical law as a function of degree n for the average accuracies of the potential coefficients. Using this law, he extends his 360 degree and order solution results of $n = 600$, which is close to the folding frequency for the 4-sec instrument sampling (Figs. C-1 and C-2). He reports 377, 467, 556 degree truncation at 160-km altitude, and 288, 377, 449 degree truncation at 200 km for different instrument precision. For $1/2$ deg \times $1/2$ deg mean anomaly block sizes, he calculates 377, 467, 556 at 160-km altitude, and 288, 377, and 449 maximum harmonic degree at 200-km altitude.

C.3 Summary

The studies demonstrate the significant impact of satellite gradiometry on improving the models of the Earth's gravity field. Preliminary studies of the effect of orbit errors, instrument drift, and satellite attitude errors indicate manageable influence on

the recovery. Special techniques and combinations of different components will reduce the propagation of these errors on gravity field parameters.

The estimates about the effect of different satellite altitudes and instrument precision vary among different solutions, partly because of the different statistics reportedly used in these studies. Results displayed in Figures C-1 and C-2 should be interpreted accordingly. Presently, the accuracy estimates for the gravity anomaly recovery, which include commission and omission errors based on signal-to-noise ratio of unity, are more complete.

An analysis based on the local tensor component representation by Fourier series, as outlined in Balmino et al. [C-12], would complement the regional studies.

REFERENCES

- C-1. Kahn, W., Iz, H. B., and Brown, R. D.: Estimation of Local Mean Gravity Anomaly Errors Using a Spaceborne Gravity Gradiometer. Presented at the 1988 AGU Baltimore Meeting, 1988.
- C-2. Tscherning, C. C.: Satellite Altitude Influence on the Sensitivity of Gravity Gradiometer Measurements. A study prepared for Dornier System GMBH, 1987.
- C-3. Rapp, R. H. and Cruz, J. Y.: Spherical Harmonic Expansions of the Earth's Gravitational Potential to Degree 260 Using 30' Mean Anomalies. OSU, Dept. of Geodetic Science and Surveying, Report No. 376, Columbus, 1986.
- C-4. Robbins, J. W.: Least Squares Collocation Applied to Local Gravimetric Solutions from Satellite Gravity Gradiometer Data. OSU, Department of Geodetic Science and Surveying, Report No. 368, Columbus, 1985.
- C-5. Ilk, K. H.: Regional Gravity Field Mapping: Satellite Gravity Gradiometry versus Satellite to Satellite Tracking Techniques. Presented at the XIX Assembly of the IUGG, Vancouver, 1987.
- C-6. Rapp, R. H.: The Earth's Gravity Field to Degree and Order 180 using SEASAT Altimeter Data, Terrestrial Gravity Data, and Other Data. OSU, Dept. of Geodetic Science and Surveying Rep. No. 322, Columbus, 1985.
- C-7. Reigber, C., Balmino, G., Muller, H., Bosch, W., and Moynot, B.: GRIM Gravity Model Improvement Using LAGEOS (GRIM 3-L1). J. Geophys. Res., Vol. 90, No. B 11, 1985, pp. 9285-9299.
- C-8. Jekeli, C. and Rapp, R.: Accuracy of the Determination of Mean Anomalies and Mean Geoid Undulations from a Satellite Gravity Field Mapping Mission. Report No. 307, OSU, Dept. of Geodetic Science and Surveying, Columbus, 1980.
- C-9. Rapp, R. H.: Signals and Accuracies to be Expected from a Satellite Gradiometer Mission. OSU, Dept. of Geodetic Science and Surveying, Columbus, 1988.
- C-10. Colombo, O. L.: The Global Mapping of the Gravity Field with an Orbiting Full Tensor Gradiometer: An Error Analysis. Presented at the XIX Assembly of the IUGG, Vancouver, 1987.
- C-11. Colombo, O. L.: Full Tensor Gradiometer Error Analysis in Spherical Harmonics. Presented at the Gradiometer Workshop Meeting at GSFC, April 27, 1988.
- C-12. Balmino, G., Letoquart, D., Barlier, F., Ducasse, M., Bernard, A., Saclenux, B., Bouzat, C., Runavox, J. J., Lepichon, X., and Souriau, M.: Le Projet Gradio et La Determination a Haute Resolution du Geopotentiel. Bulletin Geodesique, Vol. 58, 1984, pp. 151-179.

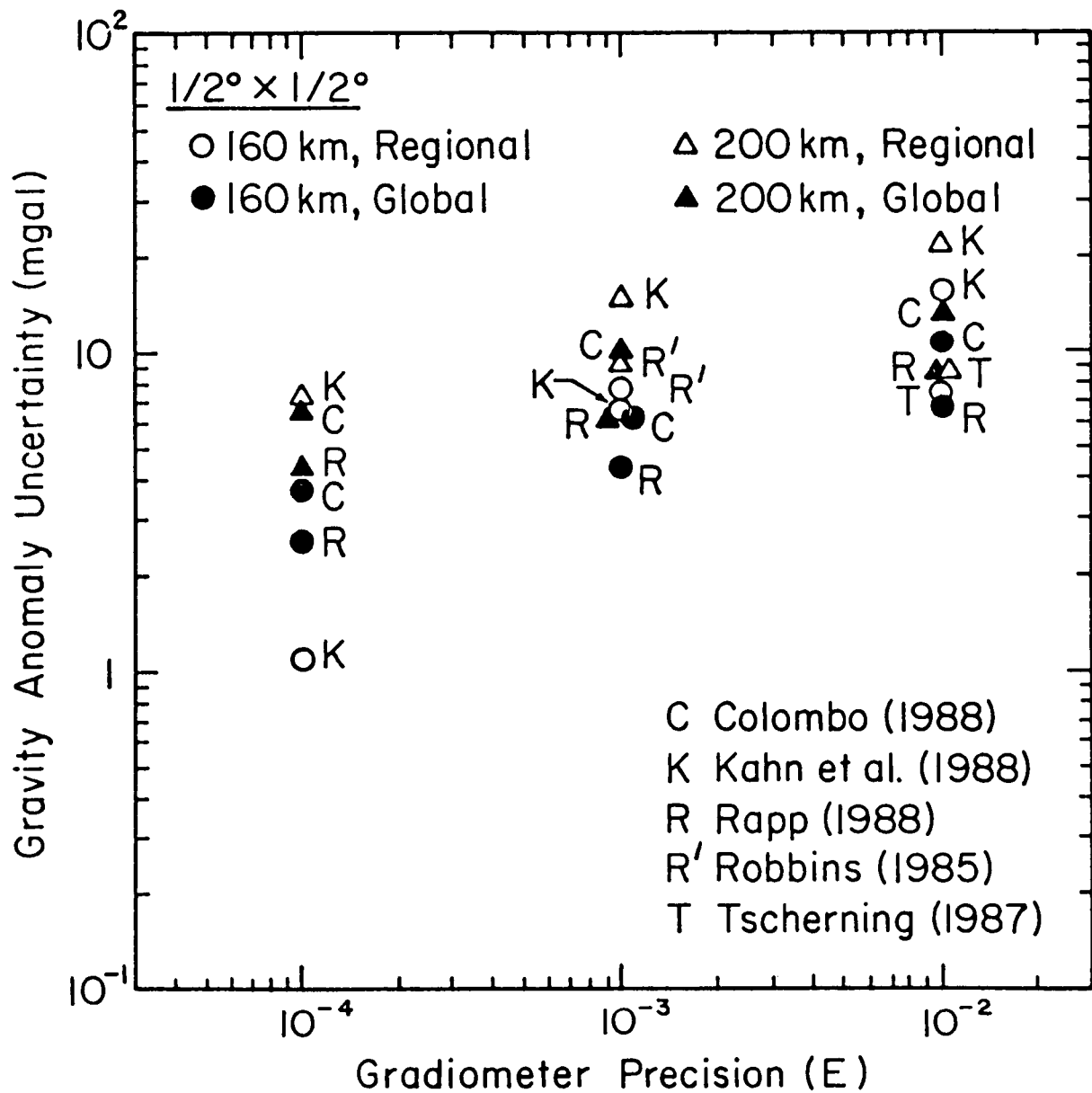


Figure C-1. Gravity anomaly uncertainty versus gravity gradiometer precision ($1/2^\circ \times 1/2^\circ$).

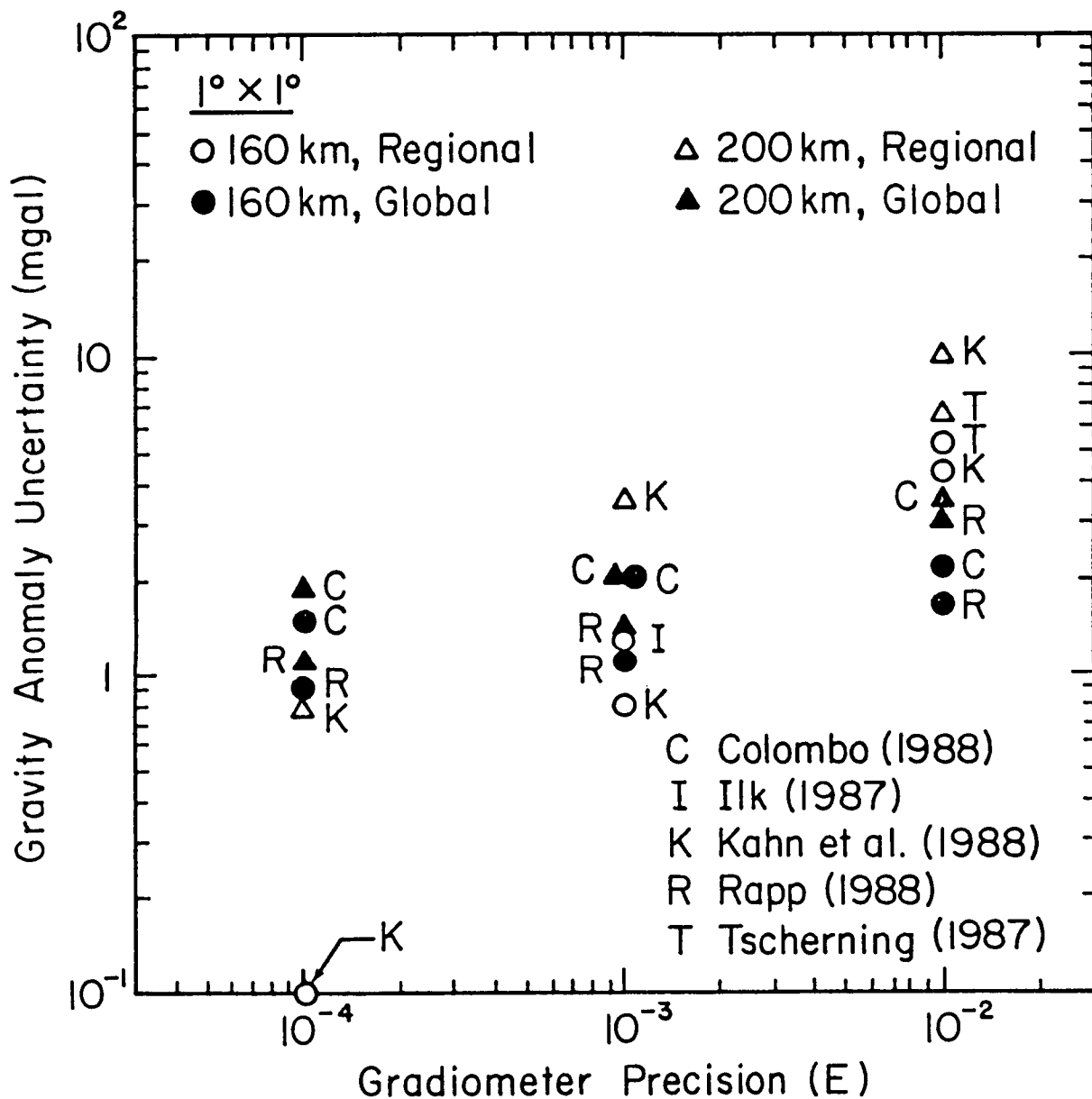


Figure C-2. Gravity anomaly uncertainty versus gravity gradiometer precision (1 deg x 1 deg).

NULL TEST OF INVERSE SQUARE LAW

Precision Measurement and Fundamental Constants II, B. N. Taylor and W. D. Phillips, Eds., Natl. Bur. Stand. (U.S.), Spec. Publ. 617 (1984).

Experimental Test of a Spatial Variation of the Newtonian Gravitational Constant at Large Distances*

H. A. Chan and H. J. Paik

Department of Physics and Astronomy, University of Maryland, College Park, MD 20742

The Poisson equation of Newtonian gravitational potential provides a source-independent null test of the Inverse Square Law. A convenient Laplacian detector consists of superconducting gravity gradiometers in three orthogonal directions. Matching and stability of the cryogenic detector are achieved by utilizing superconducting circuits. Since the Laplacian of the gravitational potential produced by an arbitrary source is zero outside the source in the Inverse Square Law, this experiment becomes a source-independent null test for the constancy of the gravitational constant. This characteristic allows a precision test of the Inverse Square Law at geological distances using natural objects like an ocean or the earth. We discuss experimental procedures and expected sensitivities of the null experiment for three different sources: a swinging pendulum, an ocean tide, and the earth itself. It appears that the empirical limits in the Inverse Square Law could be improved by three to six orders of magnitude in the range between 1 m and 10^7 km by this new null experiment.

Key words: gravitational constant; gravitational null experiment; inverse square law of gravitation; superconducting gravity gradiometer.

1. Introduction

The gravitational constant G is considered to be constant both with time and space in Newton's Universal Law of Gravitation and Einstein's General Theory of Relativity. It is possible, however, to make G a function of time [1] or a function of mass separation [2] within metric theories of gravity. A spatial variation of G has also been predicted on other theoretical grounds [3-6]. Most of these theories favor a functional dependence

$$G(R) = G[1 + \alpha(1 + \mu R)e^{-\mu R}], \quad (1)$$

which arises from a potential of the form

$$\phi(R) = \frac{GM}{R} (1 + \alpha e^{-\mu R}). \quad (2)$$

Therefore, a spatial dependence of G , if detected, could imply the existence of an additional short-range force which is superposed over the Newtonian long-range force rather than necessarily a failure of the Inverse Square Law.

Various authors have pointed out [7-9] that the existing data on absolute G and the product GM for the earth and other celestial bodies cannot rule out the possibility of α having a value as large as $1/3$, if the range μ^{-1} falls somewhere between 10 m and 10 km. Efforts have been made recently to extend the Cavendish-type experiments up to a mass separation of $R \sim 10$ m [10-14]. Inference from orbits of artificial satellites on the constancy of G for $R \leq 10^3$ km is difficult on account of the rapid fall-off of any non-Newtonian signal as μ^{-1} is reduced below the satellite altitude. As a result, the intermediate distance range $10 \text{ m} \leq R \leq 10 \text{ km}$ has been left largely untested to this date. It is highly desirable to be able to examine $G(R)$ on this range and improve the overall experimental limits in the constancy of G as a function of R . Such an experiment will test the scale invariance of the Universal Law of Gravitation and help settle issues raised by opposing theories of gravity.

In this paper, we discuss a series of experiments which could cover the desired geological scale and might improve the empirical limits on α at large distances by several orders of magnitude. These experiments are based on the principle of a *null* experiment proposed by Paik [15]. The "source-independent" nature of the experiments permits use of a large natural object like a mountain, an ocean tide, or the earth itself as a source to examine the Inverse Square Law at the characteristic distances of these objects. In the following sections, the principle of the gravitational null experiment is reviewed, experimental procedures for a laboratory, geological-scale, and earth-orbit experiment are discussed, and the expected resolutions of these experiments are presented. In addition, the principle and design of the gravitational null detector are briefly described.

2. Principle of a Null Experiment

The "source independent" null experiment invokes a well-known theorem in gravitostatics: Gauss's law for Newtonian gravity. In differential form, it is embodied in a Poisson equation

$$\nabla^2 \phi(\mathbf{x}) = -\nabla \cdot \mathbf{g}(\mathbf{x}) = 4\pi G \rho(\mathbf{x}), \quad (3)$$

where $\mathbf{g} = -\nabla \phi$ is the gravitational field (force per unit mass). Since the unique solution of Eq. (3) is the $1/R$ potential, which is characteristic of an inverse square force law, it is clear that the Poisson equation for ϕ is equivalent to a constant G , $G \neq G(R)$, in the force equation

$$\mathbf{g}(\mathbf{x}) = -\int_V G(R) \frac{\rho(\mathbf{x}')}{R^2} d^3x', \quad (4)$$

where $R = |\mathbf{x} - \mathbf{x}'|$. Notice that the Laplacian of the Newtonian potential, $\nabla^2 \phi_N$, vanishes *identically* in vacuum, *independent* of mass distribution in the rest of the universe.

Hence, a *null* experiment for the constancy of G can be performed in the following way. First, construct a detector sensitive to $\nabla^2 \phi$, which we call a gravitational "La-

*Supported in part by NASA.

placian detector." Second, using a large object of an arbitrary shape, modulate the source-detector separation periodically. Third, average the $\nabla^2\phi$ signal over many periods synchronously with the periodic motion. A statistically significant departure of $\nabla^2\phi$ from zero would then constitute a violation of the Inverse Square Law at the particular distance chosen for the experiment.

Unlike the Cavendish experiment, which basically determines G by comparing the integral in Eq. (4) with a measured force, the present experiment tests a differential equation which connects the field to a *local* quantity. As a result, the new experiment is insensitive to the global mass distribution of the source. This permits large geological objects of irregular shape to be used as a source. The source-detector separation is modulated periodically to overcome the $1/f$ noise in the Laplacian detector and to discriminate against gravity produced by stationary objects at other distances.

For a point source whose potential is given by Eq. (2), the field equation is modified by

$$\nabla^2\phi(R) = \frac{GM}{R^3} \alpha(\mu R)^2 e^{-\mu R}. \quad (5)$$

Of course, the right-hand side of this equation becomes a volume integral for an extended source:

$$\nabla^2\phi(R) = G \int_V \frac{\rho(\mathbf{x}')}{R^3} \alpha(\mu R)^2 e^{-\mu R} d^3x', \quad (6)$$

where $R \equiv |\mathbf{x} - \mathbf{x}'|$ as before. If the Inverse Square Law should fail at certain distances, the exact functional form of the gravitational potential could be determined by integrating the new field equation, Eq. (5).

3. Gravitational Laplacian Detector

The Laplacian of the gravitational potential is, by definition, a sum of three orthogonal gravity gradients (the trace of the gravity gradient tensor):

$$\nabla^2\phi = -\nabla \cdot \mathbf{g} = -\sum_{i=1}^3 \frac{\partial g_i}{\partial x_i}, \quad (7)$$

where the x_i ($i = 1, 2, 3$) form any Cartesian coordinates. A three-axis in-line component gravity gradiometer¹ could, therefore, be employed as a Laplacian detector. A sensitive superconducting gravity gradiometer to be used for this experiment has been designed and is under construction [17,18]. Here we give a brief description of the instrument.

Figure 1 is a schematic circuit diagram of a single-axis in-line component gravity gradiometer. The shaded rectangles with arrows represent superconducting proof masses that are confined to move along the direction indicated by the arrows. A persistent current I_0 is stored with opposite polarity in each of the two loops formed by pairs of flat superconducting sensing coils. When each proof mass is displaced with respect to the coils in response to a gravitational force or a platform vibration, it causes a current to flow into and out of the persistent current loop due to the Meissner effect. The signals from the two accelerometers are directly added and subtracted by two SQUIDS (Superconducting Quantum Interference Devices) to obtain a common-mode force g_i and a force gradient $\Gamma_{ii} \equiv -\partial g_i / \partial x_i$. A Laplacian detector is composed of three such single-axis gradiometers assembled along three orthogonal directions.

¹A similar null experiment in which a spherical mass shell is used as a Laplacian detector has been discussed by Paik [15] and proposed by Mills [16] independently.

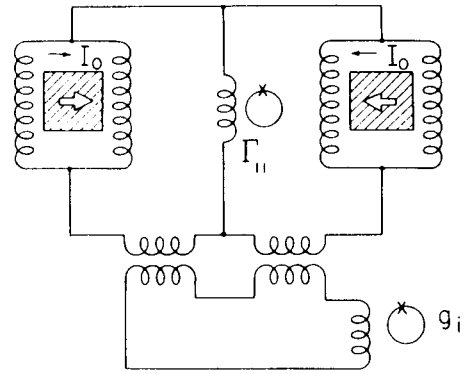


FIGURE 1. A schematic circuit diagram of a single-axis superconducting gravity gradiometer. A Laplacian detector is composed of three single-axis gradiometers repeated in three orthogonal directions.

In order to reject the common-mode forces to high precision and realize a very sensitive gravity gradiometer, the instrument must be fabricated with great care in a number of areas. The suspension springs for each proof mass must be soft along a well-defined axis and be linear. The sensitive axes of the two accelerometers in each gradiometer must be aligned. The sensitive axes of three gradiometers must then be aligned orthogonal to each other and the scale factors matched.

Figure 2 is a cut-away view of the superconducting proof mass and suspension. The suspension structure containing eight "folded cantilevers" is machined out of a single block of niobium (Nb). Plane surfaces are lapped parallel to each other before cantilevers are cut with an

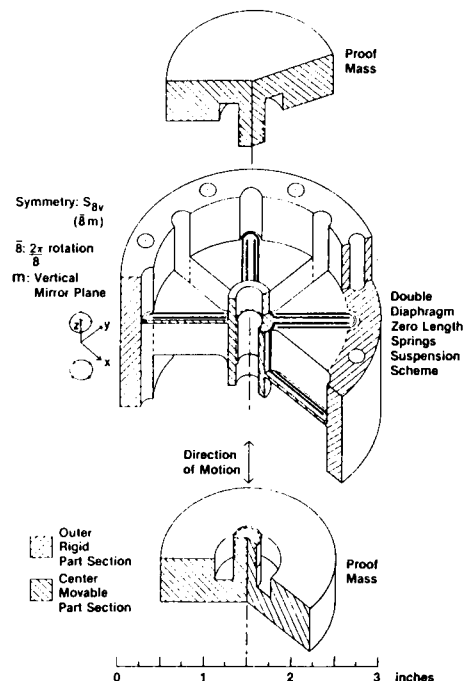


FIGURE 2. A 55° cut-away view of the niobium proof mass and suspension of a superconducting accelerometer. Two halves of the proof mass are threaded into the suspension structure to be supported by eight "folded cantilevers."

electric discharge machine. After the two halves of the Nb proof mass are threaded into the suspension structure, two "pancake"-shaped Nb coils each wound in a single layer are brought near the two outer surfaces of the proof mass to form an accelerometer. To make a Laplacian detector, six such accelerometers are mounted on six faces of a titanium cube whose deviations from orthogonality are controlled to a few arcseconds. Each pair of accelerometers located on opposing faces of the cube are coupled by the superconducting circuit shown in Fig. 1. The common-mode rejection error in each axis due to misalignment of the accelerometer axes becomes a second order effect when the cube is turned into three angular positions [19]. The uncompensated orthogonality error in the three axes gives rise to a coupling of 10^{-5} to zeroth order Newtonian gradients. The folded cantilever flexure employed here is expected to give a highly linear spring due to its pure bending motion, as well as low resonance frequencies of the proof masses.

In order to find $\nabla^2\phi$ by summing the outputs of three single-axis gradiometers, their scale-factors must be matched precisely. A support structure which enables common-mode balance and scale-factor match of a three-axis gravity gradiometer is shown in Fig. 3. An "um-

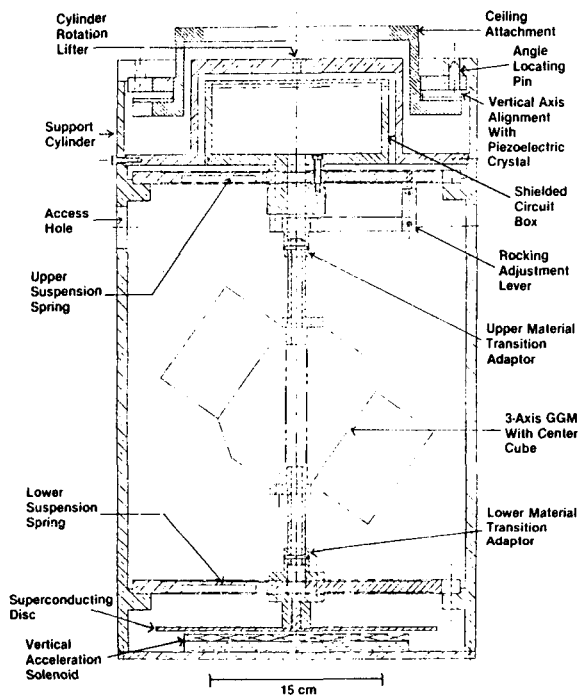


FIGURE 3. A support structure which enables common-mode balance and scale-factor match of a three-axis gravity gradiometer in an "umbrella" suspension.

rella" orientation, in which the three sensitive axes make an equal angle $\tan^{-1} \sqrt{2}$ with respect to the vertical, matches the gravity bias in three gradiometers. For common-mode balance, the gradiometer assembly is driven vertically at a desired frequency by means of a superconducting magnet. The ratio of two supercurrents in each of the three gradiometers is then adjusted until the differential output caused by the applied linear acceleration becomes sufficiently low. The scale-factor match between the three orthogonal components is accomplished by rotating the device in precise 120° steps

around the vertical and comparing outputs of the three gradiometers for the same gravity gradient signal. A set of three positioning pins is located in the support structure for this purpose.

A single-axis portion of the Laplacian detector described here has been constructed and is undergoing experimental test. The three-axis support structure is in the final stages of fabrication. An initial laboratory test of the Inverse Square Law is being prepared. The instrument-noise-limited sensitivity of the prototype Laplacian detector under construction is expected to be approximately $2 \times 10^{-11} \text{ s}^{-2}\text{Hz}^{-1/2}$. For the earth-orbit experiment, the goal is to achieve a white noise level of $2 \times 10^{-13} \text{ s}^{-2}\text{Hz}^{-1/2}$ in a larger model of the Laplacian detector. These sensitivities will be assumed to compute a minimum detectable α as a function of μ^{-1} in Section 5.

4. Experimental Procedures

4.1 Laboratory Experiment

In the laboratory scale $R \sim 10 \text{ m}$, a dynamic gravitational field could be produced conveniently by a moving source while the detector is kept at rest. In our earlier paper [20], we considered an experiment in which a rotating dumbbell is used to produce a periodic quadrupole field as in the experiment of Hirakawa *et al.* [13]. Here we replace the rotating dumbbell by a swinging pendulum. The latter generates a periodic monopole field which falls off more slowly ($\sim R^{-3}$) than the quadrupole field ($\sim R^{-5}$) and allows a larger separation experiment.

Figure 4 shows an experimental configuration of the source and the detector. Typical dimensions are $l = 0.16 \text{ m}$, $h \approx 5 \text{ m}$, $u \approx 2 \text{ m}$, and $R \approx 10 \text{ m}$. For the

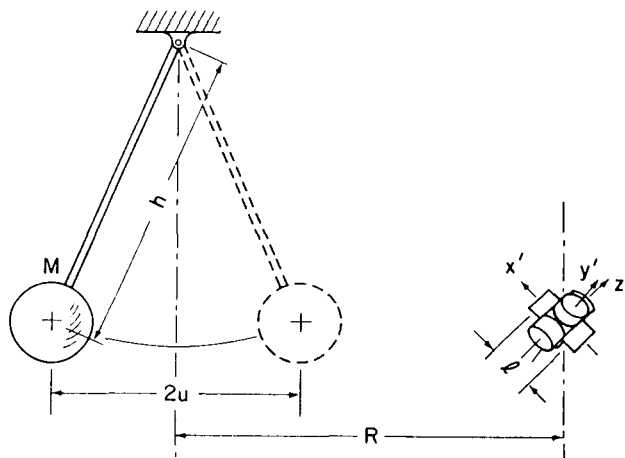


FIGURE 4. Experimental configuration of the source and the Laplacian detector in a laboratory experiment.

pendulum mass, we are constructing a spherical lead ball of 1600 kg. This will be used to test various instruments and procedures. Eventually the pendulum will carry a 10^4 kg stack of lead bricks for the Inverse Square Law experiment. If direct transmission of vibration through the building structure proves to be important, one could attempt to cancel the vibration using two identical pendula swinging in opposite directions. The detector could be located at the midpoint to double the gravity signal. This symmetric source configuration has an additional advantage of producing a uniform field in the middle thus making a distance error δR less important.

A completely source-independent null experiment requires a *true* Laplacian detector [21] which has a more sophisticated design. The three-axis gravity gradiometer that we are constructing at present is only an approximate Laplacian detector which still has a nonvanishing coupling to higher order spatial derivatives of ϕ . Hence, errors in the source geometry do not drop out completely. This residual coupling to the higher order Newtonian terms arises from the fact that a practical gradiometer measures a *difference* over a finite baseline l rather than taking a derivative at a point. For a potential given by Eq. (2), one can show [20] that the output of the three-axis gravity gradiometer is

$$\sum_{i=1}^3 \delta g_i = \frac{GMl}{R^3} \left[\alpha(\mu R)^2 e^{-\mu R} - \frac{21}{8} \left(\frac{l}{R} \right)^2 \right. \\ \left. \times \left[1 - \frac{5}{3} \frac{X^4 + Y^4 + Z^4}{R^4} \right] + O \left(\frac{l}{R} \right)^4 \right], \quad (8)$$

where $\mathbf{R} = (X, Y, Z)$ and $R = |\mathbf{R}|$. Thus, the finite baseline term varies as $(l/R)^2$ and becomes important for a relatively short distance experiment.

In the laboratory experiment, $(l/R)^2 \approx 3 \times 10^{-4}$. Since the zeroth order Newtonian term is balanced out to 10^{-5} , the second order term needs to be compensated by computation to about 3% to bring down the errors to the same level. In order to model the Newtonian gravity correctly, we drive the pendulum to swing in a predetermined plane and read the actual pendulum position using a shaft encoder mounted at the pivot. The encoder output is then used to trigger a signal averager following the Laplacian detector. In this manner, errors associated with erratic pendulum motions are prevented from entering into the signal process. The signal is averaged over many days to improve the signal-to-noise ratio.

4.2 Geological-Scale Experiment

The source-independent nature of the Laplacian experiment permits precision tests of the gravitational force law at kilometer ranges using geological sources. Figure 5 illustrates experimental arrangements for two different sources: a mountain and an ocean tide. When a mountain is used as the source, the detector could be transported horizontally, modulating the horizontal distance to the mountain $d(t)$. An ocean tide gives the advantage of not having to move the detector at all though the signal frequency of 2.3×10^{-5} Hz is well inside the $1/f$ noise of the Laplacian detector. The inherent density homogeneity and the well-defined surface profile of water make the tide a very attractive source for a geological-scale gravity experiment [22].

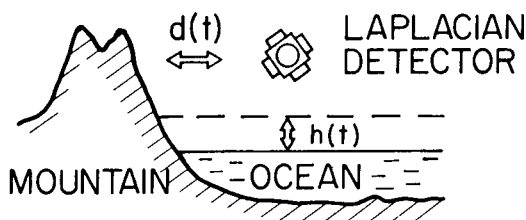


FIGURE 5. Experimental arrangements for two different geological sources: a mountain and an ocean tide. For the mountain experiment, the detector is moved horizontally to modulate $d(t)$. For the ocean tide experiment, the tide modulates a vertical distance $h(t)$ while the detector is kept at rest.

Moving a sensitive Laplacian detector without deteriorating its performance poses a major challenge in the mountain experiment. The problem could partially be overcome by modulating $d(t)$ in a square-wave fashion and averaging signals at the two end points while the detector is at rest. Although the Laplacian detector would still have to be moved gently so as to remain within the dynamic range of the SQUID detection circuits, dynamic error sources such as platform vibration and jitter could be eliminated by this procedure.

For an ocean-tide experiment, the cryostat containing the Laplacian detector could be fixed on a support tower above the water level or be lowered to the basin. The dynamic source of gravitation is the water level difference between the ebb and flow of the tide, $h \pm u$. This can be approximated as a plane sheet of mass with uniform density and thickness $2u$ for ranges smaller than the closest distance to the shore. It is well known that such a geometry produces a zero Newtonian force gradient so that our experiment becomes a *double null* experiment: a null source and a null detector.

Since the height modulation ($2u$) that is produced by an ocean tide is approximately 10 m, the resolution in α deteriorates at $\mu^{-1} > 10$ m. It is tempting to move the detector vertically on a flat plane² to a larger amplitude and improve the resolution at larger distances. In such an experiment, however, one encounters a large modulation of the vertical Newtonian gravity of the earth. Hence it is necessary to improve the common-mode rejection in the vertical direction.

4.3 Earth-Orbit Experiment

The three-axis superconducting gravity gradiometer described in this paper is under development for a gravity survey satellite of NASA [18]. After a successful test of the prototype model under construction, a larger, more sensitive model may be built and flown in a low altitude earth orbit to take a high resolution gravity map of the earth. Such a mission will give an excellent opportunity to test the Inverse Square Law at a distance range of the order of the earth's radius and improve the experimental limit of the Law by several orders of magnitude at $\mu^{-1} = 10^2$ to 10^3 km [23].

For the gravitational null experiment, the satellite could initially be launched in an elliptical orbit which modulates the satellite altitude from h_1 to h_2 at approximately 1.5×10^{-4} Hz as shown in Fig. 6. A full modula-

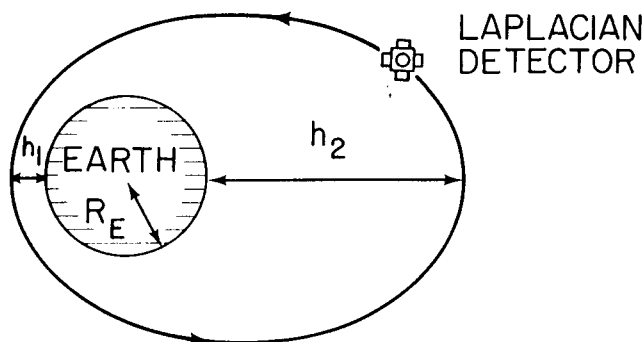


FIGURE 6. The Laplacian detector in an elliptical earth orbit.

²An elevator in a rocket launch tower or a tall urban tower could be used to transport the cryostat vertically.

tion of the non-Newtonian signal will be achieved if $h_1 \approx 200$ km and $h_2 \geq 6000$ km. There are several advantages of the earth-orbit experiment over the geological-scale experiment performed on the earth's surface. The quiet, zero- g nature of space provides an ideal environment for operation of a sensitive gravity gradiometer. The orbital motion of the satellite gives a continuous and full modulation of gravity signals at a reasonable frequency. Irregularities of the source are partially averaged out by the spin of the earth. It is also important that the satellite itself can be spun quietly in space to eliminate some of the important error terms.

The sensitivity of the flight model of the Laplacian detector is expected to be $10^{-6} \Gamma_E \text{ Hz}^{-1/2}$ at the signal frequency of $1.5 \times 10^{-4} \text{ Hz}$, where $\Gamma_E = 3 \times 10^{-6} \text{ s}^{-2}$ is the vertical bias gradient of the earth's gravity. If the signal is integrated for $\tau = 10^6 \text{ s}$ (12 days), the instrument noise level will go down to approximately $10^{-9} \Gamma_E$ implying a resolution of one part in 10^9 in the Inverse Square Law at the earth's radius $R_E = 6400$ km. An orthogonality error in the Laplacian detector, without compensation, would prevent a resolution better than one part in 10^5 . Fortunately, there are ways in which one could eliminate this error to first order and thereby reduce the coupling to the Newtonian term to a level of 10^{-10} . One interesting approach is spinning the satellite around one of the sensitive axes of the Laplacian detector. Coupling to cross component gravity gradients arising from angular errors is then modulated at harmonics of the spin frequency and can be distinguished from the Laplacian signal which remains at dc. Errors in the Laplacian itself can be shown to be of the second order in misalignment angles for the particular choice of the spin axis. A more detailed analysis of the earth orbit experiment will be published separately [23].

5. Expected Resolution of the Null Experiment

In this section we discuss the expected resolution of various versions of the gravitational null experiment. The peak-to-peak amplitudes of non-Newtonian signals for various sources can be shown to be

$$(\nabla^2 \phi)_{p-p} = \begin{cases} \frac{2GM}{R^3} \frac{\alpha(\mu R)^2 e^{-\mu R}}{1 - (u/R)^2} \times \left[\sinh(\mu u) + \frac{u}{R} \cosh(\mu u) \right], & \text{pendulum,} \\ 4\pi G \rho_w \alpha e^{-\mu h} \sinh(\mu u), & \text{ocean tide,} \\ 2\pi G \rho_E \alpha \left[(1 + e^{-2\mu R_E}) - \frac{1}{\mu R_E} (1 - e^{-2\mu R_E}) \right] \times \left[\frac{e^{-\mu h_1}}{1 + h_1/R_E} - \frac{e^{-\mu h_2}}{1 + h_2/R_E} \right], & \text{earth,} \end{cases} \quad (9)$$

where ρ_w and ρ_E are, respectively, the densities of ocean water and the earth, and the other parameters have been defined in earlier sections. We have assumed that the size of the pendulum mass is small compared to μ^{-1} or R and the earth is a sphere with a uniform density ρ_E .

The parameter values used for computation are $M = 10^4 \text{ kg}$, $R = 10 \text{ m}$ and $u = 2 \text{ m}$ for the laboratory experiment; $h = 10 \text{ m}$, $u = 5 \text{ m}$ and $\rho_w = 1.03 \times 10^3 \text{ kg} \cdot \text{m}^{-3}$ for the geological-scale experiment; and $R_E = 6400 \text{ km}$, $h_1 = 200 \text{ km}$, $h_2 = 6400 \text{ km}$.

$\rho_E = 2.7 \times 10^3 \text{ kg} \cdot \text{m}^{-3}$ (surface density) for $\mu^{-1} \leq 10^3 \text{ km}$ and $\rho_E = 5.5 \times 10^3 \text{ kg} \cdot \text{m}^{-3}$ (mean density) for $\mu^{-1} \geq 10^4 \text{ km}$. The instrument sensitivities assumed for the three experiments are $2 \times 10^{-11} \text{ s}^{-2} \text{ Hz}^{-1/2}$ (at 0.3 Hz), $2 \times 10^{-10} \text{ s}^{-2} \text{ Hz}^{-1/2}$ (at $2.3 \times 10^{-5} \text{ Hz}$) and $2 \times 10^{-12} \text{ s}^{-2} \text{ Hz}^{-1/2}$ (at $1.5 \times 10^{-4} \text{ Hz}$), respectively, the latter two coming from the $1/f$ noise of the SQUID. In addition, an integration time of $\tau = 10^6 \text{ s}$ (12 days) has been assumed for all experiments.

Figure 7 shows the expected resolution $|\alpha_{\min}|$ of the null experiment as well as limits set by other experiments as a function of μ^{-1} . The solid curves represent upper limits in α implied by previous experiments. Curves labeled "Panov," "Hirakawa," and "Newman" have been plotted from published results in Refs. [12-14]. The "lunar surface gravity" curve is the one obtained by Mikkelsen and Newman [9]. The limit set by "LAGEOS-lunar ranging" has been obtained by comparing two recent data points in the measurements of the geocentric gravitational constant³: one determined from laser ranging on near-earth satellites [24] and the other from laser ranging of the moon [25]. The regions lying above the solid curves are forbidden by existing data. The shaded area labeled "Long" is the region to which α is limited by Long's experiment [10]. Long's positive result constitutes an exception in a general trend which favors the Inverse Square Law and is in direct contradiction with Newman's data [14]. The three dashed curves in Fig. 7 represent the resolutions expected from the three versions of the $\nabla^2 \phi$ experiment considered in Section 4 and Eq. (9). Notice that a combination of the geological scale and the earth orbit experiment is capable of resolving α to better than 10^{-3} in ten decades over the range from $\mu^{-1} = 1 \text{ m}$ to $\mu^{-1} = 10^7 \text{ km}$ filling the gap between the laboratory and the astronomical scale. In the range of $\mu^{-1} \approx 10^3 \text{ km}$, the Laplacian experiment is expected to resolve the Inverse Square Law to better than one part in 10^9 , matching the best limit obtained from solar system observations for much larger distances.

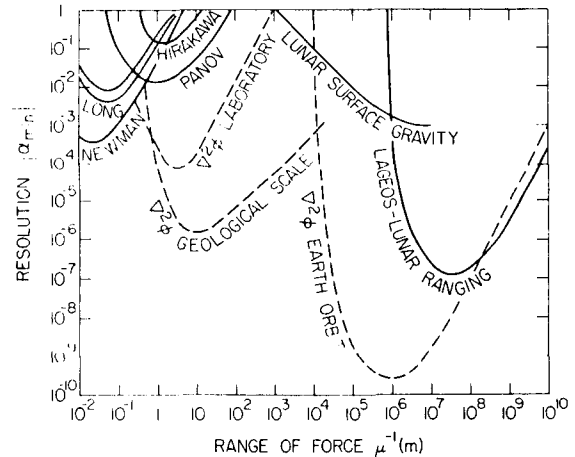


FIGURE 7. Expected resolution in α of the Laplacian experiment (dashed curves) and limits set by previous experiments (solid curves) as a function of the range μ^{-1} . The null experiment is capable of resolving the Inverse Square Law to better than 10^{-4} in ten decades of range from 1 m to 10^{10} m .

³The values of the geocentric gravitational constant in the two measurements are $GM_E = 398600.44 \pm 0.02 \text{ km}^3 \text{ s}^{-2}$ at $R = 12300 \text{ km}$ (semimajor axis for LAGEOS) and $GM_E = 398600.461 \pm 0.026 \text{ km}^3 \text{ s}^{-2}$ at $R = 384400 \text{ km}$ (mean earth-moon distance).

The proposed Laplacian experiment could remove embarrassingly large uncertainties that exist in our present knowledge of G as a function of mass separation. It is a *null* experiment which is capable of suppressing errors associated with the source. In the ocean and in earth orbit, the Newtonian terms could be eliminated completely by the additional null nature of the tide as source and by spinning the satellite quietly. As a result, excellent sensitivities are expected for the geological-scale and the earth-orbit experiment. The laboratory experiment is not completely free from source errors due to the proximity of the source and the detector. However, it will still be a useful first step in testing out the techniques of the gravitational null experiment.

In conclusion, a new concept has been developed to test one of the most fundamental hypotheses in the laws of physics: the *scale invariance* of the Inverse Square Law of Gravitation. The experimental examination of the spatial variation G constitutes a new test of General Relativity. An elegant null detector for the gravitational Inverse Square Law is being constructed using principles of superconductivity and an intricate mechanical design. We plan to carry out a series of null experiments in the coming years.

We gratefully acknowledge extensive contributions of Dr. Vol Moody and Mr. Frank Desrosier in the development of the superconducting gravity gradiometer and the construction of related experimental apparatus. We have also benefited from discussions with Dr. Peter Bender who has pointed out to us recent laser ranging data.

References

- [1] C. Brans and R. H. Dicke, *Phys. Rev.* **124**, 925 (1961).
- [2] R. V. Wagoner, *Phys. Rev. D* **1**, 3209 (1970).
- [3] E. Pechlaner and R. Sexl, *Commun. Math. Phys.* **2**, 227 (1966).
- [4] J. O'Hanlon, *Phys. Rev. Lett.* **29**, 137 (1972).
- [5] Y. Fugii, *Phys. Rev. D* **9**, 974 (1974).
- [6] D. R. Long, *Nuovo Cimento B* **55**, 252 (1980).
- [7] Y. Fugii, *Nature (London) Phys. Sci.* **234**, 4 (1971).
- [8] D. R. Long, *Phys. Rev. D* **9**, 850 (1974).
- [9] D. R. Mikkelsen and M. J. Newman, *Phys. Rev. D* **16**, 919 (1977).
- [10] D. R. Long, *Nature (London)* **260**, 417 (1976).
- [11] H. -T. Wu, W. -T. Ni, C. -C. Hu, F. -H. Liu, C. -H. Yang, and W. -N. Liu, *Phys. Rev. D* **19**, 2320 (1979).
- [12] V. I. Panov and V. N. Frontov, *Sov. Phys. JETP* **77**, 1702 (1979).
- [13] H. Hirakawa, K. Tsubono, and K. Oide, *Nature (London)* **283**, 184 (1980).
- [14] R. Spero, J. K. Hoskins, R. Newman, J. Pellam, and J. Schultz, *Phys. Rev. Lett.* **44**, 1645 (1980).
- [15] H. J. Paik, *Phys. Rev. D* **19**, 2320 (1979).
- [16] A. P. Mills, Jr., *Genl. Relativ. Grav.* **11**, 1 (1979).
- [17] H. J. Paik, E. R. Mapoles, and K. Y. Wang, in *Future Trends in Superconductive Electronics*, Ed. by B. S. Deaver *et al.* (Am. Inst. Phys. Conf. Proc. **44**, New York, 1978), p. 166.
- [18] H. J. Paik, *J. Astronaut. Sci.* **29**, 1 (1981).
- [19] H. A. Chan, unpublished analysis.
- [20] H. J. Paik and H. A. Chan, in *Proceedings of the Second Marcel Grossman Conference on General Relativity*, Ed. by R. Ruffini (North Holland, Amsterdam, in press).
- [21] H. A. Chan and H. J. Paik, in *Proceedings of the Ninth International Conference on General Relativity and Gravitation* (Jena, East Germany, 1980, in press).
- [22] F. D. Stacey, *Geophys. Res. Lett.* **5**, 377 (1978).
- [23] H. J. Paik, paper in preparation.
- [24] F. J. Lerch, R. E. Laubscher, S. M. Klosko, D. E. Smith, R. Kolenkiewicz, B. H. Putney, J. G. Marsh, and J. E. Brownd, *Geophys. Res. Lett.* **5**, 1031 (1978).
- [25] A. J. Ferrari, W. S. Sinclair, W. J. Sjogren, J. G. Williams, and C. F. Yoder, *J. Geophys. Res.* **85**, 3939 (1980).

SUPERCONDUCTING GRAVITY GRADIOMETER

Superconducting gravity gradiometer for space and terrestrial applications

M. V. Moody, H. A. Chan, and H. J. Paik

Department of Physics and Astronomy, University of Maryland, College Park, Maryland 20742

(Received 12 June 1986; accepted for publication 19 August 1986)

A three-axis superconducting gravity gradiometer with a potential sensitivity better than 10^{-3} Eötvös $\text{Hz}^{-1/2}$ is currently under development for applications in space. Although such a high sensitivity may be needed for only a limited number of terrestrial applications, superconductivity offers many extraordinary effects which can be used to obtain a gravity gradiometer with other characteristics necessary for operation in a hostile moving-base environment. Utilizing a number of recently devised techniques which rely on certain properties of superconductors, we have produced a design for a sensitive yet rugged gravity gradiometer with a high degree of stability and a common-mode rejection ratio greater than 10^9 . With a base line of 0.11 m, a sensitivity of 0.1 Eötvös $\text{Hz}^{-1/2}$ is expected in an environment monitored to a level of $10^{-2} \text{ m s}^{-2} \text{ Hz}^{-1/2}$ for linear vibration and $7 \times 10^{-6} \text{ rad s}^{-1} \text{ Hz}^{-1/2}$ for angular vibration. A conventional stabilized platform can be used at this level. The intrinsic noise level, which is two orders of magnitude lower, could be achieved by monitoring the attitude with a superconducting angular accelerometer which is under development. In addition, the new gradiometer design has the versatility of adapting the instrument to different gravity biases by adjusting stored dc currents.

I. INTRODUCTION

The Equivalence Principle of Einstein makes it impossible, even in principle, to separate gravity and acceleration by a local measurement. However, by making a differential measurement over a base line, one can cancel out acceleration and detect gravity gradients without being confused by platform motion. Although torsion balances have been used to detect gravitational force gradients for over two centuries, only in the most recent two decades have we seen serious efforts to develop moving-base gravity gradiometers.¹⁻³ Research on superconducting gravity gradiometers started more recently as an outgrowth of the superconducting transducer work for low-temperature gravitational wave detectors.⁴

In a superconducting instrument, the inconvenience of cryogenic operation is offset by the opportunity of utilizing many exotic properties of superconductors to improve the sensitivity and stability of gravity sensors. In addition to the obvious reduction of the thermal noise of the instrument, the quantization of magnetic flux can be used to obtain "perfectly" stable means of signal transduction, scale factor matching, and proof mass levitation. The availability of superconducting quantum interference devices (SQUID's) at liquid-helium temperatures is another important factor that makes the superconducting device attractive. SQUID's are highly sensitive flux measuring devices which are based on the concepts of Josephson tunneling and fluxoid quantization in superconducting loops.⁵ The commercial SQUID's we employ are coupled to input coils for measuring small currents. The sensitivity of these instruments is $1.5 \times 10^{-12} \text{ A Hz}^{-1/2}$ and the dynamic range is 10^8 .

A three-axis superconducting gravity gradiometer with a potential sensitivity better than $10^{-3} \text{ Eötvös Hz}^{-1/2}$ ($1 \text{ E} \equiv 1 \text{ Eötvös} \equiv 10^{-9} \text{ s}^{-2}$) is currently under development at the University of Maryland.⁶ This instrument has been designed primarily for applications in space. However, a sensitive

gravity gradiometer would also have a number of terrestrial applications if a satisfactory method of rejecting the high levels of environmental noise can be found. This paper describes a design for a superconducting gravity gradiometer which incorporates several new features to help deal with the problems of a dynamically noisy environment. This design maintains a high sensitivity along with the convenience of a short base line. A versatile magnetic levitation is applied to the proof masses so that the same hardware can be operated in any gravity environment from $0g_E$ to $1g_E$ (g_E is the earth's gravitational acceleration) by adjusting persistent currents in a number of superconducting coils.

Although the analysis in this paper will be confined to an in-line component gradiometer (i.e., a gradiometer which is sensitive to the diagonal components of the gravity gradient tensor, Γ_{ii}), it can be extended to a cross-component gradiometer (i.e., one which is sensitive to an off-diagonal component of the gravity gradient tensor, $\Gamma_{ij}, j \neq i$).

II. PRINCIPLE OF OPERATION

An in-line component superconducting gravity gradiometer consists of a pair of spring-mass accelerometers coupled together by a superconducting circuit to measure differential acceleration.⁷ Each accelerometer consists of a superconducting proof mass confined to move along a single axis and a spiral superconducting sensing coil located near the surface of the proof mass (see Fig. 1). An acceleration will cause a displacement of the proof mass which, because of the Meissner effect, will modulate the inductance of the coil at frequencies down to dc. The sensing coil is connected to the input coil of a SQUID amplifier forming a closed superconducting loop. This loop contains a persistent current which couples the mechanical and electrical systems. Since the flux in this loop must remain constant, the change in the inductance of the sensing coil results in a current change

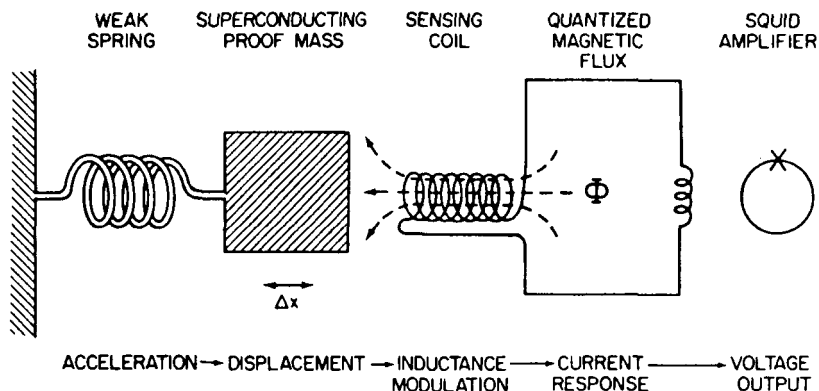


FIG. 1. Schematic diagram of a superconducting accelerometer.

through the SQUID input coil. In this manner very small accelerations can be detected.

In the present design, each proof mass is confined to move along a single axis by a pair of low-loss cantilever spring systems. In practice, the dynamic axes of the proof masses cannot be perfectly aligned and this misalignment can cause various error signals to couple to the gradiometer output. These effects will be discussed in Sec. VI. As in any coupled two-mass resonant system with only one degree of freedom, the motions of the proof masses can be decomposed into a common mode (i.e., the displacements of the proof masses are in the same direction) and a differential mode (i.e., the displacements are in opposite directions). By coupling the two proof masses together by persistent currents I_{d1} and I_{d2} , flowing in the closed superconducting loops shown by the solid lines in Fig. 2, and adjusting the ratio of I_{d1} to I_{d2} , the sensitivity of the system to common-mode accelerations can be balanced out. Using a similar design, a balance of two parts in 10^5 has been demonstrated.⁸ Although this degree of balance should be sufficient in a low noise space environment, a higher degree of rejection to common-mode noise is necessary for terrestrial applications and ground tests of the instrument.

By incorporating additional superconducting coils, shown by the dotted lines in Fig. 2, into the circuitry, the frequency of the common-mode resonance can be increased and the resonance peak passively damped without affecting the differential-mode resonance. This effect may be understood by noting that the flux in each of these loops must remain constant. The electromagnetic energy in these two loops is given by

$$E = \frac{\Phi_{c1}^2}{2(L_1 + L_2)} + \frac{\Phi_{c2}^2}{2(L_3 + L_4)}, \quad (1)$$

where Φ_{c1} and Φ_{c2} are the trapped fluxes. In a zero g environment, $\Phi_{c1} \approx \Phi_{c2}$ is chosen. In the earth's gravity environment, one of these fluxes can be greater than the other. When the gradiometer experiences a common-mode acceleration, the two inductances in each loop change in a like manner resulting in a change in E . However, during a differential acceleration, the changes in the two inductances cancel and E remains constant (in actuality, the degree of cancellation will depend on how well the two accelerometers are matched, as can be seen in Sec. III). Increasing the common-

mode frequency decreases the sensitivity of the gradiometer to common-mode accelerations while making isolation of the common-mode resonance peak from environmental noise a simpler task. This isolation, along with the passive damping, limits the amplitude of the signal produced by the common-mode peak at the input of the SQUID amplifier and allows greater dynamic range.

The upward shifting of the common-mode spring constant not only increases the rejection to common-mode accelerations, but it also increases the linearity of the gradiometer by confining the motions of the proof masses. Although the springs are designed for a high degree of linearity, the spring constant still contains higher order terms which may become significant for large displacements.

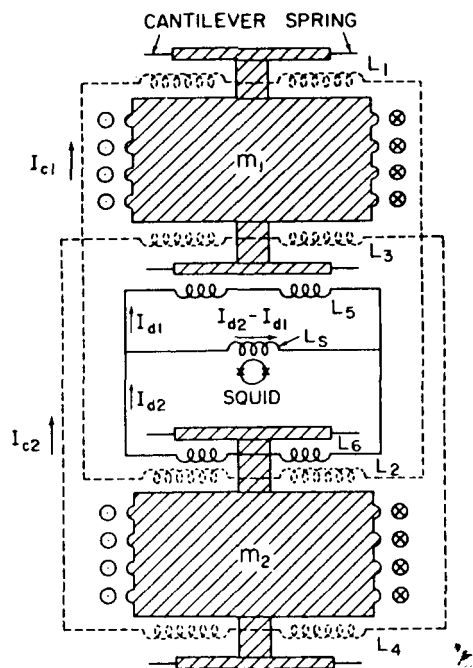


FIG. 2. Circuitry for a superconducting gravity gradiometer. The solid lines indicate the gradient sensing circuitry, while the dotted lines indicate the common-mode rejection circuitry. Also, a cross section of the negative spring coils is shown.

A conventional approach to the linearity and dynamic range problem of an inertial instrument is to use an active feedback network which senses and cancels the response of the proof mass. One disadvantage of this approach is the possible introduction of a significant noise source from the feedback signal. Since the circuit discussed above is passive and superconducting, there are no additional noise sources to increase the fundamental noise level of the gradiometer. If necessary, active "force rebalance" feedback can of course be applied to both common and differential modes in addition to the simple passive circuitry.

III. DYNAMICS OF THE INSTRUMENT

The inductance of a spiral coil of radius r located at a distance $d \ll r$ from a superconducting plane is given⁹ by

$$L = \mu_0 n^2 A d, \quad (2)$$

where n is the turns density and A is the area of the coil. With damping ignored, the equations of motion for two proof masses, m_1 and m_2 , at positions x_1 and x_2 and coupled by the superconducting circuits of Fig. 2, are

$$\ddot{x}_1(t) + \omega_{10}^2 [x_1(t) + x_{10}] - \frac{1}{2m_1} \left(\frac{L_{10}}{d_1} I_{c1}^2(t) - \frac{L_{30}}{d_3} I_{c2}^2(t) + \frac{L_{50}}{d_5} I_{d1}^2(t) \right) = g_1(t), \quad (3a)$$

$$\ddot{x}_2(t) + \omega_{20}^2 [x_2(t) + x_{20}] - \frac{1}{2m_2} \left(\frac{L_{20}}{d_2} I_{c1}^2(t) - \frac{L_{40}}{d_4} I_{c2}^2(t) + \frac{L_{60}}{d_6} I_{d2}^2(t) \right) = g_2(t), \quad (3b)$$

where ω_{10} and ω_{20} , and x_{10} and x_{20} are, respectively, the uncoupled (angular) resonance frequencies and the equilibrium positions of the proof masses. The driving specific forces for the two proof masses are denoted by $g_1(t)$ and $g_2(t)$. Also, d_i is the equilibrium spacing between the i th coil and the proof mass, and $L_{i0} = \mu_0 n^2 A_i d_i$.

The requirement that the flux in a closed superconducting loop must remain constant imposes four constraints:

$$\{L_{10}[1 + x_1(t)/d_1] + L_{20}[1 + x_2(t)/d_2]\}I_{c1}(t) = \Phi_{c1}, \quad (4a)$$

$$\{L_{30}[1 - x_1(t)/d_3] + L_{40}[1 - x_2(t)/d_4]\}I_{c2}(t) = \Phi_{c2}, \quad (4b)$$

$$\{L_{50}[1 + x_1(t)/d_5] + L_S\}I_{d1} - L_S I_{d2} = \Phi_{d1}, \quad (4c)$$

$$\{L_{60}[1 + x_2(t)/d_6] + L_S\}I_{d2} - L_S I_{d1} = \Phi_{d2}, \quad (4d)$$

where Φ_{c1} , Φ_{c2} , Φ_{d1} , and Φ_{d2} are constant fluxes. The constraint equations give, to the first order in x/d ,

$$I_{c1} = I_{c10} \left(1 - \frac{L_{10}x_1/d_1 + L_{20}x_2/d_2}{L_{10} + L_{20}} \right), \quad (5a)$$

$$I_{c2} = I_{c20} \left(1 - \frac{L_{30}x_1/d_3 + L_{40}x_2/d_4}{L_{30} + L_{40}} \right), \quad (5b)$$

$$I_{d1} = I_{d10} \left(1 - \frac{L_{50}(L_{60} + L_S)x_1/d_5 + (I_{d20}/I_{d10})L_{60}L_S x_2/d_6}{(L_{50} + L_S)(L_{60} + L_S) - L_S^2} \right), \quad (5c)$$

$$I_{d2} = I_{d20} \left(1 - \frac{L_{60}(L_{50} + L_S)x_2/d_6 + (I_{d10}/I_{d20})L_{50}L_S x_1/d_5}{(L_{50} + L_S)(L_{60} + L_S) - L_S^2} \right). \quad (5d)$$

In these equations, the following substitutions have been made:

$$I_{c10} = \frac{\Phi_{c1}}{L_{10} + L_{20}}, \quad (5e)$$

$$I_{d10} = \frac{\Phi_{d1}(L_{60} + L_S) + \Phi_{d2}L_S}{(L_{50} + L_S)(L_{60} + L_S) - L_S^2}, \quad (5f)$$

$$I_{d20} = \frac{\Phi_{d2}(L_{50} + L_S) + \Phi_{d1}L_S}{(L_{50} + L_S)(L_{60} + L_S) - L_S^2}. \quad (5g)$$

The significance of the higher order terms will, of course, depend upon a particular design. For the design presented in Sec. V, x_i/d_i is approximately 1×10^{-6} for a 1-E signal.

Upon substitution of these results into the equations of motion, one finds

$$\begin{aligned} \ddot{x}_1 + \frac{1}{m_1} \left[K_{10} + K_1 + K_3 + K_5 \left(1 + \frac{L_{60}}{L_S} \right) \right] x_1 \\ + \frac{1}{m_1} \{ (K_1 K_2)^{1/2} + (K_3 K_4)^{1/2} + (K_5 K_6)^{1/2} \} x_2 \\ + \frac{K_{10}}{m_1} x_{10} - \frac{1}{2m_1} \left(\frac{L_{10}}{d_1} I_{c10}^2 - \frac{L_{30}}{d_3} I_{c20}^2 + \frac{L_{50}}{d_5} I_{d10}^2 \right) \\ = g_1, \end{aligned} \quad (6a)$$

$$\begin{aligned} \ddot{x}_2 + \frac{1}{m_2} \left[K_{20} + K_2 + K_4 + K_6 \left(1 + \frac{L_{50}}{L_S} \right) \right] x_2 \\ + \frac{1}{m_2} \{ (K_1 K_2)^{1/2} + (K_3 K_4)^{1/2} + (K_5 K_6)^{1/2} \} x_1 \\ + \frac{K_{20}}{m_2} x_{20} - \frac{1}{2m_2} \left(\frac{L_{20}}{d_2} I_{c10}^2 - \frac{L_{40}}{d_4} I_{c20}^2 + \frac{L_{60}}{d_6} I_{d20}^2 \right) \\ = g_2, \end{aligned} \quad (6b)$$

where

$$K_{10} = m_1 \omega_{10}^2, \quad (7a)$$

$$K_{20} = m_2 \omega_{20}^2, \quad (7b)$$

$$K_1 \equiv \frac{I_{c10}^2 L_{10}^2}{d_1^2 (L_{10} + L_{20})}, \quad (7c)$$

$$K_2 \equiv \frac{I_{c10}^2 L_{20}^2}{d_2^2 (L_{10} + L_{20})}, \quad (7d)$$

$$K_3 \equiv \frac{I_{c20}^2 L_{30}^2}{d_3^2 (L_{30} + L_{40})}, \quad (7e)$$

$$K_4 \equiv \frac{I_{c20}^2 L_{40}^2}{d_4^2 (L_{30} + L_{40})}, \quad (7f)$$

$$K_5 \equiv \frac{I_{d10}^2 L_{50}^2}{d_5^2 (L_{50} L_{60} / L_S + L_{50} + L_{60})}, \quad (7g)$$

$$K_6 \equiv \frac{I_{d20}^2 L_{60}^2}{d_6^2 (L_{50} L_{60} / L_S + L_{50} + L_{60})}. \quad (7h)$$

Equations (6a) and (6b) can be rewritten in a simpler form:

$$\ddot{x}_1 + \frac{v_1}{m_1} x_1 + \frac{v_3}{m_1} x_2 + \omega_{10}^2 x_{10} - c_1 = g_1, \quad (8a)$$

$$\ddot{x}_2 + \frac{v_2}{m_2} x_2 + \frac{v_3}{m_2} x_1 + \omega_{20}^2 x_{20} - c_2 = g_2, \quad (8b)$$

by defining

$$v_1 \equiv K_{10} + K_1 + K_3 + K_5 (1 + L_{60} / L_S), \quad (9a)$$

$$v_2 \equiv K_{20} + K_2 + K_4 + K_6 (1 + L_{50} / L_S), \quad (9b)$$

$$v_3 \equiv (K_1 K_2)^{1/2} + (K_3 K_4)^{1/2} + (K_5 K_6)^{1/2}, \quad (9c)$$

and

$$c_1 \equiv \frac{1}{2m_1} \left(\frac{L_{10}}{d_1} I_{c10}^2 - \frac{L_{30}}{d_3} I_{c20}^2 + \frac{L_{50}}{d_5} I_{d10}^2 \right), \quad (10a)$$

$$c_2 \equiv \frac{1}{2m_2} \left(\frac{L_{20}}{d_2} I_{c10}^2 - \frac{L_{40}}{d_4} I_{c20}^2 + \frac{L_{60}}{d_6} I_{d20}^2 \right). \quad (10b)$$

Thus, by setting $\ddot{x}_1, x_1, \ddot{x}_2, x_2 = 0$ in Eqs. (8a) and (8b), the equilibrium positions are given by

$$x_{10} = (c_1 + g_{10}) / \omega_{10}^2, \quad (11a)$$

$$x_{20} = (c_2 + g_{20}) / \omega_{20}^2, \quad (11b)$$

where g_{10} and g_{20} are the constant terms in $g_1(t)$ and $g_2(t)$, respectively. The solutions to Eqs. (8a) and (8b) are of the form

$$x_1 = A e^{i\omega t}, \quad x_2 = B e^{i\omega t}. \quad (12)$$

Making these substitutions gives

$$\omega_{\pm}^2 = \frac{1}{2} \left\{ \frac{v_1}{m_1} + \frac{v_2}{m_2} \pm \left[\left(\frac{v_1}{m_1} - \frac{v_2}{m_2} \right)^2 + \frac{4v_3^2}{m_1 m_2} \right]^{1/2} \right\}, \quad (13)$$

where the general solutions are

$$x_1 = A_1 e^{i\omega_+ t} + A_{-1} e^{-i\omega_+ t} + A_2 e^{i\omega_- t} + A_{-2} e^{-i\omega_- t} + A_3 g_1(t) + A_4 g_2(t), \quad (14a)$$

$$x_2 = B_1 e^{i\omega_+ t} + B_{-1} e^{-i\omega_+ t} + B_2 e^{i\omega_- t} + B_{-2} e^{-i\omega_- t} + B_3 g_1(t) + B_4 g_2(t). \quad (14b)$$

By substituting Eqs. (14a) and (14b) into the equations of motion (8a) and (8b), one can show that the normal coordinates are given by

$$X_+ = \frac{m_1}{2v_3} \left[\left(\frac{v_1}{m_1} - \frac{v_2}{m_2} \right) + \left[\left(\frac{v_1}{m_1} - \frac{v_2}{m_2} \right)^2 + \frac{4v_3^2}{m_1 m_2} \right]^{1/2} \right] x_1 + x_2, \quad (15a)$$

$$X_- = -\frac{m_1}{2v_3} \left[\left(\frac{v_1}{m_1} - \frac{v_2}{m_2} \right) - \left[\left(\frac{v_1}{m_1} - \frac{v_2}{m_2} \right)^2 + \frac{4v_3^2}{m_1 m_2} \right]^{1/2} \right] x_1 - x_2. \quad (15b)$$

The right sides of these equations reduce to $x_1 + x_2$ and $x_1 - x_2$ (the common and differential modes) only if

$$m_1 = m_2 \quad (16a)$$

and

$$v_1 = v_2. \quad (16b)$$

As we will show in the next section, if ω_{10} and ω_{20} are small, the amplifier noise is negligible and the coupling to the amplifier can be reduced. In this case I_{d1} and I_{d2} are small and the terms involving K_5 and K_6 can be neglected. Also, as we will discuss in the next section, K_{10} and K_{20} can be matched by adjusting the currents in the negative spring coils. Then the condition of Eq. (16b) reduces to

$$K_1 + K_3 = K_2 + K_4. \quad (17)$$

Equation (13) now gives for the normal frequencies:

$$\omega_{\pm}^2 = \frac{1}{2m_1} [K_{10} + K_{20} + (K_1^{1/2} \pm K_2^{1/2})^2 + (K_3^{1/2} \pm K_4^{1/2})^2]. \quad (18)$$

This equation shows that there will be a contribution to the differential-mode spring constant, $m\omega_{\pm}^2$, unless the condition of Eq. (17) is satisfied by making $K_1 = K_2$ and $K_3 = K_4$. Equations (17c)–(17f) indicate that, to meet this requirement, the coil geometries (i.e., $n_i^2 A_i$) of L_1 and L_2 and of L_3 and L_4 must be matched. Equation (18) will then simplify to

$$\omega_{\pm}^2 \rightarrow \omega_{0d}^2 = \frac{1}{2} (\omega_{10}^2 + \omega_{20}^2) \quad (19)$$

and

$$\omega_{\pm}^2 \rightarrow \omega_{0c}^2 = \omega_{0d}^2 + (2/m_1)(K_1 + K_3), \quad (20)$$

where ω_{0d} and ω_{0c} are the differential- and common-mode resonance frequencies, respectively. Also, the normal coordinates become

$$X_d \equiv x_2 - x_1 \rightarrow 2(A_d e^{i\omega_{0d} t} + A_{-d} e^{-i\omega_{0d} t}) + C_d g_d, \quad (21a)$$

$$X_c \equiv \frac{1}{2}(x_1 + x_2) \rightarrow 2(A_c e^{i\omega_{0c} t} + A_{-c} e^{-i\omega_{0c} t}) + C_c g_c, \quad (21b)$$

where

$$g_d(t) \equiv g_2(t) - g_1(t), \quad (22a)$$

$$g_c(t) \equiv \frac{1}{2}[g_1(t) + g_2(t)]. \quad (22b)$$

The equations of motion can now be rewritten in the

form of two simple harmonic oscillators:

$$\ddot{X}_d + \omega_{0d}^2 (X_d - X_{d0}) = g_d, \quad (23a)$$

$$\ddot{X}_c + \omega_{0c}^2 (X_c - X_{c0}) = g_c. \quad (23b)$$

Since the displacement of a driven harmonic oscillator at frequencies below the resonance frequency is inversely proportional to the square of the resonance frequency,¹⁰ the sensitivity to common-mode acceleration is reduced by a factor of $\omega_{0c}^2/\omega_{0d}^2$.

The signal through the input coil of the SQUID is, from Eqs. (5c) and (5d),

$$\begin{aligned} I_{d2} - I_{d1} = I_{d20} - I_{d10} &+ \left[\left(\frac{I_{d20}}{d_6} - \frac{I_{d10}}{d_5} \right) X_d \right. \\ &- 2 \left(\frac{I_{d10}}{d_5} + \frac{I_{d20}}{d_6} \right) X_c \left. \right] \\ &\times \left[1 + L_s \left(\frac{1}{L_{50}} + \frac{1}{L_{60}} \right) \right]^{-1}. \end{aligned} \quad (24)$$

Thus the sensitivity to common-mode excitations may be further reduced by matching I_{d20}/d_6 and $-I_{d10}/d_5$. In fact, in this simple model, perfect common-mode rejection may be obtained in principle by adjusting I_{d20} and I_{d10} ; however, experimentally it is often easier to match several sets of parameters to moderate accuracy than to match one set to very high accuracy.

IV. SUPERCONDUCTING NEGATIVE SPRING

A description of the superconducting negative spring has been presented in a previous paper.¹¹ That paper, however, gave only a numerical solution. In this section, after a discussion of its application to the gradiometer, we present an analytical solution which allows the data to be more easily related to other geometries.

The noise power spectral density of the gradiometer can be expressed¹² as

$$S_T(f) = \frac{8}{ml^2} \left(2\pi f k_B T R(f) + \frac{\omega_{0d}^2}{2\beta_A} E_A(f) \right), \quad (25)$$

where m , l , $E_A(f)$, and β_A are, respectively, the mass of each proof mass, the gradiometer base line, the amplifier noise energy (called the "input energy resolution"), and the energy coupling factor for the amplifier. The function $R(f)$ is a frequency-dependent damping factor, which becomes equal to the inverse of the quality factor at the resonance frequency $f = \omega_{0d}/2\pi$. The first term on the right-hand side of Eq. (25) is due to the Brownian motion noise and the second term on the right is due to the noise of the amplifier. This version of the sensitivity equation is different from the version which appeared in Ref. 12. In its present form, the equation has been modified to include the fact that the magnitude of the force fluctuations at the signal frequency f is, in general, different from that at the resonance frequency. Namely, the Brownian motion noise has a frequency dependence which is governed by the nature of the loss mechanism in the spring.

The superconducting gravity gradiometer at present has its fundamental noise limited by the amplifier noise rather than the Brownian motion noise.⁸ Equation (25) indicates

that one of the most obvious ways to increase the resolution of the gradiometer is to lower its resonance frequency ω_{0d} . Lowering the mechanical spring constant while maintaining rigidity along the nonsensitive axes is a difficult task. One method of overcoming this dilemma for a superconducting gradiometer has been previously demonstrated.¹¹ This method uses a superconducting negative spring to counteract the positive mechanical spring. Each negative spring consists of a disk with a semicircular edge located in a solenoid with a length less than the thickness of the disk. The proof mass is shaped to contain several of these "disks" (see Fig. 2). The negative spring constant can be adjusted by changing the persistent current I_n in the solenoid.

The lower limit for the resonance frequency will be determined by a number of factors. Since the response of the gradiometer will fall off at frequencies above the differential-mode resonance frequency, the required bandwidth of the gradiometer is one limiting factor. A second limitation is the magnitude of the higher order terms in the spring constant. These terms can produce a nonlinear system when the first-order term becomes small.

When two large spring constants are balanced to obtain a low-frequency spring, the stability and linearity requirements for each of these springs can become much more important. In the present design, the stability of the spring constants is maintained by a number of beneficial features which are available at liquid-helium temperatures. These features include the stability of materials, the stability of persistent currents in superconducting loops, and the stable temperature environment. The linearity requirement is decreased by the common-mode rejection coils which confine the motions of the proof masses under a common-mode acceleration. Also, if necessary, the stability and linearity of the system can be further enhanced by standard feedback techniques.

To estimate the negative spring constant (see Fig. 3), we approximate that the field between the solenoid and the superconducting surface is uniform. This approximation is justified in the limit $d_0/L \ll 1$ since the current density is uniform. Then, the change in the magnetic field energy with displacement is due to a change in the effective volume of the

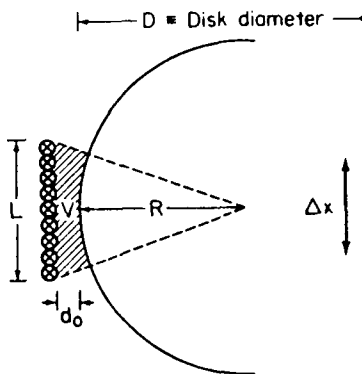


FIG. 3. Diagram for negative spring calculation showing the edge of a disk and a section of a solenoid.

solenoid. The volume as a function of displacement x is

$$V(x) = \frac{1}{2}\pi D [L(d_0 + R) - R^2\theta] = V_0 - \frac{1}{2}\pi DR^2\theta, \quad (26)$$

where

$$\theta = \tan^{-1} \left(\frac{L/2 + x}{d_0 + R} \right) + \tan^{-1} \left(\frac{L/2 - x}{d_0 + R} \right). \quad (27)$$

Here, D , L , R , and d_0 are defined in Fig. 3. The magnetic potential energy is

$$E(x) = \Phi_0^2/2L = \Phi_0^2/2\mu_0 n^2 V(x). \quad (28)$$

Expanding $E(x)$ in powers of x gives

$$E(x) = \frac{1}{2}\mu_0 n^2 I_n^2 (V_0 - c_1 x^2 + c_2 x^4 + \dots), \quad (29)$$

where

$$c_1 = \frac{\pi DR^2 L}{2(R + d_0)^3 [1 + (L/2)^2/(R + d_0)^2]}. \quad (30)$$

Dropping the higher order terms and differentiating twice with respect to x leads to the spring constant:

$$k_n = \frac{\partial^2 E}{\partial x^2} = -\mu_0 n^2 I_n^2 c_1. \quad (31)$$

For the geometry in the aforementioned demonstration, this expression gives $k_n = -1100 \text{ N m}^{-1}$, which is in good agreement with the experimental value¹¹ of -1180 N m^{-1} .

V. A PRACTICAL DESIGN

If the effect of the resonance frequency is excluded, the determining quantities for the Brownian motion and amplifier noise terms of Eq. (25) are $R(f)$ and $E_A(f)$, respectively. Presently, the most sensitive commercially available SQUID¹³ has an energy resolution of $E_A(f) = 3 \times 10^{-30} \text{ J Hz}^{-1/2}$ down to 0.1 Hz at which point $1/f$ noise becomes important. The damping factor of the proof mass motion contains contributions from both the mechanical and electromagnetic spring constants with the latter generally dominating for large coupling between the electrical and mechanical systems. Although difficult to obtain, $R(f) < 10^{-6}$ has been observed in the superconducting coils of similar design near 1 kHz.¹⁴ For the purpose of our sensitivity calculation, we assume that $R(f) \approx 10^{-6}$ can be achieved at low frequencies ($f < 1 \text{ Hz}$).

With the above values in mind, and keeping with the objectives stated in the Introduction, we propose the following parameters for a practical design: a final differential-mode resonance frequency of 1.6 Hz, a base line of 0.11 m, and a hollow niobium (Nb) proof mass 0.038 m in diameter by 0.029 m long with a mass of 0.1 kg. According to Eq. (25), this design would give a sensitivity of $2 \times 10^{-3} \text{ E Hz}^{-1/2}$. The dimensions can be reduced further if the sensitivity goal is set at a more moderate level of $0.1 \text{ E Hz}^{-1/2}$.

For the common-mode rejection (CMR) coils and negative spring coils, the primary limitation is the critical field of the proof mass material. For Stanford grade niobium at 4.2 K, the critical field is 0.12 Wb m^{-2} .⁹ A second limitation is the minimum spacing between the superconducting coils and the surface of the proof mass. These coils have been made in the past with niobium wire. With a wire coil, the minimum spacing is about $1 \times 10^{-4} \text{ m}$. One should be able to

reduce this value substantially using thin-film coils.

For the CMR coils, the field value at the surface of the proof mass should be kept approximately 10% below the critical field value. This precaution would allow the gradiometer to withstand a common-mode acceleration of up to twice the earth's gravity without the field exceeding the critical value and trapping flux in the superconductors. In order to maintain the correct spacing between the proof mass and the coils, two CMR circuits (containing persistent currents I_{c10} and I_{c20} , respectively) with one coil on each side of each proof mass are necessary (see Fig. 2). For vertical orientation, $I_{c10}^2 \approx 0.8 I_{c20}^2$ to compensate for the earth's gravitational field. Then, with $\mu_0 n I_{c10} = 0.10 \text{ Wb m}^{-2}$, $\mu_0 n I_{c20} = 0.11 \text{ Wb m}^{-2}$, $d = 1 \times 10^{-4} \text{ m}$, and $A = 1.1 \times 10^{-3} \text{ m}^2$, and with Eqs. (20) and (7), the common-mode resonance frequency is 230 Hz. With this increased stiffness, Eqs. (23) and (24) imply that a total CMRR (common-mode rejection ratio) of 1×10^9 is achievable, if I_{d10} and I_{d20} are balanced to two parts in 10^5 . Since the expressions in this paper have been calculated only to first order, this CMRR value must be viewed as an upper limit. One cannot expect that carrying out these calculations to higher orders would present a complete solution. At this level of CMR, additional factors, such as coil asymmetries and rigidity along the non-sensitive axes, may become important. These terms are difficult, if not impossible, to calculate and will have to be determined empirically for a given design.

For the negative spring coils, the field strength can be near the critical value giving $n I_n = 0.9 \times 10^5 \text{ A m}^{-1}$. The expression in Eq. (30) has a maximum value of 0.27 at $L/(R + d_0) = 2/\sqrt{3}$. If 12 disks with a diameter of $3.8 \times 10^{-2} \text{ m}$ are used, one obtains $k_n = -4.3 \times 10^3 \text{ N m}^{-1}$, which can compensate a mechanical resonance frequency of 33 Hz at 4.2 K. By lowering the temperature to 1.1 K, the critical field will increase by 25% allowing the mechanical resonance and the common-mode frequencies to be increased to 40 Hz and 300 Hz, respectively.

VI. ENVIRONMENTAL NOISE AND INSTRUMENT ERRORS

In order to realize an operational sensitivity of $2 \times 10^{-3} \text{ E Hz}^{-1/2}$ with a CMRR of 1×10^9 and a base line of 0.11 m, a linear acceleration noise level better than $2 \times 10^{-3} g_E \text{ Hz}^{-1/2}$ ($2 \times 10^{-3} \text{ E Hz}^{-1/2} \times 0.11 \text{ m} \times 10^9$) is required. The seismic noise level in a relatively quiet place is less than $10^{-6} g_E \text{ Hz}^{-1/2}$; consequently, the passive CMR will be sufficient for a stationary platform. For a moving base application, however, the platform vibration level can be as high as $10^{-3} g_E \text{ Hz}^{-1/2}$. With this vibration level, a sensitivity of $0.1 \text{ E Hz}^{-1/2}$ ($10^{-3} g_E / 0.11 \text{ m} \times 10^9$) would still be obtainable. This sensitivity would be sufficient for many applications. To extend a moving base system to a sensitivity $10^{-3} \text{ E Hz}^{-1/2}$, the platform vibrations would have to be monitored to a level of $10^{-5} g_E \text{ Hz}^{-1/2}$ to allow for compensation of the common-mode errors of the gradiometer. A vector measurement of the platform acceleration with this resolution could be made by using a triad of conventional accelerometers. Alternatively, in a three-axis gradiometer, an additional SQUID could be coupled to the

CMR circuit of each component gradiometer to obtain a simultaneous reading of the three linear acceleration components of the gradiometer.

With the common-mode error removed, the second most important error source is the angular motion of the gradiometer with respect to an inertial frame. Angular motion about an axis other than its own sensitive axis produces error signals even in a perfectly aligned gradiometer through the centrifugal acceleration, which is indistinguishable from an in-line component gravity gradient. If the gradiometer is mounted on a platform which is stationary in the earth's reference frame, the error in the gravity gradient due to centrifugal acceleration is given¹⁵ by

$$\delta\Gamma_{ii} = -2\{(\hat{n} \cdot \Omega_E)[\hat{n} \cdot \delta\Omega_p(\omega)] - \Omega_E \cdot \delta\Omega_p(\omega)\}, \quad (32)$$

where \hat{n} is the unit vector in the direction of the sensitive axis, Ω_E is the angular velocity vector for the earth, and $\delta\Omega_p$ is the uncertainty in the angular velocity vector of the platform. In the derivation of Eq. (32), the condition $\delta\Omega_p \ll \Omega_E = 7.27 \times 10^5 \text{ rad s}^{-1}$ has been assumed. In order to suppress this error to a level of $2 \times 10^{-3} \text{ E Hz}^{-1/2}$, for a vertical or horizontal orientation, the attitude rate of the gradiometer must be known or controlled to $1.4 \times 10^{-8} \text{ rad s}^{-1} \text{ Hz}^{-1/2}$. For $0.1 \text{ E Hz}^{-1/2}$, this value becomes $7 \times 10^{-6} \text{ rad s}^{-1} \text{ Hz}^{-1/2}$. The requirement for the $0.1 \text{ E Hz}^{-1/2}$ instrument could be met with conventional gyroscopes mounted to the platform. The measurement of the attitude rate at the level of $10^{-8} \text{ rad s}^{-1} \text{ Hz}^{-1/2}$ may be difficult for a conventional gyroscope. A superconducting "six-axis" accelerometer, which measures three linear and three angular acceleration components simultaneously with high sensitivity, is under development¹⁶ and could be used for this purpose.

Up to this point, this paper has dealt with a gravity gradiometer in which the sensitive axes of the component accelerometers are perfectly aligned. In a gradiometer whose sensitive axes are misaligned, linear and angular motion will generate additional errors in the gradiometer output. Linear motion orthogonal to the direction along which a single-axis gradiometer is balanced would couple directly to the gradiometer output at a level proportional to the degree of misalignment. Angular motion can couple in through axis misalignment in one of two ways. First, in the earth's field, an angular displacement will result in a change in the dc bias level for the two accelerometers. When the two sensitive axes are misaligned with respect to each other, the change in the bias level will be different for the two accelerometers. Second, the misalignment of the average sensitive axis with respect to the base line will result in a direct coupling of angular acceleration to the gradiometer output. We summarize below the error model associated with these misalignments.

The gradiometer axis alignment errors can be described in terms of a misalignment between the sensitive axes of the component accelerometers:

$$\delta\hat{n}_- \equiv \hat{n}_2 - \hat{n}_1, \quad (33)$$

and a misalignment between the average direction of the sensitive axis and the direction of the base line:

$$\delta\hat{n}_{+i} = \frac{1}{2}(\hat{n}_2 + \hat{n}_1) - \hat{l}. \quad (34)$$

In these equations, \hat{n}_1 and \hat{n}_2 are the unit vectors in the direction of the sensitive axes of the two component accelerometers and \hat{l} is the unit vector in the direction of the base line. In addition to causing a gradiometer orientation error, these alignment errors cause coupling to the gravity gradient output from the common-mode acceleration component along the $\delta\hat{n}_-$ direction and from the angular acceleration component along the $\delta\hat{n}_{+i} \times \hat{n}$ direction.

In a terrestrial environment, a common-mode acceleration along the $\delta\hat{n}_-$ direction is generated not only by linear motions, but also by angular motions which modulate the dc bias level for each accelerometer, $\mathbf{g}_E \cdot \hat{n}_i$. The error term along the $\delta\hat{n}_-$ direction is then given¹⁵ by

$$\delta\Gamma_{\hat{n}_-}(f) = (1/l)\delta\hat{n}_- \cdot [\mathbf{g}_E \cdot \theta_n(f) + \mathbf{a}_n(f)], \quad (35)$$

where $\theta_n(f)$ is the angular displacement noise and $\mathbf{a}_n(f)$ is the linear acceleration noise. The error term along the $\hat{n}_{+i} \times \hat{n}$ direction is given¹⁵ by

$$\delta\Gamma_{\hat{n}_{+i}}(f) = \delta\hat{n}_{+i} \times \hat{n} \cdot \alpha_n(f), \quad (36)$$

where $\alpha_n(f)$ is the angular acceleration noise.

Using ordinary machining techniques and taking care to relieve stress in the mechanical components, the alignment errors $\delta\hat{n}_-$ and $\delta\hat{n}_{+i}$ can be reduced to the level of 10^{-4} . One possible method of improving the mechanical alignment is through the use of piezoelectric crystals. In such a system, a set of three or four piezoelectric crystal stacks would be used to adjust the relative angle of the sensitive axes of the two accelerometers in a single-axis gradiometer. An alignment of one part in 10^8 for both $\delta\hat{n}_-$ and $\delta\hat{n}_{+i}$ appears feasible by using this method.

A second method for reducing the alignment error $\delta\hat{n}_-$ requires a three-axis gradiometer. In this method, additional superconducting circuits which are sensitive to the common-mode components of the acceleration along two axes are coupled to the proof masses of the third "orthogonal" axis. By adjusting the persistent currents in these circuits, in a manner similar to the one-dimensional balance discussed in Secs. II and III, the residual coupling between common-mode accelerations and the gravity gradient outputs due to axis misalignment is balanced out. Thus a rigorous three-dimensional balance against sensitivity to linear accelerations is obtained. However, the angular acceleration error caused by the misalignment $\delta\hat{n}_{+i}$ must be compensated for separately.

Equations (35) and (36) determine the requirements for the attitude and attitude acceleration control/knowledge for a gravity gradiometer with a given sensitivity. In order to achieve $2 \times 10^{-3} \text{ E Hz}^{-1/2}$, $\theta_n(f)$ and $\alpha_n(f)$ must be controlled or known to $2 \times 10^{-6} \text{ rad Hz}^{-1/2}$ and $2 \times 10^{-4} \text{ rad s}^{-2} \text{ Hz}^{-1/2}$, respectively, if $\delta\hat{n}_-$ and $\delta\hat{n}_{+i}$ can be reduced to the level of 10^{-8} . For $0.1 \text{ E Hz}^{-1/2}$, these requirements become $10^{-4} \text{ rad Hz}^{-1/2}$ and $10^{-2} \text{ s}^{-2} \text{ Hz}^{-1/2}$, respectively. Conventional gyroscopes could be used to satisfy these requirements. If the alignment errors cannot be reduced sufficiently below 10^{-4} , the gradiometer may be integrated with the superconducting six-axis accelerometer, which will have orders of magnitude improvement in attitude resolution over the conventional gyroscopes.

We are also investigating a "pendulum suspension"¹² for the gravity gradiometer. If properly designed, a pendulum suspension can provide isolation in the three angular and two of the three linear degrees of freedom. Since the gradiometer can be balanced in the remaining linear degree of freedom, rejection of acceleration noise in all six degrees of freedom is achieved. Details of the pendulum isolation will be presented in a forthcoming paper.

The extreme sensitivity of the gravity gradiometer requires careful isolation of the device from the thermal and electromagnetic fluctuations of the environment as well. Below the lambda point ($T_c = 2.17$ K), the liquid helium provides a stable and a gradient-free thermal environment. Since no heat is generated by an operating superconducting gradiometer, strong thermal coupling to the bath is not necessary. The sensitivity of the instrument to temperature drift is caused primarily by changes in the magnetic field penetration depth.¹⁷ However, this sensitivity to temperature drift can be tuned out by employing a method similar to the common-mode acceleration rejection technique discussed in Sec. II.⁶ The superconductor itself is a nearly perfect shield against fluctuating magnetic and electric fields. Thus, the superconducting gravity gradiometer can be isolated very effectively from the thermal and electromagnetic noise, leaving the mechanical noise mechanisms discussed above as the most important error sources.

VII. CONCLUSIONS

The necessity of operating a very sensitive gravity gradiometer in an environment with a large common-mode acceleration background requires extreme stability in the acceleration-to-current transfer functions of component accelerometers and a reliable means of balancing out the common-mode sensitivity. The perfect stability of quantized magnetic flux in superconductors can be used to obtain a very sensitive gravity gradiometer with a high CMRR. Combining experiences obtained with a prototype superconducting gravity gradiometer and new technological innovations, we have produced a design which gives a sensitivity of 2×10^{-3} E Hz^{-1/2} and a CMR in excess of 1×10^9 . A three-axis in-line component gravity gradiometer, which incorporates many of the features discussed in this paper, is under construction for space applications. This instrument has been designed for a relatively quiet environment and has been scaled up slightly to deliver a sensitivity of 10^{-4} E Hz^{-1/2}.

The new design utilizes magnetic levitation of the proof masses to null out the gravity bias, permitting operation of the instrument in an arbitrary orientation on the earth and in

space. The low-temperature environment gives an opportunity to isolate the instrument from thermal and electromagnetic fluctuations in the survey vehicle. The inherent sensitivity of all gravity gradiometers to angular motion induced errors makes the attitude control of the gradiometer platform a challenge. However, superconducting techniques can again be employed to monitor the linear and angular motions of the platform with sufficiently high sensitivity and stability. The feedback and error compensation techniques which have been developed for conventional inertial navigation systems and gravity gradiometers could be adapted to the cryogenic instruments discussed here.

ACKNOWLEDGMENTS

We acknowledge fruitful collaboration with Q. Kong and J. W. Parke on the experimental development of superconducting gravity gradiometers. We have also benefited from discussions with Professor Daniel DeBra. This work was supported in part by NASA contract NAS8-33822 and Army contract DACA72-84-C-0004.

¹R. L. Foward, Hughes Research Laboratories, Research Report 469, 1973.

²E. H. Metzger and D. R. Allen, Bell Aerospace Co. Report 9500-92044, 1972.

³M. B. Trageser, in *Proceedings of the 2nd International Symposium on Inertial Technology for Surveying and Geodesy*, edited by K. Schwartz (Canadian Institute of Surveying, Ottawa, 1981).

⁴H. J. Paik, *J. Appl. Phys.* **47**, 1168 (1976).

⁵B. B. Schwartz and S. Foner, *Superconducting Applications: SQUIDS and Machines* (Plenum, New York, 1977).

⁶H. A. Chan, M. V. Moody, H. J. Paik, and J. W. Parke, in *Proceedings of the Seventeenth International Conference on Low Temperature Physics*, edited by U. Eckern, A. Schmid, W. Weber, and H. Wahl (North-Holland, New York, 1984), pp. 927-928.

⁷H. J. Paik, *J. Astronaut. Sci.* **29**, 1 (1981).

⁸M. V. Moody, H. A. Chan, and H. J. Paik, *IEEE Trans. Magn.* **MAG-19**, 461 (1983).

⁹H. J. Paik, Ph. D. thesis, Stanford University, Stanford, California 1974.

¹⁰K. R. Symon, *Mechanics*, 2nd ed. (Addison-Wesley, Reading, MA, 1961), p. 51.

¹¹J. W. Parke, H. J. Paik, H. A. Chan, and M. V. Moody, in *Proceedings of Tenth International Cryogenic Engineering Conference*, edited by H. Colson, P. Berglund, and M. Krusius (Butterworths, London, 1984).

¹²H. A. Chan, Ph. D. thesis, University of Maryland, College Park, Maryland 1982.

¹³Model 440 DC SQUID System, Biomagnetic Technologies, Inc., San Diego, California.

¹⁴P. F. Michelson and R. C. Taber, *Phys. Rev. D* **29**, 2149 (1984).

¹⁵H. A. Chan and H. J. Paik, *Phys. Rev. D* (unpublished).

¹⁶H. A. Chan, H. J. Paik, M. V. Moody, and J. W. Parke, *IEEE Trans. Magn.* **MAG-21**, 411 (1985).

¹⁷M. V. Moody, H. A. Chan, H. J. Paik, and C. Stephens, in *Proceedings of the Seventeenth International Conference on Low Temperature Physics*, edited by U. Eckern, A. Schmid, W. Weber, and H. Wahl (North-Holland, New York, 1984), pp. 407-410.

APPENDIX F

PREDICTED DISTURBANCES

This Appendix includes details of some of the predicted disturbances for potential SGG instrument carriers. Included are aerodynamic drag, the Shuttle acceleration environment, and the Tethered Satellite System disturbances.

F.1 Aerodynamic Drag

The mean free path at orbital altitudes is large compared to satellite dimensions. Thus, the aerodynamic drag can be based on the free molecular flow model as a force proportional to the square of the spacecraft velocity in a direction opposite to the velocity vector. The force due to aerodynamic drag is given by

$$F_D = C_D \left(\rho \frac{v^2}{2} \right) A , \quad (F-1)$$

where C_D is the drag coefficient, A is the effective cross sectional area of the satellite, ρ is the atmospheric density, and v is the satellite velocity. The drag coefficient depends on the mechanism of molecular reflection, the ratio of the mean molecular speed and the satellite velocity, and the surface temperature of the satellite. For a sphere, a value between 2 and 2.2 has historically been found to be an acceptable value.

The detailed estimate of the drag experienced by each SGGM spacecraft concept considered in this study is discussed below.

F.1.1 Modeling Technique

A mathematical model was utilized to calculate the free-molecular force and moment coefficients based on classical free molecular flow theory [F-1]. Aerodynamic coefficients can be computed utilizing this model for any spacecraft configuration at a given orbital altitude and spacecraft attitude. The model considers the complete description of the spacecraft, and includes shadowing for complex configurations to account for the surface areas, which are shaded from the flow by other body components. The model includes transfer of energy and momentum, both tangential and normal, to all surfaces during the particle-orbiting body collisions.

F.1.2 Atmospheric Density

Drag estimates depend strongly on atmospheric density. Figure F-1 shows the predicted average orbital densities at 200 km during the 1998 mission time frame. Also shown in the figure is the predicted average densities at 160 km. The solar activity data, shown in Figure F-2, are based on 2σ (97.7 percentile) of the 13-month mean solar flux (10.7 cm) and the mean geomagnetic index (AP). The density model

is discussed in detail in Reference F-2. Since a Sun-synchronous orbit was assumed, the diurnal variations were not considered. The mission was assumed to occur between March and October 1998.

F.1.3 Spacecraft Configurations

Three configurations were considered in this analysis, Option I-A, the ion propulsion spacecraft with large solar arrays; Option I-B, the spherical configuration; and Option II-A, a 1.7-m diameter by 8.2-m length cylindrical configuration (Fig. F-3).

Ion Propulsion Spacecraft: This configuration is illustrated in Figure F-3 along with the spacecraft dimensions used in the model. The angle of attack (the angle the solar arrays make with the velocity vector) was varied from 0 to 10 deg, in order to determine the drag as a function of the orientation of the solar arrays. The results are shown in Figure F-4, where drag is plotted versus angle of attack for minimum and maximum values of atmospheric density predicted during a six-month mission in 1998. The drag force for a 3-m sphere is also shown in Figure F-4 for comparison.

Figure F-5 shows the drag as a function of time for a six-month mission beginning in March 1998. The 3-m sphere is again shown. One notes from the figures that, even at zero angle of attack, the drag is about 40 percent higher for this configuration than for a 3-m sphere alone. Table F-1 lists the drag coefficients for the various spacecraft components and for different angles of attack. In these calculations, the reference area 7.07 m^2 was used.

Spherical Configurations: The drag for the 3-m spherical configuration was indicated in Figure F-4. The average orbit drag for the 3-m sphere is between 96 mN and 120 mN during the six-month mission.

1.7-Meter Cylindrical Configuration: The velocity vector is along the long axis of the cylinder for zero angle of attack. The average monthly drag versus mission time is shown in Figure F-6. The nominal drag force during the mission for zero angle of attack is approximately 53 mN. Drag versus angle of attack is shown in Figure F-7, and Figure F-8 shows the drag versus roll angle about the cylindrical axis of the spacecraft.

Shuttle Orbiter: The expected drag acceleration versus orbit altitude for the Orbiter is shown in Figure F-9.

F.1.4 Orbit Altitude Considerations

The expected aerodynamic drag versus orbital altitude is shown in Figure F-10 for a 3-m spherical spacecraft. The nominal atmospheric density for the March-October 1998 time frame has been assumed. One notes from the figure that, by reducing the altitude from 200 to 160 km, the drag increases by almost a factor of 5.

F.2 Shuttle/Spacelab Acceleration Levels

Several Shuttle flights have utilized low-g accelerometers to measure the Shuttle acceleration environment. A very large amount of raw data has been obtained, but only partially analyzed. This is especially true for frequencies below 1 Hz [F-3].

The handling of low-g acceleration data is very challenging. The signals for measuring microgravity levels can be easily masked by ordinary electronics noise. Shifts in accelerometer calibration is also a problem. The large amount of data generated creates data reduction problems. For example, one sample per second on a single axis produces one-half mission data points for a typical Shuttle mission. Figures F-11 through F-13 and Table F-2 illustrate typical results that are available.

Figure F-11 shows results from the 1983 Spacelab 1 mission. The accelerometers had a sensitivity of 10^{-6} g and a bandwidth of 30 Hz. Samples were recorded at a rate of 80 sec⁻¹. Table F-2 summarizes the acceleration levels and frequencies measured for several events and "quiet times" during this mission. During quiet times, acceleration levels at the pallet location varied from 0.13 to 0.45 mg in the 8 to 40 Hz frequency range.

Spacelab 3 carried a package of Bell Miniature Electrostatic Accelerometers which have a resolution of 10^{-6} g and a bandwidth of 50 Hz. Data was sampled at the rate of 300 samples sec⁻¹. Figure F-12 shows the raw data spectrum, while Figure F-13 displays the power spectral density filtered to display the 0 to 7.5 Hz acceleration environment.

At this time, no definitive statement can be made about the full spectral range of disturbances. This is especially true for frequencies below 1 Hz. However, from the data available, one can estimate the Shuttle/Spacelab acceleration environment at about the 10^{-3} to 10^{-4} g level. Table F-3 summarizes the expected acceleration levels from various sources.

F.3 Tethered Satellite System (TSS) Disturbances

An investigation of the acceleration levels and motion characteristics of the TSS was made. Although the TSS is a very versatile system, it has complex dynamics and the acceleration levels are not benign. When this complexity is added to the severe requirements imposed by the SGGM, it appears that the TSS may not be suitable as a carrier. The rationale for this conclusion is presented below.

For simplicity, consider the TSS as two masses, M_1 and M_2 , in the form of a dumbbell with separations from the center of gravity, r_1 and r_2 , respectively. The major forces acting on the TSS are shown in Figure F-14(a), where Ω_0 is the orbital angular velocity. These forces will appear as tension in the tether separating the two masses, and will result in acceleration at the tethered mass. The magnitude of this force is given approximately as $4 \times 10^{-4} \text{ km}^{-1} (L)$, where L is the distance from the tethered satellite to the center of gravity of the system. Superimposed on this force will be forces due to differential atmospheric drag, the oblateness of the Earth,

micrometeoroids, radiation pressure, and disturbances coupled from the upper platform such as crew motion (for manned systems), and station-keeping [F-4].

The acceleration from the tether force discussed above is perceived as "artificial gravity." This force may be either held constant, or varied by deploying or retracting the tether. This is illustrated in Figure F-14(b), where various tethered masses are plotted versus tether tension. For a 550-kg satellite on the end of a 100-km tether, the acceleration would be about 0.04 g.

The vertical tether orientation is relatively stable; however, the disturbance forces identified above will cause tether libration about the vertical. In order to understand the libration motion and control, an orbital/libration dynamics simulation of the TSS has been made [F-5]. One of the missions considered in the simulation was the deployment of a 550-kg mass tethered from the Shuttle (weight $\sim 101,338$ kg). The Shuttle altitude was 235 km and the probe was deployed downward to an altitude of 135 km (100-km tether length). The satellite was assumed to be capable of position control through RCS thrusters. The Shuttle RCS was also utilized and the tether tension/length was controlled. Figures F-16 and F-17 illustrate some of the results from this simulation.

Figure F-15 defines the coordinate system used and the projection of the satellite motion in the x-y plane. Note the wide variation when the satellite reaches the lower altitude where atmospheric density is higher. Figure F-15 also shows the tension forces that the satellite experiences. The acceleration varies between 0.04 and 0.06 g. In addition, as can be seen from the figure, a fine structure variation in acceleration also exists.

Figure F-16 shows the x-, y-, and z-coordinates; the variation of the center of mass of the system; and the pitch angle and pitch angle rate (the roll angle does not vary as greatly, and is not shown) as functions of mission time. The tether length is adjusted during the mission in an attempt to control libration dynamics, as can be noted from the z-coordinate variation. The satellite RCS system was also used to control the satellite.

One notes from these results that the disturbances experienced by the tethered satellite would be quite severe for an instrument having the demanding requirements of the SGG. Although disturbances may be partially controlled, it appears that the TSS is not a suitable platform for the SGM.

REFERENCES

- F-1. Warr, J. W., III: An Orbital Aerodynamics Computer Program to Calculate Force and Moment Coefficients on Complex Vehicle Configurations. LMSC/HREC D162498, Lockheed Missile and Space Company, Huntsville, AL, August 1970.
- F-2. Johnson, D. L. and Smith, R. E.: The MSFC/JTO Orbital Atmosphere Model and the Data Bases for the MSFC Solar Activity Prediction Technique. NASA TM-86522, November 1985.
- F-3. Chassay, R. P. and Schwaniger, A. J., Jr.: Low-g Measurements by NASA. NASA TM-86585, December 1985. See also "Measurement and Characterization of the Acceleration Environment on Board the Space Station." Workshop Proceedings, Teledyne Brown Engineering, Guntersville, AL, August 11-14, 1986.
- F-4. Baracat, W. A. and Butner, C. L.: Tethers in Space Handbook. NASA Publication, 1986.
- F-5. Bodley, C. S., Park, A. C., and Grosserode, P. J.: Tethered Satellite System Orbital Dynamics Model 1B, Rev. A. DPD No. 596, Martin Marietta Corp., Denver Aerospace, Denver, CO, February 1985.

TABLE F-1. DRAG COEFFICIENTS AS A FUNCTION OF
ANGLE OF ATTACK (OPTION I-A)

ANGLE OF ATTACK (DEG.) (α)	DRAG COEFFICIENT		
	3-M SPHERE	SOLAR ARRAYS (2) + ATTACHMENTS*	TOTAL
0	2.13	1.26	3.39
4	2.13	1.42	3.55
6	2.13	1.78	3.91
8	2.13	2.17	4.30

* INCLUDES LATERAL (TOP, BOTTOM), FRONTAL, REAR, OUTER, AND
INNER SURFACE

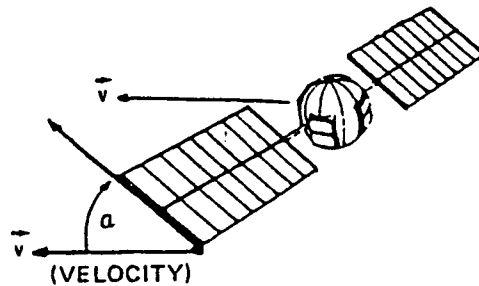


TABLE F-2. PEAK ACCELERATIONS FROM SPACELAB 1 [F-3]

	MODULE			PALLET		
	X-DIRECTION	Y-DIRECTION	Z-DIRECTION	X-DIRECTION	Y-DIRECTION	Z-DIRECTION
"QUIET TIME" 11.18-11.23 HRS AMPLITUDE (mg) FREQUENCY (Hz)	0.35 - 0.4 20 - 35	0.25 22 - 40	0.5 - 0.65 17 - 40	0.13 - 0.25 22	0.2 - 0.45 22	0.13-0.25 8 - 16
COUGH TEST 11.314 - 11.315 HRS AMPLITUDE (mg) FREQUENCY (Hz)	1.0 10	1.0 11	2.8 9	0.2 10	0.3 8	0.7 10
X-PUSH-OFF 11.340 - 11.355 HRS AMPLITUDE (mg) FREQUENCY (Hz)	2.8 12	3.0 21	2.5 9	0.6 12	1.0 6	1.2 8
Y-PUSH-OFF 11.375 - 11.385 HRS. AMPLITUDE (mg) FREQUENCY (Hz)	0.1 16	1.0 21	2.4 8	0.3 18	0.5 15	0.5 8
Z PUSH-OFF 11.404 - 11.406 HRS. AMPLITUDE (mg) FREQUENCY (Hz)	1.1 12	1.0 20	1.7 16	0.7 15	1.1 17	1.0 9
VERNIER THRUSTER FIRING 202050-202110 SEC. (111 NEWTONS) AMPLITUDE (mg) FREQUENCY (Hz)	0.3 - 0.5 17	0.3 - 0.6 25	0.5 - 1.0 18	NOT AVAILABLE	NOT AVAILABLE	NOT AVAILABLE
PRIMARY THRUSTER FIRING 188.670-188.930 HRS. (3,870 NEWTONS) AMPLITUDE (mg) FREQUENCY (Hz)	25 - 29 9	20 - 29 9	2.5 - 2.9 9	10 - 15 8	10-15 16	20 - 29 16
TUNNEL TRUNNION DISTURBANCE 188.431 - 188.435 HRS. AMPLITUDE (mg) FREQUENCY (Hz)	12 13	6.0 20	9.0 15	2.5 12	2.4 25	3.0 12

TABLE F-3. ESTIMATES OF ACCELERATION LEVELS DUE TO SHUTTLE DISTURBANCE SOURCES

SOURCE	LINEAR (MILLI-g)	ROTATIONAL (MILLIRAD/S ²)
RCS THRUSTERS		
- VERNIER SYSTEM	0.2	0.3
- PRIMARY SYSTEM	40	20
CREW MOTION	0.1	0.2
GRAVITY GRAD. TORQUE	-	2×10^{-3}
AERODYNAMIC DRAG	$10^{-3} - 10^{-4}$ (VARIES WITH ALT.)	-
CENTRIFUGAL FORCE	LX1 UNITS/S ² (LINEAR ACCELERATION)	1 (FOR EARTH REFERENCE)

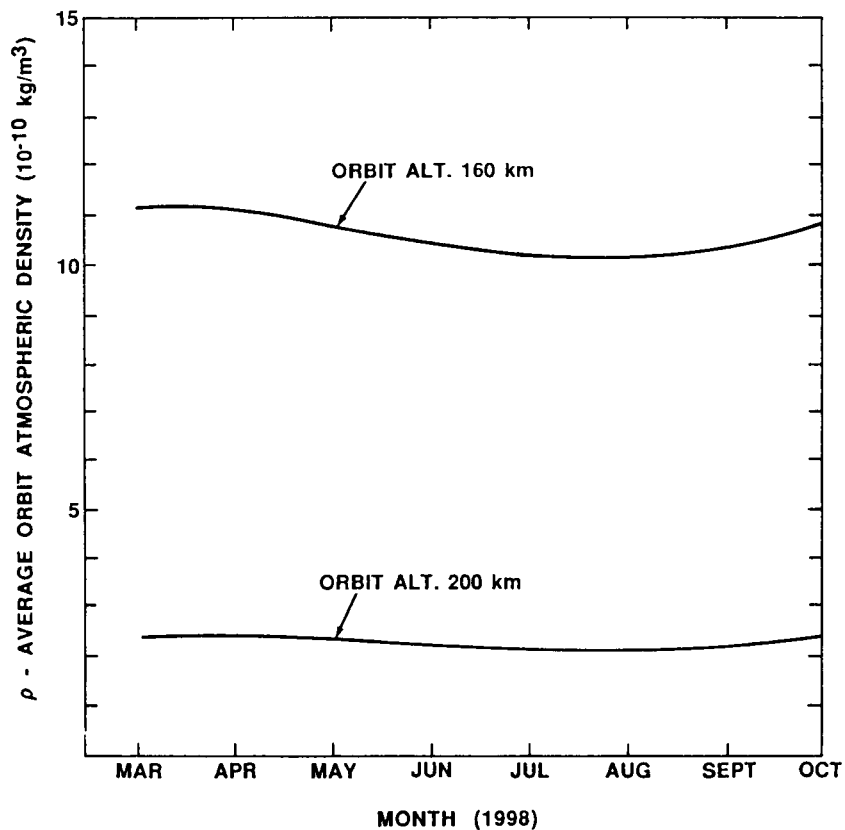


Figure F-1. Predicted average orbital atmospheric densities for 200-km and 160-km altitudes.

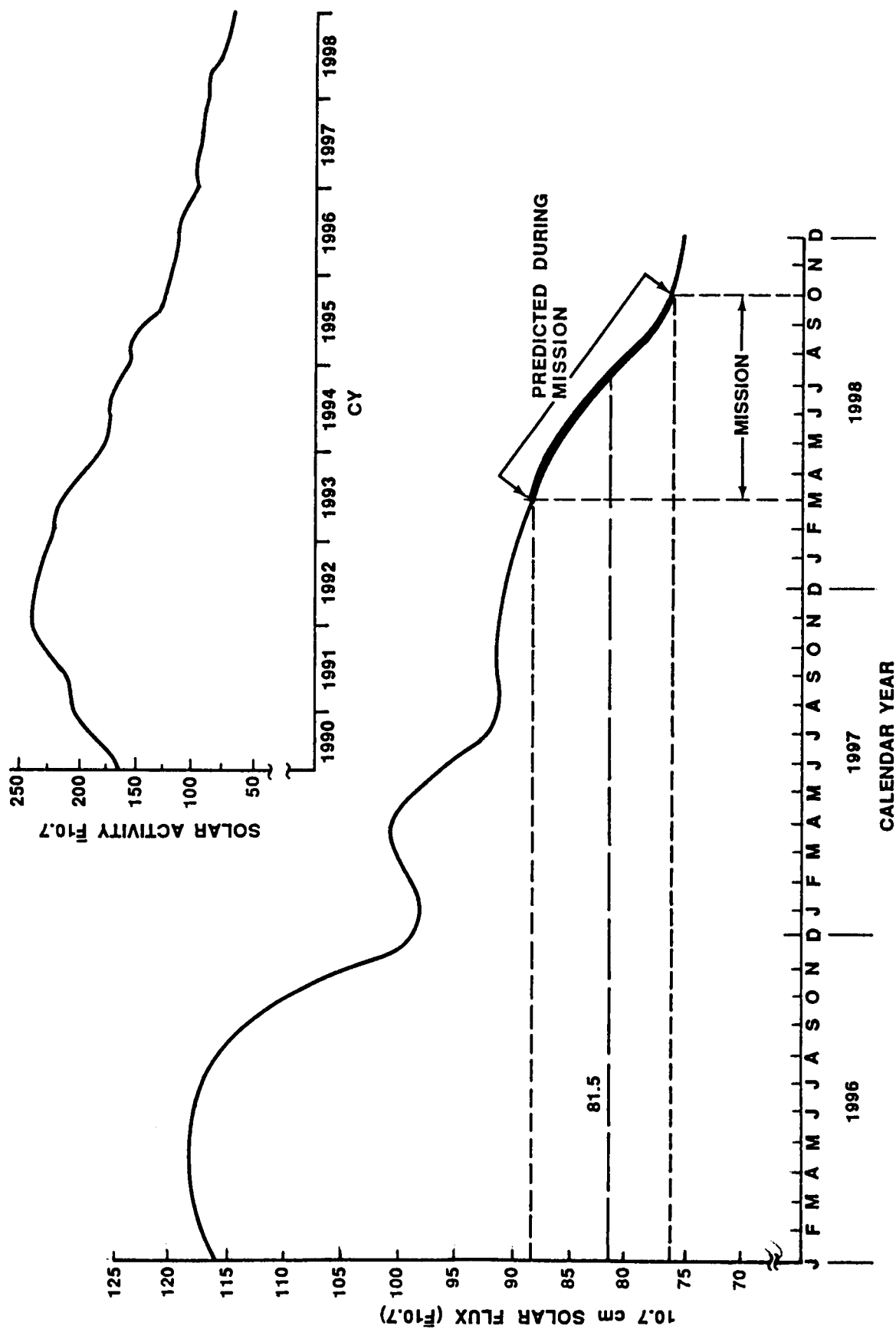


Figure F-2. Statistical estimate of solar activity [F-2], 97.7 percentile.

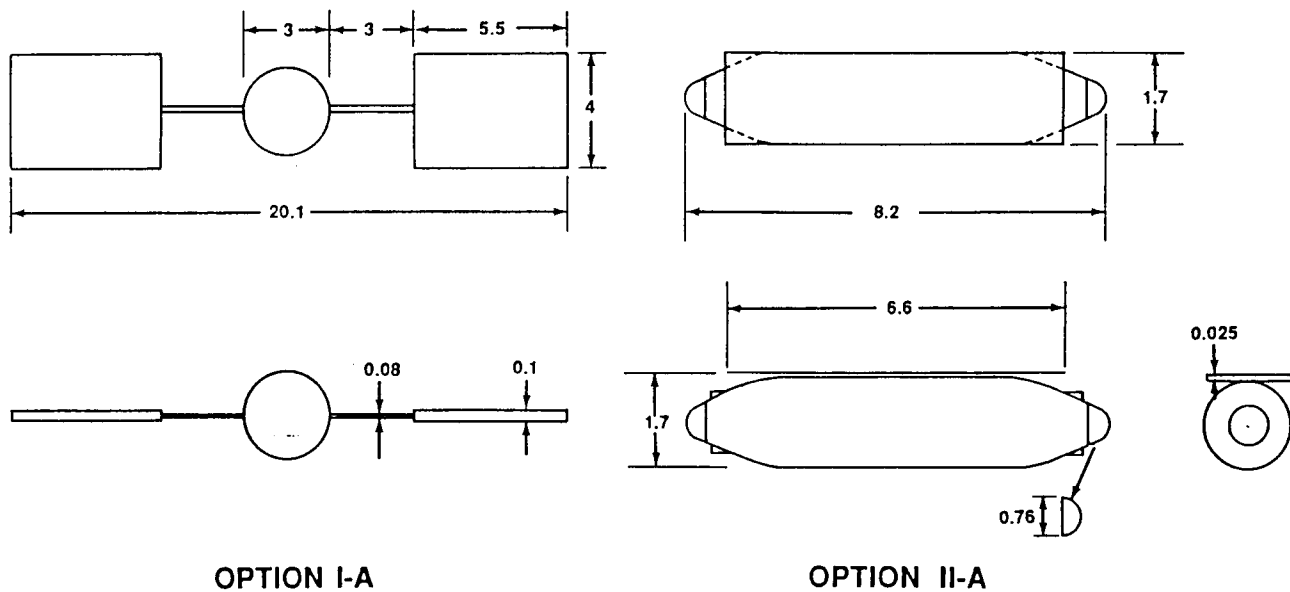


Figure F-3. Configurations used in drag analysis (dimensions are in meters).

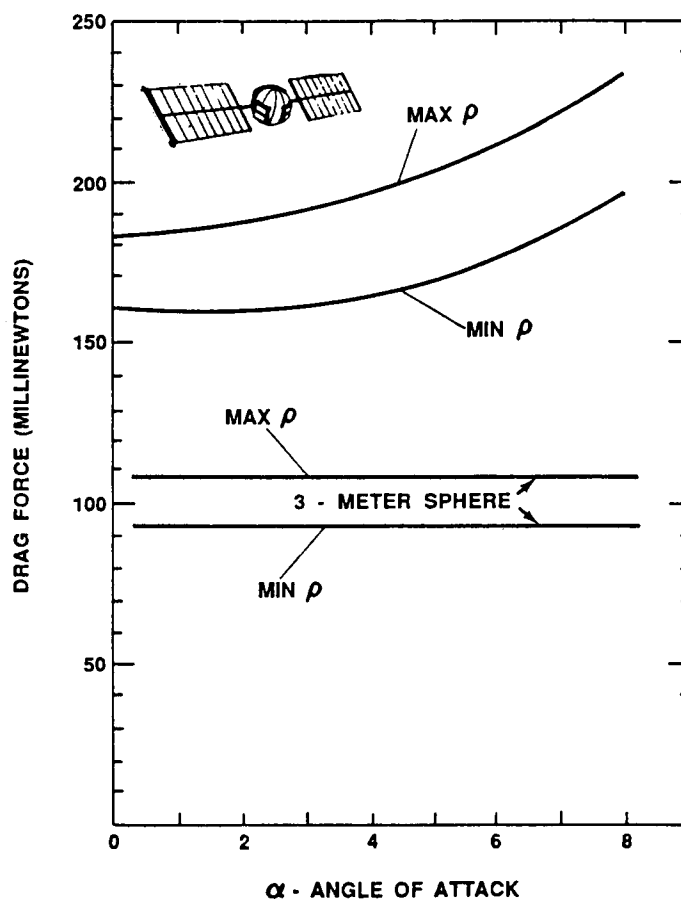


Figure F-4. Drag force as function of angle of attack (Option I-1).

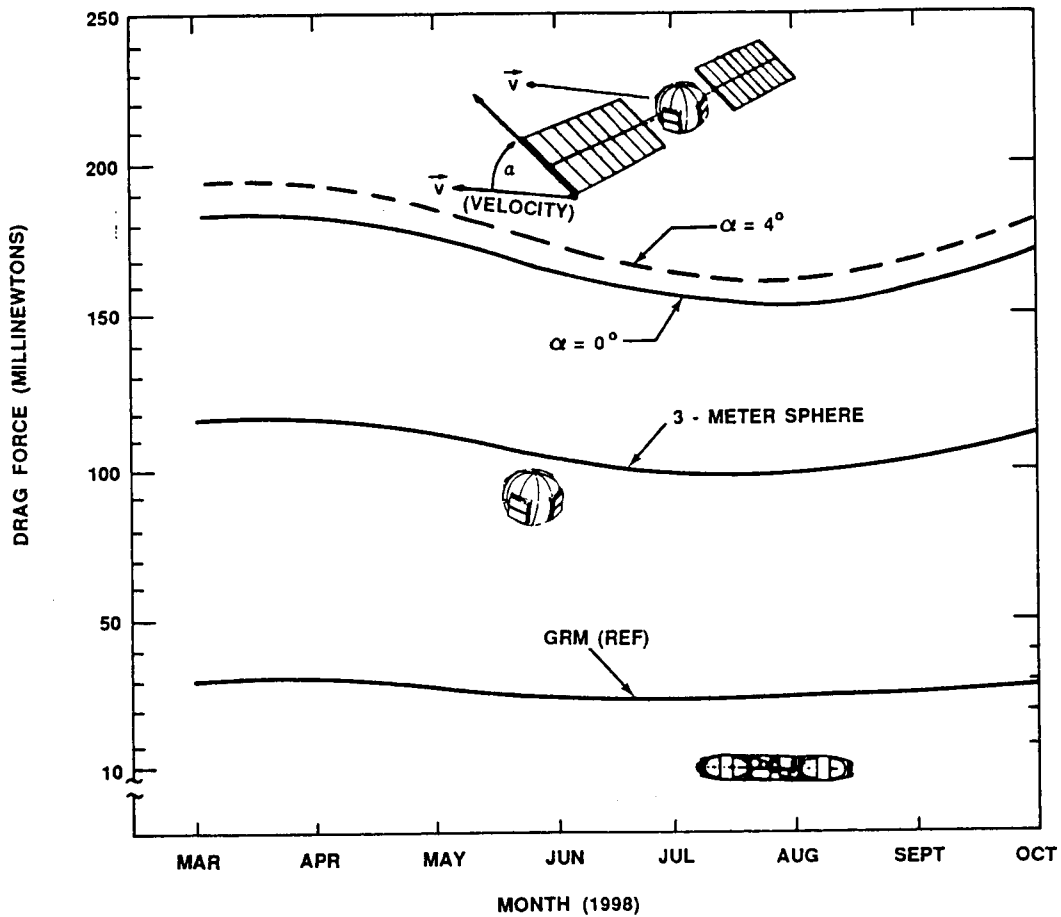


Figure F-5. Drag force as a function of mission time (Option I).

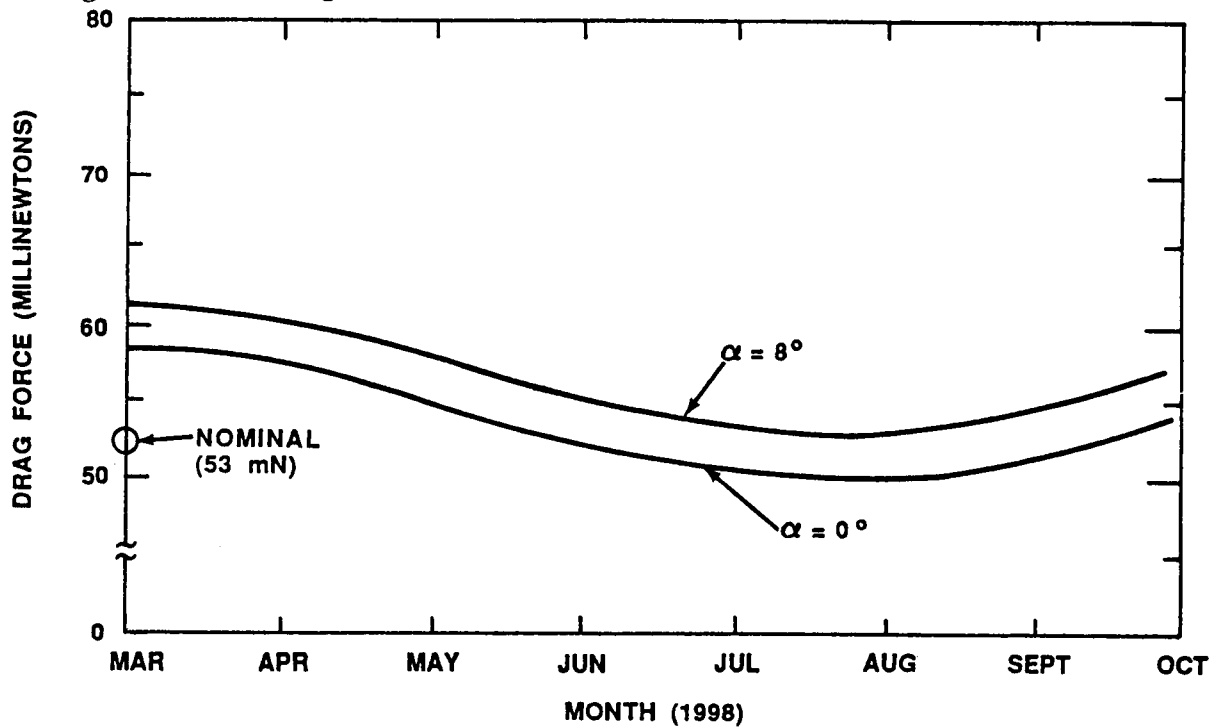


Figure F-6. Drag force as a function of mission time (Option II-A).

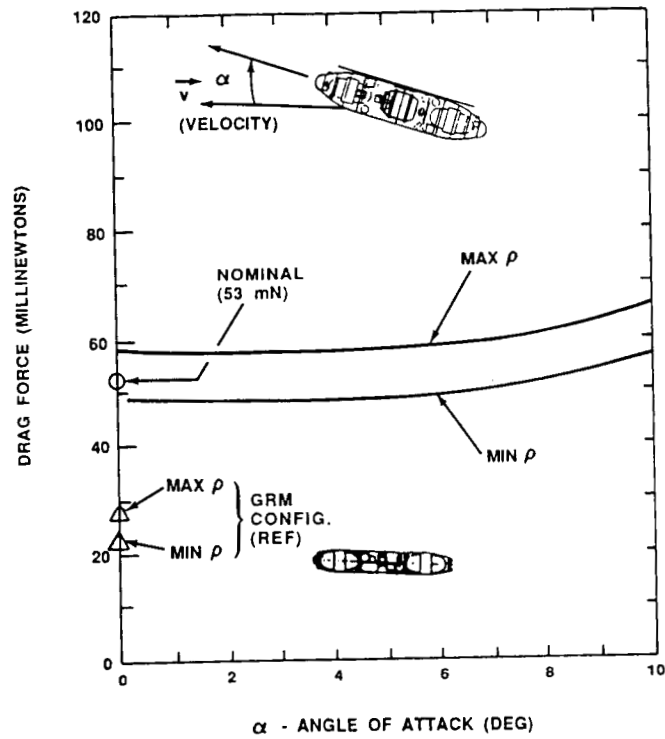


Figure F-7. Drag force as a function of angle of attack (Option II-A).

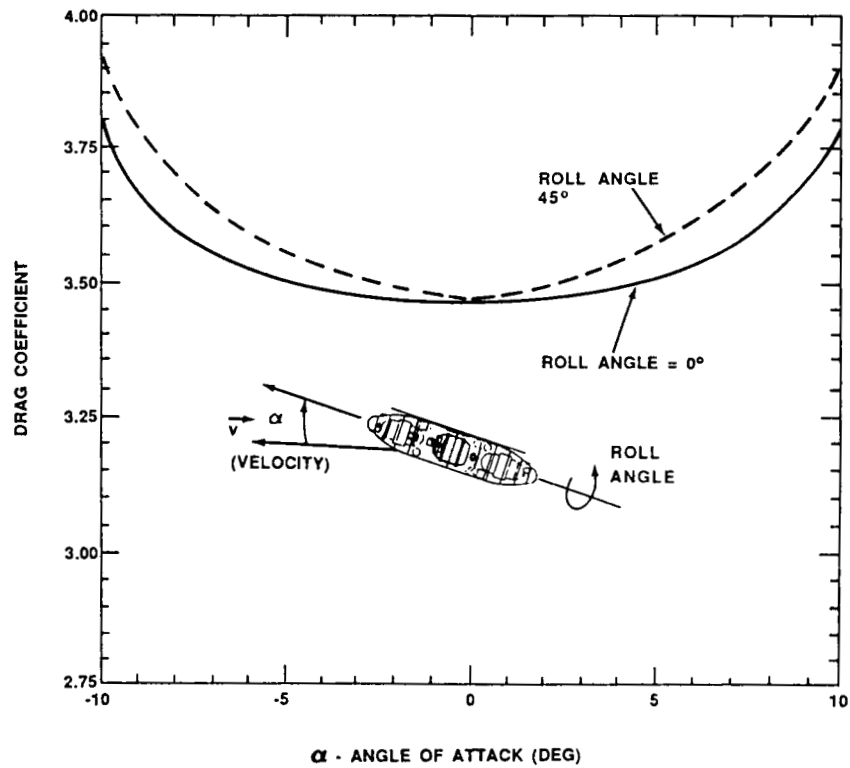


Figure F-8. Roll angle influence on drag coefficient (Option II-A).

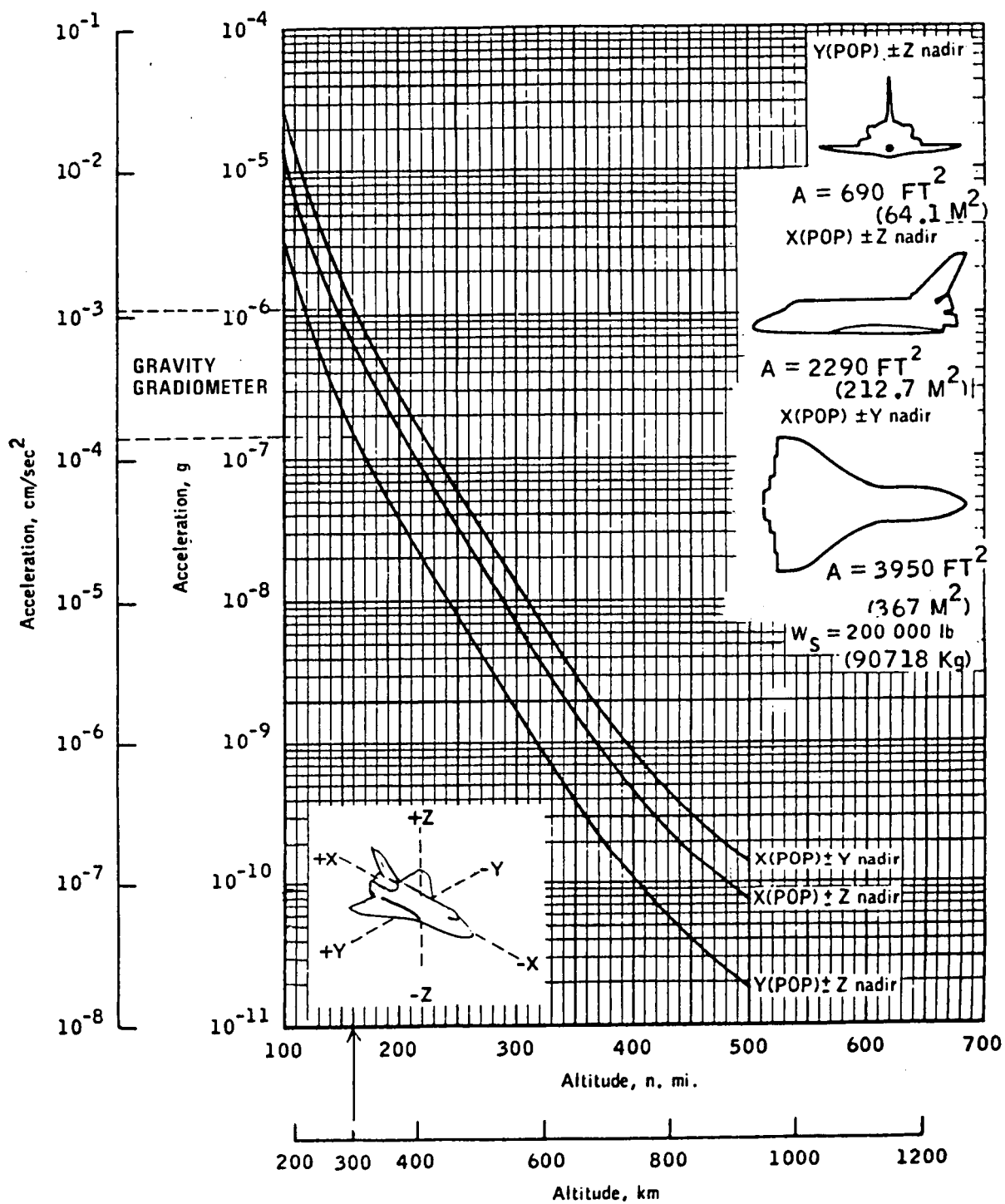


Figure F-9. Atmospheric drag on Shuttle Orbiter versus orbit altitude for selected Orbiter orientations.

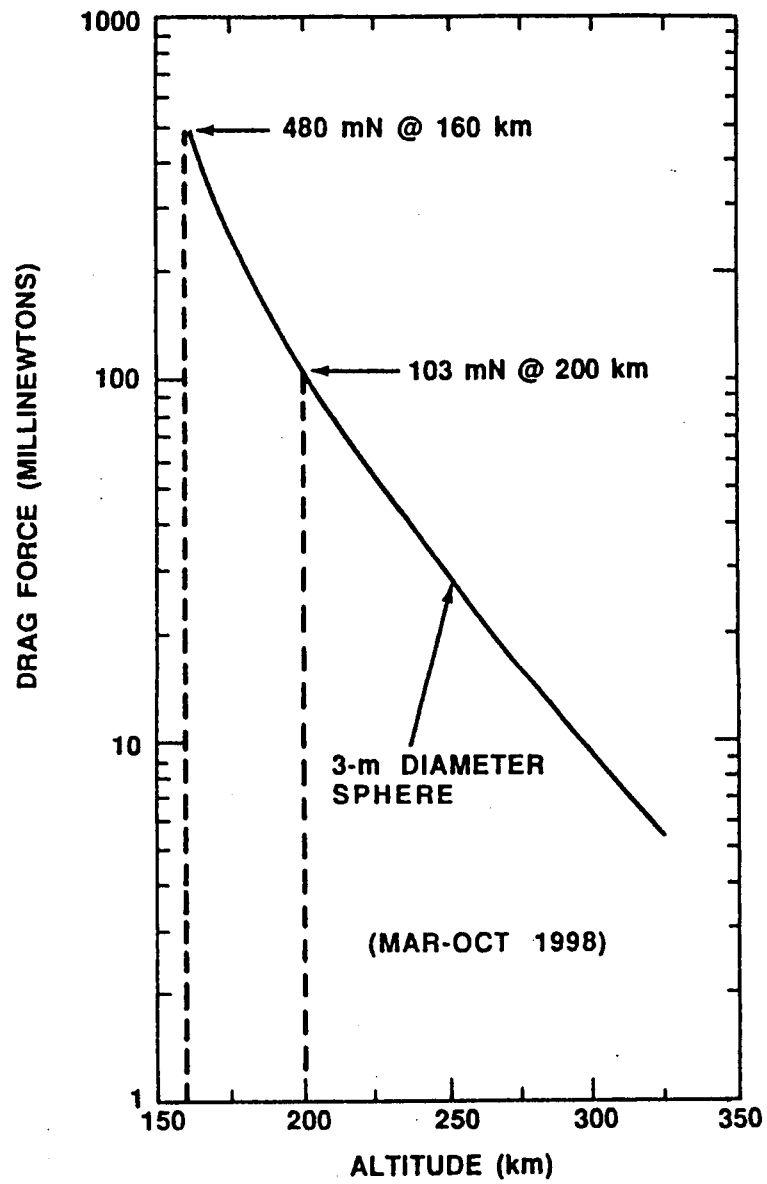


Figure F-10. Expected aerodynamic drag versus orbital altitude.

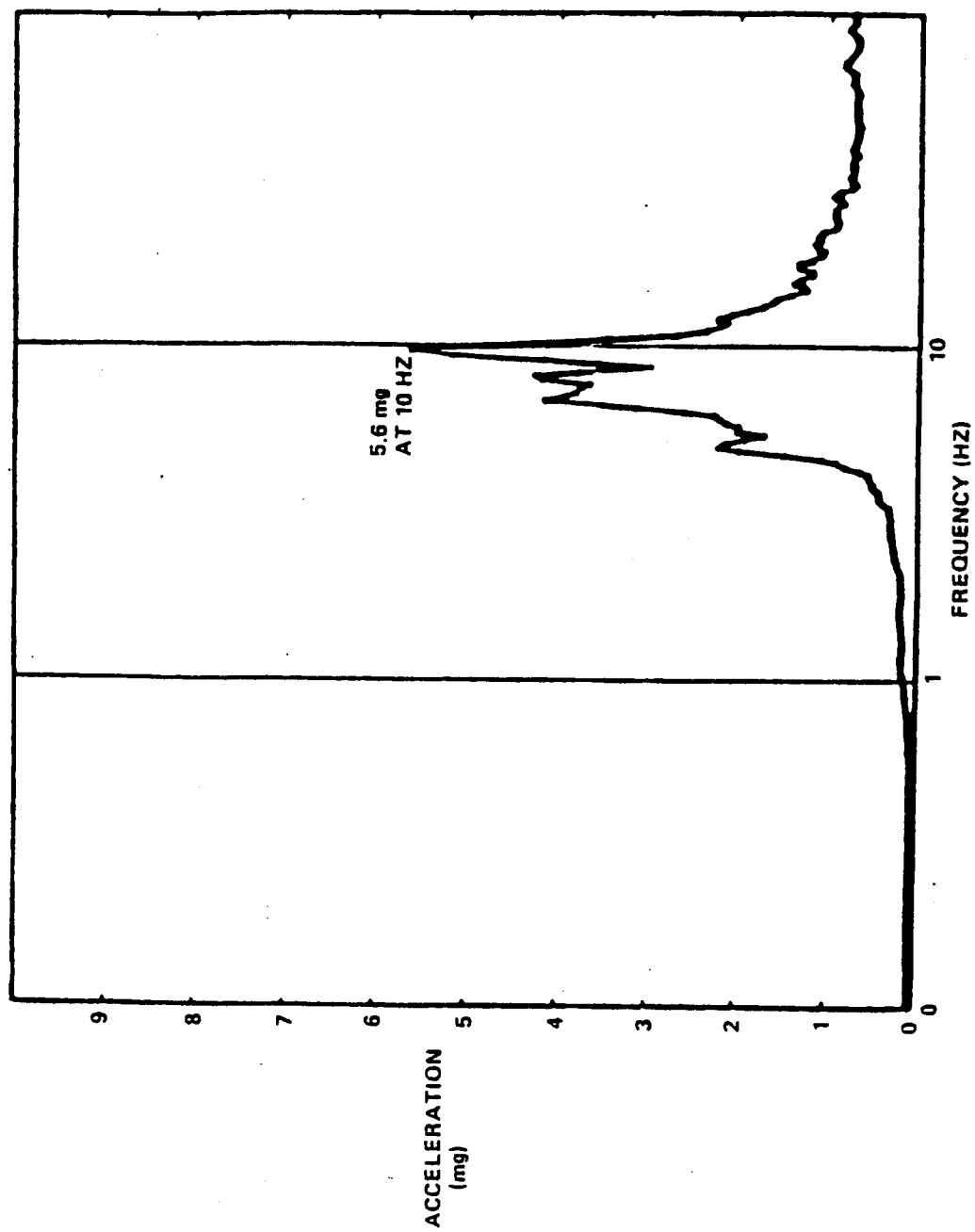


Figure F-11. Shock spectra from crew-induced acceleration (cough test) [F-3].

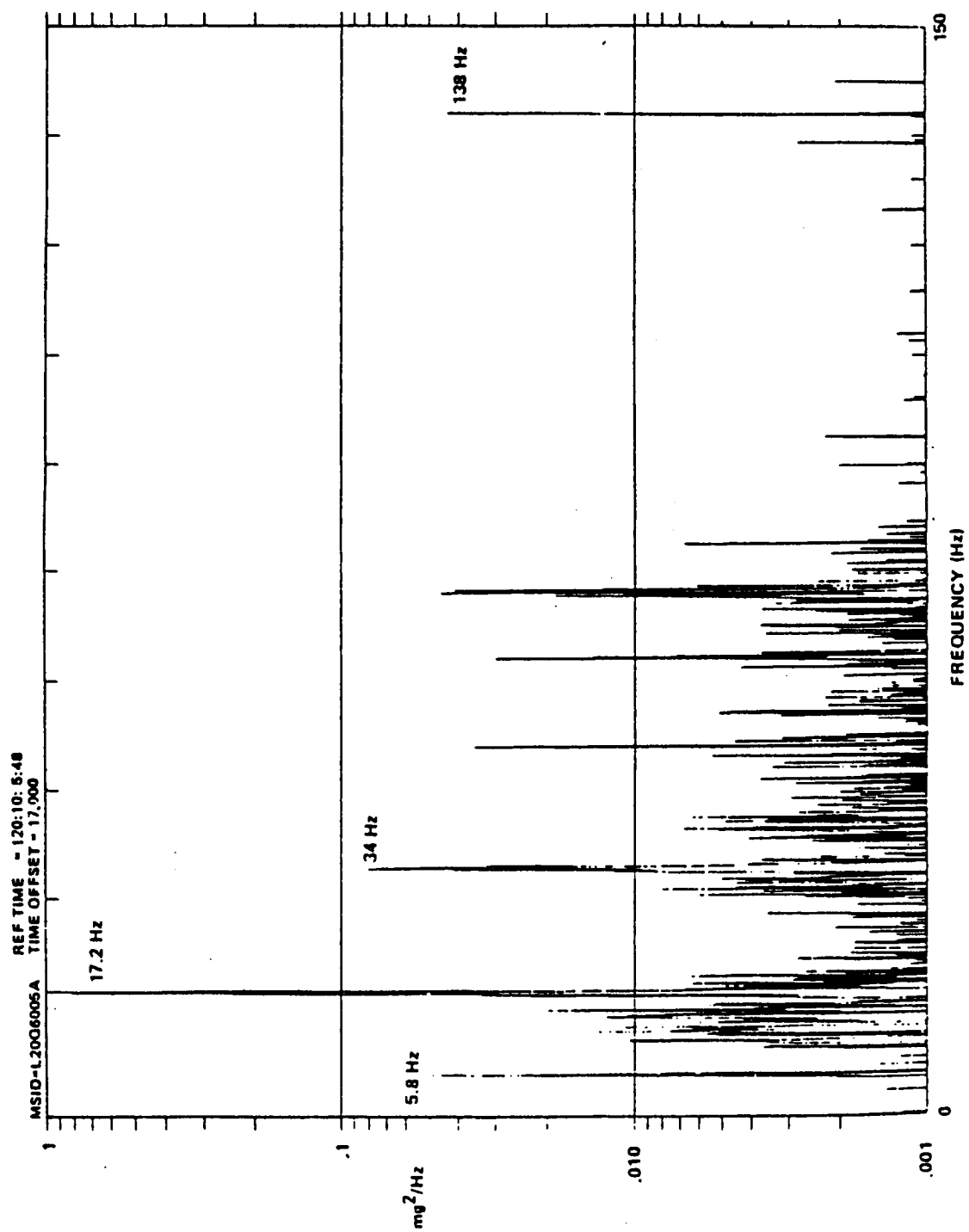


Figure F-12. Power spectral density from Spacelab 3 (raw data) [F-3].

MSID-L7006005A REF TIME - 120:10: 5:48
TIME OFFSET - 17.000

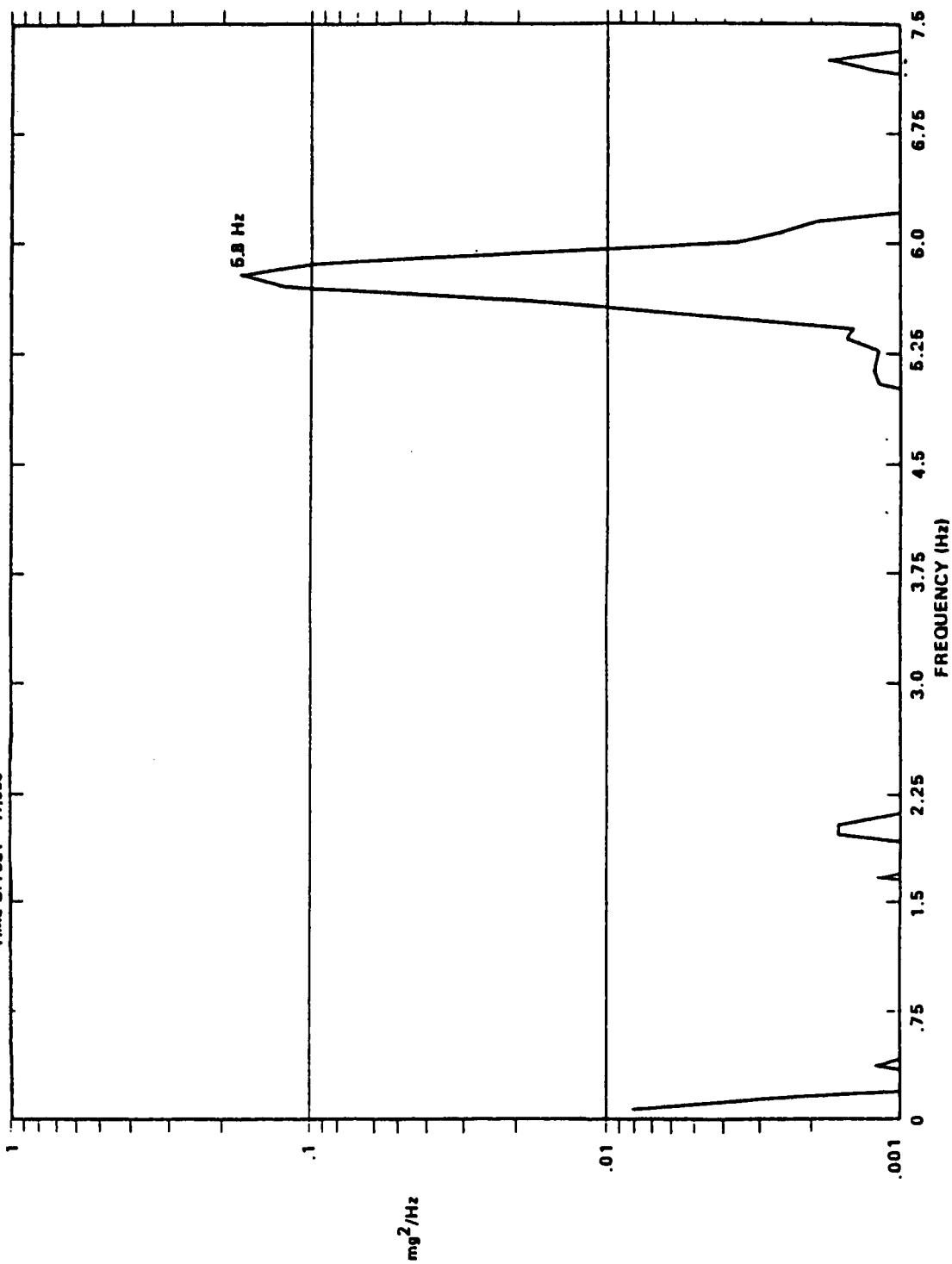
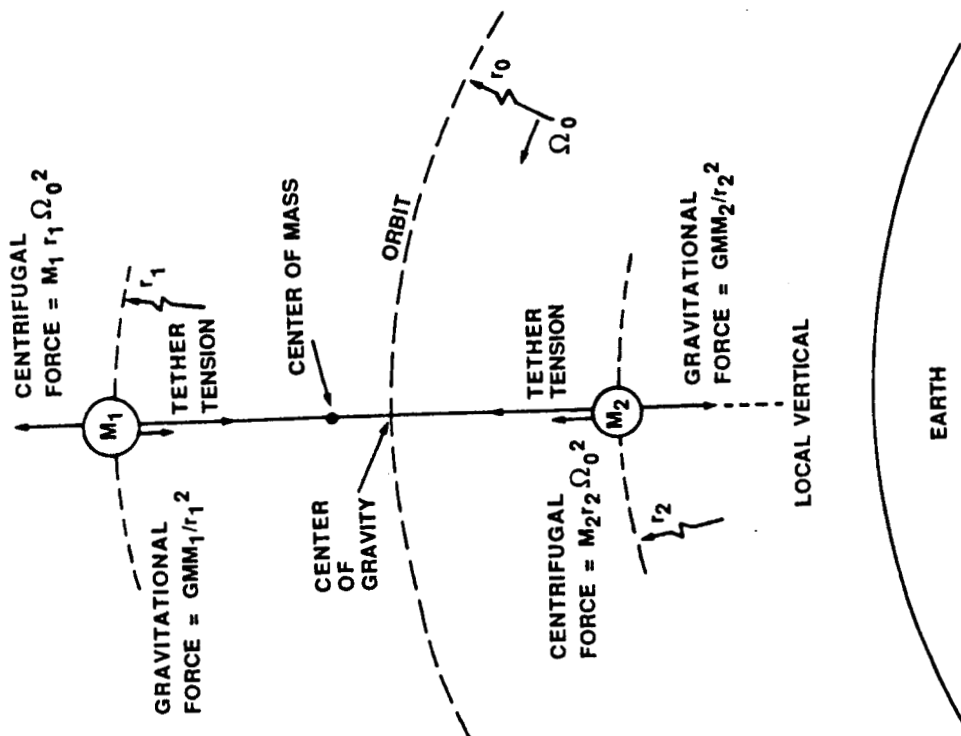
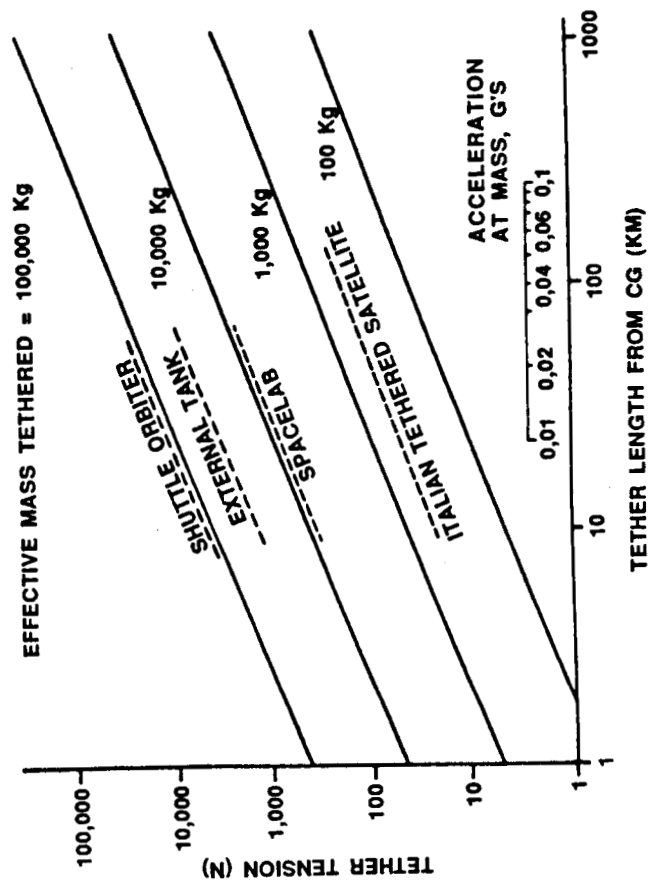


Figure F-13. Power spectral density from Spacelab 3 [F-3]
(filtered data: 0 to 7.5 Hz bandpass).



(a) FORCES ON TETHERED SATELLITES.



(b) "ARTIFICIAL GRAVITY" AT TETHERED MASS.

Figure F-14. "Artificial gravity" forces on a tethered mass in orbit [F-4].

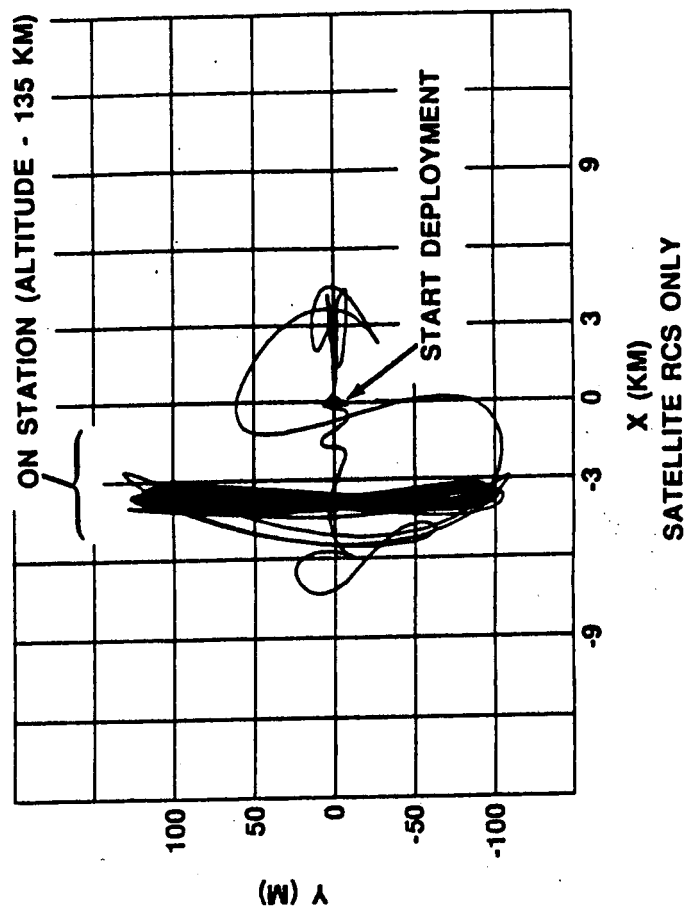
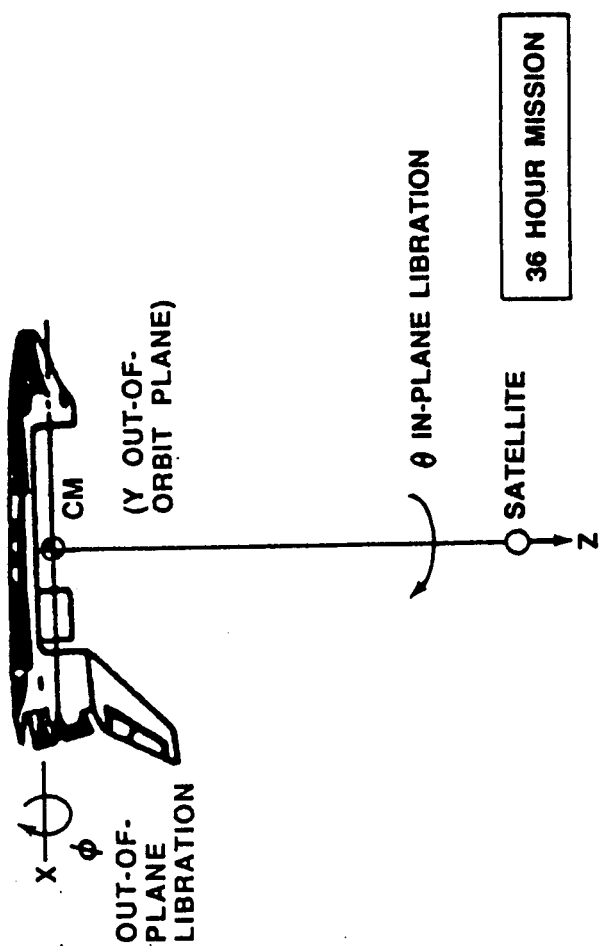
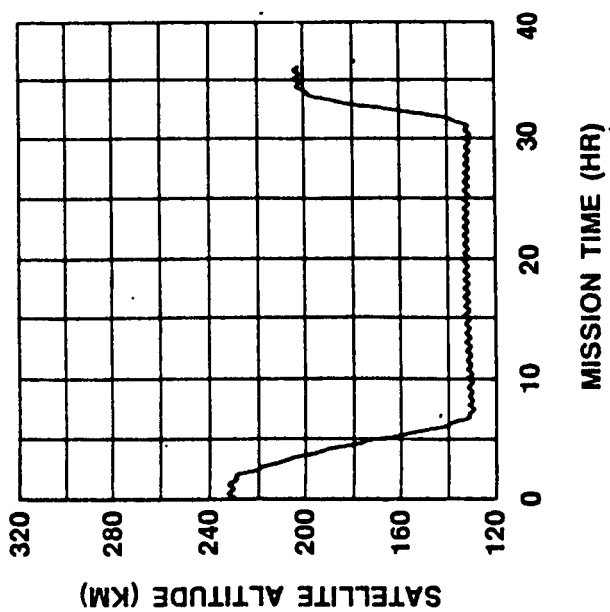
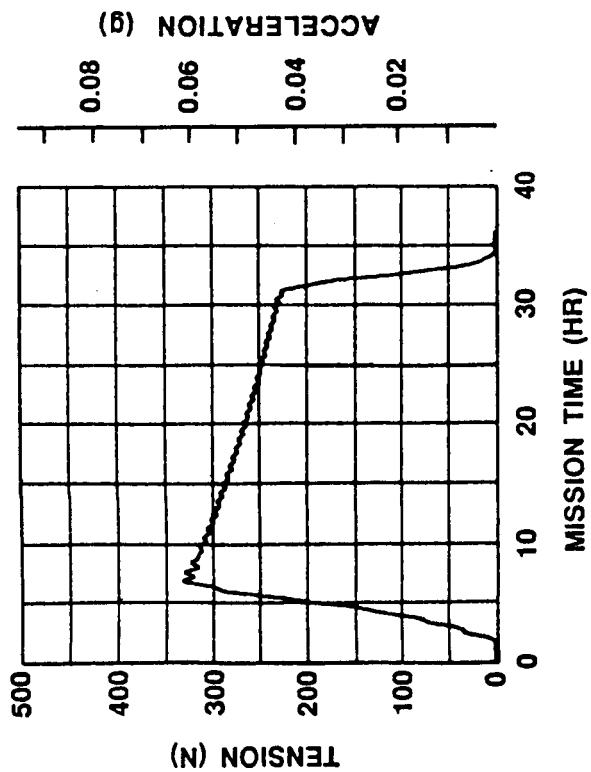
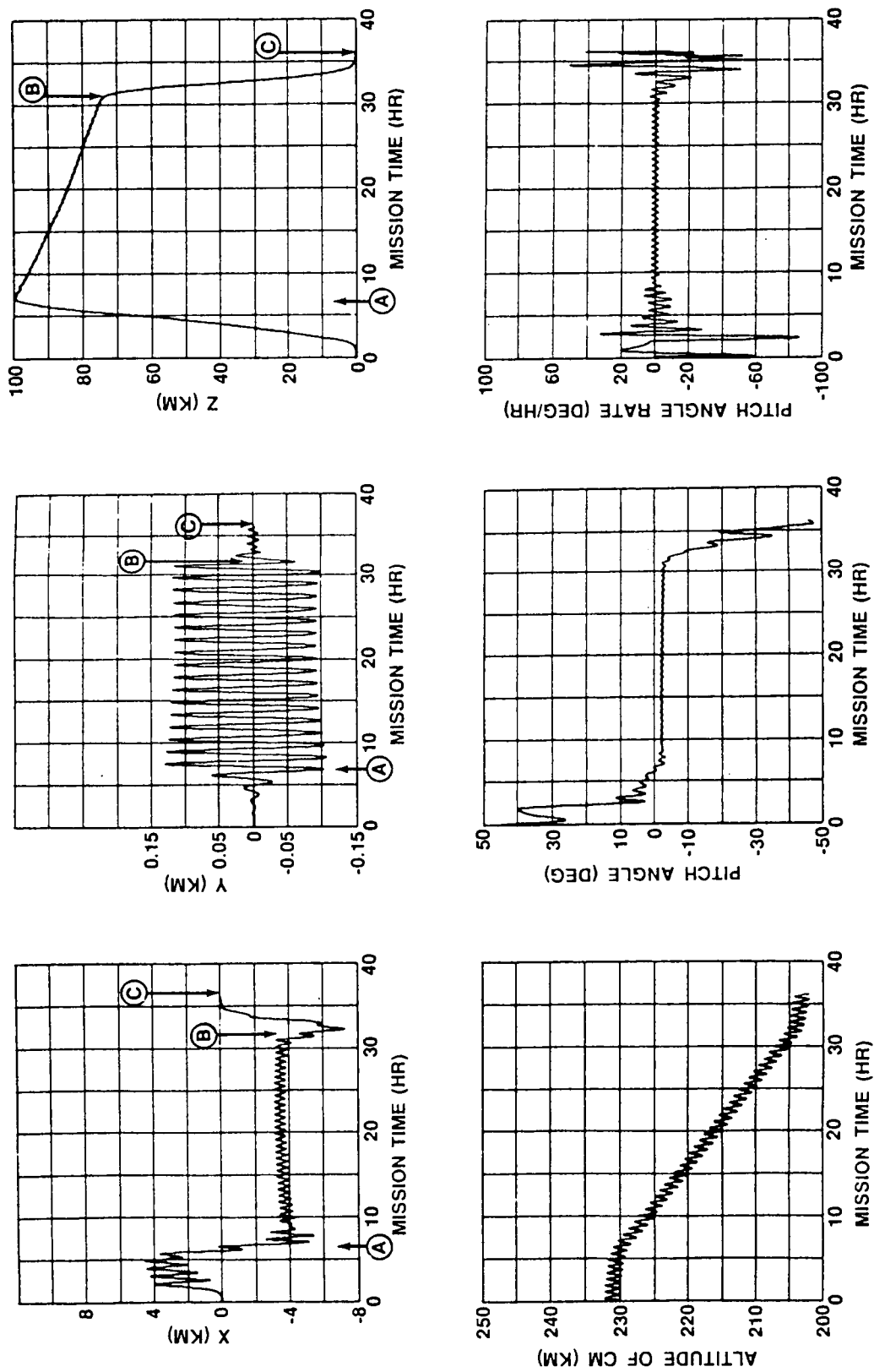


Figure F-15. Tethered satellite motion [F-5].



NOTES:

(A) ON-STATION, (B) BEGIN RETRIEVAL (C) END MISSION

Figure F-16. Tethered satellite motion as function of time [F-5].

APPENDIX G

CONTROL SYSTEM SIMULATION

G.1 Introduction

This Appendix describes a preliminary computer simulation of the SGGM control system. The derivation of equations of motion, environmental force models, a preliminary control system configuration, and exemplary simulation results are included.

In developing the preliminary control system scheme for the SGGM, several assumptions were made. First, it was assumed that the controlled attitude would be constant relative to a local-vertical-fixed reference system. Consequently, the spacecraft translational dynamics needed only to be computed relative to this local-vertical reference. Another benefit from this assumption was that the translational dynamics could be represented by Hill's equations [G-1]. The displacements from a nominal, circular orbit were assumed to be relatively small compared to distances from the center of the Earth; thus, the Earth's gravitational forces and torques needed only to be carried to the first order, or gradient level in terms of the nominal circular orbit. (The nominal circular orbit shall be referred to as the reference or ideal orbit.) Since the SGG is very sensitive, self and mutual gravity fields are important. However, in this preliminary study, these effects have not been included.

In the simulation discussed in this Appendix, the Earth-fixed spacecraft orientation was chosen. Figure G-1 schematically shows the spacecraft orbital geometry with the Experiment Module located inside the spacecraft undergoing small deviations from a nominal circular orbit. The Experiment Module is assumed to be controlled in both attitude and translation by controlling the venting of the helium gas, as discussed in Section 4.2.1. The Experiment Module is enclosed inside the outer structure to shield it from the drag forces produced by the residual Earth atmosphere at the assumed 200 km orbital altitude.

The outer body is controlled by a more conventional propulsion system, hydrazine. The thrusters for this system must be pulsed on and off in order to achieve the desired thrust level since they are limited physically by both a minimum thrust level and a minimum pulse-on time. It was also assumed that the sensors and actuators used for control were ideal and the aerodynamic forces were assumed to be adequately described by free molecular flow.

G.2 Simulation Description

The coordinate frames used in this simulation are illustrated in Figure G-1. The basic, inertial reference (pseudo inertial) coordinate system is defined as the E-frame. It is centered in the Earth with the z-axis pointing toward the vernal equinox, the y-axis aligned with the Earth spin axis, and the x-axis completing a right-handed, orthogonal set. The ascending node frame is defined as the A-frame. This frame has its origin at the center of the Earth; A_y is directed along the orbit normal; A_z is directed along the line of intersection of the orbit plane and the equatorial plane, positive toward the ascending node; and A_x completes the right-hand set.

The third frame is the local vertical frame, L. It is defined with the origin at the position of the nominal orbit with radius R_o . The L_z -axis is along the radius vector (the local vertical direction), and the L_y -axis is defined to be parallel to the orbit normal. L_x completes the right-handed triad, pointing generally along the velocity vector. The local vertical frame rotates on a circular path at a constant angular rate, ω_o . Additional reference frames, V1 and V2, are defined with origins at the centers of mass of bodies 1 and 2, respectively, with orientations parallel to the body geometric frames.

The inertial angular velocities of the spacecraft and Experiment Module are ω_1 and ω_2 , respectively. Body 1 is the spacecraft, or the outer body, and Body 2 is the Experiment Module, or the inner body. The motion of each is described by Hill's equations in translation, and by the angular momentum equations in rotation (the Newton-Euler equations expressed in terms of angular momentum).

G.2.1 Equations of Motion

The Experiment Module is assumed to be in a circular orbit at 200 km altitude. It will be actively controlled by compensating for the aerodynamic drag and by using thrusters to counter sensed accelerations. Displacements from the ideal orbit are expected to be quite small, thus making linear approximations (i.e., gradients) very accurate. Hill's equations utilize this assumption, and will adequately describe the motion, at least in this preliminary study. As the spacecraft design matures, higher order terms and additional refinements will be introduced. Hill's equations are described in Section G.3.1 [see equations (G-28) through (G-30)]. The rotational motion of each body is described by angular momentum equations:

$$\overset{\circ}{\vec{H}} = -\vec{\omega} \times \vec{H} + \vec{T}_g + \vec{T}_a + \vec{T}_j, \quad \text{where } \vec{H} = \vec{I} \cdot \vec{\omega} \quad (G-1)$$

where the circle above the H denotes the time derivative in body axes.

The rotational kinematic equations are defined, using quaternion relationships,

$$\dot{\vec{q}} = 0.5 \vec{\omega} \cdot \vec{q}, \quad \text{where } \vec{\omega} = \begin{bmatrix} 0 & \omega_3 & -\omega_2 & \omega_1 \\ -\omega_3 & 0 & \omega_1 & \omega_2 \\ \omega_2 & -\omega_1 & 0 & \omega_3 \\ -\omega_1 & -\omega_2 & -\omega_3 & 0 \end{bmatrix}. \quad (G-2)$$

The quaternions can be used to construct direction cosine matrices to transform between body and inertial coordinate frames.

G.2.2 Environmental Force Model

The environmental force models used in this simulation are as follows.

Earth Gravity Force and Torque: The spherical gravity force, \vec{F}_g , is given by

$$\vec{F}_g = - \left(\frac{G M_E m_S}{|\vec{R}|^3} \right) \vec{R} \quad , \quad (G-3)$$

where M_E and m_S are the mass of the Earth and spacecraft, respectively. Equation (G-3) can be written as

$$\vec{F}_g = - \left(\frac{G M_E m_S}{|\vec{R}_O|^3} \right) \left[\vec{R}_O + \vec{r}_S - \frac{3 \vec{R}_O \vec{R}_O}{|\vec{R}_O|^2} \cdot \vec{r}_S \right] \quad , \quad (G-4)$$

where the factor in square brackets is the gravity gradient force. Figure G-2(a) illustrates the geometry.

Since the orbital rate, ω_o , is given by

$$\omega_o^2 = \frac{G M_E}{|\vec{R}_O|^3} \quad , \quad (G-5)$$

the gravitational torque can be written as

$$\vec{T}_g = 3 \omega_o^2 \frac{\vec{R}_O \times \vec{I} \cdot \vec{R}_O}{|\vec{R}_O|^2} \quad , \quad (G-6)$$

where \vec{I} is the moment of inertia of the spacecraft.

Newton's Force Equation: Since

$$\ddot{\vec{R}}_O = -\omega_o^2 \vec{R}_O \quad , \quad (G-7)$$

$$m_S \ddot{\vec{r}}_S = m_S \omega_o^2 \left[-\vec{r}_S + 3 \frac{\vec{R}_o \vec{R}_o}{|\vec{R}_o|^2} \cdot \vec{r}_S \right] + \vec{F}_D , \quad (G-8)$$

where \vec{F}_D is the aerodynamic drag force on the spacecraft.

Newton-Euler Rotation Equation:

$$\vec{I} \cdot \dot{\vec{\omega}} = -\vec{\omega} \times \vec{I} \cdot \vec{\omega} + 3 \omega_o^2 \left(\frac{\vec{R}_o \times \vec{I} \cdot \vec{R}_o}{|\vec{R}_o|^2} \right) + \vec{T}_D , \quad (G-9)$$

where $\vec{\omega}$ is the angular velocity of the spacecraft and \vec{T}_D is the aerodynamic torque on the spacecraft.

Free-Molecular Flow Aerodynamic Model: The differential aerodynamic drag force is given by

$$d\vec{F} = \rho \vec{V}_{REL} \vec{V}_{REL} \cdot \hat{n} dA , \quad (G-10)$$

where ρ is the atmospheric density, \vec{V}_{REL} is the velocity of surface dA relative to the air molecules, dA is the differential surface area, and \hat{n} is the unit vector normal to the area [Fig. G-2(b)].

The relative velocity can also be written as

$$\vec{V}_{REL} = \vec{\omega}_o \times \vec{R}_o + \dot{\vec{r}} - \vec{\omega}_E \times (\vec{R}_o + \vec{r}) , \quad (G-11)$$

where $\vec{\omega}_E$ is the Earth rotation rate.

One may also write equation (G-10) as

$$\vec{F}_D = q \vec{C}_D A_{REF} , \quad (G-12)$$

where q is the dynamic pressure given by

$$q = \frac{1}{2} \rho \vec{V}_{REL}^2 . \quad (G-13)$$

The aerodynamic torque is given by

$$\vec{T}_D = q \vec{C}_M A_{REF} L_{REF} \quad . \quad (G-14)$$

Here, A_{REF} is the effective cross sectional area of the spacecraft.

By referring to Figure G-2(c), one may write the drag coefficient as

$$\vec{C}_D = - \frac{\pi R^2}{A_{REF}} (1 + \sin \alpha) \begin{bmatrix} \sin \alpha \sin \beta \\ \cos \alpha \\ \sin \alpha \cos \beta \end{bmatrix} , \quad (G-15)$$

where

$$\cos \alpha = \hat{U}_y \cdot \left(\frac{\vec{V}_{REL}}{|\vec{V}_{REL}|} \right) \quad (G-16)$$

and

$$\tan \beta = \frac{\hat{U}_x \cdot \vec{V}_{REL}}{\hat{U}_z \cdot \vec{V}_{REL}} \quad . \quad (G-17)$$

Here, \hat{U}_x , \hat{U}_y , and \hat{U}_z are unit vectors along the x, y, and z axes, respectively.

Because of symmetry,

$$\vec{C}_M = 0 \quad . \quad (G-18)$$

G.3 Control System Design and Analysis

G.3.1 Linearized Models

Translational Equations: The translational equations of motion are derived here for the outer spacecraft. Those of the Experiment Module will be identical. All forces, except gravity, are included in the vector denoted as \vec{f} . Referring to Figure G-3, the coordinate frame A lies in the plane of the orbit such that the Y_A -axis is parallel to the Y-axis of the local vertical frame. The position vector \vec{R}_O is, therefore, defined by

$$\vec{R}_O = R_O \cos \omega_O t \vec{Z}_A + R_O \sin \omega_O t \vec{X}_A, \quad (G-19)$$

where t is time and ω_O is the constant angular rate of the local vertical frame, given by equation (G-5). Differentiating equation (G-19) twice with respect to time leads to

$$\ddot{\vec{R}}_O = -R_O \omega_O^2 (\cos \omega_O t \vec{Z}_A + \sin \omega_O t \vec{X}_A). \quad (G-20)$$

R_1 is the position vector of the center-of-mass of the spacecraft with respect to the local vertical. From Newton's second law, the sum of the forces acting on the spacecraft must equal the time rate of change of the linear momentum. Thus,

$$m_1 (\ddot{\vec{R}}_O + \ddot{\vec{R}}_1) = \vec{F}_g + \vec{f}. \quad (G-21)$$

The force due to gravity is defined by

$$\vec{F}_g = \left(\frac{-G M m_1}{|\vec{R}_O + \vec{R}_1|^3} \right) (\vec{R}_O + \vec{R}_1). \quad (G-23)$$

If it is assumed that $|\vec{R}_1| \ll |\vec{R}_O|$, and a binomial expansion is used, keeping only first order terms in \vec{R}_1 , the gravitational force can be written as

$$\vec{F}_g = \frac{-G M_E m_1}{|\vec{R}_O|^3} (\vec{R}_O + \vec{R}_1) \left(1 - \frac{3 \vec{R}_1 \cdot \vec{R}_O}{|\vec{R}_O|^2} \right). \quad (G-23)$$

Using equation (G-25), equation (G-23) can be written as

$$\vec{F}_g = -m_1 \omega_O^2 (\vec{R}_O + \vec{R}_1) \left(1 - \frac{3 \vec{R}_1 \cdot \vec{R}_O}{|\vec{R}_O|^2} \right). \quad (G-24)$$

Substituting equation (G-24) into equation (G-21) yields

$$\ddot{\vec{R}}_1 = -\omega_O^2 \vec{R}_1 \left(1 - \frac{3 \vec{R}_1 \cdot \vec{R}_O}{|\vec{R}_O|^2} \right) + \omega_O^2 \vec{R}_O \left(\frac{3 \vec{R}_1 \cdot \vec{R}_O}{|\vec{R}_O|^2} \right) + \frac{\vec{f}}{m_1}. \quad (G-25)$$

In order to express the components of equation (G-25) in a rotating local vertical frame, the following notations are first defined: $\dot{\mathbf{R}}$ is the time derivative of \mathbf{R} as seen by an observer fixed in inertial space, and $\dot{\mathbf{R}}_0$ is the time derivative of \mathbf{R} as seen by an observer in the local frame. Thus,

$$\dot{\mathbf{R}} = \dot{\mathbf{R}}_0 + \vec{\omega}_0 \times \mathbf{R} \quad . \quad (\text{G-26})$$

Since ω_0 is constant, equation (G-26) can be differentiated with respect to time to produce

$$\ddot{\mathbf{R}} = \ddot{\mathbf{R}}_0 + \vec{\omega}_0 \times (\vec{\omega}_0 \times \mathbf{R}) + 2 \vec{\omega}_0 \times \dot{\mathbf{R}}_0 \quad . \quad (\text{G-27})$$

Using equations (G-25) and (G-27) and ignoring second-order effects, the equations that govern translational motion of the spacecraft are obtained as

$$\ddot{X}_1 = - 2 \omega_0^2 Z_1 + \frac{f_x}{m_1} \quad , \quad (\text{G-28})$$

$$\ddot{Y}_1 = - \omega_0^2 Y_1 + \frac{f_y}{m_1} \quad , \quad (\text{G-29})$$

$$\ddot{Z}_1 = 2 \omega_0^2 X_1 + 3 \omega_0^2 Z_1 + \frac{f_z}{m_1} \quad , \quad (\text{G-30})$$

where f again includes all forces other than those produced by gravitational effects.

In these equations, X_1 , X_2 , and Z_1 define the components of \mathbf{R}_1 with respect to the local vertical frame. This formulation avoids the numerical problems of referencing the spacecraft position from the center of the Earth. This is especially useful for contact dynamics simulation which requires the relative position between the inner and outer bodies.

Rotational Equations: The rotational equations of motion for the satellite and Experiment Module are the well-known Newton-Euler equations:

$$\dot{\vec{\mathbf{I}}} \cdot \vec{\omega} = - \vec{\omega} \times \vec{\mathbf{I}} \cdot \vec{\omega} + \vec{\mathbf{T}} \quad , \quad (\text{G-31})$$

where $\vec{\omega}$ is the angular velocity of the vehicle, $\vec{\mathbf{I}}$ is the inertia dyadic about the vehicle center-of-mass, and $\vec{\mathbf{T}}$ is the torques acting about the vehicle center-of-mass.

Note that the Newton-Euler equations are not restricted to small angle rotations of the vehicle.

The torque vector consists of gravity gradient, contact, and attitude control system torques. Equation (G-31) is expressed in a vehicle-fixed frame so that the inertia dyadic will remain constant. This equation does not limit the body axes to align with the principle moment of inertia axes. In other words, the inertia matrix does not have to be diagonal. The gravity gradient torque acting on the body is

$$\vec{T}_g = 3 \omega_o^2 \left(\frac{\vec{R}_o}{|\vec{R}_o|} \right) \times \vec{I} \cdot \left(\frac{\vec{R}_o}{|\vec{R}_o|} \right) . \quad (G-32)$$

The rotational equations of motion are derived here for the outer spacecraft. Those of the Experimental Module will be identical.

The fundamental equations used for both the V1- and V2-frames are

$$\dot{\vec{H}} = \vec{I} \cdot \dot{\vec{\omega}} \quad (G-33)$$

$$\frac{d}{dt} \vec{H} = \vec{T} . \quad (G-34)$$

Consider the local-vertical frame, L, and the body-fixed frame, V1, shown in Figure G-3. Assume the V1-frame is originally aligned with the L-frame. Due to disturbances, the V1-frame differs from the L-frame by small perturbation angles denoted by θ_1 , θ_2 , θ_3 . The transformation from the L frame to the V1 frame is given to first order by

$$\vec{C}_{[V1L]} = \begin{bmatrix} 1 & \theta_3 & -\theta_2 \\ -\theta_3 & 1 & \theta_1 \\ \theta_2 & -\theta_1 & 1 \end{bmatrix} . \quad (G-35)$$

If the spacecraft is assumed to have a nominal angular velocity of ω_o about the orbit-normal axis, the angular velocity of the spacecraft can be expressed in the body frame as

$$\vec{\omega} = \dot{\vec{\theta}} + \vec{C}_{[V1L]} \cdot \omega_o \hat{j} , \quad (G-36)$$

$$\vec{\omega} = \begin{pmatrix} \dot{\theta}_1 + \omega_o \theta_3 \\ \dot{\theta}_2 + \omega_o \theta_1 \\ \dot{\theta}_3 - \omega_o \theta_2 \end{pmatrix} . \quad (G-37)$$

Equations (G-33) and (G-34) can be combined into the Newton-Euler equation, equation G-31). Assuming that the matrix I is diagonal, this equation can be expanded as

$$\begin{aligned} I_1 \dot{\omega}_1 &= (I_2 - I_3) \omega_2 \omega_3 + T_1 , \\ I_2 \dot{\omega}_2 &= (I_3 - I_1) \omega_3 \omega_1 + T_2 , \\ I_3 \dot{\omega}_3 &= (I_1 - I_2) \omega_1 \omega_2 + T_3 . \end{aligned} \quad (G-38)$$

Then, from equation (G-37),

$$\dot{\omega} = \begin{pmatrix} \ddot{\Theta}_1 + \omega_0 \dot{\Theta}_3 \\ \ddot{\Theta}_2 \\ \ddot{\Theta}_3 - \omega_0 \dot{\Theta}_1 \end{pmatrix} . \quad (G-39)$$

After combining equations (G-37), (G-38), and (G-39), and retaining only the first order terms in the six perturbation variables, the resulting equations are

$$\begin{aligned} I_1 (\ddot{\Theta}_1 + \omega_0 \dot{\Theta}_3) &= (I_2 - I_3) (\omega_0 \dot{\Theta}_3 - \omega_0^2 \Theta_1) + T_1 , \\ I_2 \ddot{\Theta}_2 &= T_2 , \\ I_3 (\ddot{\Theta}_3 - \omega_0 \dot{\Theta}_1) &= (I_1 - I_2) (\omega_0 \dot{\Theta}_1 + \omega_0^2 \Theta_3) + T_3 . \end{aligned} \quad (G-40)$$

Equation (G-40) can be written in the more convenient form:

$$\begin{aligned} I_1 \ddot{\Theta}_1 &= (I_2 - I_3 - I_2) \omega_0 \dot{\Theta}_3 - \omega_0^2 (I_2 - I_3) \Theta_1 + T_1 , \\ I_2 \ddot{\Theta}_2 &= T_2 , \\ I_3 \ddot{\Theta}_3 &= (I_1 + I_3 - I_2) \omega_0 \dot{\Theta}_1 + \omega_0^2 (I_1 - I_2) \Theta_3 + T_3 . \end{aligned} \quad (G-41)$$

These equations are linearized rotational equations of motion for a rigid body undergoing perturbations away from a nominal orbit, normal rotation.

The torque applied to each body includes both environmental disturbance torques and control torques. The gravity gradient torque readily lends itself to the linearized equations of motion because of its relatively simple form, i.e.,

$$\vec{T}_g = 3 \omega_o^2 \hat{a} \times \vec{I} \cdot \hat{a} , \quad (G-42)$$

where \hat{a} is the unit vector lying along the radius vector:

$$\hat{a} = \vec{R} / |\vec{R}| . \quad (G-43)$$

The vector a can be expressed in the V1-frame by the use of equation (G-35):

$$\hat{a}_{[V1]} = \begin{pmatrix} -\Theta_2 \\ \Theta_1 \\ 1 \end{pmatrix} . \quad (G-44)$$

The gravity gradient torque is easily found by substituting equation (G-44) into equation (G-42), resulting in

$$T_g = 3\omega_o^2 \begin{pmatrix} (I_3 - I_2)\Theta_1 \\ (I_3 - I_1)\Theta_2 \\ 0 \end{pmatrix} . \quad (G-45)$$

The linear expression for T_g can be substituted into equation (G-25) with the result:

$$I_1 \ddot{\Theta}_1 = (I_2 - I_3 - I_1)\omega_o \dot{\Theta}_3 + 4\omega_o^2(I_3 - I_2)\Theta_1 + T_1 , \quad (G-46a)$$

$$I_2 \ddot{\Theta}_2 = 3\omega_o^2(I_3 - I_1)\Theta_2 + T_2 , \quad (G-46b)$$

$$I_3 \ddot{\Theta}_3 = (I_1 + I_3 - I_2)\omega_o \dot{\Theta}_1 + \omega_o^2(I_1 - I_2)\Theta_3 + T_3 , \quad (G-46c)$$

where T_1 , T_2 , and T_3 do not contain the gravity gradient torque. Equations (G-46) can be expressed in the following state variable form:

$$\begin{aligned}
\frac{d}{dt} \begin{Bmatrix} \theta_1 \\ \dot{\theta}_1 \\ \theta_2 \\ \dot{\theta}_2 \\ \theta_3 \\ \dot{\theta}_3 \end{Bmatrix} = & \begin{bmatrix} 0 & 1 & 0 & 0 & 0 & 0 \\ 4\omega_0^2 \frac{(I_3 - I_2)}{I_1} & 0 & 0 & 0 & 0 & \omega_0 \frac{(I_2 - I_3 - I_1)}{I_1} \\ 0 & 0 & 0 & 1 & 0 & 0 \\ 0 & 0 & 0 & 0 & 0 & 0 \\ 0 & \omega_0 \frac{(I_1 + I_3 - I_2)}{I_3} & 0 & 0 & 0 & 0 \\ 0 & 0 & 0 & 0 & \omega_0 \frac{2(I_1 - I_2)}{I_3} & 0 \end{bmatrix} \begin{Bmatrix} \theta_1 \\ \dot{\theta}_1 \\ \theta_2 \\ \dot{\theta}_2 \\ \theta_3 \\ \dot{\theta}_3 \end{Bmatrix} \\
+ & \begin{bmatrix} 0 & 0 & 0 \\ 1/I_1 & 0 & 0 \\ 0 & 0 & 0 \\ 0 & 1/I_2 & 0 \\ 0 & 0 & 0 \\ 0 & 0 & 1/I_3 \end{bmatrix} \begin{Bmatrix} T_1 \\ T_2 \\ T_3 \end{Bmatrix} . \tag{G-47}
\end{aligned}$$

G.3.2 Experiment Module Control

Thruster Geometry: A proportional thruster pod arrangement, as shown in Figure G-4, is located at the tip of each of the four protrusions from the Experiment Module through the outer spacecraft surface. By adjusting the valve controlling the helium gas flow to a vent, its thrust can be very accurately controlled (see Section 4.2.1). Thus, by firing the appropriate thruster, torques for attitude control can be achieved. This thruster arrangement provides for simple thruster selection control logic with some failure mode redundancy.

Control Logic: The form of the control law implemented on the Experiment Module is that of a simple OD (proportional plus derivative) controller. The PD controller adds positive phase angles to the frequency response of the system so that the system stability is improved. It also increases the bandwidth and, thus, the response speed of the system. If the Laplace transform is applied to equation (G-46b), the result for the Experiment Module is

$$(122 \text{ s}^2 + 2.94 \text{ E-}5) \theta_2(s) = T_2(s) \tag{G-48}$$

A block diagram of equation (G-48), which includes the PD controller loops, is shown in Figure G-5. The '122' in the inner feedback path is the proportional gain, and the '172.51' in the outer path is the derivative or rate gain. These gains were selected to give a closed-loop natural frequency of 1 rad sec⁻¹ and a damping ratio of 0.7. The open- and closed-loop frequency responses are shown in Figure G-6(a) and G-6(b), respectively, where the magnitude is given by the solid lines and the phase by dashed lines. The disturbance rejection properties of the control system are easily appreciated by examining the low-frequency gains, as illustrated in the figure.

The PD controller for the other axes of the Experiment Module were designed in the same manner as described here.

G.3.3 Outer Spacecraft Control

Thruster Geometry: The thruster system, containing 24 thrusters, is used to control the outer spacecraft and to counteract external disturbances such as aerodynamic drag (Fig. G-7). Eight of these are intended strictly for drag compensation and are located on opposing ends of the outer body in groups of four.

Helium gas proportional thrusters are not practical for the outer spacecraft because of the large drag forces experienced at an altitude of 200 km. The eight hydrazine drag compensating thrusters located along the long axis must be pulsed on and off and operate frequently in order to develop the small force needed. The other 16 thrusters are located along axes which experience only a small component of drag, and will thus be fired only as necessary to keep the outer spacecraft aligned with the inner body.

Control Logic: The spacecraft controller is a PID (proportional plus integral plus derivative feedback) type system. The integral feedback term was included on the spacecraft controller to counteract the approximately constant aerodynamic drag term. (Variation in aerodynamic drag forces should be investigated in subsequent studies utilizing a higher fidelity model.) The drag disturbance is not considered in the Experiment Module analysis. The rotational equation of motion about axis 2 is

$$(18803 \text{ s}^2 - 0.0736) \theta_2(s) = T_2(s) \quad . \quad (G-49)$$

This equation is the spacecraft equivalent to equation (G-48). The block diagram of the closed-loop system is shown in Figure G-8.

The constants shown in Figure G-8 (320.967, 9.4015, 3598.89) are the proportional, integral, and derivative (rate) gains, respectively. These gains were selected to give a closed-loop natural frequency of 0.1 rad sec^{-1} and a damping ratio of 0.7. The open- and closed-loop frequency responses are shown in Figures G-9(a) and G-9(b), respectively. The solid lines represent the magnitude, while the dashed lines show the phase. This figure clearly illustrates the low-frequency disturbance rejection capability of the closed-loop system.

G.4 Simulation Results

Figures G-10 through G-12 illustrate the transient response of the SGGM spacecraft, starting at zero inertial attitude rate with, displacement error, zero velocity error, zero attitude error, and orbital angular rate error.

Figure G-10 illustrates the outer spacecraft control system (primary thrusters) compensating for the induced drag forces. Figure G-11 shows the transient response of the outer spacecraft as the position control system compensates for the drag forces and removes the induced errors. Drag forces initially induce an error along the spacecraft Y-axis (local horizontal) with respect to the ideal circular reference orbit. The action of the integral feedback in the control law removes these errors. The spacecraft response is shown in the figure by the dashed line. Note that the maximum excursion was approximately 1.7 cm and the spacecraft is returned to its original position in about 100 sec. The dash-dot curve of Figure G-11 illustrates the

correction for errors along the spacecraft Z-axis (local vertical) that result from dynamic coupling between the two axes in the orbital plane. This error is also removed by the integral feedback of the control system. Rotational control is illustrated in Figure G-12. The response is entirely along the X-axis (orbit normal) of the spacecraft as the control system commands thruster firings to rotate the vehicle at orbital rate to remove any attitude errors that have accumulated. The inner Experiment Module responses are similar to those illustrated in Figures G-10 through G-12.

REFERENCE

- G-1. Kaplan, M.: Modern Spacecraft Dynamics and Control. John Wiley and Sons, New York, 1976, pp. 111-113.

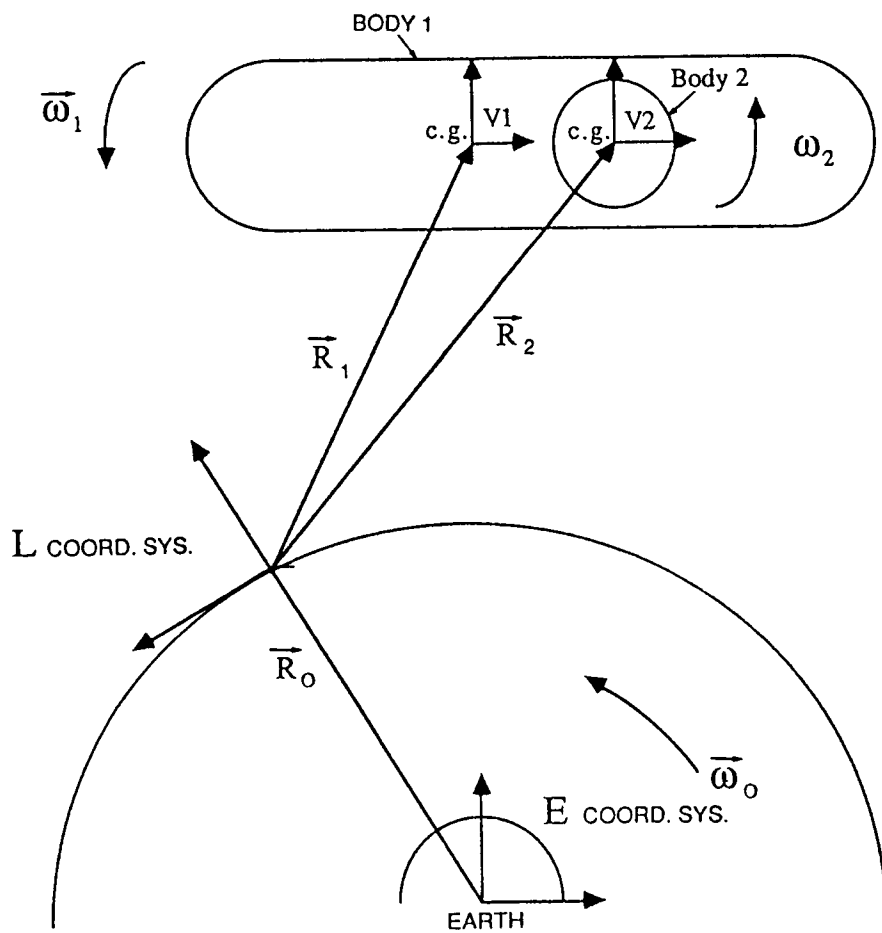
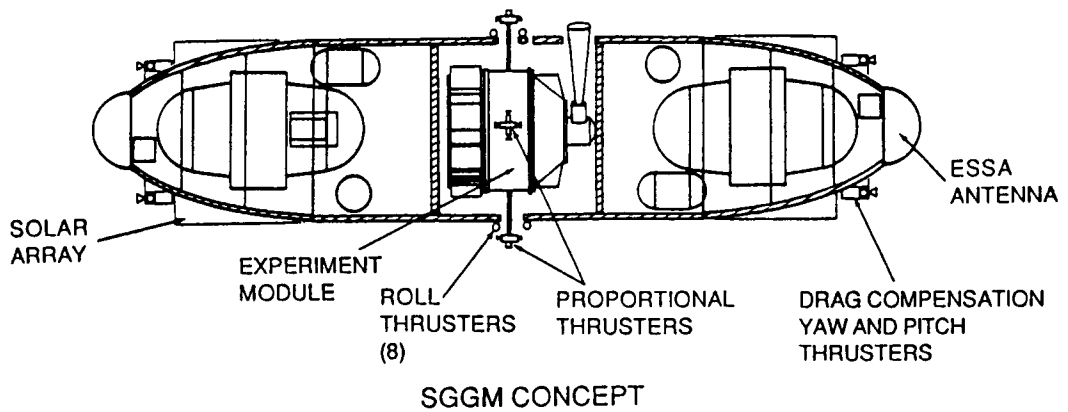
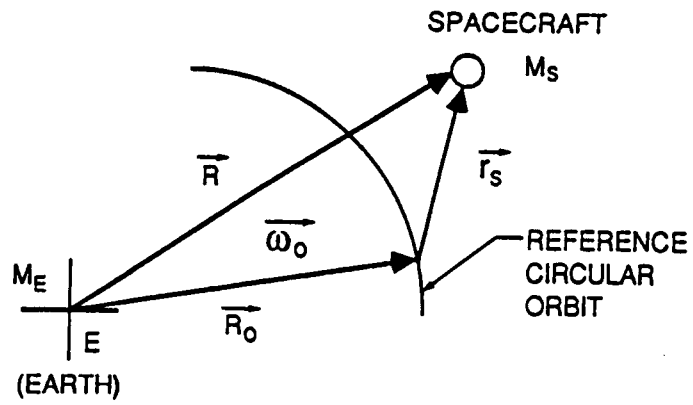
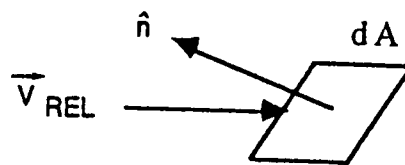


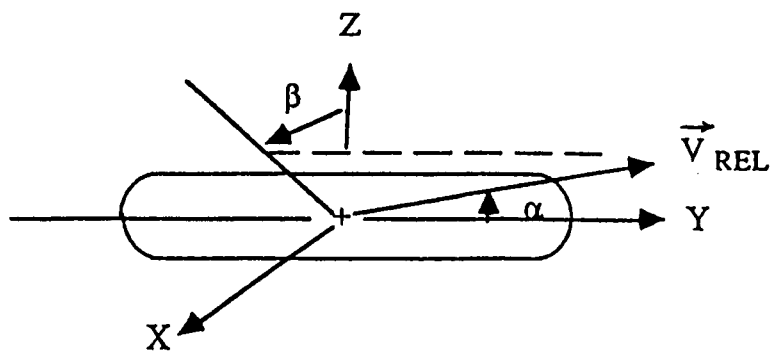
Figure G-1. Simulation geometry.



(a) SPHERICAL GRAVITY FORCE



(b) FREE-MOLECULAR FLOW



(c) AERODYNAMIC DRAG

Figure G-2. Environmental force model-geometric relationships.

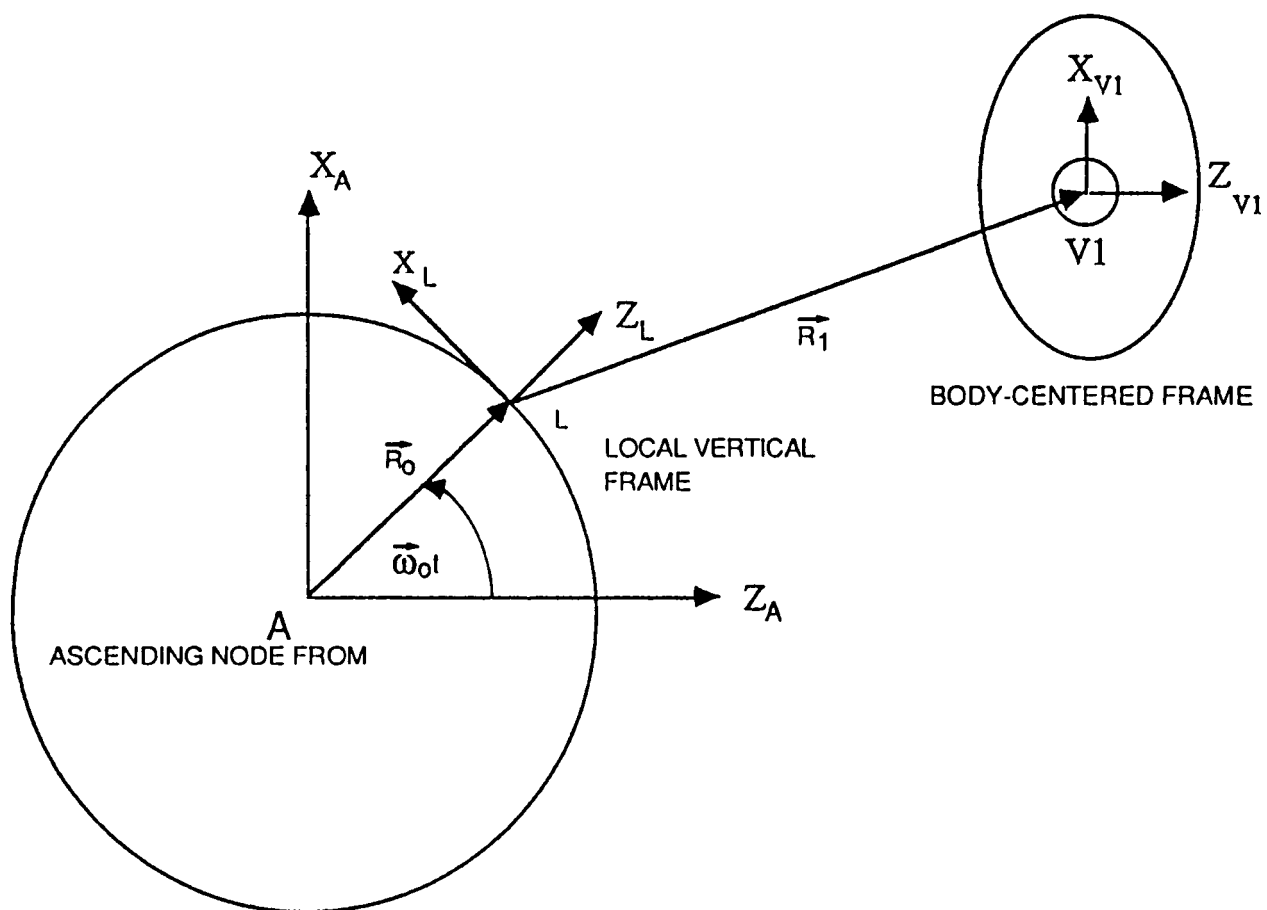


Figure G-3. Ascending node (A), local vertical (L), and body-centered reference frames (V_1, V_2).

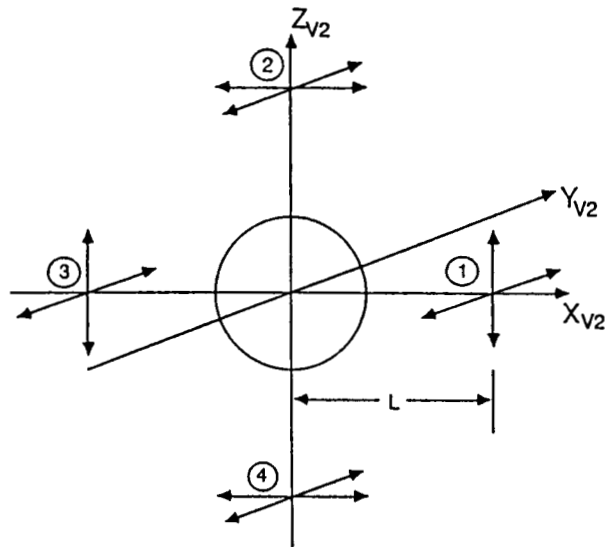
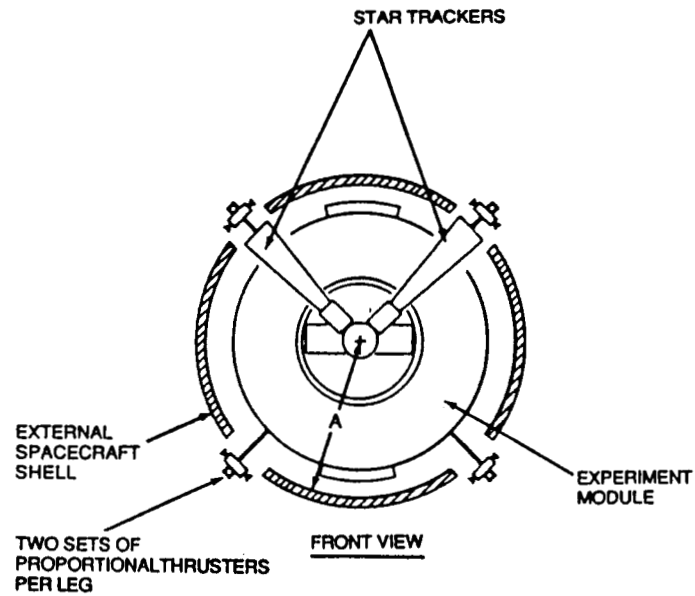


Figure G-4. Experiment module thruster geometry.

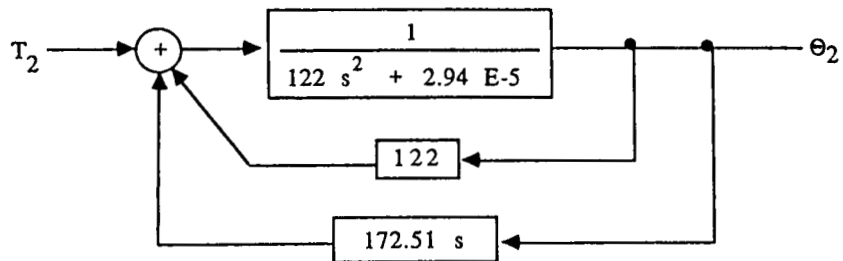


Figure G-5. Block diagram of PD controller for the Experiment Module.

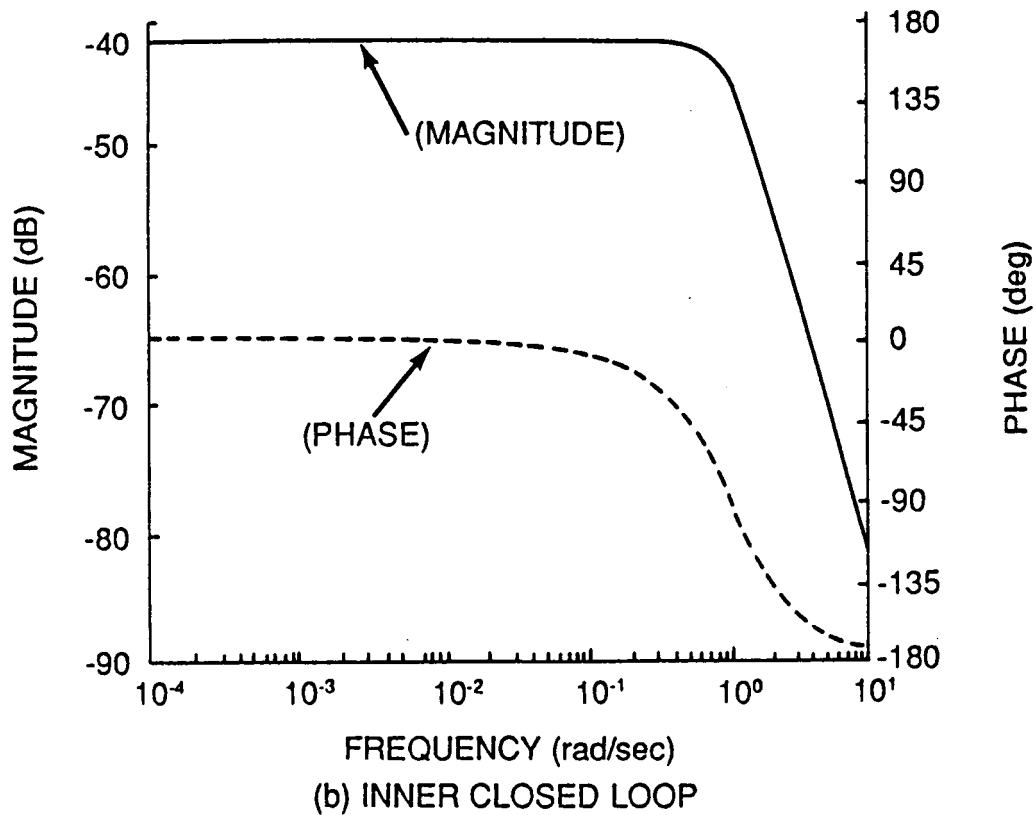
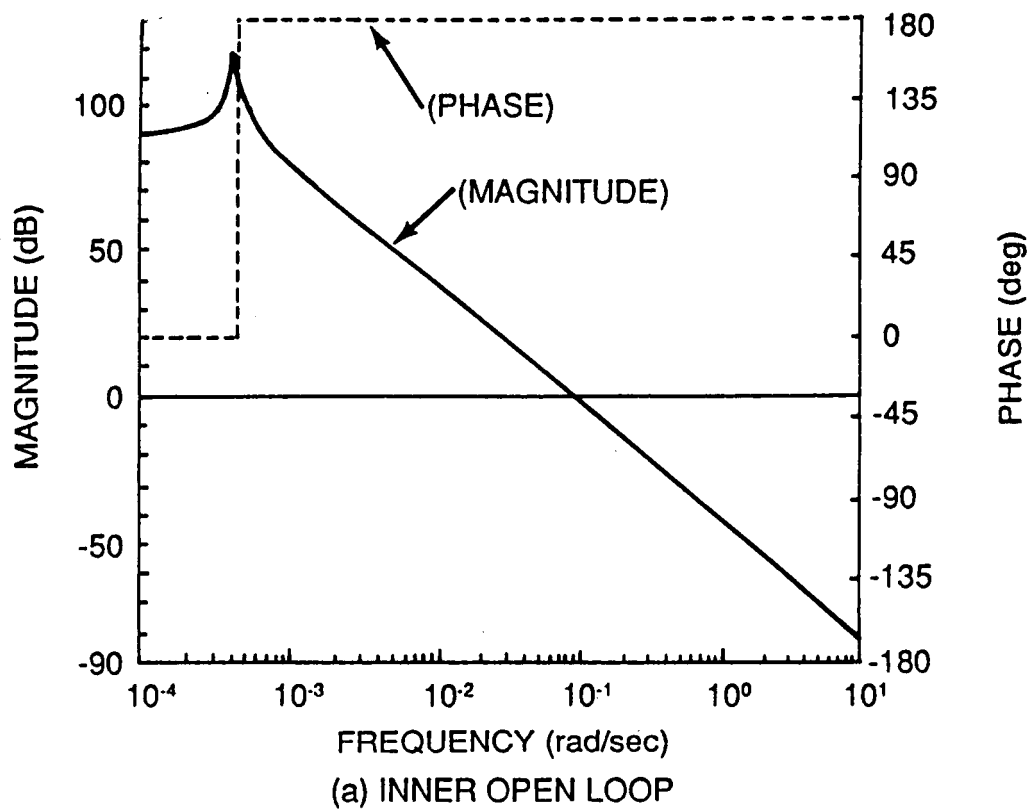


Figure G-6. Experiment Module frequency response.

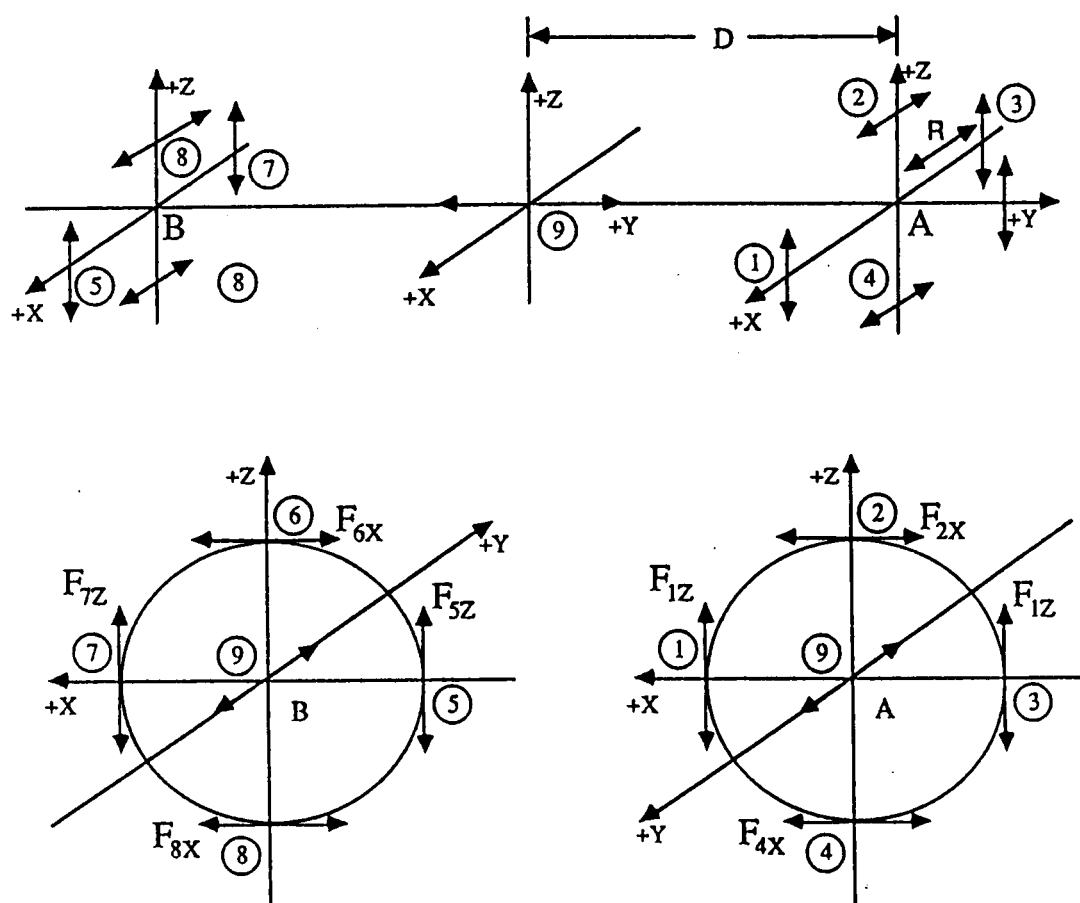
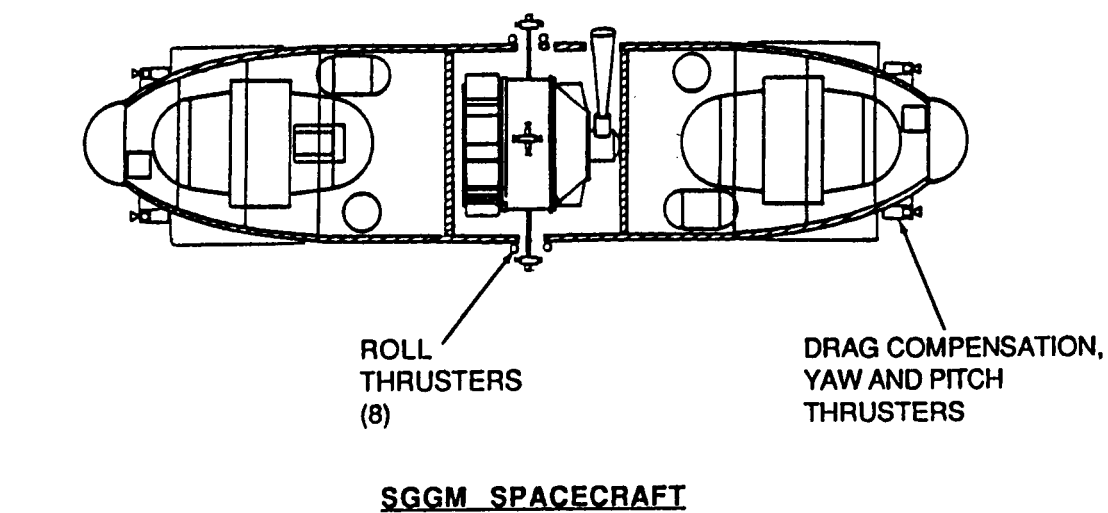


Figure G-7. Outer spacecraft thruster control.

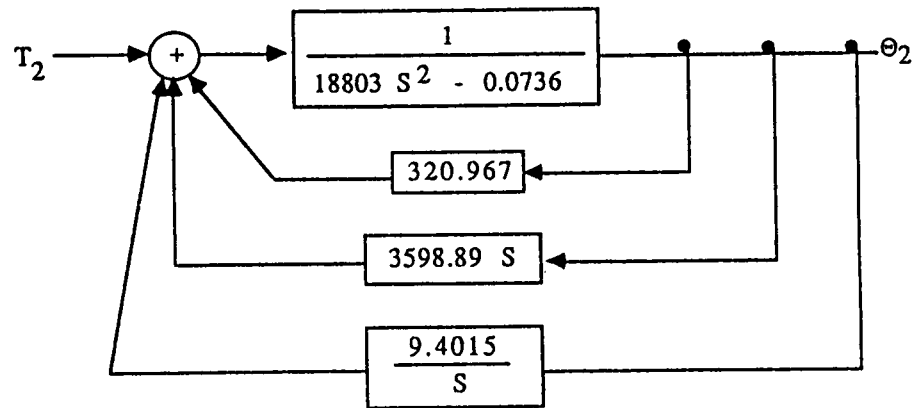


Figure G-8. Block diagram of PDI controller for the outer spacecraft.

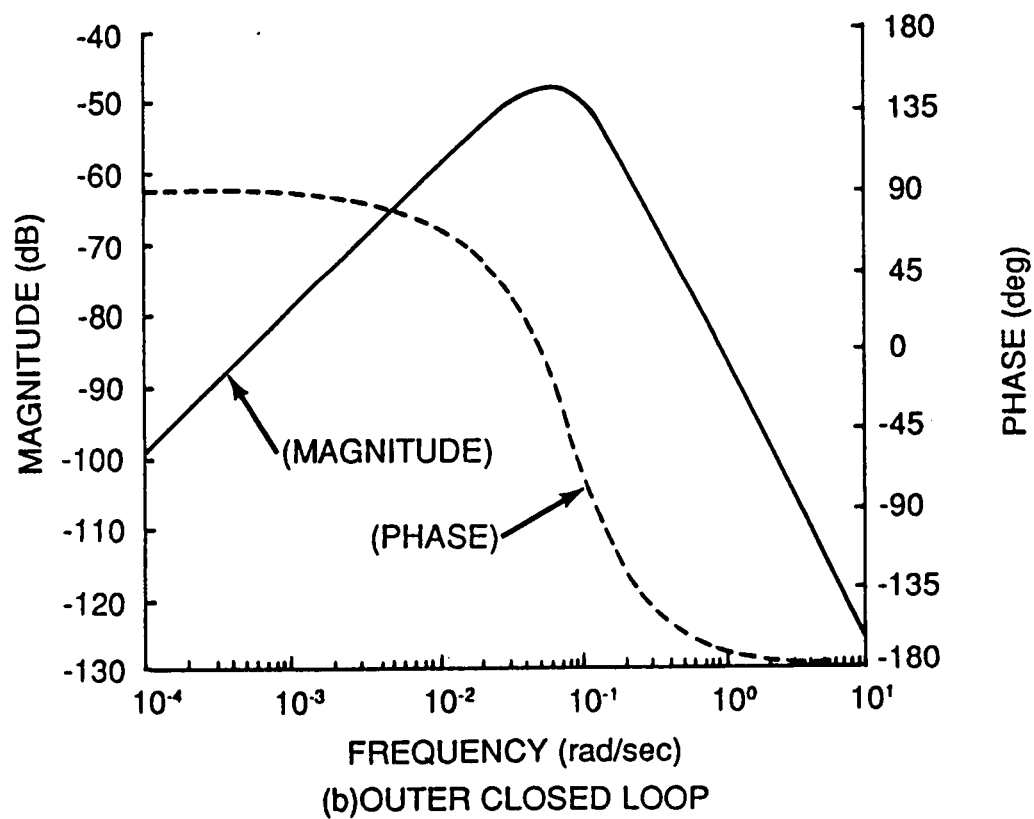
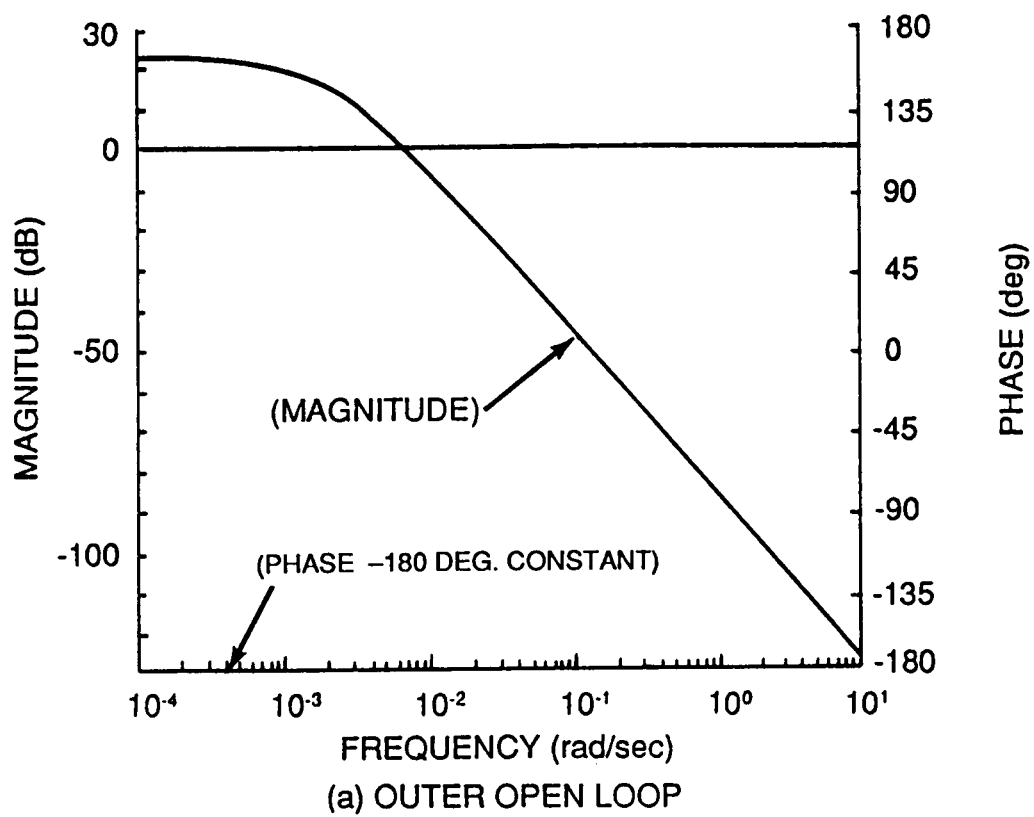


Figure G-9. Outer spacecraft frequency response.

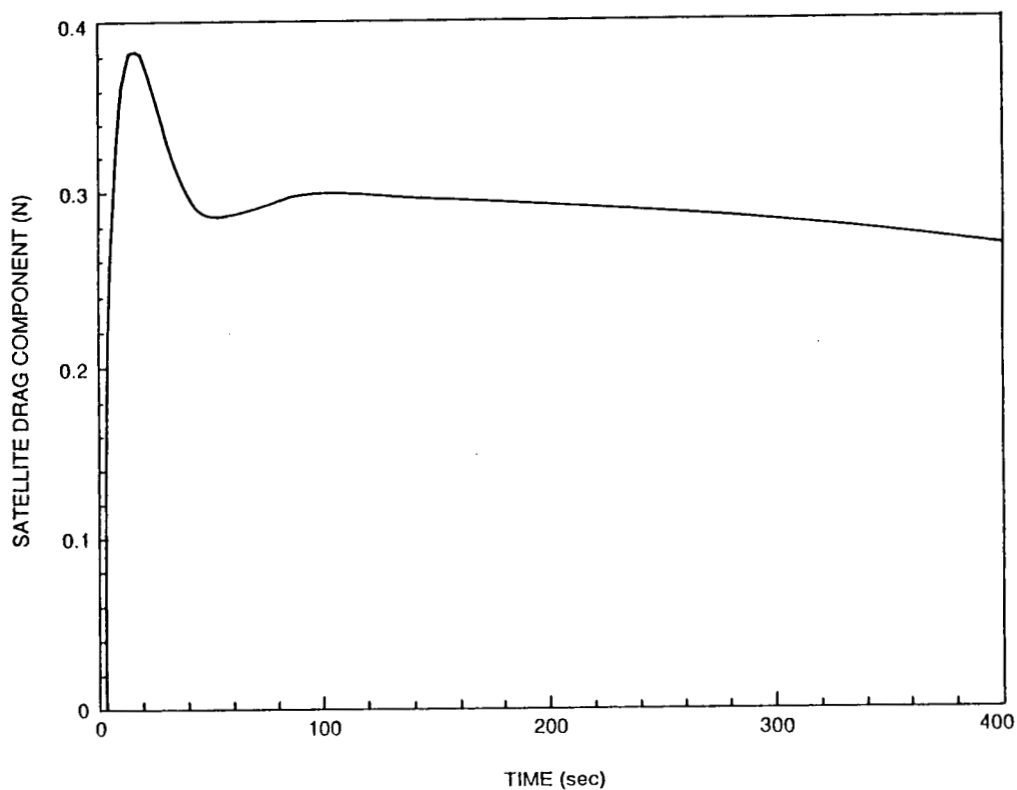


Figure G-10. Spacecraft primary thruster compensation for drag forces.

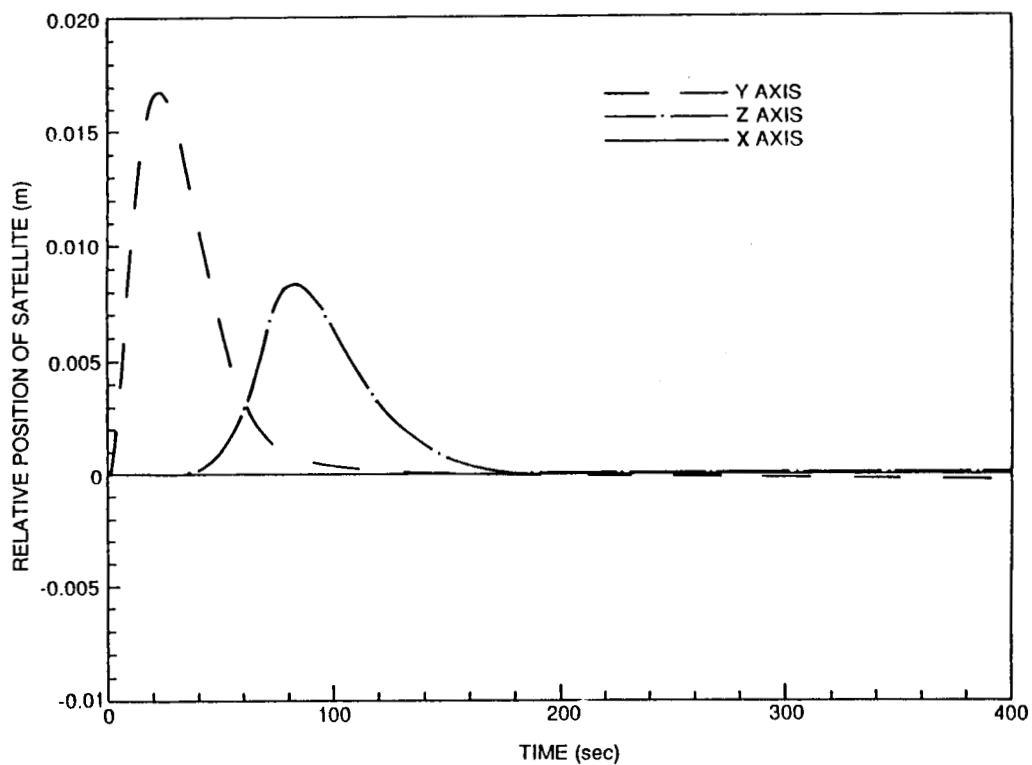


Figure G-11. Linear transient response of spacecraft-position relative to body centered frame.

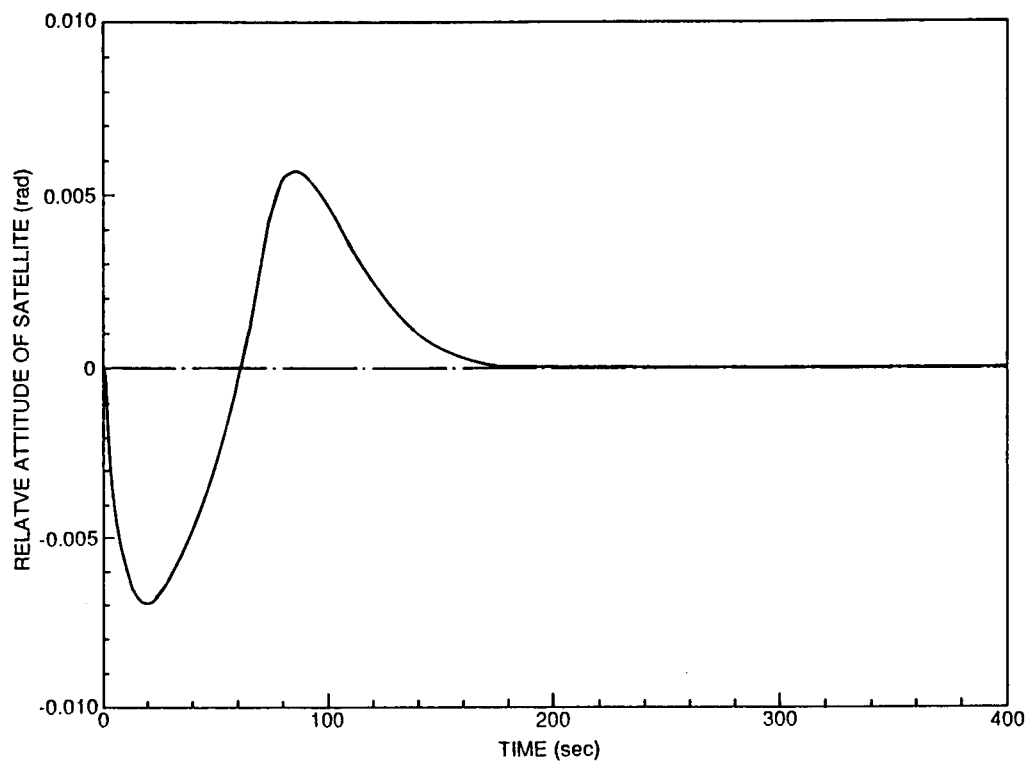


Figure G-12. Rotational transient response of outer spacecraft.

1. REPORT NO. NASA TM-4091		2. GOVERNMENT ACCESSION NO.		3. RECIPIENT'S CATALOG NO.	
4. TITLE AND SUBTITLE Superconducting Gravity Gradiometer Mission - Volume II: Study Team Technical Report				5. REPORT DATE November 1988	
				6. PERFORMING ORGANIZATION CODE M-601	
7. AUTHOR(S) Samuel H. Morgan and Ho Jung Paik,* Editors				8. PERFORMING ORGANIZATION REPORT #	
9. PERFORMING ORGANIZATION NAME AND ADDRESS George C. Marshall Space Flight Center Marshall Space Flight Center, AL 35812				10. WORK UNIT NO. RTOP 676-59-33	
				11. CONTRACT OR GRANT NO.	
12. SPONSORING AGENCY NAME AND ADDRESS Office of Space Science and Applications National Aeronautics and Space Administration Washington, D.C. 20546				13. TYPE OF REPORT & PERIOD COVERED Technical Memorandum	
				14. SPONSORING AGENCY CODE	
15. SUPPLEMENTARY NOTES Marshall Space Flight Center, Alabama, Program Development Office *Department of Physics and Astronomy, University of Maryland, College Park, MD 20742.					
16. ABSTRACT This report is based upon the scientific and engineering studies and developments performed or directed by a Study Team composed of various Federal and University activities involved with the development of a three-axis Superconducting Gravity Gradiometer integrated with a six-axis superconducting accelerometer. This instrument is being developed for a future orbital mission to make precise global gravity measurements. The scientific justification and requirements for such a mission are discussed. This includes geophysics, the primary mission objective, as well as secondary objectives, such as navigation and tests of fundamental laws of physics, i.e., a null test of the inverse square law of gravitation and tests of general relativity. The instrument design and status along with mission analysis, engineering assessments, and preliminary spacecraft concepts are discussed. In addition, critical spacecraft systems and required technology advancements are examined. The mission requirements and an engineering assessment of a precursor flight test of the instrument are discussed.					
17. KEY WORDS Geodesy, Geodynamics, Gravity, General Relativity, Gradiometers, Accelerometers, and Superconductivity			18. DISTRIBUTION STATEMENT Unclassified -- Unlimited Subject Category: 46		
19. SECURITY CLASSIF. (of this report) Unclassified		20. SECURITY CLASSIF. (of this page) Unclassified		21. NO. OF PAGES 249	
				22. PRICE A12	